


# The effects of high fat diet feeding on cardiac function in the C57BL6/J mouse strain

**A thesis submitted for the degree of Doctor of Philosophy**

***Henrik CA Isackson***

**Exeter College**

**&**

**Department of Cardiovascular Medicine**

**University of Oxford**

**Hilary term, 2013**

**Supervisors:**

**Doctor Charles S Redwood**

**Professor Hugh Watkins**

# 1 Introduction

This chapter aims to give an introduction to the processes that govern cardiac contraction on the single cardiomyocyte level. Since the thesis concerns effects on contractility from a condition altering the metabolic substrate dependence, glucose and fatty acid metabolism will be covered briefly along with an introduction to the condition of diabetic cardiomyopathy and mouse models available to study the effects of diabetes.

## 1.1 Cardiomyocyte contractility

### 1.1.1 The initiation of cardiomyocyte contraction

Cardiac contraction is initiated by a rise in [$Ca^{2+}$] surrounding the contractile apparatus. This leads to binding of $Ca^{2+}$ to the thin filament which will facilitate the interaction between the thin and thick filament through the actomyosin cross bridge cycling process, generating force upon ATP hydrolysis. Alterations in the process of intracellular $Ca^{2+}$ handling and myofilament dynamics will affect the contractile performance of the cardiomyocyte.

#### *1.1.1.1 Excitation contraction coupling*

Like striated skeletal muscle, the myocardium is excited by an electrical impulse, the action potential (AP). As the AP, generated in the sinus node, travels through the atrioventricular (AV) node and splits into the Purkinje fibres, it excites the ventricular cardiomyocytes in a synchronised fashion ensuring effective expulsion of blood from the left (LV) and right ventricles (RV), into the systemic and pulmonary circulation,

respectively. The delay between the arrival of the AP and contraction is due to the process of excitation-contraction (EC) coupling (Sandow, 1952), a process in which $Ca^{2+}$ plays a pivotal role. The temporal relationship between the AP, [$Ca^{2+}$] rise in the cytoplasm, and muscle contraction was first directly illuminated Ashley and Ridgway in 1968, using microinjection of the blue luminescent protein aequorin into muscle fibres of *Balanus nubilus.* They could describe the central role of the ion in determining force generation as the peak $Ca^{2+}$ amplitude coincides with the maximum rate of force generation (Ashley and Ridgway, 1968). From this it can be assumed that the intracellular rise and decay of $Ca^{2+}$ needs to be under tight regulation in order to maintain efficient contraction. The basis for this is anatomical as well as functional in nature.

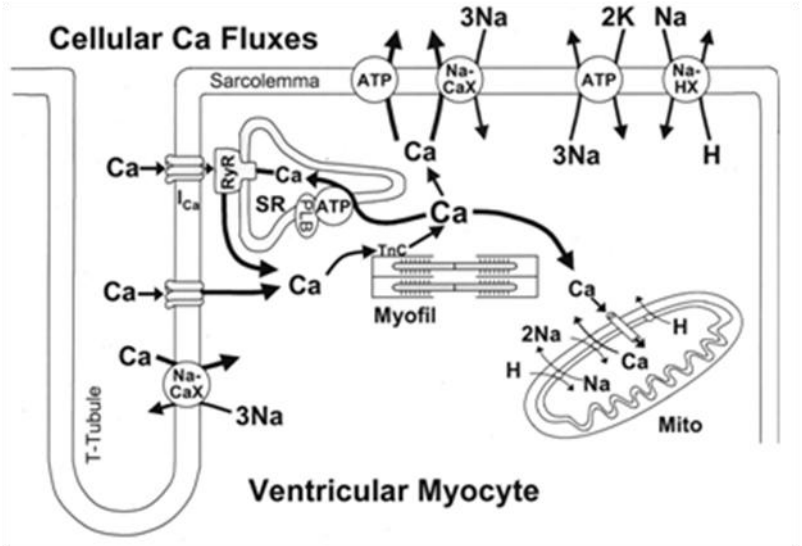



**Figure 1: Cardiomyocyte $Ca^{2+}$ handling** A summary of ion transport events involved in EC- coupling and intracellular $Ca^{2+}$-homeostasis **(Bers, 2000)**

1.1.1.1.1 Calcium induced calcium release (CICR)

As seen in Figure 1, four structures are central in CICR: the transverse tubuli (T-tubuli) system of the sarcolemma, the L-type calcium channels (LTCC), the sarcoplasmatic

reticulum (SR), and the ryanodine receptor (RyR). The sarcolemmal membrane of the cardiomyocyte displays invaginations that protrude into the myocyte surrounding the myofibrillae assuming a transverse orientation to these at the level of the Z-disk. These are referred to as transverse (T)-tubuli. The AP travels along the cardiomyocyte sarcolemma and into the T-tubuli. This structure thus provides easy access to the depths of the myocyte aiding in synchronizing the contractile process of the myofibrillae in the cardiomyocyte. The T-tubuli membrane harbours the voltage sensitive LTCC (Orchard and Brette, 2008). Upon arrival of the AP the LTCC will open which enables a small influx of $Ca^{2+}$ from the extracellular space into the cytoplasm along a concentration gradient. The rise in cytosolic [$Ca^{2+}$] due to the LTCC is however insufficient to initiate contraction. The SR is a membranous organelle in the cardiomyocyte cytoplasm. It is spatially associated with the T-tubuli. Its main function is to sequester and release $Ca^{2+}$ to initiate and terminate contraction. The $Ca^{2+}$ sensitive RyRs of the SR are located adjacent to the LTCC. This junction is made up of 10-25 LTCC and 100-200 RyR. The LTCC and RyR duo has been termed a "couplon". LTCCs only activate the RyRs in the associated couplon, where [$Ca^{2+}$] reaches 20-50 μM, as spatial [$Ca^{2+}$] diffusion to neighbouring couplons will result in dilution below the critical concentration threshold. The SR holds a high concentration of $Ca^{2+}$ and as the RyR binds $Ca^{2+}$ its open probability will increase with a resulting large efflux of $Ca^{2+}$ from the SR into the cytoplasm ([$Ca^{2+}$]=200-400 μM) initiating contraction by binding to troponin C (cTnC). An increase in cytosolic [$Ca^{2+}$] will inhibit the LTCC providing a negative auto-inhibitory mechanism (Bers, 2008) via a $Ca^{2+}$ sensitive calmodulin dependent mechanism. This process bridging the AP and contraction is referred to as CICR.

The sodium calcium exchange channel (NCX) of the sarcolemma is bidirectional and can both extrude and import $Ca^{2+}$ to the cytoplasm. Since it does not co-localize with the RyR its importance in initiation of contraction is minor compared to the LTCC. Its function may be regarded as more important in the extrusion of $Ca^{2+}$ from the cytoplasm to relax the cardiomyocyte in order to lower intracellular [$Ca^{2+}$] and shift the $Ca^{2+}_{free}$ <--> cTnC-Ca equilibrium to the left (Bers, 2008).

#### 1.1.1.1.2 Cytosolic $Ca^{2+}$ extrusion

There are two major pathways for $Ca^{2+}$ extrusion from the cardiomyocyte cytoplasm: trans-sarcolemmal extrusion and SR reuptake.

$Ca^{2+}$ is extruded from the cytoplasm across the sarcolemma against a concentration gradient via two different routes: the electrogenic NCX channel and the $Ca^{2+}$ ATPase. For every $Ca^{2+}$ extruded via the NCX 3 $Na^{+}$ are imported. $Na^{+}$ enters the cytoplasm along a concentration gradient and thus drives the export of $Ca^{2+}$. Thus, the net effect for each ion exchange is depolarising suggesting that an increase in NCX flux which may be arrhythmogenic given its potential to generate local APs (Bers, 2008; Venetucci et al., 2008). The $Ca^{2+}$ ATPase utilises ATP to carry $Ca^{2+}$ against its concentration gradient to the extracellular space, no exchange of ions are involved. The reuptake of $Ca^{2+}$ into the SR is considered to be the major contributor to cytosolic $Ca^{2+}$ decay. It occurs through the ATP dependent action of the sarcoendoplasmatic reticulum ATPase (SERCA2a). In rabbit, like humans, the dependence of the SERCA has been estimated to approximately 70%, whereas in rat it is larger: approximately 92%. The majority of $Ca^{2+}$ not extruded by the SERCA is handled via the NCX: 28% in rabbit and 7% in rat. The sarcolemmal

$Ca^{2+}$ATPase and mitochondrial $Ca^{2+}$ uniporter are of lesser importance and account for ca. 1% each (Bers, 2000, 2002).

### *1.1.1.2 Myofilament dynamics*

1.1.1.2.1 The sarcomeric protein assembly

The sarcomere is the smallest contractile unit of striated muscle and schematically depicted in Figure 2. Two main structures of the sarcomere, the thin and thick filaments interact through the formation and release of cross bridges which causes the contraction of the tissue. Thus the sarcomere varies in length during the contraction relaxation cycle. Its physiological length range of motion is approximately 1.8-2.3 μm (Hanft et al., 2008). Each sarcomere is demarcated by the Z-disks.

For illustrative purposes the sarcomeric proteins can be divided into four structures containing different protein species:

*The thick filament:* Myosin heavy chains (MHC), myosin light chains (MLC), and myosin binding protein C (cMyBP-C).

*The thin filament:* Actin, troponin, and tropomyosin

*The Z-disk:* A multiprotein structure involved in signalling as well as acting as an anchoring point for thin filaments.

*Titin filaments:* Titin is a passive tension modulator.

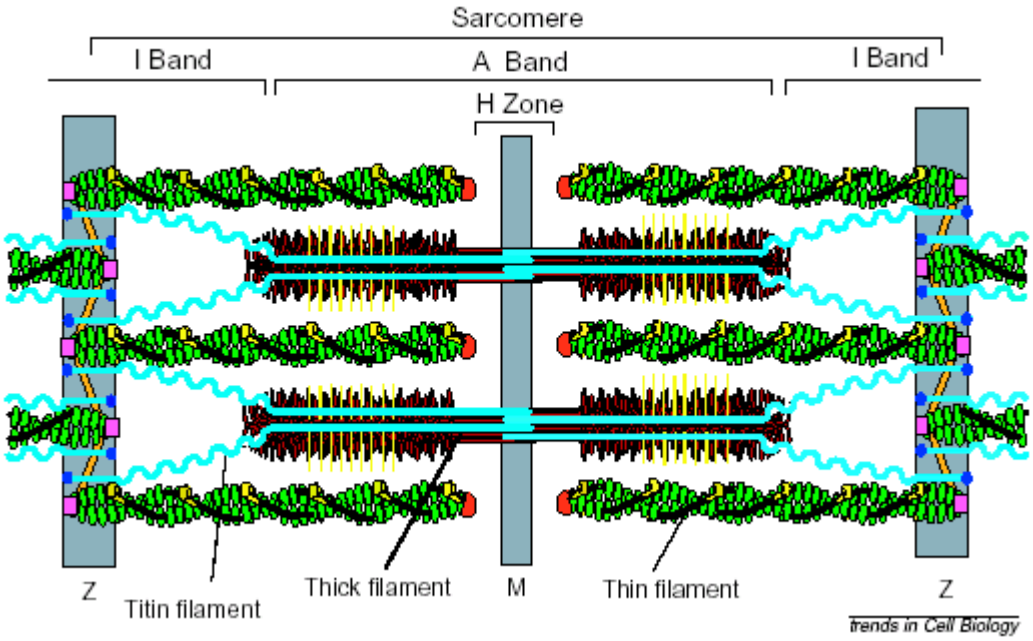



**Figure 2: Cardiac sarcomeric protein assembly** Schematic drawing of the cardiac sarcomere (Gregorio and Antin, 2000)

## The thick filament

The thick filament is ca. 1.6 µm long. Its backbone is made up from cardiac myosin of myosin II of the myosin super family of protein. It consists of two MHCs of 220 kDa and two MLCs: the essential and regulatory light chains (ELC and RLC), 19 and 22 kDa respectively (England and Loughna, 2013).

*Cardiac myosin heavy chain (cMHC*)

Two isoforms of cMHC is expressed in the heart: α and β, expressed by the genes *MYH6* and *MYH7* respectively. Thus three myosin permutations exist: V1: α-α, V2: α-β, and V3 β-β (VanBuren et al., 1995). The two isoforms share 93% sequence homology. This difference results in clear functional discrepancies between the two as the α isoform ATPase activity is 2-3 times higher compared to β. Mouse ventricular myocardium,

which exhibits a much higher heart rate, expresses mainly the α isoform, unlike humans who express β to 95-97% in the myocardial ventricles (Suzuki et al., 2009).

Structurally the MHCs are divided into rod, neck (S2), and head (S1) regions. The rod regions are intertwined and extend via S2 to S1 which harbours one actin binding as well as ATPase site crucial in strong cross bridge formation and release (Al-Khayat et al., 2013).

*Cardiac myosin light chains (MLCs)*

The two different MLCs are conventionally labelled the ELC and RLC. The light chains are both situated in the S2 region of the MHC fulfilling stabilising and regulatory roles. The ELC is expressed from the *MYL3* gene and is identical to the slow skeletal muscle form. It is believed that ELC is in direct contact with actin via its positive N-terminal during contraction but also that it may play a regulatory role in S1 positioning before the cross bridge formation (Hernandez et al., 2007; Muthu et al., 2011). The RLC is expressed from the *MYL2* gene. The role of the RLC is clearer as it has been observed as a target, through phosphorylation, of myosin light chain kinase (MLCK). It is considered an important modulator of cross bridge kinetics and force development in addition to a neck region stabilising role. Phosphorylation of RLC has long been proposed to alter the positioning of the S1 away from the thick filament through the addition of negative charge, moving it closer to the thick filament, thus facilitating the cross bridge formation with increased $Ca^{2+}$ activated isometric force, and also myofilament $Ca^{2+}$ sensitivity (Sweeney et al., 1993). Recent computational modelling in combination with experimentation suggests, however, that the effect may be transferred by a stiffening of the S2 lever arm (Sheikh et al., 2012).

*Cardiac myosin binding protein C (cMyBP-C)*

cMyBP-C is expressed from the *MYBPC3* gene and weighs ca. 142 kDa. It is localised to 9 "stripes" in the C zone region of the thick filament (Luther et al., 2008). It consists of eight immunoglobulin and three fibronectin like domains and has multiple serine and threonine phosphorylation sites used as substrates by protein kinase A (PKA), $Ca^{2+}$-calmodulin activated kinase (CaMKII), and protein kinase C (PKC). PKA phosphorylation of cMyBP-C mediates approximation of S1 to the thick filament (Ge et al., 2009), suggesting to facilitate the formation of cross bridges and enhancing cardiac function upon β-adrenergic stimulation. The cardiac isoform of cMyBP-C has an extra N-terminal domain compared to skeletal muscle. Both isoforms are subject to disease causing mutations in the form of hypertrophic cardiomyopathy (HCM), and distal arthrogryposis (DA). Recently, using electron tomography technique it was established that cMyBP-C extend the thick-thin filament lattice and interact with actin, via its N-terminal end (Luther et al., 2011), an interaction which may work as a tether that can be relieved upon phosphorylation, inducing enhanced interfilament sliding speed. Indeed, the N-terminal domain of the cardiac isoform holds a number of phosphorylation sites (Ge et al., 2009).

**The thin filament**

The thin filament contains five major proteins: Actin, troponin C (cTnC), I (cTnI), and T (cTnT), and tropomyosin. The structure extends from the Z-line towards the centre of the sarcomere. Thin filament based regulation of contraction is mediated by conformational changes in troponin and tropomyosin due to the binding of $Ca^{2+}$ to TnC.

*Actin*

Actin is expressed from the *ACTC1* gene and has a molecular weight of 42 kDa (Squire, 1997). Actin monomers (G-actin) polymerise into helical actin filaments (F-actin). The assembly of the actin helix is dependent on $Ca^{2+}$ and ATP; both held within the monomers. ATP hydrolysis to ADP and $P_i$ is necessary for polymerisation into F-actin (Squire et al., 2005). In the periphery of the actin monomer residues required for attachment of myosin S1, and hence cross bridge formation, are located (Milligan et al., 1990).

*Tropomyosin*

Tropomyosin is an α–helical coiled coil dimer stabilised through hydrophobic interactions and salt bridges due to the regular heptad amino acid repeat. It lies in the helical groove of actin in a partial over lapping head-to-tail fashion, and stretches over 40 nm, 7 G-actin, and one troponin triad. In the heart, it is principally composed of α – tropomyosin expressed from the *TPM1* gene. Tropomyosin is considered to play an important role in regulation of cardiac contractility. As it stretches along the actin filament it has the important function to cover and expose myosin S1 binding sites on the actin filament. Tropomyosin has been proposed to assume three different states of conformation in relation to the actin filament, referred to as the three state model. This involves the blocked B-state, the $Ca^{2+}$ induced state (C), and the myosin induced open (M) state. Under conditions of low [$Ca^{2+}$] troponin will constrain tropomyosin so that it blocks the outer actin myosin docking site (B). Upon $Ca^{2+}$ binding to cTnC, tropomyosin will move towards the inner part of the actin monomer but still block a considerable part of the myosin binding site (C). Not until myosin interacts weakly with actin will

tropomyosin assume its full azimuthal shift in relation to the actin filament which exposes sites for strong cross bridge formation (M) (Lehman et al., 2000). Due to the overlap between tropomyosin molecules, the effect of $Ca^{2+}$ binding to one troponin is spread beyond the 7 actin monomers directly covered by the specific troponin-associated tropomyosin homodimer. Tropomyosin is thus regarded as a central molecule in cooperative activation along the thin filament (Murakami et al., 2008; Squire et al., 2005; Vanburen and Palmer, 2010).

*Troponin*

The troponin complex is composed of a globular region (involving the interaction of the C-terminus of cTnT, cTnI and cTnC) and an extended portion (N-terminus of cTnT) that sits along the tropomyosin molecule. It is ca. 20 nm long and occurs with a regular spacing of 38 nm along the thin filament, thus one per tropomyosin homodimer. The troponin triad is the $Ca^{2+}$ -sensing component of the myofilament and responsible for mediating the $Ca^{2+}$ -activation of contraction. Binding of $Ca^{2+}$ to cTnC induces a conformational change that shifts tropomyosin to expose the myosin S1 binding site on the thin filament (Squire et al., 2005; Takeda, 2005).

Cardiac troponin C

cTnC is ca. 18 kDa and expressed from *TNNC1.* It is the $Ca^{2+}$ binding protein of the troponin complex. Extraction of TnC from a skinned muscle preparation removes $Ca^{2+}$ dependence of contractile activation, and the $Ca^{2+}$ sensitivity is restored by its replacement. cTnC has a total of three $Ca^{2+}$ binding sites of which one (site II) has lower

affinity and is responsible for contractile regulation whereas the other two (the C-terminal sites III and IV) have a role in maintaining structural integrity of the molecule. The occupation of the regulatory site induces a conformational change relieving the inhibitory effect of cTnI which shifts the tropomyosin molecule, exposing the S1 binding sites (Gordon et al., 2000).

### Cardiac troponin I

cTnI is ca. 23 kD heavy and expressed from *TNNI3.* As described above, upon $Ca^{2+}$ binding the affinity of cTnC to cTnI is increased, moving cTnI away from actin and bringing tropomyosin with it thereby facilitating actin-myosin interaction. cTnI, unlike the skeletal isoforms has an N-terminal extension of 32 residues which includes the target sites for PKA phosphorylation, serines 23 and 24 (S23/24). Upon β-adrenergic stimulation phosphorylation of these sites is known to cause a decrease in $Ca^{2+}$ sensitivity but also to increase the rate of return to the blocking state which may accelerate the cross bridge detachment step and relaxation (Dong et al., 2006; Gordon et al., 2000). Protein kinase C (PKC) has been shown to phosphorylate cTnI at S43 and S45 causing a decrease in $Ca^{2+}$ sensitivity and depressed myosin ATPase activity (Kobayashi et al., 2008). More recent work has illuminated a novel phosphorylation site, S150, seemingly phosphorylated by AMP activated kinase (AMPK). The effect appears to sensitise the myofilament to $Ca^{2+}$ (Nixon et al., 2012b; Oliveira et al., 2012).

Cardiac troponin T

cTnT has a molecular weight of 37 kDa and is expressed from *TNNT2.* cTnT is the most elongated component of the troponin complex, stretching over ca. 20 nm along the actin filament and lying across the overlap of two TM homodimers. This could suggest a regulatory role in thin filament activation, apart from its function in coordinating the binding of other troponin subunits (Gordon et al., 2000). The cTnT molecule has been proposed to be phosphorylated on T206 by PKC with a consequent reduction in maximum force generation, $Ca^{2+}$-sensitivity, and cross-bridge cycling rate (Kobayashi et al., 2008; Sumandea et al., 2003).

**The Z-disk proteins and titin filaments**

The cardiac Z-disk is a multiprotein structure, ca. 100 nm wide, separating two adjacent sarcomeres. It serves as anchoring point for the thin filaments and also the passive spring function protein titin. One of the major constituent proteins is α-actinin which forms the cross-linking network supporting the force transmission from thin and titin filaments between sarcomeres (Squire et al., 2005; Wang and Su, 2010).

Titin is expressed in three isoforms in the cardiac myocyte: one foetal form (3.6-3.8 MDa) and two adult variants termed N2B (~3.0 MDa), and N2BA (~3.3-3.5 MDa), due to differential splicing from the *TTN* gene. It is the largest known expressed intracellular protein, spanning a whole half-sarcomere; it has a passive spring function, regulating diastolic filling pressure in the cardiomyocyte alongside of extracellular collagen on the whole heart level. Its N-terminus lies at the Z-disk where it binds ankyrin, α-actinin and telethonin and overlaps in an antipolar fashion with titin from the adjacent sarcomere. It extends to the M-line and interacts with the thick filament proteins of myosin and

cMyBP-C (LeWinter and Granzier, 2010). Not the entire titin protein is extensible. This property is rather confined to a distinct segment of immunoglobulin repeats interspersed by a segment rich in proline, glutamate, valine, and lysine residues (PEVK) subject to modification though phosphorylation. The remaining segments of titin are not distensible and suggested to hold a structurally organising function. The relative composition of N2B/N2BA isoforms is a means to change the passive stiffness of the myocardium as N2B isoform is stiffer than N2BA explained by its shorter extensible region. It is also noteworthy that the bidirectional spring nature of the titin molecules helps to restore resting sarcomere length from extreme states at short sarcomere lengths, i.e. at the end of systole (LeWinter and Granzier, 2010; Pyle and Solaro, 2004). Titin is a target substrate for phosphorylation by PKA, (Yamasaki et al., 2002), cGMP dependent-protein kinase G (PKG) (Kruger et al., 2009), and CaMKII (Hamdani et al., 2013b). Phosphorylation by PKA and PKG increased the compliance of the titin filament inducing increased accommodation ability for venous return under stress. However, protein kinase C (PKC) and CaMKII have been shown to phosphorylate titin inducing the opposite effect (Hidalgo et al., 2009).

#### 1.1.1.2.2 Thick and thin filament interaction – the sliding filament theory and cross-bridge cycling

The early 1950's saw a dramatic turn in the understanding of muscle contraction as independent researchers published results from microscopic observations of muscle during contraction in the same issue of the journal *Nature.* In these accompanying articles the length of skeletal muscle was manipulated by stretch and physiological contraction. The observation of a constant A-band width during whole sarcomere

shortening enabled the researchers to conclude that the observed rodlets of myosin in the A-band and actin in the I-band, seen to shorten with whole length reduction, slide in between each other. They both also postulated the innate property of actin-myosin interaction to be responsible for this shortening and the processes' dependency on ATP-hydrolysis (Huxley and Niedergerke, 1954; Huxley and Hanson, 1954).

As mentioned previously in this introduction, it is now known that myosin interacts with actin via its S1 region, which harbours actin binding sites as well as an ATP hydrolysis cleft. The conformation change responsible for the movement of the myosin head is dependent on ATP binding and hydrolysis, and the strong interaction with actin is dependent on $Ca^{2+}$ in order to expose the S1 binding site on actin. The whole process whereby this occurs is called the cross bridge cycle; it can be described in the following steps starting from the point of actomyosin interaction at the end of the power stroke (Figure 3):

1. ATP binding to myosin
2. Actomyosin dissociation
3. ATP hydrolysis forming a complex of myosin, ADP, and $P_i$
4. Actin, myosin, ADP, and $P_i$ re-associate in a weak bond.
5. Strengthened bond upon $Ca^{2+}$ association to TnC
6. The power stroke occurs, either proceeded by $P_i$ release or induced by the strong binding itself
7. Actin, myosin, and ADP at the end of the power stroke after the release of free energy, force generation and $P_i$ is followed by an isomerisation in which the strong actomyosin interaction is weakened and ADP is released

8. Return to step 1: actomyosin awaits ATP. (Gordon et al., 2000; Gordon et al., 2001).

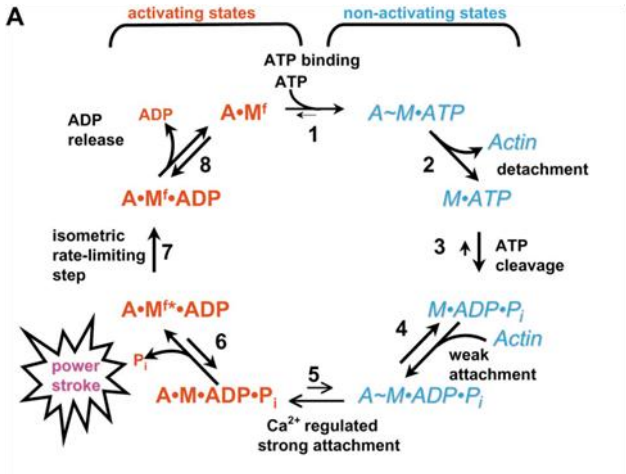



**Figure 3: Actomyosin cross-bridge cycling A:** Schematic representation of constellation between actin, myosin, $Ca^{2+}$ and the hydrolysis state of ATP during the cross bridge cycle. **(Gordon et al., 2001).**

### *1.1.1.3 $Ca^{2+}$ handling and myofilament - interplay*

As stated previously, intracellular $Ca^{2+}$ handling and myofilament dynamics can be regarded as the two major players in orchestrating cardiomyocyte contraction. Their actions are, however not, independent. This is exemplified by the finding that an increase in myofilament $Ca^{2+}$ sensitivity has been shown to be arrhythmogenic by increasing diastolic $Ca^{2+}$ levels, SR $Ca^{2+}$ load and release, and ventricular early after depolarisations (EAD). The underlying reason for this is that cTnC is a significant $Ca^{2+}$ buffer in the cardiomyocyte cytosol. Increased $Ca^{2+}$ sensitisation prolongs cytosolic $[Ca^{2+}]$ decay due to slowed release from cTnC, and increased $Ca^{2+}$ efflux through the NCX with increased risk of ventricular ectopic depolarisation due to the electrogenic nature of this ion channel. Increased cytosolic $[Ca^{2+}]$ causes increased SR $Ca^{2+}$ uptake and

release after pauses which disturb the dynamic $Ca^{2+}$ equilibrium between SR and cytosol, with increased incidence of pause dependent arrhythmias due to RyR conveyed $Ca^{2+}$ sparks (Schober et al., 2012; Venetucci et al., 2008). The general feature of increased myofilament $Ca^{2+}$ sensitivity in hypertrophic cardiomyopathy (HCM) may thus help explain the increased risk of malignant ventricular arrhythmias associated with this condition (Robinson et al., 2007; Watkins et al., 2011).

## 1.2 Regulation of cardiomyocyte contractility

The heart is required to alter its performance in accordance with the metabolic demand of the body's peripheral tissues. Acutely so to supply skeletal muscle with nutrients and relieve them of their metabolic waste products, thereby regulating whole organism pH homeostasis, upon increased physical activity. To do this it needs to increase the volume of blood it supplies the circulation with per time unit: its cardiac output (CO). There are two major ways of increasing the CO: increased frequency of contraction (chronotropic response) and increased ejection volume. The latter parameter is dependent both on the diastolic and systolic function of the heart. Upon increased physical activity the venous return from the peripheral circulation will increase and the pre-load of the heart as a consequence. This will cause passive strain on the ventricles elongating the sarcomeres. The immediate increase in force of contraction upon stretch of the ventricles is known as the Frank-Starling law of the heart and had been known for some time (Katz, 2002), before the work of its namesakes: Otto Frank and Ernest Starling (Frank, 1895; Patterson and Starling, 1914) who in independent studies described the length tension relationship in myocardium. The "Frank-Starling law of the heart" is a fundamental concept of cardiac regulation.

A less well known phenomenon for the adaptation of CO to peripheral demands is the delayed, cardiac confined, inotropic response, known as the Anrep effect. This constitutes a delayed force response to increased pre-load. As the Frank-Starling response induces a variation in output within a beat to beat time frame, the Anrep effect requires ca. 10-15 minutes to take effect due to more elaborate intracellular signalling events proposed to increase cytoplasmic $Ca^{2+}$ levels via ATII signalling (Cingolani et al., 2012).

### 1.2.1 Physiological regulation of myofilament interaction

#### *1.2.1.1 Mechanistic regulation of sarcomeric contractility*

A well established method to study force generation by the contractile apparatus in the absence of the $Ca^{2+}$ handling processes involves the chemical disruption of membranes by treating the tissue with a non-ionic detergent, such as Triton X-100. As the sarcolemma and SR are disrupted, the [$Ca^{2+}$] of the surrounding solution can be precisely set and pharmacological agents applied directly without depending on an established route of transport into the cell. Intracellular signalling events responsible for posttranslational modification of sarcomeric proteins are also disrupted. Three parameters will be discussed in reference to mechanical sarcomeric-confined regulation of cardiac contractility: i) force production, ii) $Ca^{2+}$-sensitivity, and iii) cooperative activation along the think filament (Shiels and White, 2008).

The relationship of force generation and sarcomere length (SL) at the single cell level was illustrated by Fabiato and Fabiato in 1975 using demembranated rat cardiomyocytes to measure isometric force at fixed pCa 5 at different degrees of passive

stretch. The relationship was found to be inversely U-shaped with a maximum force output at an approximate SL of 2.2 μm (Fabiato and Fabiato, 1975).

It has been shown that the myofilament $Ca^{2+}$ sensitivity is dependent on SL. In rat skinned cardiac trabeculae increasing the SL from 1.85 to 2.25 μm continuously sensitised the myofilament disclosing the linear relationship between SL and $EC_{50}$ (Dobesh et al., 2002). The mechanism behind this is speculated to be a reduction of interfilament spacing upon stretch which would facilitate cross bridge interaction upon $Ca^{2+}$ activation. Under physiological conditions the reduction in interfilament spacing is believed to depend mainly upon two different mechanisms: The first being how the intact cell is a body of, relatively, constant volume, thus it will thin in response to elongation (Hanft et al., 2008). This was illuminated by Fuchs et al showing how applying varying amounts of dextran upon stretch, thus keeping the interfilament spacing constant, abolished the length dependent increase in $Ca^{2+}$ sensitivity (Fuchs and Smith, 2001). Second, titin filaments will exert a radial force upon stretch as they are connected to both thin and thick filament at their opposite poles in the sarcomere. This can be shown through trypsin degradation of titin, which reduces the interfilament reduction upon stretch in skinned cardiac tissue (Cazorla et al., 2001).

The most straightforward hypothesis to explain this is a direct alteration of the $Ca^{2+}$ binding affinity of cTnC upon stretch. This question was addressed by Fuchs and co-workers who showed how binding affinity of $Ca^{2+}$ in skinned cardiac muscle was increased with SL (Hofmann and Fuchs, 1988; Wang and Fuchs, 1994). To further study the mechanism of this change Martyn and Gordon labelled cysteine residues of TnC with a fluorescent probe, thereby showing an alteration in protein conformation with SL. Importantly, the researchers also showed that this change was not primarily due to a

change in SL per se, but rather an increase in strongly binding cross bridges (Martyn and Gordon, 2001). By introducing non-cycling cross bridges into the myofilament Moss and co-workers were able to close to abolish the length dependency of thin filament activation (de Tombe et al., 2010; McDonald, 2011) which suggests an SL dependent positive feedback mechanism to further increase force output during $Ca^{2+}$ activation. This effect has recently been tested by the use of blebbistatin in demembranised rat trabeculae. The conclusions from this study was that close to complete (98%) myosin-actin inhibition did very little to alter $Ca^{2+}$ affinity and cooperativity, suggesting the latter to be intrinsic to the thin filament (Sun et al., 2009).

#### *1.2.1.2 Intracellular signalling regulation of sarcomeric contractility*

1.2.1.2.1 Thin filament phosphorylation

cTnI and cTnT are both known to be modified through phosphorylation by different kinases.

*1.2.1.2.1.1 Functional effects of cTnI phosphorylation*

cTnI is targeted by a range of different kinases. These include, but are not limited to, the β-adrenergic cAMP-dependent PKA, ATII / α-adrenergic-mediated PKC, protein kinase D (PKD), and AMPK (Layland et al., 2005; Nixon et al., 2012b; Oliveira et al., 2012; Solaro and Kobayashi, 2011).

β-adrenergic stimulation occurs during physiological sympathetic drive from the autonomic nervous system to increase CO in response to or in apprehension of increased peripheral metabolic demand. By stimulation of β–receptors intracellular signalling cascades are activated resulting in increased activity of PKA. Apart from

effects on myofilament function this kinase separately influences intracellular $Ca^{2+}$ handling (Layland et al., 2005), which will be discussed below. The myofilament effects are conveyed through phosphorylation of S23/24 in the cardiac specific N-terminal extension of cTnI, and include increased cross bridge cycling rate and decreased $Ca^{2+}$ sensitivity (Kentish et al., 2001; Layland et al., 2005). It is noteworthy that studies of skinned myocardium devoid of cMyBP-C, another substrate of PKA, indicate that that the former effect is primarily one of the thick filament protein, whereas the latter is a primary effect from S23/24 phosphorylation of cTnI (Solaro and Kobayashi, 2011).

PKC exist in different isoforms and has been reported to phosphorylate cTnI at multiple sites. S43/45 phosphorylation by PKC reduces ATPase activity, force production and cross bridge cycling rate. It has however also been reported to phosphorylate S23/24 with similar effects as PKA, and T144 reducing the myofilament shortening velocity (Layland et al., 2005).

PKD (PKCμ) has been shown to phosphorylate cTnI on the S22/23 residues, in analogy with PKA with similar effects of $Ca^{2+}$ sensitisation and increased cross bridge cycling rate (Haworth et al., 2004) inducible via endothelin-1 (ET-1) stimulation (Cuello et al., 2007), in rodent cardiomyocytes even though the effect on cross bridge cycling appears mediated via cMyBP-C S302 phosphorylation (Bardswell et al., 2010).

AMPK is conventionally known as an intracellular energy sensor increasing its activity in response to AMP. Partly due to it being a disease gene for familial hypertrophic cardiomyopathy (HCM) (Blair et al., 2001), it has generated interest in its wider roles. Recently its role as a physiological modifier of sarcomeric function has started to emerge. Its modification of S150 has in two papers been shown to increase $Ca^{2+}$

sensitivity of both force and actomyosin ATPase activity (Nixon et al., 2012b; Oliveira et al., 2012).

*1.2.1.2.1.2 Functional effects of cTnT phosphorylation*

The functional relevance of cTnT phosphorylation is less clear than that for cTnI. *In vitro* studies have revealed multiple PKC dependent sites of phosphorylation, such as T197, S201, T206, and T287 (Solaro and Kobayashi, 2011). Studies on these sites have been performed in skinned muscle fibres *in vitro* by phospho-mimicking mutagenesis or PKC phosphorylation, showing decreased force generation, actomyosin ATPase activity, $Ca^{2+}$ sensitivity and cooperativity along the thin filament (Sumandea et al., 2003).

*1.2.1.2.1.3 Functional effects of tropomyosin phosphorylation*

There is a report on α-tropomyosin phosphorylation at S283 with effects in the form of impaired relaxation due to decreased $Ca^{2+}$ dissociation rate from thin filaments, thus appearing to impair ventricular filling (Nixon et al., 2012a). The authors do not speculate in which kinases are responsible for this posttranslational modification.

1.2.1.2.2 Thick filament phosphorylation

RLC and cMyBP-C are both established phosphoproteins of the thick filament.

*1.2.1.2.2.1 Functional effects of RLC phosphorylation*

The RLC is phosphorylated by the myosin light chain kinase (MLCK), a $Ca^{2+}$-calmodulin activated kinase specifically targeting RLC on S14/15 (Scruggs and Solaro, 2011). Phosphorylation increases $Ca^{2+}$ sensitivity and force generation capacity. X-ray diffraction work by Moss and colleagues has shown that RLC phosphorylation decreases interfilament lattice spacing (Colson et al., 2010; Muthu et al., 2012; Scruggs and Solaro, 2011).

*1.2.1.2.2.2 Functional effects of cMyBP-C phosphorylation*

cMyBP-C has multiple phosphorylation sites and is a known target of PKA upon β-adrenergic stimulation, $Ca^{2+}$ calmodulin kinase II (CaMKII), as well as PKC, mainly in the cardiac specific C0-C1 domains. The effects of PKA are the most thoroughly studied. Apart from functional effects it has also been suggested that phosphorylation levels of cMyBP-C are inversely related to its degradation rate, which could have effects on thick filament stability. PKA phosphorylation of cMyBP-C occurs at S273, -282, -302, and -307 (Barefield and Sadayappan, 2010). Its action is suggested to alter myosin orientation to facilitate actomyosin interaction and inotropic response of the heart (Bardswell et al., 2010; Colson et al., 2010; Colson et al., 2012).

1.2.1.2.3 Titin phosphorylation

The passive tension regulator titin not only alters its functional properties through isoform expression ratios but also more acutely though phosphorylation by several proposed kinases: PKA, PKC, PKG, CaMKII, in the spring regions. As opposed to PKA and

PKG, the effect of PKC and CaMKII appears to be to stiffen the titin spring impairing diastolic filling. PKA and PKG derived phosphorylation of titin has been suggested to be reduced in end stage human heart failure and diabetes mellitus (DM), contributing to impaired diastolic function (Hamdani et al., 2013b; Hidalgo et al., 2009; Kruger and Linke, 2011).

#### *1.2.1.3 How does stretch affect sarcomeric phosphorylation levels?*

As mentioned above, the stimulation of β-adrenergic receptors has a wide influence on the phosphorylation profile of sarcomeric proteins. The receptors are activated by neurohormonal influences in the form of catecholamines. However, both the Frank-Starling and the Anrep effect are phenomena intrinsic characteristic to the heart muscle itself, and are seen in isolated cardiac preparations independent of intact circulation and nervous system (Cingolani et al., 2012).

The Frank-Starling mechanism occurs within a very short time frame, so as to alter cardiac function on a beat to beat basis. It can be regarded as a mechanism depending on direct mechanistic regulation. Phosphorylation does however play an important role on a longer time scale as stretching of isolated intact tissue preparations has been shown to increase phosphorylation of sarcomeric proteins. Monasky et al isolated rabbit cardiac ventricular trabeculae which were stimulated at taut and optimal sarcomere length, observing a change in phosphorylation status of tropomyosin, RLC, cTnI, cTnT, and cMyBP-C. Incubation with PKA and PKC inhibitors differentially changed the phosphorylation profile such that stretch induced PKA-activation was concluded to phosphorylate tropomyosin, cTnI, RLC and cMyBP-C, whereas PKC accounted for modification of tropomyosin and RLC. PKC inhibition had a more pronounced effect on

impairing the prolongation of relaxation time seen in response to stretch (Monasky et al., 2012).

### 1.2.2 Cardiac redox signalling and contractile regulation

#### *1.2.2.1 ROS generation*

There are 3 three major sources of ROS in the cardiac myocytes: mitochondrial ETC, nitric oxide synthase (NOS), and NADPH oxidases (NOX)s. The mitochondrial ETC generates $O_2^-$ via $O_2$ reduction during cellular respiration through complex I and III (Santos et al., 2011). NOS may start to generate $O_2^-$ instead of NO when the cofactor tetrahydrobiopterin (BH4) is in a state of deficiency which is associated with generation of peroxynitrite ($ONOO^-$) in the case of concomitant NO and $O_2^-$ generation, this is termed NOS-uncoupling. NOX2 and 4 are expressed in the cardiac myocytes. NOX2 is situated in the sarcolemma and is acutely activated by ATII, ET-1, as well as mechanical stretch which causes activation of its cytosolic $O_2^-$ producing subunits. NOX4 has a more constitutively active profile and is speculated to mainly produce $H_2O_2$ (Santos et al., 2011). Both isoforms are activated by NADPH (Burgoyne et al., 2012) .

ROS species have been suggested to modify $Ca^{2+}$ handling as well as myofilament protein function in the cardiomyocyte.

### 1.2.3 Physiological regulation of intracellular $Ca^{2+}$ handling

The second component of cardiomyocyte contractility, intracellular $Ca^{2+}$ handling, is also under influence of phosphorylation via adrenergic signalling, as well as auto-regulatory $Ca^{2+}$ induced mechanisms described previously (Bers, 2011; Eisner et al., 2012). More

recently, results have also emerged showing how the production of ROS may have a direct effect in regulation of $Ca^{2+}$ dynamics in the cardiac myocyte (Prosser et al., 2011).

#### *1.2.3.1 $Ca^{2+}$ transient regulation through phosphorylation*

β-adrenergic stimulation affects major components of EC-coupling: LTCC, the RyR, and SERCA via phospholamban (PLN).

PKA exerts an important regulatory effect via phosphorylation of the SERCA modulator protein PLN, which in its unphosphorylated state interacts with the ATPase to inhibit its function (Bers, 2002). An accelerated decay of $Ca^{2+}$ transients is a necessity to facilitate increased lusitropy and accommodate an increased heart frequency upon sympathetic drive. Also, the relieved inhibition of SERCA will increase SR $Ca^{2+}$ load which will facilitate release through the RyR upon their activation. Thus, phosphorylation of PLN will both increase the $Ca^{2+}$ transient's amplitude as well as its decay rate, and decrease its duration. Therefore phosphorylation of PLN is central in conveying an effective increase in CO. The relevant effects of phosphorylation of LTCC and RyR are under dispute, but seem secondary to that of PLN (Bers, 2008; Eisner et al., 2012). Whether or not PKA has an effect on NCX is disputed. Activation of this protein through phosphorylation rather seems conveyed by PKC (Bers, 2008).

CaMKII is present at the T-tubuli-SR nodal points where it binds to LTCC and RyR. This localisation is enhanced by a local rise in intracellular [$Ca^{2+}$] (Bers, 2011). Its effect in phosphorylating the LTCC is to reduce its open probability, thus working as a negative feedback mechanism to limit the activation of the RyR at resting levels, whereas at increased frequency of stimulation the effect is the opposite, to increase the influx of

$Ca^{2+}$ through the LTCC (Bers and Grandi, 2009). The mechanism for this change in effect is unknown but it seems of importance to contractile adaptation at higher frequencies as inhibition of CaMKII in rat cardiac myocytes blunted frequency dependent acceleration of relaxation (DeSantiago et al., 2002). The effect of CaMKII phosphorylation of RyR points towards an activating mechanism, although the results are reported as divergent (Bers and Grandi, 2009; Niggli et al., 2012).

#### *1.2.3.2 Physiological contractile regulation through redox signalling*

ROS may modify $Ca^{2+}$ channels directly through oxidative modification or indirectly, via activation of ROS sensitive kinases (Wagner et al., 2012). The effects of direct modifications of ROS has been proposed as mainly relevant in pathophysiology but recent work has demonstrated its physiological relevance as stretch causes a microtubule dependent activation of NOX2 situated in the T-tubuli, and direct $O_2^-$ modification of RyR, increasing its sensitivity to $Ca^{2+}$, as demonstrated by an increased $Ca^{2+}$ spark frequency upon stretch. Due to the high reactivity of $O_2^-$, close proximity between the source and target of modification is a necessity (Prosser et al., 2011). CaMKII, known to inhibit the LTCC channel in the T-tubule has been shown to be activated under pro-oxidative conditions (Zhang et al., 2013), as has PKA (Burgoyne et al., 2012) which increases PLN phosphorylation and $Ca^{2+}$ reuptake rate into the SR .

The functional effect on the myofilament from altered redox balance is one, which as for $Ca^{2+}$ handling, may depend on both direct oxidative modifications (Lovelock et al., 2012) as well as second hand modification by redox sensitive intermediary enzymes, such as kinases. Known myofilament kinases, such as PKA, PKD, both decreasing $Ca^{2+}$ sensitivity via S23/24 phosphorylation and PKC, increasing $Ca^{2+}$ sensitivity via T144 are reported

as activated by ROS. The same kinases also have reported effects to increase cross-bridge cycling via cMyBP-C phosphorylation (Avner et al., 2010; Santos et al., 2011; Steinberg, 2013).

#### 1.2.3.2.1 The slow force response to stretch – the Anrep effect

PKA, PKC, as well as CaMKII are reported as activated by oxidative stress. The secondary effects of raised ROS production therefore have the potential to overcome the short diffusion distance of $O_2^-$ and cause an array of effects upon both $Ca^{2+}$ handling and potentially myofilament protein (Wagner et al., 2012). For example, a study of myocardial infarction induced endocardial dysfunction was correlated to PKA mediated depression of $Ca^{2+}$ sensitivity on the myofilament, independently of direct oxidative effects on cTnI and increased [cAMP] (Andre et al., 2012).

As mentioned previously, the Anrep effect is a delayed increase in force to increased pre-load. Stretch-induced release of ROS is one proposed inotropic mechanism working by increasing intracellular [$Ca^{2+}$] (Cingolani et al., 2012). The release of ATII upon myocardial stress and subsequent ET-1 is a primary event suggested to initiate a series of distal signalling events taking part in conveying the Anrep effect as blocking the $ET_A$ receptor abolished the effect (Cingolani et al., 1998). A final mediating agent, via mitochondrial and NOX derived ROS production (Caldiz et al., 2007), in achieving an increased $Ca^{2+}$ transient amplitude is proposed to be activation of the sodium-hydrogen exchanger (NHE) which raises intracellular [$Na^+$] in exchange for $H^+$. The increase in [$Na^+$] will in turn activate the NCX-mediated import of $Ca^{2+}$ (Cingolani et al., 2012). Blocking of NHE1 using siRNA injection blunted the slow force response in rat cardiac ventricles (Perez et al., 2011).

The relative role of direct myofilament sensitisation to $Ca^{2+}$ as a factor in the delayed force response is hard to decipher although the effect from NHE inhibition was close to complete (Perez et al., 2011) suggesting it to be mainly of $Ca^{2+}$ handling origin. As described above, two kinases known to modify myofilament $Ca^{2+}$ sensitivity, PKA and PKC, have both been shown to be activated by ROS (Wagner et al., 2012). Also, as demonstrated by Kockskämper et al. the slow force response in humans is associated with phosphorylation of RLC by MLCK. Inhibition of MLCK attenuated the delayed force response to stretch in human ventricular tissue, and however independent of ATII inhibition in ventricular samples, showed a dependence on ATII signalling but independence of NHE in atrial tissue from the same species (Kockskamper et al., 2008a; Kockskamper et al., 2008b). Thus, there is still plenty of work to be completed to understand the subcellular mechanisms underlying the Anrep effect.

### 1.3 Cardiac metabolism

The heart has a high energetic requirement due to the constant demand from myofilament ATPase and ion pumps. Its ATP storage capacity is very low in relation to its hydrolysis rate (5 µg/g wet weight vs. 30 µg/g wet weight/min at rest). The healthy human heart normally derives 50-70 % of its ATP from mitochondrial fatty acid β-oxidation with the remainder derived from cytosolic anaerobic glycolysis and mitochondrial glucose oxidation. This ratio between utilised nutrients is subject to dramatic changes in different disease situations of the myocardium (Lopaschuk et al., 2010). See Figure 4 for a summarised description of cardiac metabolism.

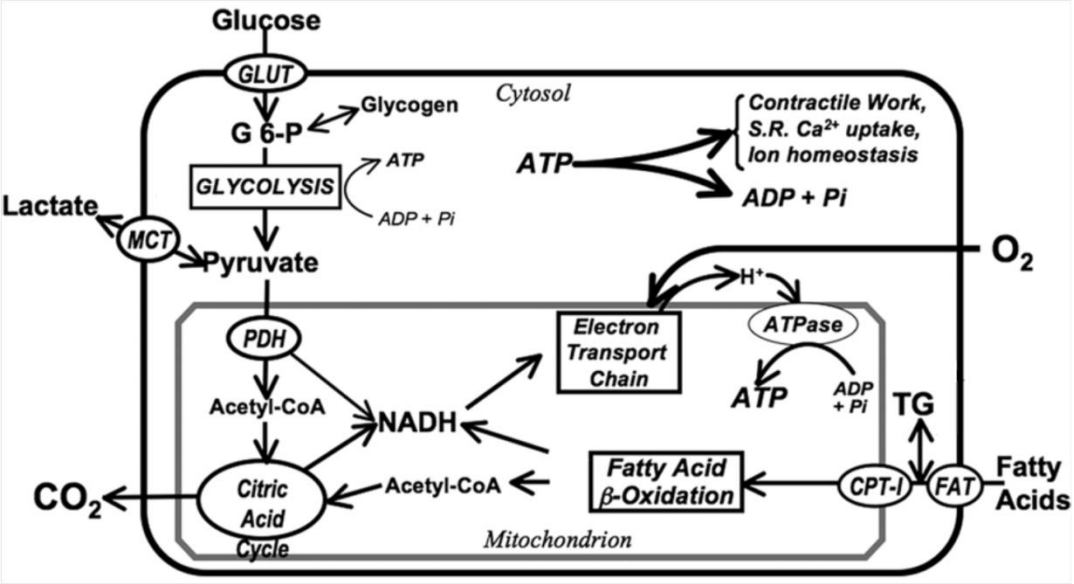



**Figure 4: Cardiac metabolism** Summary of the transport and chemical events involved in cardiac glucose and fatty acid metabolism. Adopted from Lopaschuk et al. (Lopaschuk et al., 2007)

### 1.3.1 **Myocardial fatty acid oxidation**

Under basic working condition in the myocardium, heart function can be maintained by the perfusion of either only palmitate or glucose alone (Montessuit and Lerch, 2012). It is however known that the heart prefers mitochondrial fatty acid oxidation on which it depends to 50-70 % for ATP formation (Lopaschuk et al., 2010). The reason for this may be that, in situations of ample $O_2$-supply, higher energy content is derivable from fat, as well as our increased ability to store fat for long term utilisation in situations of starvation. For a high energy demand organ as the heart, very short durations without access to nutrients may prove detrimental. This discussion will be returned to below.

The basic metabolic fluxes of cardiac metabolism are shown in Figure 4. The main source of free fatty acids (FFA) for the heart is present as circulating triglycerides (TG) which need to be hydrolysed to FFA by lipoprotein lipase in the endothelial cell membranes of myocardial capillaries (Carley and Severson, 2005) before transport into the cardiomyocyte via the FAT/CD36 or the FATBP sarcolemmal FFA transporters.

Unlike the FATBP the FAT/CD36 transporter can translocate between the cytosol and sarcolemma offering rapid changes in substrate import capacity. After this the FFAs are esterified to fatty acyl CoA, in an ATP consuming process by fatty acyl CoA synthase. Fatty acyl CoA can be stored either as TG or shuttled into the mitochondria for β-oxidation. This transport is dependent on the carnitine palmitoyl transferase1 (CPT1) residing in the outer mitochondrial membrane. CPT1 is inhibited by malonyl-CoA which links the activity of the energy sensor AMPK to the degree of mitochondrial FFA metabolism. The malonyl-CoA synthesis is under control of acetyl CoA carboxylase (ACC) (Carley and Severson, 2005) whose activity in turn is controlled by AMPK. In the transport of fatty-acyl CoA by CPT1 acyl carnitine is formed which is once again converted to fatty acyl-CoA in the transport over the inner mitochondrial membrane by CPT2. It then enters the β–oxidation process processed by acyl CoA dehydrogenases generating acetyl-CoA which feeds into the Krebs cycle. ATP is generated when produced $FADH_2$/NADH enters the mitochondrial ETC. FATBP, CD36, CPT1 as well as β–oxidation enzyme transcription is under control of peroxisomal proliferator activated receptor (PPAR)α and peroxisomal proliferator activated receptor γ coactivator-1 (PGC1)α (Lopaschuk et al., 2010).

### 1.3.2 **Myocardial glucose metabolism**

Insulin is a major inducer of glucose metabolism through its control of GLUT4 translocation to the sarcolemma. Apart from inducing GLUT4 translocation it also activates phosphofructokinase 1 (PFK-1) (Boudina et al., 2009) thus driving glycolysis. In brevity cardiac insulin signalling is initiated upon insulin binding to the sarcolemmal insulin receptor (IR) and subsequent autophosphorylation of the IR resulting in

intracellular signalling cascade via the insulin receptor substrate (IRS) which activates phosphatidylinositol 3 kinase (PI3K), which in turn activates phosphoinositide-dependent kinase 1 that activates Akt through phosphorylation inducing glucose uptake and metabolism (Bertrand et al., 2008).

Even though glucose derived ATP is less per molecule than FFA, one advantage is its lesser dependence on $O_2$ due to anaerobic glycolysis. This makes glucose a useful "rescue" substrate in situations of metabolic stress when the $O_2$ availability may not be enough to sustain efficient metabolism of FFA. This has been shown by inhibiting the glycolytic flux in combination with ischemia which causes prolonged contractile recovery time and aggravated myocardial damage, possibly via impaired intracellular $Ca^{2+}$ homeostasis (Jeremy et al., 1993; Jeremy et al., 1992).

Glucose uptake over the sarcolemmal membrane occurs through passive diffusion down a concentration gradient, through the glucose-transporter family proteins (GLUTs). The gradient is maintained as the hexokinase-catalysed first step of glycolysis has a higher glucose handing capacity than the GLUTs in its conversion of glucose to glucose-6-phosphate (G-6-P). GLUT1 and GLUT4 are the two glucose transporters expressed in cardiomyocytes; GLUT1 in foetal and early life and the insulin dependent GLUT4 in adult myocardium. GLUT4 cycles between the sarcolemma and cytoplasm in response to adrenergic signalling, increased work load, and insulin (Montessuit and Lerch, 2012). In addition to stimulating FFA transport into the mitochondria, AMPK also induces GLUT4 translocation to the sarcolemma in its purpose to maintain the supply of ATP in the cardiomyocyte. This happens as AMPK phosphorylates the RAB-inactivating protein group TBC1D1 and 4. Upon phosphorylation the RAB group of proteins bind GTP which is necessary for GLUT4 vesicle fusion with the plasma membrane of the cell (Coven et al.,

2003; Dyck and Lopaschuk, 2006; Hardie et al., 2012; Russell et al., 1999). After import over the sarcolemmal membrane, glucose is phosphorylated to G-6-P and metabolised through glycolysis via PFK-1 or stored as glycogen (Abel et al., 2012). Through anaerobic glycolysis G-6-P is converted to pyruvate which is imported into the mitochondria, where it is converted to acetyl-CoA and NADH through the action of pyruvate dehydrogenase (PDH) and feeds into the Krebs's cycle. Under anaerobic conditions pyruvate will be converted to lactate (Lopaschuk et al., 2007).

### 1.3.3 Myocardial substrate selectivity, cross-talk, and its alteration in disease states

As mentioned previously, there are different advantages to the use of FFA or glucose as substrate. In situations of rest where the ATP consumption rate is relatively low and $O_2$ of plenty, it seems the heart favours the use of FFA to a 50-70 % rate (Lopaschuk et al., 2010) whereas in situations of decreased $O_2$ supply and metabolic stress glucose provides an $O_2$ -sparing alternative (Montessuit and Lerch, 2012). Per molecule palmitate, 105 ATP is generated and 23 oxygen atoms consumed (~2.28 phospho/ $O_2$ (P/O) ratio), and 31 ATP:12 oxygen (~2.58) being the equivalent ratio for glucose. Thus, the switch to glucose will generate approx. 0.3 more ATP per oxygen. It is also noteworthy that glucose simply generates NADH as opposed to FFA which also generates $FADH_2$. $FADH_2$ is less efficient in generating the ATP fuelling proton gradient in the ETC (Lopaschuk et al., 2010).

The discussion of what is the more energetically favourable nutrient in cardiac metabolism may however be a futile one and the interplay between the two processes of glucose and FFA metabolism more important. Indeed there is a counter balancing

communication, or “cross-talk”, between the two processes which is mainly controlled through the activity of PDH. Increased FFA oxidation reduces PDH activity and thus pyruvate mitochondrial import and vice versa. Also, increased FFA-oxidation inhibits phosphofructokinase, thus inhibiting cytosolic glycolysis (Lopaschuk et al., 2010).

To conclude, in an organ with a high energy demand an excessive capacity for rescue in times of poor nutrient supply is of importance. For energy storage, fat is more effective than glycogen. Thus, even though the process of ATP extraction per FFA-molecule is less efficient compared to glucose, it would make sense to primarily depend on the former.

In disease states, the availability of one substrate may be severely limited thus posing a restriction on the heart’s ability to act as an omnivore. I have chosen to illustrate this by looking at the situations that arise under the conditions of chronically reduced oxygen supply, as in coronary arteriosclerosis, and obesity where fatty acid oxidation substrate is of plenty, and insulin resistance limits the intracellular glucose availability.

#### *1.3.3.1 Myocardial metabolism in ischemia*

As blood supply and $PO_2$ drops, the heart’s opportunity to rely on oxidative processes for metabolism will be reduced. The raised circulatory [FFA] in response to the adrenergic drive in combination with raised malonyl-CoA resulting in increased CPT1 activity, will fuel the fatty acid metabolism of the heart. Since the oxygen is not available to supply the oxidative process, the ATP levels in the cardiomyocytes will drop, along with increased [NADH] and [$FADH_2$] which act to inhibit the Krebs cycle further adding to the impairment of ATP generation. The anaerobic cytosolic glycolysis will be employed fully and due to the impaired drainage of metabolic waste products, lactic acid

will soon accumulate from the increased [pyruvate] which will cause intracellular pH to drop. Along with disturbed ionic homeostasis due to ATP depletion, the myofilament ATP access will be restricted and contractures will tend to occur due to increased [$Ca^{2+}$] and impaired actomyosin cross bridge detachment (Lopaschuk et al., 2010). The more drastic the cut of blood supply, the more severe the described changes are, potentially causing infarction.

#### *1.3.3.2 Myocardial metabolism in obesity and diabetes*

In obesity, increased reliance on fatty acid oxidation is reported. This may partly be due to increased circulating lipid substrate but also an independently increased presence of CD36 in the sarcolemma. Interestingly, insulin dependent diabetic models, such as the streptozotocin (STZ) induced model of diabetes type 1, also show an increased fatty acid metabolism, possible due to increased lipoprotein lipase activity, hydrolysing FFA from TG, likely due to a relative inability to import glucose via GLUT4. The increased reliance on FFA-oxidation and FFA-uptake has been proposed to increase intracellular storage of TG in the cardiomyocyte as the uptake exceeds consumption rate even though the latter is reported as increased. The increased FFA oxidation rate is believed to occur partly due to transcriptional regulation through PPARα and PGC1α even though early changes have been reported to occur without concomitant upregulation of said factors. FFA themselves are known to activate nuclear PPARα receptors in an autopromoting fashion. Apart from promoting FFA metabolism PPARα has also shown to reduce GLUT4 and PDK4 expression. PDK4 acts to promote PHD activity through phosphorylation. Thus, intracellular lipid accumulation is likely not due to depressed FFA-oxidation (Lopaschuk et al., 2007; Lopaschuk et al., 2010). Due to increased FFA-oxidation, hearts in obese

subjects may suffer from increased vulnerability to ischemia due to changes described previously: depressed PDH activity and higher generation of lactate, already in the non-ischemic state.

The condition of obesity induces many co-morbidities: hypertension due to activation of the renin-angiotensin-aldosterone-system (RAAS), insulin resistance, and coronary atherosclerosis to mention those with direct implications on circulatory homeostasis. This makes the origin of individual changes seen in the cardiac phenotype hard to trace. However, impaired cardiac function in the form of diastolic dysfunction, in the context of impaired glucose handling, without hypertension and coronary atherosclerosis is recognised as the clinical entity of diabetic cardiomyopathy (Boudina and Abel, 2007; Khavandi et al., 2009).

### 1.4 Diabetes mellitus and cardiac contractility

Diabetes mellitus (DM) is a condition where peripheral tissue utilisation of glucose is impaired resulting in elevated circulating [glucose]. Insulin is crucial for glucose uptake in skeletal muscle, liver, adipose tissue, and heart. DM is traditionally divided into type 1 and type 2 DM. Type 1 DM is due to reduced insulin production in the pancreatic β-cells and type 2 DM is due to a peripheral insulin resistance where β-cells initially compensate through increased insulin secretion up to maximum insulin production and secretory capacity whereby the β-cells eventually fail. The point at which β-cells fail varies between individuals. Both types of diabetes are associated with increased cardiovascular morbidity.

### 1.4.1 **Diabetic cardiomyopathy**

Diabetic cardiomyopathy constitutes a complication to diabetes mellitus (DM), type 1 and 2, independently of coronary disease and hypertension (Boudina and Abel, 2007; Khavandi et al., 2009). Diastolic dysfunction has been shown to exist in 30 % of patients with DM type 2 without clinical symptoms related to heart failure. An increased prevalence of diastolic dysfunction is also seen in patients with pre-diabetic impaired glucose tolerance (Dinh et al., 2010). Indeed, a cardiac selective genetic model of insulin receptor knock-out reproduced a cardiac phenotype of diabetic cardiomyopathy, despite systemic euglycaemia (Belke et al., 2002).

### 1.4.2 **Proposed pathogenetic mechanisms in diabetes**

#### *1.4.2.1 Lipotoxicity*

As discussed previously, FFA oxidation is increased in obesity (Lopaschuk et al., 2007; Lopaschuk et al., 2010; Martyn and Gordon, 2001). It has been reported to precede hyperglycaemia and cardiac dysfunction and thus qualifies as a potential agent in the induction of cardiac dysfunction (Abel et al., 2008). In a model of diabetes, the Zucker fatty rat, an approximate 100 % increase in FFA oxidation along with 70 % increase in FFA esterification was reported (Carley and Severson, 2005). This indicates a surplus of FFA import that will be stored as intracellular lipids. Indeed, a non-purpose increase in uptake of FFA but reduced oxidation capacity has been reported in the context of cardiac insulin resistance (Abel et al., 2012). This excess lipid handling by the heart has proven detrimental to cardiac function. As neutral fats per se TGs are not suspected to impair cardiac function but harmful effects of cardiac steatosis are conveyed through activation of intracellular signalling pathways, or non-TG lipids, such as ceramide or diacylglycerol

(DAG) (Goldberg et al., 2012). The phenomenon is referred to as lipotoxicity (Wende et al., 2012). Central processes mentioned in cardiac lipotoxicity are increased apoptosis and mitochondrial dysfunction. The lipid intermediary species ceramide has toxic properties activating autophagic and ROS generating mitochondrial dysfunction-inductive pathways (Abel et al., 2012). It may also be that ceramide induces a vicious circle as itself appears to have insulin resistance causing properties (Wende et al., 2012). DAG is known to activate PKC which might inhibit insulin signalling through IRS phosphorylation (Abel et al., 2012).

#### *1.4.2.2 Myocardial fibrosis in diabetes*

Interstitial myocardial fibrosis has been implicated as an early pathogenetic factor in the development of diabetic cardiomyopathy. Hyperglycaemia, hyperinsulinaemia, and insulin resistance has been suggested to increase profibrotic transforming growth factor (TGF) β signalling, In a type 2 DM fat rat model the level of TGF β II receptors was found upregulated along with an increase in collagen in relation to total tissue weight at a prediabetic stage (Mizushige et al., 2000) which suggest that myocardial fibrosis may play an important role in whole myocardium decreased compliance. Collagen 3 is reported as the collagen isoform reported to be upregulated in diabetes associated fibrosis (Goyal and Mehta, 2012).

#### *1.4.2.3 Effects on $Ca^{2+}$ handling*

Studies on $Ca^{2+}$ transients in isolated cardiomyocytes, along with cell dynamics have revealed disturbances as a result of diabetes. For the sake of quick induction the STZ

inducible model of type 1 DM is the most frequently reported on. In rats, STZ-induced DM resulted in prolonged decay time of the $Ca^{2+}$ transient along with increased baseline [$Ca^{2+}$], and increased time of recovery after caffeine induced SR depletion, suggesting impaired SR activity. This was associated with decreased unloaded shortening amplitude after induction through patch-clamp pipette mediated membrane depolarisation suggesting impaired LTCC induced $Ca^{2+}$ release at matched stimulation voltages (Bracken et al., 2006). A different study in the same model reported more florid changes, translatable to an *in vivo* phenotype of systolic and diastolic dysfunction. These researchers were able to associate the *in vivo* phenotype with impaired relaxation and contraction on a single cell level together with an increase in time to peak and time to baseline on the top of decreased amplitude of the $Ca^{2+}$ transient. The levels of SERCA2a, RyR, and NCX were depressed from diabetes offering a plausible explanation for changes seen (Choi et al., 2002). A third study of the same model also showed depressed decay rate of the $Ca^{2+}$ transient in association with reduced SR $Ca^{2+}$ load and depressed SERCA2a levels at a stage of isolated diastolic dysfunction (Lacombe et al., 2007).

In diet induced diabetes type II the phenotype can be regarded as milder and the disease progression more true to the pathophysiological situation in humans. In a HFD model in C57BL6/J mice the unloaded shortening amplitude of isolated cells and their relaxation rate were increased compared to control independently of changes in diastolic intracellular [$Ca^{2+}$] and the $Ca^{2+}$ transient profile (Howarth et al., 2005). Genetic models of type II DM, such as the *Ob/ob* mouse exhibited a reduced shortening time and impaired relaxation along with elevated baseline [$Ca^{2+}$] and decay rate (Li et al, 2006). In patients with subclinical heart dysfunction, isolated cardiomyocytes displayed a

prolonged rise of the $Ca^{2+}$ transient along with a reduction in RyR mRNA and protein levels with unaltered SERCA levels (Reuter et al., 2008).

As seen above, effects of diabetes and impaired glucose handling on $Ca^{2+}$ handling in the cardiomyocyte are diverse. It is however important to bear in mind the great variability in modes of induction and severity in the models described. Also, previously mentioned co-morbidities of RAAS activation and hypertension are likely to be important in interpreting the diverse results.

#### *1.4.2.4 Effects on myofilament function*

The effects on myofilament function from type 1 DM is widely published on in rodent models. Studies show desensitization to $Ca^{2+}$ and decreased ATP tension cost in combination with decreased cross bridge cycling rate. Changes seen are partly postulated as due to changes in MHC isoform expression (α→β-MHC), posttranslational modifications, and/or to cTnT foetal isoform upregulation (Hofmann et al., 1995; Ishikawa et al., 1999; Rundell et al., 2004). The MHC shift seen in small rodent models of diabetes appears to be under insulin transcriptional regulation (Giger et al., 2007) and may contribute to impaired diastolic function as the ATP turnover and thus cross bridge cycling rate is slower in β compared to α MHC. For the same reason, the strong binding state of the actomyosin interaction is prolonged, causing a higher force generating capacity and thus reduced ATP usage per force unit produced (VanBuren et al., 1995). As the β isoform is already the predominant MHC expressed in adult human cardiac ventricles, the effect of MHC isoform switch on cross bridge cycling rate is probably of less importance in the pathogenesis of diastolic dysfunction in this species. Investigations into the myofilament function in type II DM models are scarcer. However,

both *ob/ob* and *db/db* animal models show the same MHC isoform shift (Buchanan et al., 2005). A study of 7 patients with DM, of which 5 had established diastolic dysfunction showed myofilament desensitization to $Ca^{2+}$ (Jweied et al., 2005).

Titin, which contributes to passive tension, has also been shown to change isoform composition due to impaired insulin signalling adding to reduced diastolic compliance because of increased N2B/N2BA ratio (Kruger et al., 2010). Also, a reduction in total phosphorylation of N2B was seen in human cardiomyocytes with DM together with aortic stenosis, compared to just aortic stenosis, associated with increased passive stiffness (Falcao-Pires et al., 2011).

#### *1.4.2.5 Concomitant recordings of $Ca^{2+}$ handling and myofilament function in diabetes*

To obtain a clear view of the functional origin behind disturbances in cardiac function, it is important to gain insight into both $Ca^{2+}$ handling processes and myofilament function, separately. There are relatively few such studies.

In type 1 DM STZ-induced cardiomyopathy Ishikawa and co-workers investigated $Ca^{2+}$ transient profile as well as myofilament function in rat trabeculae reporting slowed cytosolic $Ca^{2+}$ decay rate independent of myofilament activation. $Ca^{2+}$ sensitivity was found unaltered (Ishikawa et al., 1999).

In a study of dietary induced cardiac dysfunction, *Ob/ob* transgenic mice with impaired glucose handling were interrogated with respect to $Ca^{2+}$ handling and MHC isoform expression levels; this showed reduced single cell contraction and relaxation velocities in conjunction with elevated diastolic [$Ca^{2+}$] and reduced $Ca^{2+}$ transient decay rate, and

increased β-MHC expression. Unfortunately the isolated functional impact of the MHC was not interrogated (Li et al., 2006). Howarth et al showed an increased relaxation rate of isolated cardiomyocytes independent of $Ca^{2+}$ transient alterations (Howarth et al., 2005). This is an interesting finding which shows a counterintuitive outcome at the single cell level compared to the established whole organ phenotype of impaired diastolic function. Needless to say, accessibility to myofilament study techniques would have added more weight to their study. A study reporting improvements in cardiac function upon saturated fat feeding in induced heart failure did not find alterations in $Ca^{2+}$ transients but noticed changes in myofilament protein expression levels. In this study, functional assessment of said protein was also left out which again reduces the conclusive impact of the study, despite reported inhibited MHC isoform shift through high saturated fat feeding with no reported differences in total phosphorylation levels of cMyBP-C, cTnI, TnT, nor RLC (Cheng et al., 2011).

Jweied et al interrogated myofilament function in human type 2 DM through the study of cardiac myocytes preserved through flash freezing, a method disabling the subsequent study of intracellular $Ca^{2+}$ handling. As findings suggested depressed myofilament $Ca^{2+}$ sensitivity which is associated with increased cTnC dissociation rate (Ishikawa et al., 1999), intracellular $Ca^{2+}$ transient assessment would have added valuable information to explain to expected impaired relaxation (Jweied et al., 2005). As Cheng and co-workers suggest, the effects of dietary lipids on cardiac myofilament function appear to be under-investigated (Cheng et al., 2011).

### 1.4.3 The cardiac phenotype in type 2 diabetes mellitus is usually confounded – diabetes, RAAS, and oxidative stress

As mentioned previously, the origin behind the cardiac phenotype seen in diabetes type 2 can be hard to pin down due to multiple systemic obesity induced effects. Pure deficiency in myocardial insulin signalling is therefore hard to separate from the systemic and tissue based co-morbidities of hypertension and oxidative stress respectively or in combination.

The effect of renin in inducing elevated blood pressure is a well known physiological response to reduced filling pressure in the arterioles of the renal glomeruli in order to maintain circulatory homeostasis through peripheral arterial vasoconstriction (Guyton, 2001). Recently, further effects have been discovered by the effector substance ATII; namely reduction in pancreatic β-cell insulin secretion upon glucose stimuli. Inhibiting ATII receptors using valsartan has shown to improve glucose homeostasis without reduction in body fat stores in a HFD model of insulin resistance (Cole et al., 2010). Thus, circulatory and glucose homeostasis seem to have a common denominator.

The diabetic myocardium has different sources responsible for the generation of ROS. Upon increased β-fatty acid oxidation, reducing agents NADH and $FADH_2$ are fed into the ETC generating $O_2^-$ from complex I and III. This is reported to occur in leptin deficient and leptin-receptor deficient obese mouse models of insulin resistance and DM type 2 (Lopaschuk et al., 2010). NOXs may also prove to play a role in the pathogenesis of diabetic cardiomyopathy. Li et al were able to repeat their cardiomyocyte phenotype of impaired shortening dynamics and depressed $Ca^{2+}$ decay rate in a *ob/ob* mouse through stimulation of isolated wild type single myocytes with ATII, and subsequently reverse it with apocynin, an inhibitor of NOX (Li et al., 2006). As mentioned previously, NOX2 has

recently been shown to affect contractile function through direct modifications of the RyR, increasing its sensitivity to $Ca^{2+}$ (Prosser et al., 2011), and has been suggested to be involved the Anrep effect, by contributing to elevating the $Ca^{2+}$ transient amplitude in response to stretch (Cingolani et al., 2012).

The effects of hypertension on cardiomyocyte function may involve ATII mediated oxidative stress via NOX activity. In a short duration (24-36 hr) aortic banding model of pressure overload, a NOX2 -/- mouse line displayed increased tolerance to pressure overload, maintaining LV systolic and diastolic function and single cardiomyocyte unloaded dynamics. The NOX2 -/- model also had reduced development of fibrosis in response to the pressure overload (Grieve et al., 2006). A physiological mode of increased afterload is exercise in which NOX activity was found increased in a dog exercise model and related to increased RyR activity through S-glutathionylation. The effect was inhibitable by the use of apocynin (Sanchez et al., 2008). Exercise induced cardiac fatigue is a state where prolonged hard physical exercise induces a transient LV dysfunction due to prolonged state of increased after load. In a model of prolonged strenuous exercise in rats apocynin administration relieved the phenotype suggesting a detrimental role of NOX (Vitiello et al., 2011). The administration of deoxycorticosterone acetate (DOCA)-salt to induce mild hypertension results in diastolic dysfunction on a whole organ as well as single cell level and, on the myofilament level, increased $Ca^{2+}$ sensitivity and S-glutathionylation of cMyBP-C (Lovelock et al., 2012). As obvious from the above, common morbidities with the HFD induced metabolic syndrome have their own separate effects on processes and parameters of cardiomyocyte contraction, which need to be taken into account in judging the origin of phenotypic changes due to insulin resistance.

## 1.5 Mouse models of diabetes

Diabetes is a condition of several pathogenetic backgrounds which calls for a variety of different models to be available for the researcher wishing to study the effects on cardiac function. Below is a division into type 1 and 2 DM mouse models.

### 1.5.1 Type 1 DM-models

#### *1.5.1.1 Pharmacologically induced*

STZ injection is a commonly used method to induce type 1 DM through irreversible inhibition of β-cell function. STZ is glucose analogue and enters the β-cells through GLUT2 transport. The mode of administration offers the experimenter two major ways of inducing diabetes. High dose induction will have a direct toxic effect on the β-cells and immediately render the mouse glucose intolerant by DNA alkylation, $NDA^+$ depletion, ATP reduction and hence impaired insulin production. STZ also increases free radical production speculated to have a further toxic effect on the DNA. Although an immediate hyperglycaemia is induced from high dosage administration, spontaneous regeneration of β-cells can occur which warrants close monitoring of glucose levels to ensure a valid model throughout a study period (King, 2012).

However, a repeated low dose administration will induce expression of glutamic acid decarboxylase (GAD) autoantigens which generate an autoimmune reaction towards the β-cells (Shen and Bornfeldt, 2007; Van Belle et al., 2009), insulitis and reduction in cell volume over time (King, 2012).

The former method of induction is precise in its timing. Thus, the effects of interest can be studied within short term, but the relevance to diabetic patients in the western world may be limited due to the severity of the insult (Wang et al., 2008) which would only be seen in untreated patients during the debut stages of the disease. The low dose regimen may be closer to the human pathogenetic process, however the induction is longer (20-30 days) (Van Belle et al., 2009) compared to a single high dose induction.

#### *1.5.1.2 Genetic*

Mice transgenically rendered to express the rat-insulin-promoter-glycoprotein (RIP-GP) on their β-cells are susceptible for infection by the lymphocytic choriomeningitis virus (LCMV). Upon infection with LMCV the β-cells will be recognised by the T-cells that induce an immune response, rendering the mouse insulin deficient within 1-2 weeks. Since specifically targeting the β-cells the viral transfer does not cause any systemic inflammatory response (Shen and Bornfeldt, 2007; Van Belle et al., 2009). Variation in the degree of glucose intolerance depend on replication levels of the virus (King, 2012).

A novel model of type 1 DM is the pancreatic islet beta-cell apoptosis through targeted activation of caspase 8 (PANIC-ATTAC) model. A mutated FK506 binding protein (FKBP) is expressed fused to caspase 8, under the insulin promoter. In a monomeric form the construct does not induce apoptosis but upon administration of a dimerising compound it is activated and induces the phenotype which consists of a 90% reduction in pancreatic insulin and also observable reduction in β-cells (King, 2012). This model has the interesting feature of being fully reversible allowing researcher to study effects of improved glucose control independently of insulin administration (Van Belle et al., 2009; Wang et al., 2008).

#### *1.5.1.3 Spontaneous models*

For a natural induction model the non-obese diabetic (NOD) mouse is available. This inbred mouse line has a debut of diabetes at the age of 40 weeks, due to a T-cell mediated reaction to β-cells, although the process starts at 5 weeks of age already (Van Belle et al., 2009). This is a rather long induction period which adds to costs of maintaining colonies, for breeders and researchers alike adding a significant disadvantage to what is perhaps the model best mimicking the human type 1 DM autoimmune pathogenesis (Atkinson and Leiter, 1999). With a spontaneous inflammatory response responsible for the β-cell destruction it has been noted as a valuable model in studying the pathogenetic process of human type 1 diabetes mellitus and also modulation of autoimmune processes in therapeutic purposes (King, 2012).

In summary the STZ induced model of type 1 DM is the most prevalently used in the study of effects of diabetes on cardiomyocyte contractility. A critical voice may argue that several parallel stress processes are induced with a rapid and drastic elevation of blood glucose and close to total and immediate abruption of insulin signalling. For example, with parallels to human disease, ketoacidosis is a well known and severe complication due to the inability of using glucose as a substrate whereby extensive fatty acid metabolism generate ketone bodies with metabolic acidosis as a consequence.

### 1.5.2 **Type 2 DM-models**

#### *1.5.2.1 Diet induced*

The simplest model, and perhaps the one most faithful to the real life situation, is the high calorie diet induced obese mouse. Boost of caloric count in mouse chow is usually achieved by increasing the content of refined sugars (high sugar diet – HSD), fats (high fat diet – HFD) or both (high fat sugar diet – HFSD). The effect in terms of obesity and diabetes does not only depend on source of calories but also of the subject mouse strain. AKR/J, DBA/2J, and BTBR $T^{+}$ tf/J are considered highly responsive to HFD, the C57BL6/J intermediate, whereas A/J and Balb/cJ are considered diet resistant (Baribault, 2010; Fearnside et al., 2008). The C57BL6/J is known not to progress to β-cell failure and end-stage diabetes complications in the form of diabetic nephropathy upon diet treatment alone (Baribault, 2010) which is in line with the early and often subclinical condition of the metabolic syndrome in humans (Antonova et al., 2010). HFD feeding as opposed to HSD appears to be a better stimuli for development of insulin resistance and hyperglycaemia as high sucrose diet did not induce hyperglycaemia nor hyperinsulinaemia after four months of feeding in C57BL6/J (Surwit et al., 1995).

#### *1.5.2.2 Spontaneous*

*The* ob/ob *and* db/db *mice:* These mouse lines express autosomal recessive heritage patterns of leptin and leptin-receptor deficiency respectively. Leptin is a hormonal regulator of appetite secreted from adipose tissue. It functions as a sensor of organism nutrient status and affects feeding behaviour as well as basal energy expenditure. Deficiency in leptin effect generates voracious mice with a high disposition to accumulate fat. The diabetic effects are more dramatic in the *db/db* mouse with

progression to β-cell failure, increased hyperglycaemia, weight loss, ketosis and death within 10 months. The *ob/ob* mouse expressed on a C57BL6/J background exhibits only transient hyperglycaemia due to an ability to compensate though increased insulin secretion (Srinivasan and Ramarao, 2007) .

*New Zealand obese (NZO) mice:* Unlike the leptin deficient mice, the NZO is of polygenic origin, selectively bred over generations, with individuals of disposition to obesity. These animals display hyperphagia, obesity, mild hyperglycaemia, hyperinsulinaemia and impaired glucose tolerance (Srinivasan and Ramarao, 2007). However, it seems much of the origin of the obese phenotype lie at the leptin signaling level, like the *db/db* and *ob/ob* mice, with a deficient transport over the blood brain barrier as the functional lesion, as centrally administered leptin still has proleptinic effects which are absent upon peripheral administration (King, 2012).

### 1.5.3 **A model of hypoinsulinaemia and peripheral insulin resistance**

*Non-obese Ins2$^{Akita}$ mice:* Due to a mutation in the pro-insulin gene *INS2,* insulin generated in the β-cells of these mice fails to be secreted rendering the mouse hypoinsulinaemic and hyperglycaemic without accompanying obesity (Srinivasan and Ramarao, 2007). Due the impaired secretion ER overload develops and stress eventually renders the process toxic causing β-cell death (King, 2012). Recently it has also been shown to exhibit skeletal muscle, liver, and brown adipose tissue insulin resistance, classical features of diabetes type 2 (Hong et al., 2007). From a cardiovascular point of view this model is interesting as it allows the opportunity to study the effects of impaired insulin signalling in the absence of obesity induced hypertension, especially so

since it appears to show signs of LV hypertrophy relieved by muscle insulin sensitizing phloridzin administration (Hong et al., 2007).

## 1.6 Aim of this thesis, choice of model, and study design

### 1.6.1 **Aim of this thesis**

I aimed to compare the effects of HFD on the principal mechanisms of cardiac contractile regulation – $Ca^{2+}$ handling and myofilament dynamics – in relation to whole organ function, and to contribute to the knowledge of disease progression. To gain a comprehensive understanding, I set out to examine cardiac function in an established model of physiologically induced obesity at two different time points, employing a top to bottom approach involving a combination of whole organ, single cardiomyocyte, as well as myofilament functional assessments. By allowing a subgroup of the HFD fed group to revert to control chow I also aimed to investigate the correlation between systemic phenotype reversal and cardiac function through diet induced weight loss, the first step in clinical treatment of obesity.

### 1.6.2 **Choice of model**

I have chosen to use the HFD induced C57BL6/J mouse model of the metabolic syndrome as a study model. This is an intermediate degree, physiologically induced model of the metabolic syndrome unlikely to progress into end stage overt insulin dependent diabetes (Baribault, 2010). It is thus suited to model the state of pre-diabetic silent insulin resistance, a growing ground for later more severe complications. This model is also known to effectively lose weight and reverse its high calorie induced

phenotype of impaired glucose handling (Parekh et al., 1998) making it suitable to investigate the effects of weight loss.

### 1.6.3 **Study design**

*In vivo* whole body parameters, cardiac function and plasma chemistry assays were carried out at critical time points throughout the study in complement to *post mortem* dissection in order to characterise organs by gross weight, histology, *in vitro* function, and molecular biology. After 30 weeks part of the HFD fed animals were reversed to a normal diet for 10 weeks to obtain information on reversibility of HFD induced changes.

# 2 Material and methods

## 2.1 Mouse line

C57BL6/J mice were used throughout the study, purchased from Charles River UK. The C57BL6/J line is prone to develop obesity and insulin resistance in response to a HFD (Fearnside et al., 2008).

## 2.2 Mouse husbandry

All animal work carried out in this thesis was sanctioned by the animal care and ethical review (ACER) committee of Oxford University in accordance with the animal scientific procedures act (ASPA) of 1986.

5-6 mice were kept per individually ventilated cage (IVC) with free access to food and drinking water. The animal facility was subjected to an 8:16 h dark-light cycle. The mice enjoyed standard animal technician care. Due to the expected diabetic condition of the study group special attention was given to excessive wetting of cage bedding material.

## 2.3 Diets

Feeding of special diets (HFD: Cat. No. 824072 and Ctrl: Cat. No.: 831195, Special Diet Services, Witham, UK) commenced at an age of 8 weeks, 4 weeks past weaning. This constituted study time point zero; the reference point throughout this study.

The major bioavailable nutrients of the HFD were: fat 60 %, protein 20 %, and carbohydrate 20%

The major bioavailable nutrients of the Ctrl diet were as follows: fat 7.4 %, protein 17.5 %, and carbohydrate (starch)75%.

## 2.4 Reagents and solutions

All reagents were purchased from Sigma Aldrich if not stated otherwise. Custom prepared solution recipes can be found in Appendix I.

## 2.5 Whole organism and plasma chemistry assessments

### 2.5.1 Growth development curve

The mice were weighed in the morning every 7$^{th}$ day using the same 0.1 g sensitivity scale (Ohaus CS200), throughout the study.

### 2.5.2 Quantitative magnetic resonance (QMR)

To estimate the fat to lean tissue relationship mice were subjected to QMR every 10 weeks. QMR is based on the magnetic resonance technique where a radio frequency magnetic field uniforms the spin direction of $H^+$. The abruption of the magnetic field is followed by a return towards initial entropy levels, a return rate which differs between fat and water and can be read by the radio frequency emitted from the tissues. The mice were weighed and then allowed to freely walk into the measuring chamber before being restrained and subject to scanning which was held to a minimum duration of 5 minutes. Each scan session was preceded by a calibration with oil and water samples for fat and water respectively.

### 2.5.3 **Glucose handling abilities**

#### *2.5.3.1 Fasting blood glucose*

An initial inquiry into glucose handling abilities was performed by measuring overnight (12-16 hrs) fasting blood glucose (b-glc) from tail vein at w 5. This was immediately obtained through the Bayer Ascencia Contour meter (reader and test strips, Bayer UK). 3 µl of whole blood was used, obtained after restraining the mouse and cutting the surface of the tail skin overlying the tail vein.

#### *2.5.3.2 Intraperitoneal glucose tolerance test*

The subject mice were fasted over night and kept at 38 °C for 30 min to induce vasodilatation to facilitate bleedings from the tail vein. The procedure is described in the below 7 time points:

-30 min: Mice were restrained and an incision was made distally over a tail vein to induce bleeding. B-glc was immediately obtained through the Bayer Ascencia Contour meter. Blood was thereafter collected in EDTA-coated Microvette® CB 300 K2E tubes from Sarstedt (Nürnbrecht, Germany) by capillary force, and stored on ice for subsequent plasma separation.

0 min: Mice were restrained and b-glc measured. Intraperitoneal injection of 10 µl/g bodyweight of 0.9% NaCl, 0.2 g/ml D-glucose solution, i.e. 2 g glucose/kg bodyweight, was administered.

30 min: Mice were restrained and b-glc measured. Blood was collected from the tail vein for plasma separation.

60 min: Mice were restrained and b-glc measured.

90 min: Mice were restrained and b-glc measured.

120 min: Mice were restrained and b-glc measured.

180 min: Mice were restrained and b-glc measured.

From 0 min onwards bleeding could be reinitiated by removing the coagulated blood from the first incision.

B-glc was plotted against time to compare the glucose handling capacities. The area under curve of the resulting graph was used to quantify glucose tolerance ability (Du et al., 2012).

### 2.5.4 **Plasma analysis**

#### *2.5.4.1 Plasma separation*

Plasma was separated from whole blood by centrifugation of EDTA coated capillary tubes at 20 x g for 10 minutes at 4 °C. The supernatant was aliquoted and stored at -80 °C until use.

#### *2.5.4.2 Determination of plasma insulin concentration*

Plasma insulin concentration was determined using the Enzyme-linked immunosorbent assay (ELISA) -technique. The colorimetric Crystal Chem. Inc. Rat Insulin Assay (Cat no.

90010) was utilised and carried out according to the manufacturer's instructions. The standard curve was constructed using mouse insulin from the same supplier (Cat no. 90020).

## 2.6 *In vivo* cardiac phenotyping

### 2.6.1 *In vivo* haemodynamics

Central aortic and left ventricle pressure was recorded under general anaesthesia (GA) induced with 4 % isoflurane. After induction the mouse was placed on a heating pad set at 38 °C to avoid hypothermia during the recording. Anaesthesia was thereafter maintained at 2 % isoflurane administered via a nose cone. The right carotid artery was dissected and cannulated with an ultra-miniature 1.4 F pressure catheter (Cat. No.: SPR-671 Millar Mikro-tip, ADInstruments, UK). As the cannula was advanced towards the left ventricle a pause was made in the ascending aorta to record central aortic pressure. As the catheter passed the aortic valve a distinct increase in pressure was noted which confirmed the correct position of the catheter in the LV; it was thereupon secured in the neck region. During recording 1.5 % isoflurane was used. At all times 100 % $O_2$ was used as carrier gas for the anaesthetic.

A fifteen minute baseline recording was secured for circulatory stabilisation and analysis of baseline parameters after which the animal was sacrificed through cervical dislocation.

*The following parameters were investigated:* Central systolic and diastolic aortic pressure (SAP & DAP respectively), mean aortic pressure (MAP=(2 x diastolic)+systolic)/3) (assuming a 2:3 time ratio between systole and diastole), and left ventricle end diastolic

and systolic pressure (LVEDP & LVESP respectively). Maximum pressure development rate during systole and diastole (+dP/dt & -dP/dt respectively) were derived from the pressure trace. All analysis was performed in the data acquisition software PowerLab 4SP (ADInstruments, UK.)

This acquisition and analysis was carried out by Dr Mohamed Bellahcene.

### 2.6.1 **Transthoracic echocardiography (TTE)**

Echocardiographic imaging of left ventricular systolic and diastolic function was obtained using the Vevo 2100 Imaging System (VisualSonics, Toronto, Canada) including a 30 MHz linear array transducer on a bench-mounted adjustable heating platform, under GA. Anaesthesia was induced with 4 % isoflurane. At all times 100% $O_2$ was used as an anaesthetic carrier gas. After induction the mouse was placed on a 38 ˚C heating pad to avoid hypothermia and anaesthetic gas was administered via a nose cone. Electrodes on the heat pad enabled electrocardiographic (ECG) recordings from front and hind extremities during image acquisition. Preparations for echocardiographic analysis were in the form of shaving the thoracic area and application of pre-warmed ultrasound coupling gel to improve sound conductance and signal to noise ratio. Systolic recordings were performed at a heart rate above 450 beats per minute and diastolic recording between 320-380 beats per minute. The heart rate was regulated by modifying isoflurane percentage. After acquisition the animal was allowed to recover in a 37 ˚C air incubator. All acquisition and analysis was performed in a blinded fashion.

*The following systolic parameters were analysed:* Left ventricular ejection fraction (LVEF), left ventricular end systolic dimension (LVESD), left ventricular end systolic volume (LVESV), left ventricular fractional shortening (FS).

*The following diastolic parameters were analysed:* Left ventricular end diastolic dimension (LVEDD), end diastolic anterior and posterior LV wall thickness. A mitral valve flow Doppler generated profile is seen in fFigure 5 from which E/A ratio, and isovolumic relaxation time (IVRT) were extracted.

This acquisition and analysis was carried out by Dr Arash Yavari.

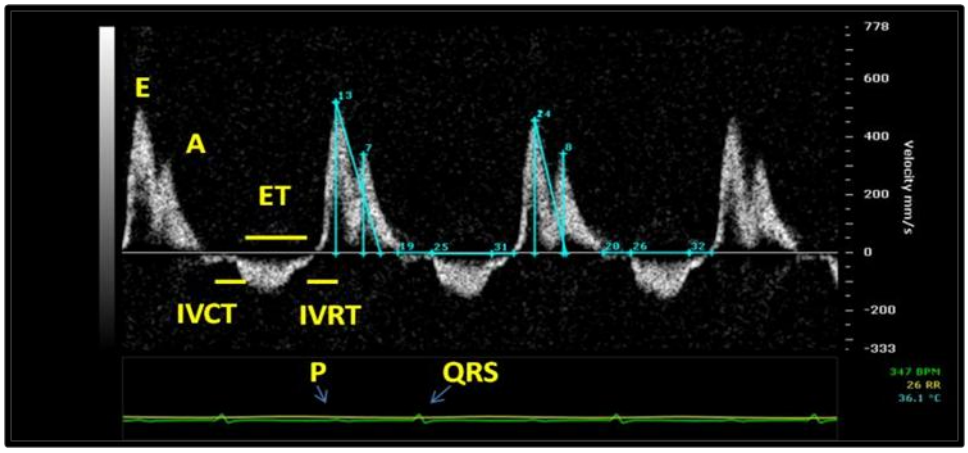



**Figure 5: Cardiac transmitral valve Doppler flow profile:** Representative trace from transmitral valve Doppler recording at low heart rate (347 beats per minute).

## 2.7 Tissue harvesting

The mice were sacrificed through cervical dislocation in accordance with UK Home Office regulations. Death was confirmed through the absence of the corneal reflex. Tissue harvest followed the same sequence on each occasion. The heart was removed after thoracotomy. It was immediately submerged in ice cold phosphate buffered saline (PBS) and perfused retrogradely through the aorta with the same solution using a 22 G cannula. Excess liquid was removed by blotting the heart on absorbent paper. The organ was thereafter weighed on a 0.001 g sensitivity scale and placed in a CRYO.S™ vial. It

was frozen through submersion in liquid $N_2$. The liver was removed, rapidly rinsed in cold PBS, blotted and weighed followed by bilateral epididymal fat depots, kidneys, and retroperitoneal fat depots. All removed organs were weighed. The tibia length (TL) was measured using callipers.

## 2.8 Histology

### 2.8.1 Organ preservation

#### *2.8.1.1 Cryosection preparation*

Organs used for cryosectioning were submerged in optimal cutting temperature compound (OCT) and subsequently frozen on dry ice, and stored at -20 °C until sectioning.

### 2.8.2 Sectioning and staining

#### *2.8.2.1 Cryosectioning*

Cryosections were cut at an angle of 4° and thickness of 7 µm using the Leica CM3050S, and stored at -20 °C until use.

#### *2.8.2.2 Oil red O stain for lipid*

Cryosections that had been air dried over night were fixed in formalin for 5 minutes followed by rinsing in running tap water for 10 min, 60 % isopropranol for 2 minutes, Oil Red O solution for 15 minutes before a final 2 minute rinse in 60 % isopropranol. This concluded the lipid stain. Counterstaining was performed for nuclei in aluminium

haematoxylin for 5 minutes before rinsing with distilled water for 5 minutes and mounting in glycerine mounting jelly.

This was carried out by Dr Alexander Stockenhuber.

## 2.9 Molecular biology

### 2.9.1 Frozen homogenisation

Tissues were crushed in a liquid $N_2$-cooled mortar and pestle and finely ground before being aliquoted into pre-weighed and cooled 1.5 ml microcentrifuge tubes. The weight of each aliquot was recorded.

### 2.9.2 Standard protein extraction procedure

Protein was solubilised by suspending in urea lysis buffer on ice, and passing though a 22G needle. Six passages through the needle were carried out, followed by vortexing for 20 s and sonication (Branson 200 Ultrasonic cleaner) for 5 minutes. Samples were thereafter centrifuged at 330 x g for 2 min. The supernatant was supplemented with protein X 6 loading buffer and kept at 95 ˚C for 5 minutes before storage at -20 ˚C.

### 2.9.3 Myofilament isolation

Myofilaments were purified from whole cardiac tissue as described previously (Solaro et al., 1971). Briefly the following procedure was carried out with samples maintained at a temperature of 0-4 °C: The tissue was homogenised with Polytron in lysis buffer and

centrifuged at 15000 x g for 20 min. The pellets were resuspended in Standard isolation buffer followed by centrifugation at 15000 x g for 5 min. This process was repeated twice. The pellets were thereafter resuspended in EGTA buffer, followed by centrifugation at 15000 x g for 5 min. This was repeated once. The pellets were resuspended in Triton X-100 buffer, followed by centrifugation at 15000 x g for 5 min, repeated twice. The pellets were finally resuspended in Standard isolation buffer, followed by centrifugation at 15000 x g for 5 min. This process was repeated twice.

### 2.9.4 **Protein concentration determination**

The bicinchoninic acid (BCA) assay from Pierce® (Reagent A - Cat. No. 23228, Reagent B - Cat. No. 1859078) was used to determine total protein concentration in lysed tissue samples. The assay was carried out according to manufacturer's instructions. Bovine serum albumin (BSA) in serial dilution was used as a standard curve and absorbance measured at λ=562 nm using the Fluostar Omega spectrophotometer from BMG Labtech (Ortenberg, Germany).

### 2.9.5 **Sodium dodecyl sulphate polyacrylamide gel electrophoresis (SDS-PAGE)**

Solubilised protein were loaded onto polyacrylamide gels and subjected to constant voltage of 150 V to maintain migration towards the cathode. At this stage the tertiary structure of the protein had been denatured and reduced to a polypeptide chain covered in negative charge resulting in migration distance to depend solely on the protein's molecular mass. The comigration of a molecular marker (GE Healthcare Full Range Rainbow Marker, Cat. No. 28925341) alongside the samples of interest provided molecular weight calibration. Percentage acrylamide in the gels varied depending on the

weight of target proteins with smaller proteins warranting higher ranged concentrations of acrylamide (10-12%).

### 2.9.6 Protein total phosphorylation level determination by ProQ diamond staining

Solubilised proteins were separated by SDS-PAGE in a conventional manner and the gels subjected to the following procedure based on manufacturer's instructions: The gels were fixed over-night at 4 °C in methanol 50 % v/v and glacial acetic acid 10 % v/v after which they were rinsed in MQ water for 10 minutes, three times, before staining in ProQ Diamond reagent (Invitrogen Cat. No. P 33300) for 90 minutes under shaking. The gels were subsequently destained in 50 mM sodium acetate and acetonitrile 20 % v/v, pH 4.0 for 30 minutes; this was repeated twice followed by washing in MQ water 2 x 5 minutes. The image was developed through UV transillumination in the Bio-Rad ChemiDoc™ scanner system. All steps after the addition of the ProQ Diamond staining reagent was carried out in a light proof box.

### 2.9.7 Total protein levels determined by SyproRuby staining

Sypro Ruby was used as a post stain after ProQ Diamond staining. After initial image development the gel was washed in MQ $H_2O$ for 5 min followed by incubation in SyproRuby reagent (Invitrogen Cat No. S12001) over night whilst shaking. Thereafter the gel was washed in 10 % (v/v) methanol and 7 % (v/v) acetic acid for 30 min. Before imaging, as described for ProQ Diamond, the gel was rinsed in MQ $H_2O$ twice for 5 minutes.

### 2.9.8 **Immunoblotting**

Solubilised proteins were separated as described above and transferred onto a polyvinyl difluoride membrane (BioRad Immun-Blot® PVDF, Cat No. 162-0177) under constant current (300 mA) for 90 minutes. The surface of the membrane not occupied by protein originating from the gel was thereafter blocked through incubation in 5% w/v dry milk/PBS-T (T: 0.1 % Tween 20), curled in a 50 ml Falcon™ tube under constant rolling for 2 hrs at room temperature.

Depending on the molecular target the membrane was incubated in blocking solution substituted with relevant primary antibody over night at 4% under constant rolling followed by 3 x 30 min washing in PBS-T before incubation with secondary horse-radish peroxidise (HRPO) conjugated antibody for 45 minutes at room temperature. Exposure in the Bio-Rad ChemiDoc™ scanner was preceded by 3 x 30 minutes washing in PBS-T and 30 min washing in PBS. The signal was developed using ECL Plus detection system from GE Healthcare (Cat. No. RPN2132). Exposure duration was customised to obtain optimum signal intensity.

For investigations involving sample sizes larger than what single gels could harbour expression levels in subject groups were related to the average of same controls run on the different gels. Thus, absolute comparisons between blots were avoided.

#### *2.9.8.1 Antibodies utilised*

**Primary antibodies - all suspended in 5 % w/v dry milk in PBST**

| *Target* | *Species* | *Supplier* | *Cat. No.* | *Dilution* |
|---|---|---|---|---|
| p-Akt (S473) | Rabbit | Cell Signaling | 4060 | 1:1000 |
| pan-Akt | Rabbit | Cell Signaling | 4691 | 1:1000 |
| p-GSK3β (S9) | Rabbit | Abcam | ab30619 | 1:1000 |
| pan-GSK3β | Rabbit | Abcam | ab31366 | 1:1000 |
| p-cTnI (S23/24) | Rabbit | Cell Signaling | 4004S | 1:2000 |
| pan-cTnI | Mouse | Abcam | ab7829 | 1:1000 |
| NOX2 | Rabbit | Abcam | ab80508 | 1:1000 |
| p-AMPK (T172) | Rabbit | Cell Signaling | 2535 | 1:1000 |
| α-actinin | Rabbit | (N/A) | 653 (clone) | 1:5000 |
| β-tubulin | Rabbit | Abcam | ab6046 | 1:5000 |

**Secondary antibodies, both IgG HRP conjugate, suspended in 5% milk (w/v) in PBST**

| | | | |
|---|---|---|---|
| Anti-Rabbit | Promega | W401B | 1:5000 |
| Anti-Mouse | Santa Cruz | sc-2375 | 1:4000 |

#### *2.9.8.2 Membrane stripping*

To re-use membranes after an initial immunoblotting they were stripped by incubation in 2% SDS, 25mM Tris-HCl, 0.8 % v/v 2-mercaptoethanol at 50 ˚C for 40 min. Complete stripping of secondary antibody was confirmed by re-developing the membrane for 600 s exposure with no signal after initial blocking with 5 % milk PBST.

### 2.10 Quantitative reverse transcriptase-polymerase chain reaction (qRT-PCR)

Total RNA was extracted using the RNeasy Fibrous Tissue mini kit, following the manufacturer's (QIAGEN) instructions. RNA concentration was determined with a Nanodrop spectrophotometer. One microgram of total RNA was reverse transcribed

with High Capacity cDNA Reverse transcription Kit (Applied Biosystems). qRT–PCR with default temperature settings for fast run was used to detect mRNA levels of select target genes. Samples were prepared with Fast Universal Master Mix for amplification reactions using a StepOnePlus system (Applied Biosystems) and run in duplicates in a total reaction volume of 10 µl. All Taqman oligos, except titin were inventoried products of Applied Biosystems. The relative quantities of target gene mRNA levels were normalized against the endogenous control β-actin.

This was carried out and analysed by by Dr Gabor Czibik.

### 2.10.1 **Oligos used**

| *Target gene* | *Protein expressed* | *Applied Biosystem Cat. No.* |
|---|---|---|
| COL3A1 | Collagen 3 | Mm01254476_m1 |
| SLC2A4 | GLUT4 | Mm01245507_g1 |
| MCPT1 | mCPT1 | Mm00487200_m1 |
| MYH7 | β-MHC | Mm00600555_m1 |
| PDK1 | PDK1 | Mm00554306_m1 |
| PGC1A | PGC1α | Mm00447181_m1 |
| PPARA | PPARα | Mm00440939_m1 |
| UCP2 | UCP1 | Mm00627597_m1 |
| ACTB | β-actin | 4352341E |

Titin isoforms N2B and N2BA mRNA levels were assessed using custom made oligos according to da Silva Lopes (da Silva Lopes, 2011).

*N2B*

For ward primer: 5' - GCAAAGCCTCCAATGAGT ATGG - 3'
Reverse primer: 5' - AGGAAGTAATTTACGAACTTTCTTTTCAG - 3'
Probe: 5' - TGCACAGCCACACTAACT GTGACAGTGC - 3'

*N2BA*
Forward primer: 5' - ACAGTGGGAAAGCAAAGACATC - 3'
Reverse primer: 5' - AGGTGGCCCAGAGCTACTTC - 3'
Probe: 5' - GAAAGAGCTGCCCCTGTGATCA - 3'

## 2.11 Total tissue collagen levels

To determine the total myocardial collagen levels a calorimetric biochemical assay from QuickZyme Biosciences (Leiden, the Netherlands) was utilised. The assay is based on HCl hydrolysis of protein content. Hydroxyproline is unique to collagen and thus after tissue hydrolysis the hydroxyproline quantity can be used to quantify the collagen content. Quantification is based on hydroxyproline oxidation and subsequent staining to generate a colorimetric reaction enabling absorbance measurement to be carried out at λ=570 nm.

Myocardial tissues cleared of basal vessel structures and atria, were homogenised whilst frozen using a liquid $N_2$ chilled mortar and pestle, as described above, and subsequently aliquoted. The assay was carried out according to manufacturer instructions. Briefly, as follows: The sample was hydrolysed in 6M HCl at 95 °C for 20 hrs along with mouse collagen standards of known concentrations including a zero collagen blank and thereafter cooled to room temperature followed by centrifugation at 13 000 g for 10 min. The supernatant was diluted with an equal volume 4 M HCl after the sample was allowed to react with the assay buffer for 20 min at room temperature whilst shaking. Staining of oxidised hydroxyproline residues was then carried out using detection reagent A and B in a 2:3 mixture ratio for 60 min at 60 °C. After the assay mixture had been cooled to room temperature the absorbance measured at λ=570 nm in relation to standard curve constructed with mouse collagen of known concentrations gave the collagen concentration in the extracted samples. Established concentrations were normalised to the weight of raw tissue used.

## 2.12 Total tissue triglyceride levels

To measure total TG content of tissues, a commercial colorimetric assay was used (Cayman Chemical Company, MI, USA, Cat. No. 10010303).

The chemical basis for this assay can be described in a series of enzymatic reactions: TG is hydrolysed to free fatty acids and glycerol by a lipoprotein lipase. The glycerol is thereafter phosphorylated by glycerol kinase to glycerol-3-phosphate and oxidised by glycerol-3-phosphate oxidase generating dihydroxyacetone phosphate and hydrogen peroxide. Peroxidase catalyses a colorimetric reaction between hydrogen peroxide, 4-aminoantipyrine and N-ethyl-N-(3-sulfopropyl)-*m*-anisidine. Absorbance stands in relation to the amount of glycerol and thus TG in the sample.

Ventricular tissue samples were homogenised using a mortar and pestle whilst frozen. Separate aliquots were weighed and homogenised in a supplied standard diluent assay reagent by passing 6 times through a 22 G needle on 1 ml syringe, followed by centrifugation at 84 g for 10 minutes. The supernatant was loaded in 10 µl duplicate volumes in a 96 well plate and coincubated with "triglyceride enzyme mixture" for 15 minutes at room temperature. Absorbance was subsequently measured at λ=540 nm. A 1 g/ml triglyceride solution was included in the kit and a serial dilution standard curve was constructed giving standard curve from 0-200 mg/ml. The resulting sample [TG] was normalised to the raw tissue weight.

## 2.13 Chemiluminescent determination of tissue reactive oxygen species (ROS) generation rate

Ventricular tissue aliquots were lysed in Krebs-HEPES buffer using the Kinematica® (Luzern, Switzerland) Polytron - aggregate® tissue homogeniser system. Homogenisation was performed on ice at maximum speed for 1 minute. Subsequently protein concentration was measured using the BCA assay. Sample concentration was adjusted to 250 µg/ml with Krebs-HEPES buffer.

All ROS chemiluminescence assays were carried out using the Berthold single tube luminometer FB12 (Berthold detection systems, Germany) which was connected to a circulating water bath maintaining temperature at 37 °C (Kim et al., 2005). All chemiluminescence signal amplitudes were read after a plateau of minimum 3 minutes duration .

#### *2.13.1.1 Superoxide ($O_2^-$)*

$O_2^-$ was measured using the fluorescent probe lucigenin (bis-*N*-methylacridinium nitrate) at a concentration of 5 µM (Kim et al., 2008; Reilly et al., 2011). Figure 6 shows a typical fluorescence trace. An inhibitor approach was used to interrogate two intracellular sources of $O_2^-$: 3-benzyl-7-(2-benzoxazolyl)thio-1,2,3-triazolo[4,5-d]pyrimidine (VAS 2870) in a concentration of 40 µM (ten Freyhaus et al., 2006) for NOX and N-Nitro-L-Arginine Methyl Ester (L-NAME), in a concentration of 10 mM, for NOS. NOS operates by deriving NO from the conversion of L-arginine to L-citrulline (Pfeiffer et al., 1996), thus L-NAME will work as a non functional L-arginine analogue, inhibiting NOS activity. For the study of NOX activity the signal was stimulated by 0.1 mM NADPH (Antoniades et al., 2012; Reilly et al., 2011) and inhibited using VAS2870 at said

concentration. The VAS2870 inhibitable signal of the stimulated signal was used as a measure of NOX $O_2^-$ contribution. Lucigenin was dissolved in a x 500 stock in MQ $H_2O$. Both inhibitors were prepared in x 100 stocks (VAS2870 in di-methyl sulfoxide (DMSO) and L-NAME in $H_2O$). All reagents were added to the reaction vial and mixed for appropriate dilution. To ensure saturation of the effect, inhibitor concentrations were used according to published literature.

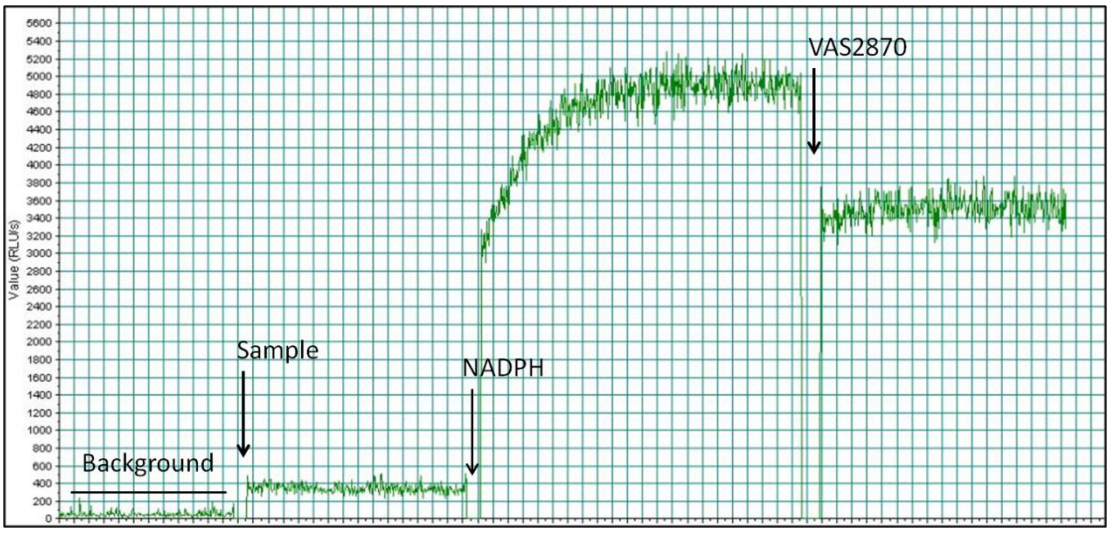



**Figure 6: $O_2^-$ production rate assessment through lucigenin assisted luminometry:** Representative trace of lucigenin derived fluorescence recorded in a FB12 luminometer. The addition of 500 µg protein induced a prompt sustainable increase in $O_2^-$ generation rate. Addition of NADPH stimulated a further increase which was partly inhibited by the addition of VAS2870. On the X-axis, one square equals one minute time duration.

### *2.13.1.2 Peroxynitrite ($ONOO^-$)*

$ONOO^-$ was measured using the fluorescent probe luminol (*o*-Aminophthaloyl hydrazide) at a concentration of 100 mM. The fraction of luminescence attributed to $ONOO^-$ was dissected by the urate inhibitable signal after 30 min incubation. Urate was used at a concentration of 1 mM (Antoniades et al., 2012).

Luminol was prepared in DMSO and urate in $H_2O$ for x 100 stock solutions, and added to the reagent vial and mixed to reach appropriate dilution.

## 2.14 Study of single cardiomyocyte dynamics and $Ca^{2+}$ transients

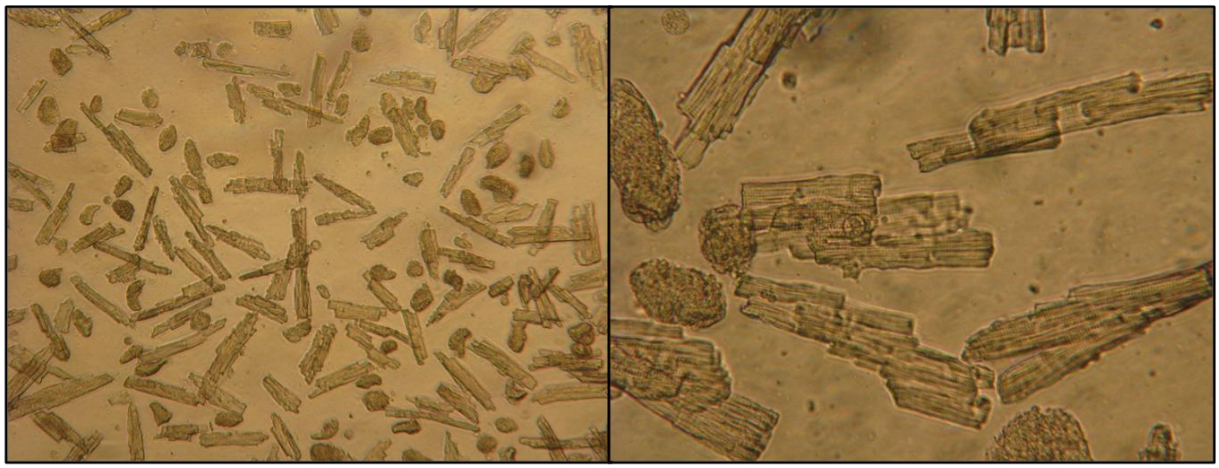
### 2.14.1 **Cell isolation and preparation**

A typical yield of cardiac myocytes are shown in Figure 7. Mice were sacrificed through cervical dislocation and their hearts rapidly excised after thoracotomy. Immediately, the hearts were placed in ice cold Tyrode's solution and cleaned of pericardial tissues to clearly expose the aortic root. The heart was placed on wetted paper cloth and the aortic root cannulated onto a 1 ml syringe using a 22 G needle with cut tip. Its position was secured by double ligation using braided silk wax 5/0 suture (Cat. no. 10B10S220, Pearsalls Ltd, Taunton, UK). The syringe was previous to the procedure filled with cold Tyrode's solution and immediately after cannulation the heart was manually perfused for 10 s at an approximate rate of one drop per second. This confirmed the correct position of the cannula and ensured clearing the coronary circulation of blood.

The heart was perfused with 37 ˚C Ca-free Tyrode's solution at 100 cm $H_2O$ pressure connected to a Langendorff-style rig at an approximate rate of 1 drop per second, for 3 min followed by 9 minutes perfusion with digestive enzyme enriched Tyrode's solution to digest extracellular connective tissue. After this the heart was disconnected from the perfusion rig and the ventricles and interventricular septum minced using scissors before 5 min incubation in collagenase solution under shaking at 37 ˚C. Released cells were separated from undigested tissues by passing the suspension through a 200 µm

aperture monofilament nylon filter cloth mesh (Cadisch premium meshes Ltd, London, UK). Filtered solution was diluted once using enzyme stopping solution.

Cardiac myocytes were enriched by centrifugation at 100 x g rpm for 2 min and the pellet resuspended in enzyme stopping solution. Centrifugation was thereafter repeated and the pellet resuspended in storage solution.



A. B.

**Figure 7: Isolated murine cardiomyocytes A:** Wide field view of successful cardiomyocyte isolation with a majority of rod shaped cardiomyocytes 10 x magnification. **B:** 40 x magnification visualising the sarcomeric striations.

Myocytes for use in contractility and $Ca^{2+}$ handling experiments were washed first in 250 µM $CaCl_2$ perfusion solution and finally washed and resuspended in 500 µM $CaCl_2$ perfusion solution.

### 2.14.2 **Single cell contractility recordings**

The assay was carried out using sarcomere length detection. This was made possible by the use of an inverted microscope (Leica, DM IRB) equipped with the Ionoptix Myocam CCD camera system resulting in time-SL traces as shown in Figure 8.

Recordings were carried out under a field stimulation voltage of 40 V, and frequency of 1 Hz and 3 Hz sequentially in a transparent bottom chamber mounted on the inverted microscope stage continuously perfused with 1.4 mM $CaCl_2$ Tyrode's solution. Stimulation electrodes were aligned with the bath edges. The temperature was adjusted to 37±1 °C and measured intermittently throughout the procedure. Free rod shaped cells with clear striations were used for recordings.

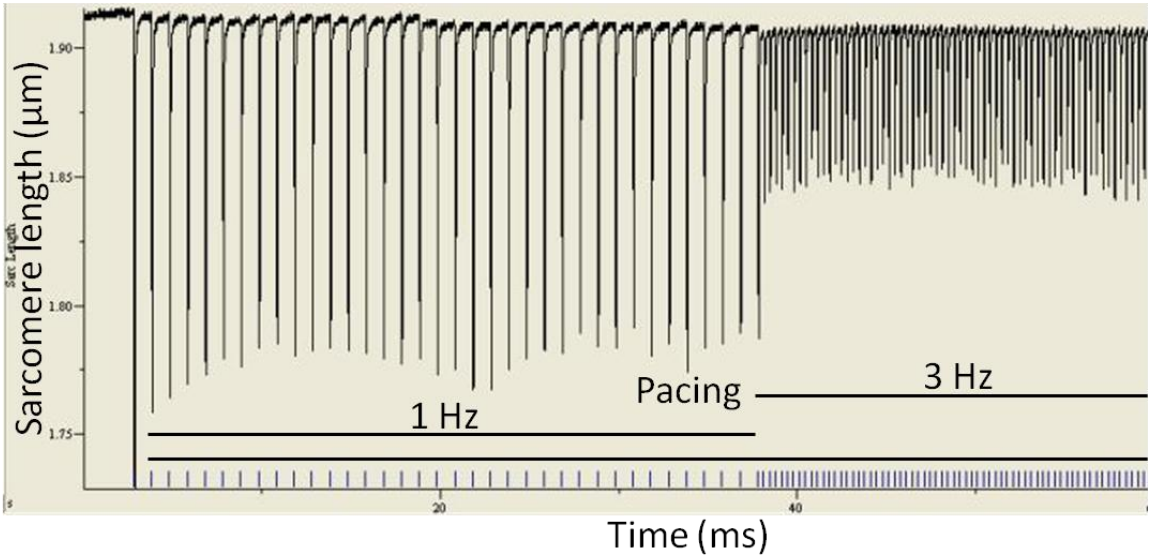



**Figure 8: Single cardiomyocyte contractility trace:** SL recording during electrical field stimulation of single unloaded cardiac myocyte at 1 and 3 Hz sequentially.

Data were analysed using the Ionwizard 6.2.0.59 software from Ionoptix LLC. A series of 10 contractile cycles was regarded as the minimum required for analysis. At least 10 cells were recorded from each preparation. For statistical analysis all values derived from individual cells from each animal were averaged. The parameters derived from this analysis were: SL (µm), FS (%), time to 50 % maximum contraction and time to 50 % relaxation.

### 2.14.3 **Single cell intracellular $Ca^{2+}$ transient recording**

1 μM cell permeant Fura-2 acetoxymethyl (AM) ester (Cat. No. F1221, Life Technologies™, UK) was dissolved in 250 μM $CaCl_2$ perfusion solution with 2 μl 20% DMSO suspended-Pluronic® F-127 (Cat. No. P3000MP, Life Technologies™, UK) in black 1.5 ml microcentrifuge tubes and then entered the cell $Ca^{2+}$ reintroduction procedure described above. A total of 5 minutes was allowed for the Fura-2 AM dye to enter the cells.

Transients were recorded (depicted in Figure 9) by selective field fluorescence registration at 340/380 nm, with a switching rate of 1000 Hz, over the cell of interest, and subsequent recording of cell adjacent-background. Background fluorescence was recorded and deducted at both 340 and 380 nm wavelength immediately after the cell recording, and at the point of analysis, respectively. The field was positioned as to only record from cells with clear uniform striations and debris free background, respectively. Conditions of recording were the same as those described for contractility recordings.

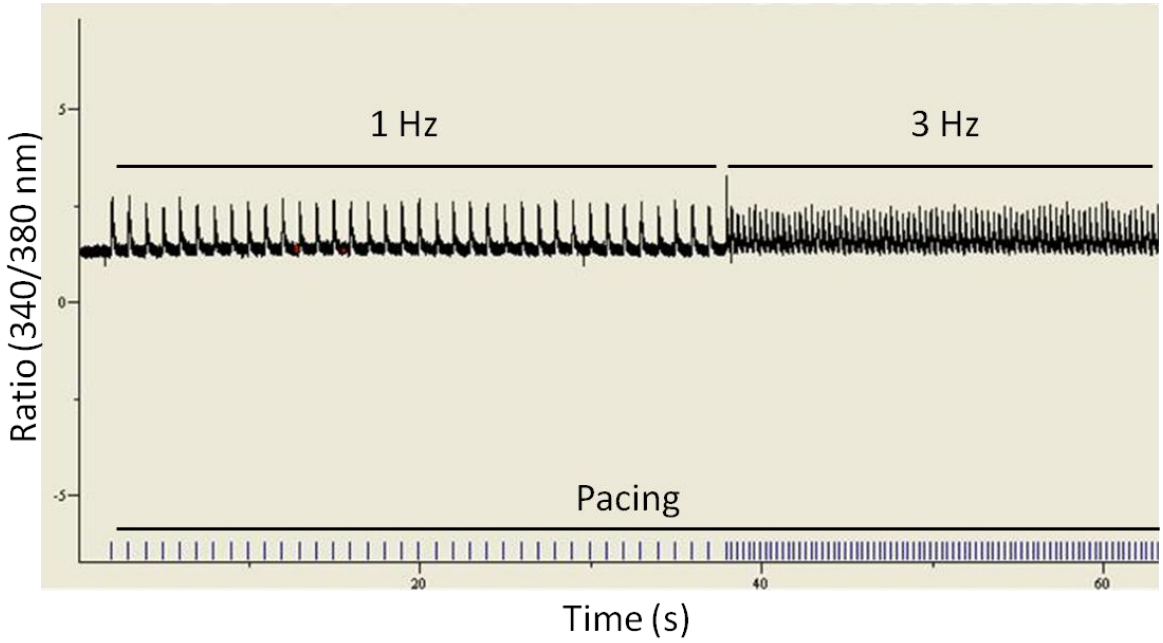



**Figure 9: Single cardiomyocyte $Ca^{2+}$ transient trace:** Fura-2 fluorescence trace from unloaded cardiomyocyte during electrical field stimulation at 1 and 3 sequentially.

As with the contractility data, traces were analysed using the Ionwizard 6.2.0.59 software from Ionoptix LLC. A series of 10 contractile cycles was regarded as the minimum required for analysis. At least 10 cells were recorded from each preparation. For statistical analysis all values derived from individual cells from each animal were averaged. The parameters derived from this analysis were baseline and peak $Ca^{2+}$ (340 nm / 380 nm fluorescence) ratio, time to 50 % peak and time to 50 % decay.

## 2.15 Demembranated trabeculae

### 2.15.1 Preparation of demembranated trabeculae

Mice were sacrificed by cervical dislocation and the hearts rapidly excised through thoracotomy and placed in ice cold PBS. The hearts were then subjected to retrograde

aortic PBS-perfusion before freezing in liquid $N_2$. The hearts were kept at -80 °C until the time of experiment.

Before an experiment the heart was thawed in ice cold dissecting solution. Subsequently the LV was opened from the posterior whilst pinned down in a Petri dish submerged in dissecting solution. Trabeculae were freed from its walls and immediately thinned further to a diameter of 100-150 μm and length of 1.5-3 mm. Dissection was aided by a Star 13 ED stereomicroscope (CETI, Belgium).

Samples were demembranated in dissecting solution + 1 % Triton X-100, on a rotating disc, over night at 4 °C.

Aluminium "T-clips" were added to each end of the preparation for mounting. The clips were pierced at one end enabling the preparation to be mounted on hooks attached to force transducer and length controller respectively. The preparation was mounted in dissecting solution and SL adjusted before transfer to a relaxing solution containing bath where it was incubated for 10 minutes before the start of recordings.

### 2.15.2 **Force recording from demembranated trabeculae**

A 1400A permeabilised fibre system from Aurora Scientific Inc. (Aurora, Ontario, Canada) was used. The force transducer and length controller of choice were the 403A and 315C respectively. It was mounted on an inverted microscope (Nikon Diaphot™).

The temperature was maintained at 10 °C and the SL was adjusted by measuring the laser diffraction patter. The laser unit used was model 902A from Aurora Scientific Inc. comprising a class II (<1 mW) laser of 635 nm wavelength, and 0.15 mm beam diameter.

The 902A includes a pre-marked glass bridge to place on an established distance from the preparation enabling quick interpretation of sarcomere diffractions.

Preparation diameter was recorded at each end of the preparation as well as in the middle using an ocular graticule. The average value was used to describe preparation diameter. Preparation length ($L_o$) was recorded between the edges of opposing aluminium clips.

Three major interventions were carried out to characterise the myofilament function of the demembranated trabeculae: $Ca^{2+}$ isometric force dose response, rapid shortening and re-stretch at maximum tension, and passive tension upon stretch.

Each preparation was subjected to all interventions in the following sequence:

1. Initial confirmation of function
2. $Ca^{2+}$ induced isometric force generation at SL 2.2 µm
3. Rapid shortening and re-stretch at maximum tension at SL 2.2 µm
4. Rapid shortening and re-stretch at maximum tension at SL 2.0 µm
5. Rapid shortening and re-stretch at maximum tension at SL 2.4 µm
6. Passive tension upon stretch

#### *2.15.2.1 Initial confirmation of function*

Each preparation was stretched to SL 2.2 µm and thereafter activated in pCa 4.7 ($F_{max}$) to confirm its functional response to $Ca^{2+}$. The preparation was then allowed to relax and the SL was re-measured and length adjustments made if necessary. Before start of data recording a last maximum activation was carried out to create a start time $T_0$ reference value of tissue performance.

### *2.15.2.2 $Ca^{2+}$ induced isometric tension*

In order to investigate the [$Ca^{2+}$] to force relationship the preparation was subjected to a series of different ascending free $Ca^{2+}$ concentrations always interceded by relaxation at pCa 9.0 (pCa approx 6.82, 6.45, 6.28, 6.09, 5.97, 5.85, 5.68, 5.51, 5.23, 4.95, and 4.7). The values were known to correspond to certain ratios of relaxing: activating solution at 27 ˚C and thus all intermediate pCa solutions were generated by mixing relaxing solution and activating solution. All relaxing and activating solutions used were prepared in one single batch. Force was seen to plateau at the higher concentrations. The $pCa_{50}$-value derived from the fitted Hill equation (Equation 1) indicates $Ca^{2+}$ sensitivity whereas the Hill coefficient (*nH)* indicates cooperativity of activation along the thin filament. The raw datas was fitted to Equation 1 using GraphPad 4.0. Only preparations in which the last maximum activation was > 80 % of $F_{max}$ $T_0$ was used for further experiments and analysis. Only the active contraction part was used, so that force was measured from bottom until the plateau, which avoids the confounding factor of the baseline moving between the baths.

$$\boldsymbol{F = F_{\min} + \frac{(F_{max} - F_{\min})}{1 + 10^{((pCa_{50} - pCa) * nH)}}}$$

**Equation 1**: Four parameter Hill equation used to approximate the $Ca^{2+}$ force dose relationship

Maximum tension ($F_{max}$) was recorded at pCa 4.7 and normalised to preparation cross sectional area. A cylindrical cross section was assumed and thus its area (A) was approximated as $A=\pi r^2$ where r=radius.

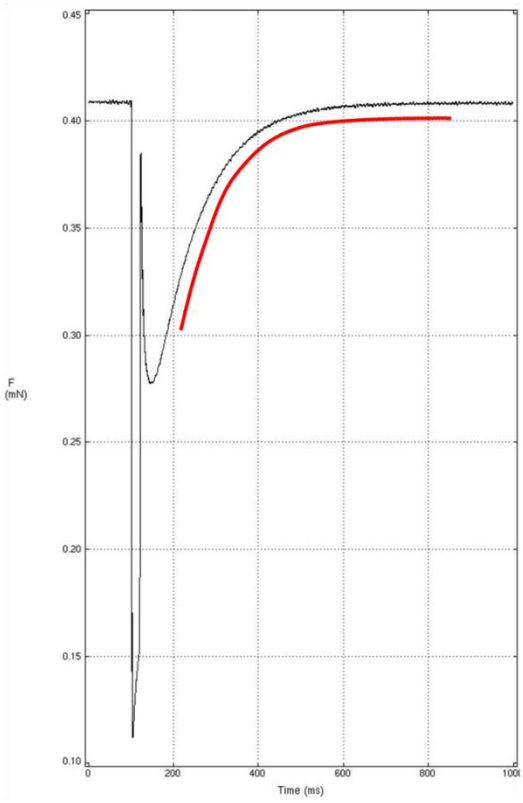



**Figure 10: Tension trace during slack and re-stretch of a cardiac LV trabecula**: 1000 ms force trace recording acquired to assess cross bridge cycling rate in demembranated cardiac trabecula. The immediate rise in tension upon re-stretch is interpreted as passively transmitted tension. The segment marked in red was considered as cross bridge derived tension rise and relevant for analysis.

### *2.15.2.3 Rapid shortening and re-stretch*

To assess cross bridge cycling rate a rapid (0.5 ms) 0.8 $L_o$ slack of the preparation was maintained for 20 ms before a rapid (0.5 ms) return to $L_o$ (Bardswell et al., 2010). The slack duration was considered enough for all cross bridges to establish new binding positions along the actin filament. Upon re-stretch all newly formed cross-bridges should once again break to leave the preparation in a functionally unloaded state. The rate of tension regeneration was established by fitting the segment marked in red in Figure 10 to the following equation (Equation 2) using MatLab R2010a:

$$\boldsymbol{F(t) = Fi + Fa(1 - e^{-ktr\,x\,t})}$$

**Equation 2: Single exponential curve fit used to assess tension redevelopment rate (ktr) after slack and re-stretch** F(t)= force at any time point(t) at a given $Ca^{2+}$ concentration, $F_i$= force immediately after re-stretch, and $F_a$=maximum force after re-stretch (Edes et al., 2007).

### *2.15.2.4 Passive tension upon stretch*

Passive compliance in cardiac muscle can be attributed to collagen and titin (Wu et al., 2000). To assess the compliancy of the preparation the passive tension generated upon stretch in a relaxed state with cross bridge inhibition in the form of 20 mM BDM was measured.

The traces typically resembled the one presented in Figure 11. The preparation was manually shortened to slack tension. This tension level established the baseline for the reading. After this the preparation was stretched manually to 2.0 μm and left for a duration of 2.5 min to reach a plateau. The tension level at the end of this time period was recorded and the following stretches were performed in 0.2 μm increments. After each stretch the duration allowed to plateau was doubled so that after setting the SL to 2.6 μm the preparation was left for 20 min before terminating the experiment sequence. The tension development rate was assessed by a curve fitting according to an exponential growth function according to (Equation 3) in GraphPad 4.0.

$$\boldsymbol{F = F_0\, x\, e^{k\, x\, SL}}$$

**Equation 3 Exponential growth equation used to approximate passive tension development rate as function of SL in skinned cardiac trabeculae** F= force at relevant sarcomere length (SL), $F_0$=force at slack

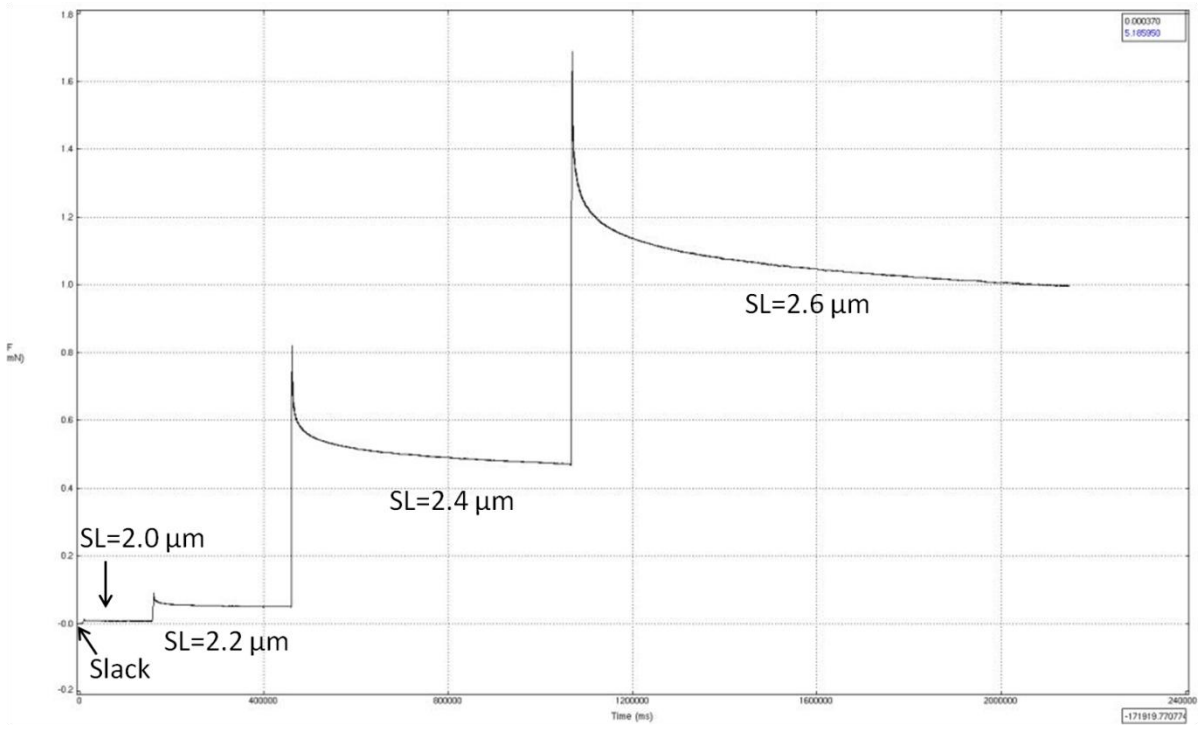



**Figure 11: Tension trace during passive stretch of relaxed cardiac LV trabeculae:** Tension trace recorded to assess compliance to passive stretch in a demembranated cardiac trabeculae. The trabeculae was stretched stepwise in relaxing solution supplemented with cross-bridge inhibitor BDM.

#### *2.15.2.5 Analysis of demembranated trabeculae data*

Trace recording and semi automatic analysis-software was included in the 1400A permeabilised fibre system for absolute force. $K_{tr}$ analysis was completed in MatLab R2010a.

### 2.16 C2C12 cell culture and incubation experiments

C2C12 myoblasts were cultured on 6-well plates (Sterilin) at 37 ˚C in Dulbecco's modified Eagle's media (DMEM) supplemented with foetal bovine serum (FBS) 10 % v/v, L-glutamine (2 mM), and penicillin (0.1 U/mL)/streptomycin (0.1 mg/mL). Incubation experiments were carried out for 4 hours with solvent (2-Hydroxypropyl)-β-cyclodextrin (1 % w/v), ATII (10 nM), ATII + apocynin (100 µM), ATII + VAS2870 (100

μM), and ATII + $O_2^-$ scavenger tiron (5 mM) to characterise NOX and $O_2^-$ influence on AMPK activation. At termination of the incubation the wells were rapidly rinsed with 37 ˚C PBS, followed by in well protein extraction with urea lysis buffer and subsequent SDS-PAGE and immunoblotting.

### 2.17 Statistical analysis

For unpaired comparison of two groups', with Gaussian distributions, means Student's t-test was employed. When the groups were not of Gaussian distribution Mann-Whitney U-test was deemed appropriate.

For comparison of three groups with equal variances and a Gaussian distribution the one way ANOVA was used with Tukey's post-hoc testing for mean differences between groups. When there were differences in variability the Kruskal-Willis test with Dunn's post-hoc testing was used.

Degrees of statistical difference between group means were displayed as: *=$p<0.05$, **=$p< 0.01$, and ***=$p<0.001$.

All statistical analysis was carried out in GraphPad 4.0.

# 3 Verification of the HFD fed C57BL6/J mouse as a model for studying the influences of obesity and systemic insulin resistance on cardiac function

## 3.1 Introduction

This study aims to identify and follow effects on cardiac contractility in response to HFD. It was suspected that changes in cardiac phenotype and their possible reversibility may be associated with changes on a systemic level, especially that of perturbed glucose homeostasis. To investigate this, the HFD-induced C57BL6/J mouse model of the metabolic syndrome was selected as a study model. The feeding trial followed the scheme drawn out in Figure 12. *In vivo* whole body parameters and plasma chemistry assays were carried out at specific time points throughout the study in complement to *post mortem* dissection in order to characterise organs by gross weight, histology, *in vitro* function, and molecular biology. After 30 weeks one half of the control and one third of the HFD cohorts were culled. Half of the remaining HFD cohort was put on control diet to investigate potential benefits of diet restrictions in alleviating the phenotype. The second time point of investigation was at 40 weeks. At this point the study included three separate cohorts: 40 weeks control diet, 40 weeks HFD, and 30 weeks HFD + 10 weeks control diet (Rev).

An initial pilot study was carried out to confirm an induction of cardiac dysfunction from HFD.

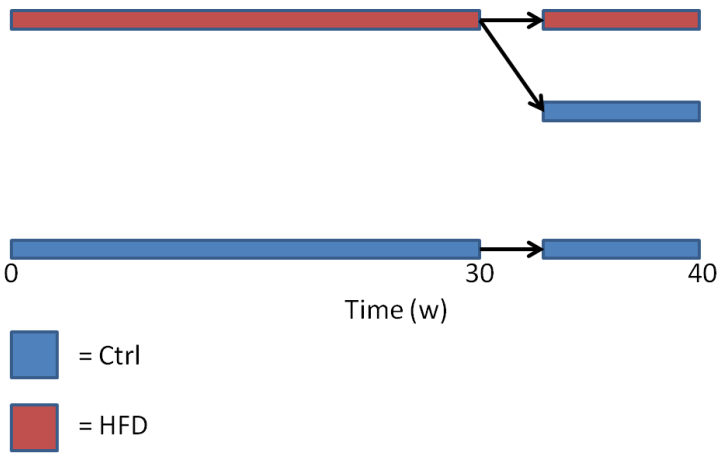



**Figure 12: Study time line** Age matched male C57BL6/J mice were fed a ctrl or 60 % HFD for 30 weeks before the initial cardiac phenotyping and sacrifice for tissue harvest took place. Another 10 weeks of feeding then continued whereby half the HFD fed animals were put back on ctrl diet as reversal intervention, followed by the second and last phenotyping stage at 40 w.

## 3.2 Weight development

### 3.2.1 Total body weight

The mice were followed by weekly weighing in order to characterise the weight gain response to HFD. The results of feeding are shown in Figure 13. Before feeding commenced there was no difference in weight between the groups. At 30 w the HFD fed animals were on average 35 % heavier than the controls and after 40 w the difference was 32 %. A reversal to ctrl diet from w 30 onwards resulted in a drastic weight loss with no difference compared to the HFD group before the diet switch (Ctrl (n=73): 37.9 g ± 3.0 SD; HFD (n=77): 52.1 g ± 4.6 SD; Rev (n=47): 51.1 g ± 6.2 SD); at 40 w there was no statistically significant difference in weight between reversal mice and the control group (Ctrl (n=32): 41.1 g ±4.1 SD; HFD (n=40): 54.0 g ±5,7 SD; Rev (n=26): 42.1 g ± 4.9 SD).

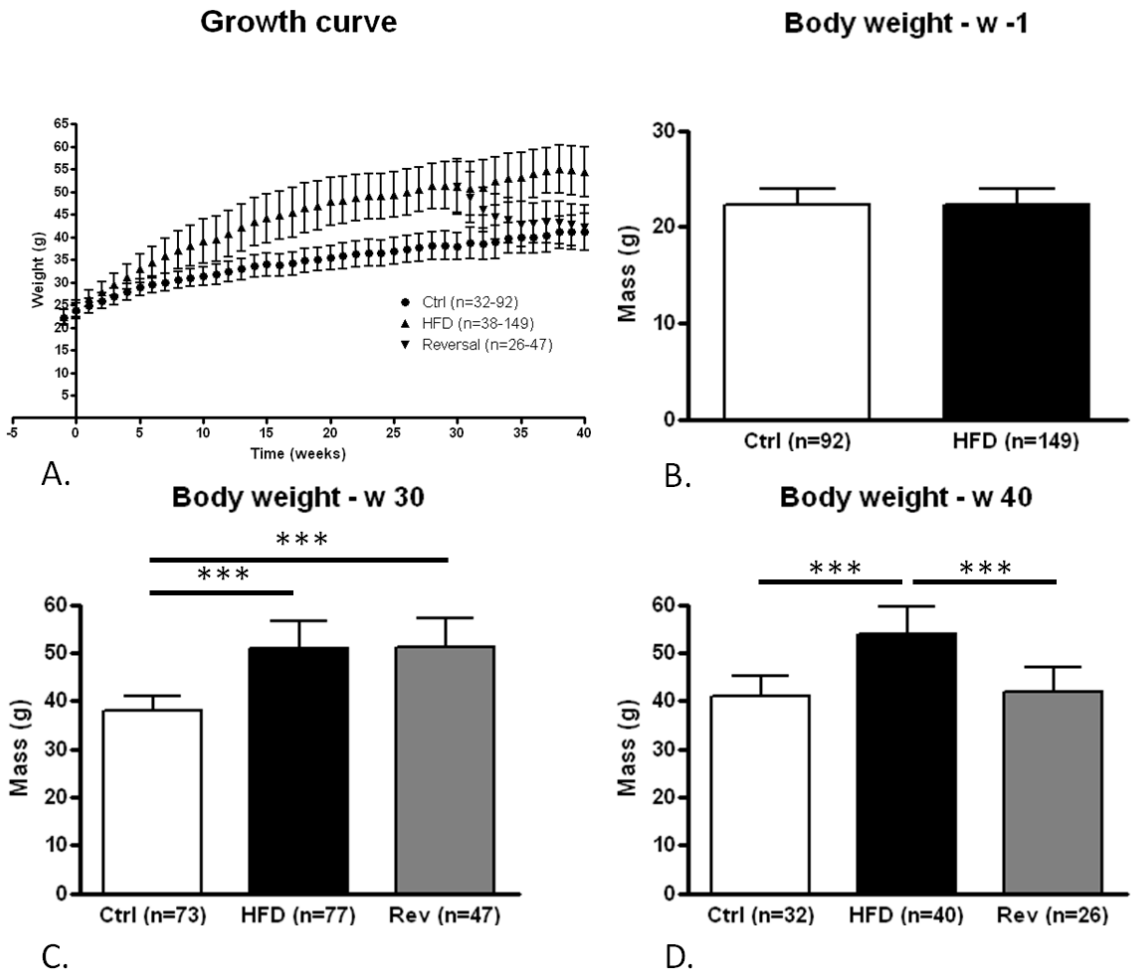



**Figure 13: The effect of HFD on weight development in the male C57BL6/J mouse A:** Weight development over the course of the study. **B:** Body weights in designated control and HFD animals one week before start of feeding. **C:** Body weights at 30 weeks. **D:** Body weights at 40 weeks. All error bars describe SD. ***=p<0.001.

### 3.2.2 **Body composition analysis by quantitative magnetic resonance (QMR)**

To verify that the main tissue target of increased body weight was adipose tissue, QMR was employed at three time points throughout the study. Results are presented in Figure 14.

This investigation revealed a significant increase in total body fat content at w 29 (Ctrl (n=11): 22.6 % ± 4.7 SD; HFD (n=12): 40.5 % ± 2.1 SD) and w 38.

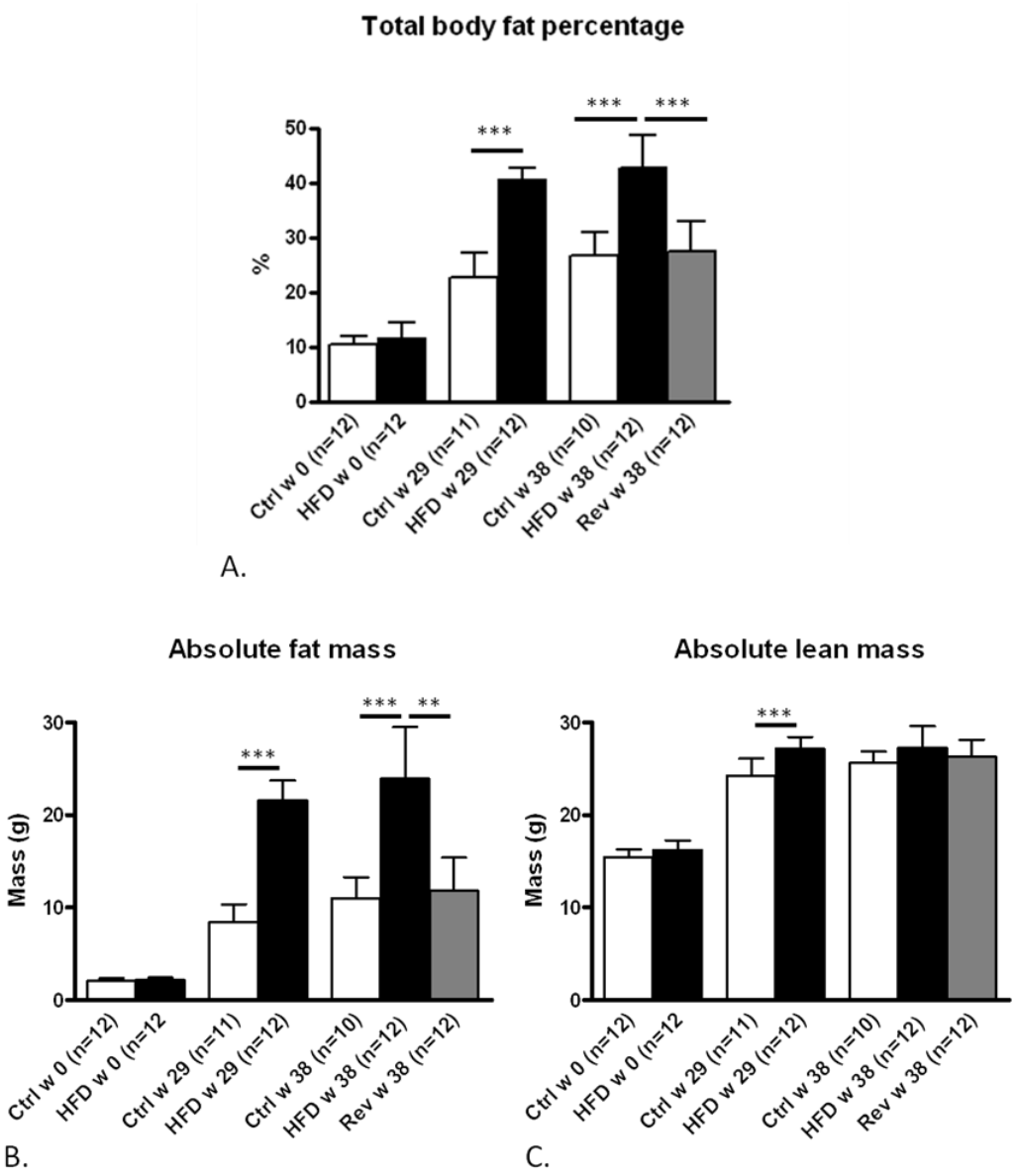



**Figure 14: Distribution of lean and fat mass upon HFD feeding in the male C57BL6/J mouse A:** Body fat percentage at w 0, 29, and 38. **B:** Absolute body fat mass per animal at w 0, 29 and 38. **C:** Absolute lean body mass per animal w 0, 29, and 38. All error bars describe SD. **=p<0.01, ***=p<0.001.

The difference observed at 29 was completely reversed by a switch to ctrl diet (Ctrl (n=10): 26.7 % ± 4.1 SD; HFD (n=12): 42.6 % ± 6.1 SD; Rev (n=12): 27.4 % ± 5.4 SD). There was no significant difference in lean mass between the two groups at the start of the study. At w 29 the HFD group displayed a small increase in total lean mass compared to ctrl animals (Ctrl (n=11): 24.2 g ± 1.9 SD; HFD (n=12): 27.2 g ± 1.3 SD); a difference no longer detected at w 38.

## 3.3 Glucose homeostasis

As shown in Figure 15, after 5 w, fasting glucose and insulin levels were significantly elevated in the HFD group. These changes were maintained throughout the study (29 w glucose: (Ctrl (n=10): 4.9 mM ± 0.84 SD; HFD (n=12): 7.52 mM ± 2.0 SD); 29 w insulin: ((Ctrl (n=10): 0.31 ng/ml ± 0.1 SD; HFD (n=12): 1.29 ng/ml ± 0.7 SD). Diet reversal successfully reversed the impaired glucose handling (39 w glucose: (Ctrl (n=10): 4.2 mM ± 0.4 SD; HFD (n=12): 6.7 mM ± 1.3 SD); Rev (n=12); 4.7 mM ± 1.7 SD); insulin: ((Ctrl (n=10): 0.46 ng/ml ± 0.23 SD; HFD (n=9): 2.1 ng/ml ± 0.64 SD; Rev (n=12): 0.59 ng/ml ± 0.46 SD).

To obtain more robust evidence of impaired glucose handling, mice were subjected to IPGTT. This enabled the monitoring of blood glucose clearance over time adding weight to the evaluation. The area under curve of the plot of [glucose] against time is a measure of peripheral tissue insulin resistance. Results are shown in Figure 16. Comparisons of the area under curves between the groups showed that there was a significant impairment in glucose handling in the HFD group from as early as after 8 w on HFD (Ctrl (n=11): 2203 min*mM ± 358 SD, HFD (n=12): 3508 min*mM ± 622 SD) and throughout the study (w 29: (Ctrl (n=10): 2242 min*mM ± 467 SD, HFD (n=12): 4024 min*mM ± 781 SD). Ten weeks of diet reversal fully returned glucose handling ability to control level (w 39: (Ctrl (n=10): 2495 min*mM ± 413 SD, HFD (n=12): 4168 min*mM ± 1138 SD, Rev (n=12): 2458 min*mM ± 624 SD).

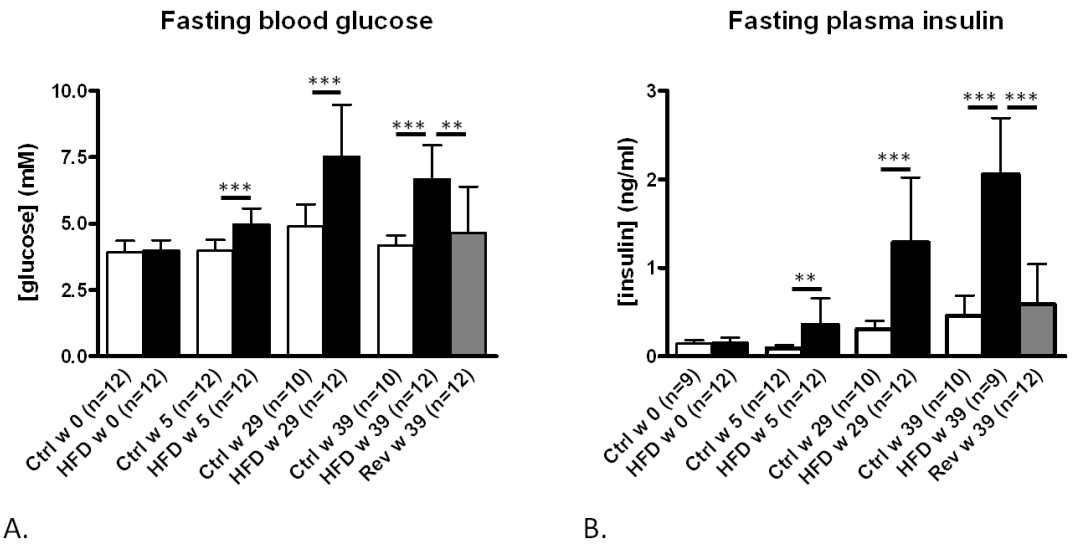



**Figure 15: Effect of HFD on fasting blood glucose and insulin in the C57BL6/J mouse A:** Fasting blood glucose and **B:** insulin recorded at multiple time points throughout the study. All error bars describe SD. **=p<0.01, ***=p<0.001.

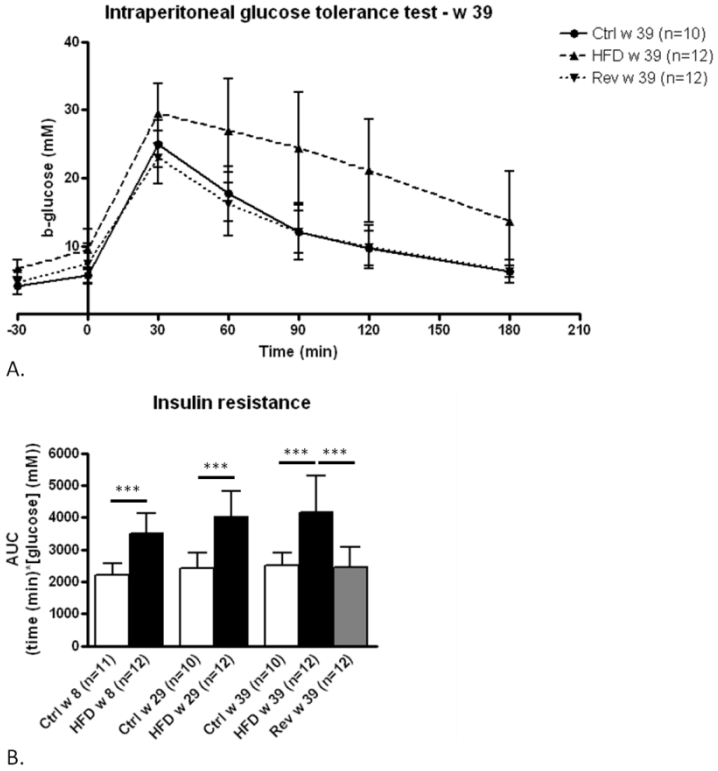



**Figure 16: Effect of HFD feeding on peripheral insulin resistance in the C57BL6/J mouse A:** Intraperitoneal glucose tolerance test (IPGTT) from w 39 **B:** Insulin resistance described by the area under curve (AUC) from IPGTTs recorded at w 8, w 29, and w 39. All error bars describe SD. ***=p<0.001.

## 3.4 Cardiac *in vivo* phenotyping

The effects of HFD feeding on cardiac function were assessed through pressure catheterisation of the LV during GA, *in vivo* haemodynamics, as well as TTE under GA.

### 3.4.1 *In vivo* haemodynamics

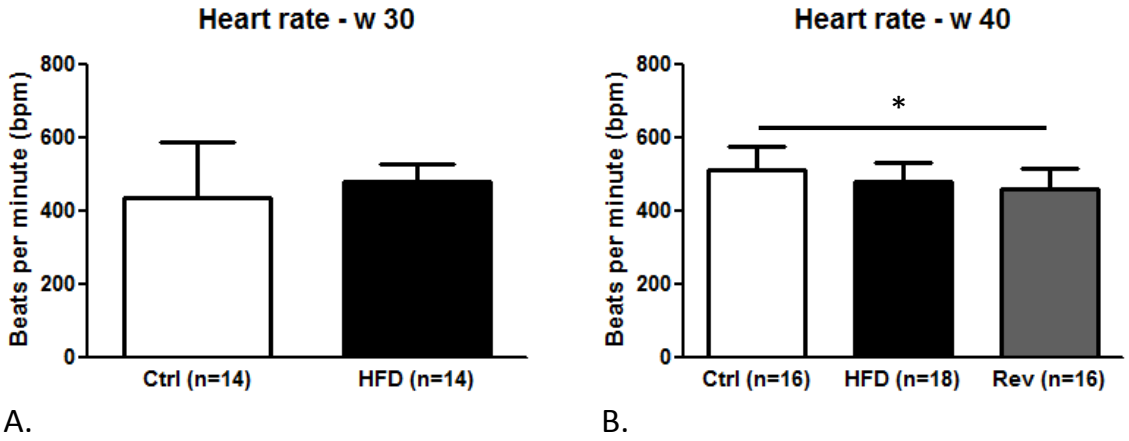



**Figure 17: Heart rate as assessed by intraventricular pressure catheterisation: A:** Heart rate at 30 w. **B:** Heart rate at 40 w.

As seen in Figure 17: Heart rate as assessed by intraventricular pressure catheterisation: A: Heart rate at 30 w. B: Heart rate at 40 w. there was no difference in heart rate at w 30. However, ten weeks after diet reversal the reversal group showed a decrease in heart rate compared to the control group, however the HFD group showed no differences compared to control nor reversal animals (ctrl (n=16): 512 BPM ± 64SD, HFD (n=18): 481 ± 53 SD, rev (n=16): 461 ± 57 SD).

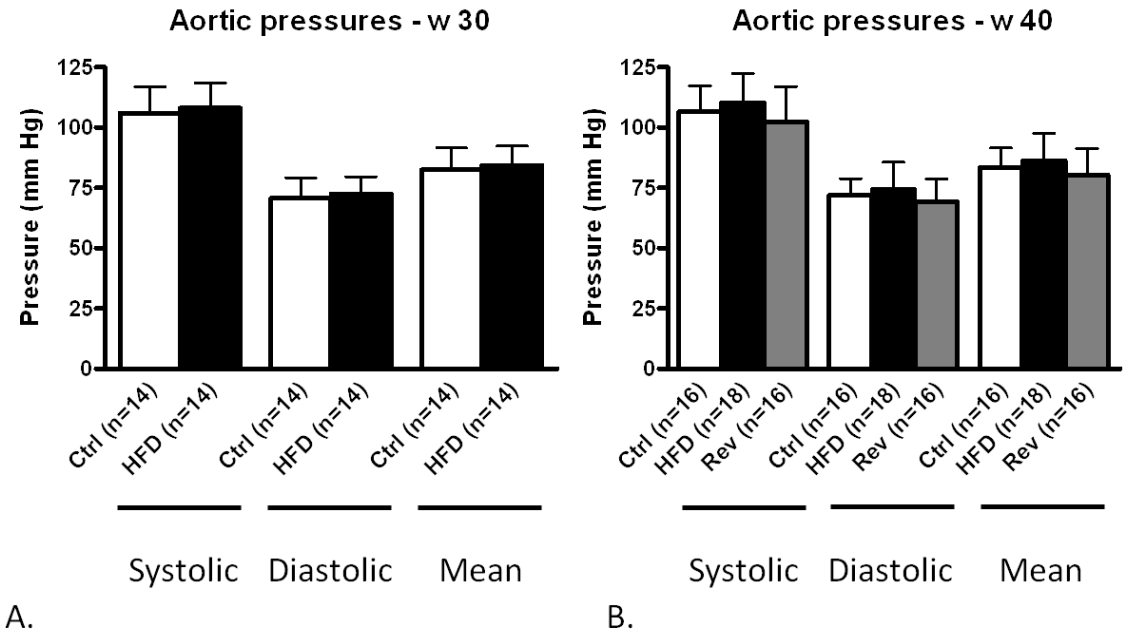



**Figure 18: Pressure recording from the proximal aorta A:** Aortic systolic and diastolic pressures and derived mean arterial pressures recorded at 30 w. **B:** Aortic systolic and diastolic pressures and derived mean arterial pressure recorded at 40 w. All error bars describe SD.

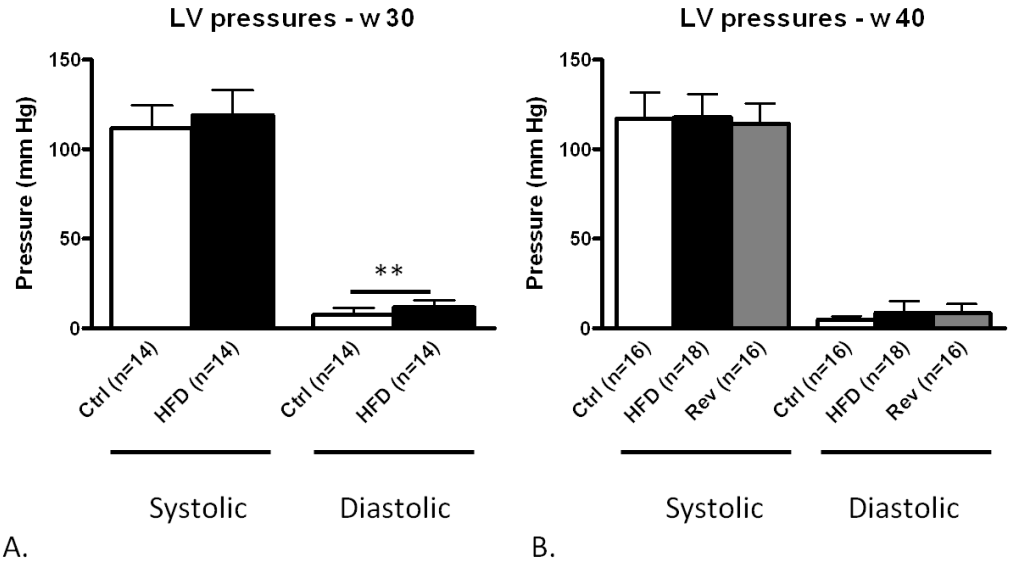



**Figure 19: Pressure recording from the left ventricle A:** Left intraventricular systolic and diastolic pressures recorded after 30 w. **B:** Left intraventricular systolic and diastolic pressures recorded after 40 w. All error bars describe SD. **=p<0.01. (LV=left ventricular)

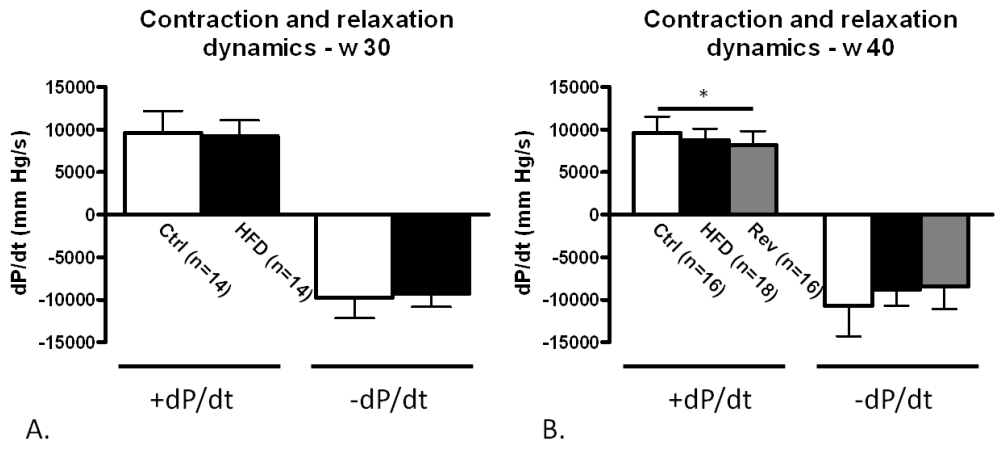



**Figure 20: Maximum left ventricle pressure acceleration and deceleration rates A:** Maximum and minimum pressure development rate over time during systole and diastole respectively at 30 w. **B:** Maximum and minimum pressure development rate over time during systole and diastole respectively at 40 w. All error bars describe SD. *=p<0.05.

As shown in Figure 18 there were no established significant differences in arterial blood pressure at neither 30 nor 40 w as assessed by pressure catheterisation. Left ventricular end diastolic pressure (LVEDP) was increased after 30 w, shown in Figure 19 (Ctrl (n=14): 7.52 mmHg ± 3.92 SD, HFD (n=14): 11.7 mmHg ± 4.00 SD), a difference that was not distinguishable at 40 w even though a visible trend was noticed. There were no differences in LV end systolic pressures at either 30 or 40 w. Analysis results of maximum and minimum pressure development rates are illustrated in fFigure 20, and disclosed impaired systolic pressure development capacity in the reversal animals after 40 w compared to control (Ctrl (n=16): 9591 mmHg/s ± 1904 SD, HFD (n=18): 8742 mmHg/s ± 1350 SD, Rev (n=16): 8142 mmHg/s ± 1682 SD). No differences were distinguished in pressure deceleration rate during diastole even though visible trends were noticed towards decreased deceleration rate in the HFD and reversal animals.

### 3.4.2 **Transthoracic echocardiography (TTE)**

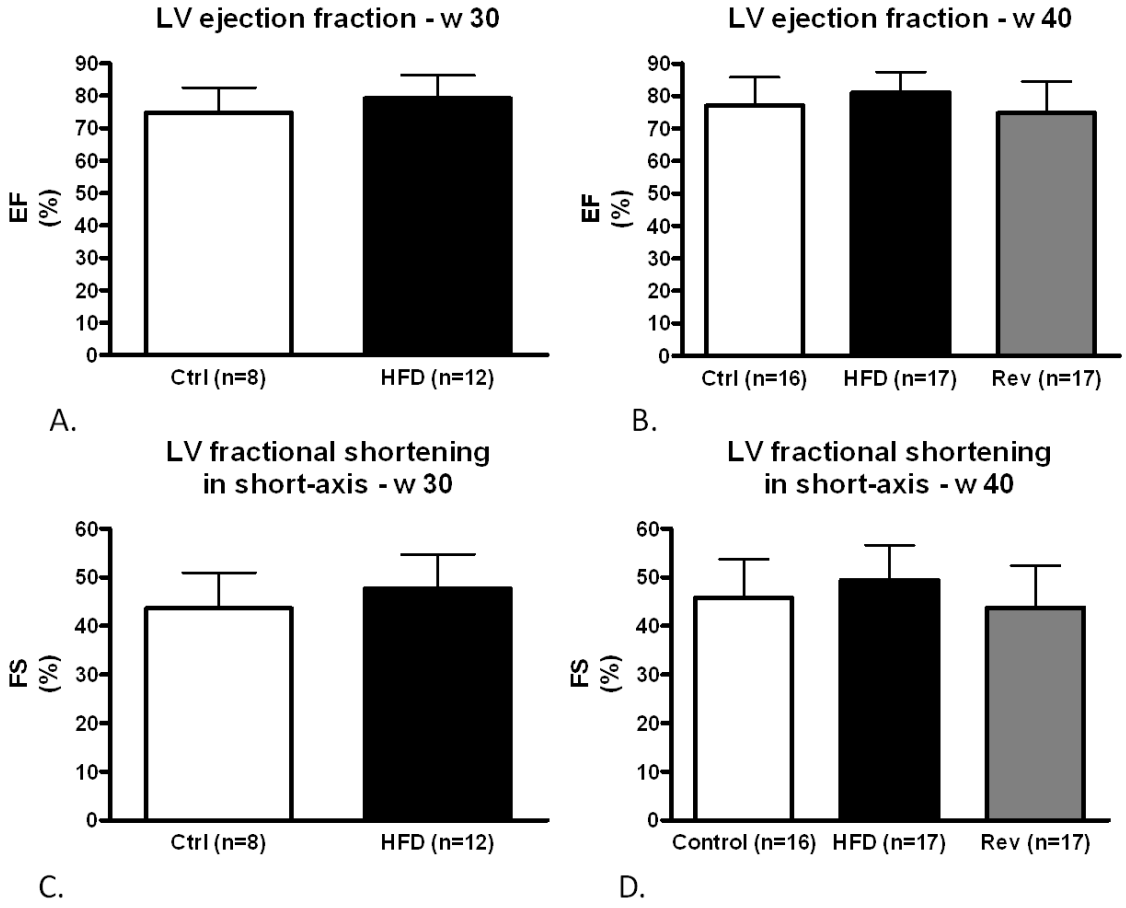



**Figure 21: Left ventricle ejection fraction and shortening by transthoracic echocardiography A:** Left ventricular ejection fraction at w 30 **B:** Left ventricular ejection fraction at w 40 **C:** Left ventricular fractional shortening in the transverse section at 30 w **D:** Left ventricular fractional shortening in the transverse section at 40 w. All error bars describe SD.

Systolic performance was assessed through calculated ejection fraction (EF) and FS of the LV in the transverse short axis view. Results are illustrated in Figure 21. There were no obvious trends with regards to systolic performance at either 30 or 40 w.

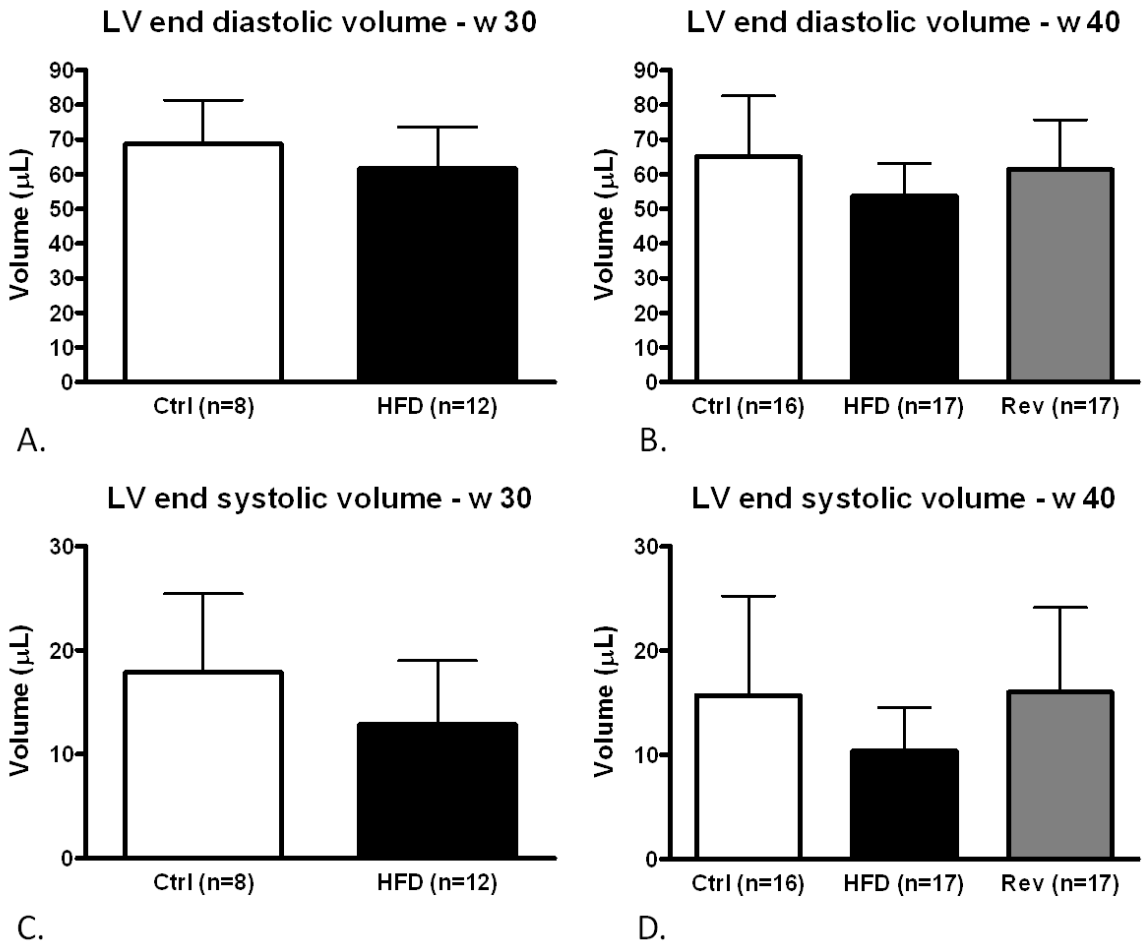



**Figure 22: Left ventricle end diastolic and systolic volumes by transthoracic echocardiography A:** The left ventricular end diastolic volume at 30 w **B:** The left ventricular end diastolic volume at 40 w **C:** The left ventricular end systolic volume at 30 w **D:** The left ventricular end systolic volume at 40 w. All error bars describe SD.

Calculated LV end diastolic and end systolic volumes were used to assess myocardial diastolic and systolic performance respectively, results seen in Figure 22. There was a trend towards decreased end diastolic as well as end systolic volume at both time points, as well as a trend towards reversal at w 40. No statistical significances were obtained. A decreased end diastolic volume is compatible with impaired diastolic function and a decrease in systolic volume would be interpreted as an expression of a hyper-contractile phenotype.

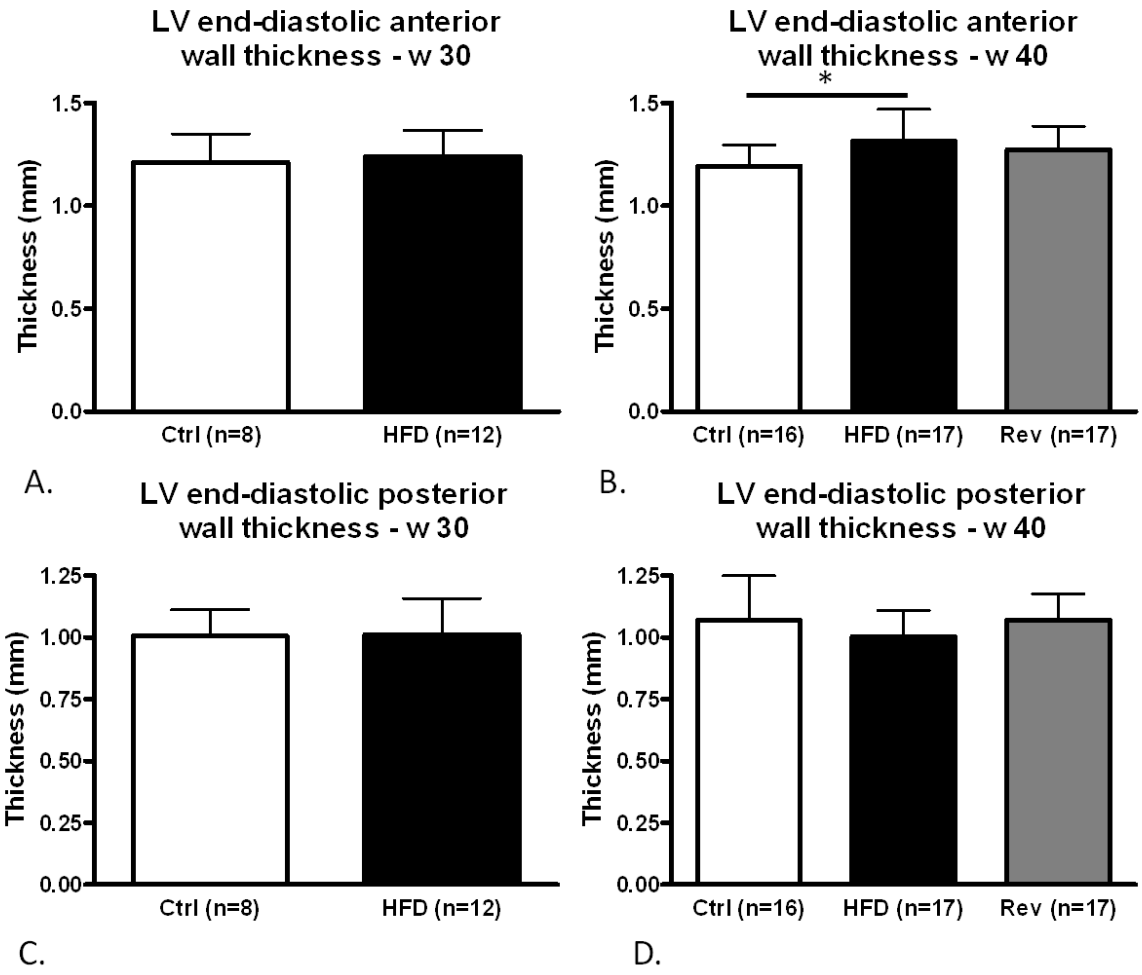



**Figure 23: Left ventricle end diastolic wall diameters by transthoracic echocardiography A:** Left ventricular end-diastolic anterior wall thickness at w 30 **B:** Left ventricular end-diastolic anterior wall thickness at w 40 **C:** Left ventricular end-diastolic posterior wall thickness at w 30 **D:** Left ventricular end-diastolic posterior wall thickness at w 40. All error bars describe SD. *=p<0.05.

End diastolic anterior and posterior wall thickness measurements revealed an increased end diastolic anterior wall thickness of the LV, as shown in Figure 23, at 40 w (Ctrl (n=16): 1.19 mm ± 0.10 SD, HFD (n=17): 1.31 mm ± 0.16 SD, Rev (n=17): 1.27 ± 0.11 SD). This could be interpreted as anterior wall hypertrophy but also as a sign of impaired relaxation.

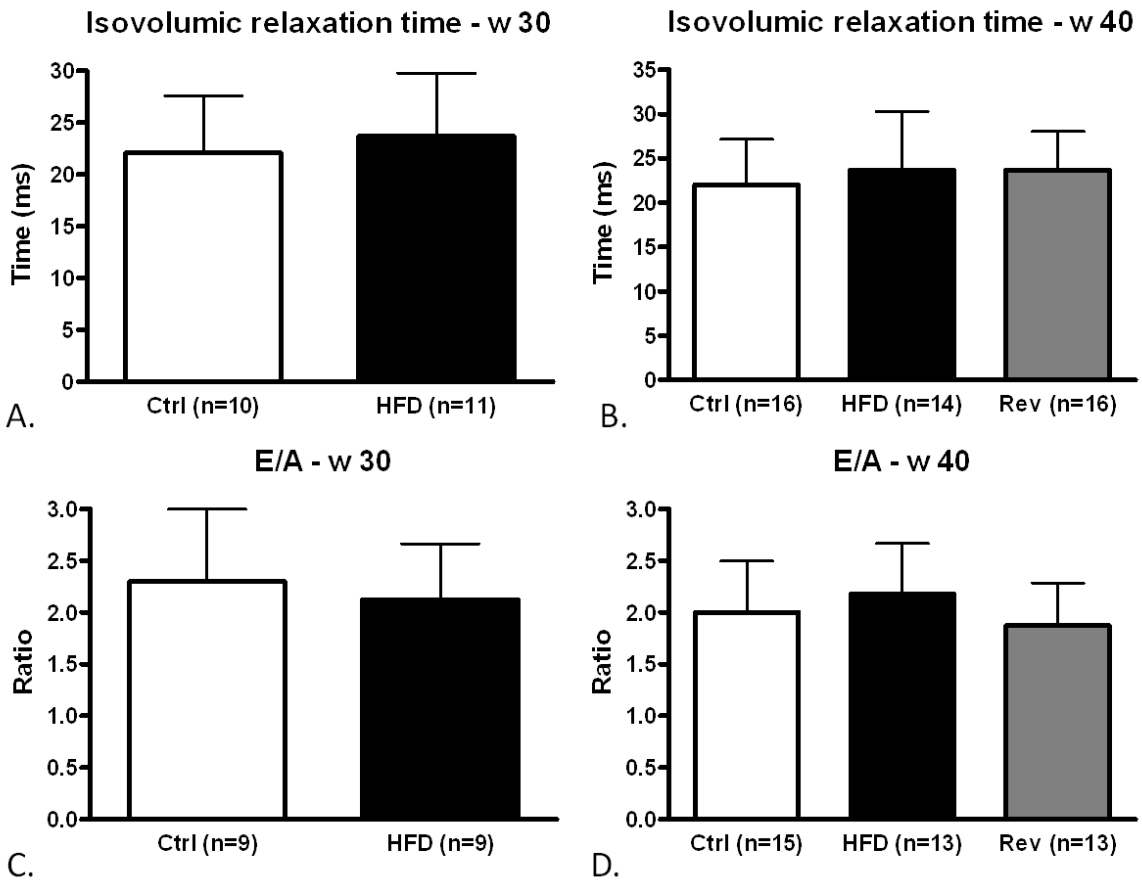



**Figure 24: Diastolic function as by transmitral Doppler flow pattern A:** Isovolumic relaxation time at w 30 **B:** Isovolumic relaxation time at w 40 **C:** E/A ratio at w 30 **D:** E/A ratio at w 30. All error bars describe SD.

Doppler recordings of the transmitral blood flow profile during diastole were obtained as a measure of diastolic performance. As can be seen in Figure 24 none of the obtained parameters isovolumic relaxation time (IVRT) and E/A ratios, showed any significant changes or consistent trends suggestive of impaired diastolic function.

## 3.5 Post mortem dissection findings

Post mortem dissection data on organ weight are displayed in Table 1. There were no gross changes in heart weight normalised to TL at either time point as a measure of hypertrophy or decompensated heart failure as shown in Figure 25 A. Lungs were weighed to exclude severe backwards heart failure and lung parenchymal oedema due to stasis; no differences were found.

To confirm the results of QMR abdominal fat depots were measured from the retroperitoneal and epididymal stores. Results are shown in fFigure 255 B. Abdominal fat depots (retroperitoneal + epididymal) were found to be increased by ~80% and ~69% at 30 (Ctrl (n=33): 2163 mg ± 674 SD, HFD (n=33): 3827 mg ± 422 SD) and 40 w (Ctrl (n=26): 2383 mg ± 618 SD, HFD (n=34): 4034 mg ± 1047 SD, Rev (n=40): 2025 mg ± 648 SD) respectively.

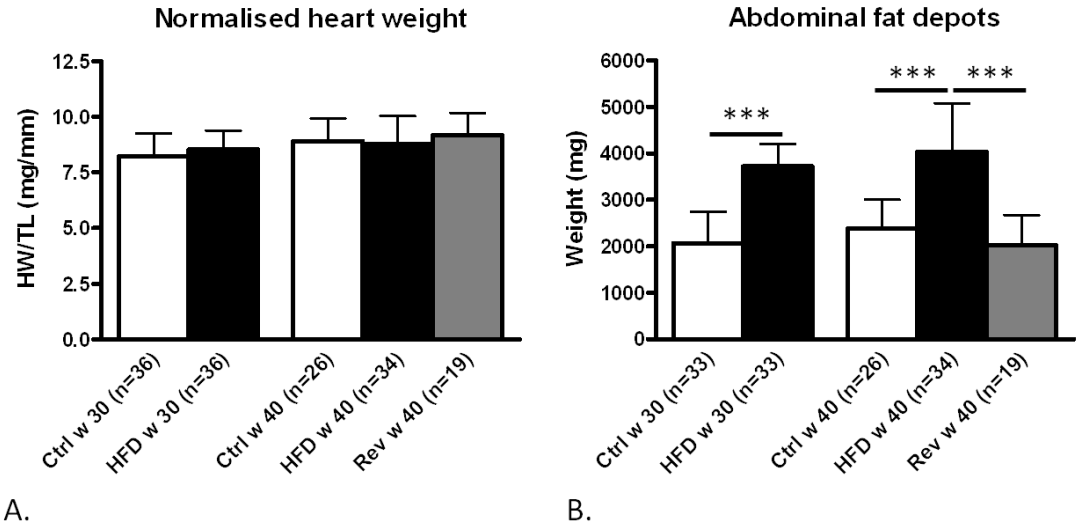



**Figure 25: Effects of HFD on heart size in the C57BL6/J mouse A:** Heart weight normalised to tibia length at 30 and 40 w **B:** Abdominal fat depot masses at 30 and 40 w. All error bars describe SD. ***=p<0.001.

The livers of HFD animals were found grossly enlarged at 30 and 40 w (Table 1). Oil Red-O staining of sectioned liver tissue is shown in Figure 266 and confirmed the

increased presence of hepatic lipid material in HFD fed animals. The increase in liver weight was completely reversed by 10 w on a normal diet.

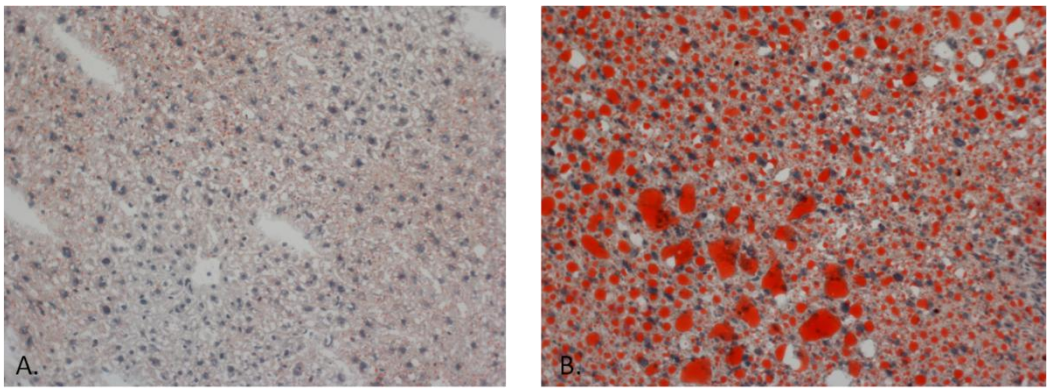



**Figure 26: Hepatic lipid accumulation assessment as by Oil-Red O staining A:** Ctrl liver tissue stained with Oil Red-O at w 40. **B:** HFD liver tissue stained with Oil Red-O at w 40.

An increase in kidney size was seen at both 30 and 40 w. This was only partly reversible by diet. For full declaration of organ weights at w 30 and w 40 see Table 1.

| **Table 1 A.** | | **Organ weight (mg)** | | | | | |
|---|---|---|---|---|---|---|---|
| **Organ** | **Group** | **Week 30** | | | **Week 40** | | |
| | | **Mean** | **SD** | **n** | **Mean** | **SD** | **n** |
| **Heart** | ***Ctrl*** | 160.4 | 21.2 | 36 | 176.3 | 20.2 | 26 |
| | ***HFD*** | 166.1 | 16.8 | 36 | 171.4 | 23.6 | 34 |
| | ***Reversal*** | N/A | N/A | N/A | 182.2 | 22.9 | 30 |
| **Lungs** | ***Ctrl*** | 168.9 | 23.4 | 31 | 175.8 | 19.8 | 25 |
| | ***HFD*** | 182.0 | 40.1 | 32 | 194.3 | 52.0 | 33 |
| | ***Reversal*** | N/A | N/A | N/A | 191.2 | 25.8 | 16 |
| **Liver** | ***Ctrl*** | 1482.4 | 173.6 | 33 | 1604.2 | 307.1 | 25 |
| | ***HFD*** | 2483.3 | 699.3 | 33 | 2518.9 | 690.2 | 33 |
| | ***Reversal*** | N/A | N/A | N/A | 1843.3 | 500.3 | 18 |
| **Kidneys** | ***Ctrl*** | 449.1 | 53.8 | 33 | 475.5 | 51.0 | 25 |
| | ***HFD*** | 549.0 | 53.7 | 33 | 570.1 | 61.3 | 31 |
| | ***Reversal*** | N/A | N/A | N/A | 537.6 | 61.0 | 17 |

| | | | | | | | |
|---|---|---|---|---|---|---|---|
| **Retroperitoneal fat** | ***Ctrl*** | 662.0 | 221.7 | 33 | 1331.7 | 589.0 | 26 |
| | ***HFD*** | 1802.2 | 440.8 | 33 | 1999.8 | 694.8 | 34 |
| | ***Reversal*** | N/A | N/A | N/A | 953.1 | 402.7 | 19 |
| **Epididymal fat** | ***Ctrl*** | 1406.4 | 476.7 | 33 | 1051.6 | 527.3 | 26 |
| | ***HFD*** | 1920.4 | 401.2 | 33 | 2034.4 | 558.5 | 34 |
| | ***Reversal*** | N/A | N/A | N/A | 1071.4 | 406.3 | 19 |
| **Tibia length (TL)** | ***Ctrl*** | 19.5 | 0.5 | 36 | 19.8 | 0.5 | 25 |
| | ***HFD*** | 19.5 | 0.6 | 36 | 19.6 | 0.6 | 33 |
| | ***Reversal*** | N/A | N/A | N/A | 19.7 | 0.5 | 18 |
| **Heart/TL (mg/mm)** | ***Ctrl*** | 8.2 | 1.0 | 36 | 8.9 | 1.0 | 26 |
| | ***HFD*** | 8.5 | 0.8 | 36 | 8.8 | 1.3 | 34 |
| | ***Reversal*** | N/A | N/A | N/A | 9.3 | 1.2 | 30 |
| **Liver/TL (mg/mm)** | ***Ctrl*** | 76.0 | 8.9 | 33 | 81.0 | 15.0 | 26 |
| | ***HFD*** | 127.0 | 34.1 | 33 | 128.7 | 35.0 | 34 |
| | ***Reversal*** | N/A | N/A | N/A | 92.6 | 25.2 | 19 |
| **Kidneys/TL (mg/mm)** | ***Ctrl*** | 23.0 | 2.7 | 33 | 24.0 | 2.5 | 26 |
| | ***HFD*** | 28.2 | 2.8 | 33 | 29.2 | 3.3 | 32 |
| | ***Reversal*** | N/A | N/A | N/A | 27.0 | 3.1 | 19 |

| **Table 1 B.** | **Week 30** | **Week 40** | | |
|---|---|---|---|---|
| **Organ** | **Ctrl vs HFD** | **Ctrl vs HFD** | **HFD vs Rev** | **Ctrl vs Rev** |
| **Heart** | ns | Ns | ns | ns |
| **Lungs** | ns | Ns | ns | ns |
| **Liver** | p<0.001 | p<0.001 | p<0.001 | ns |
| **Kidneys** | p<0.001 | p<0.01 | ns | ns |
| **Retroperitoneal fat** | p<0.001 | p<0.001 | p<0.001 | ns |

| | | | | |
|---|---|---|---|---|
| **Epididymal fat** | p<0.001 | p<0.001 | p<0.001 | ns |
| **Tibia length (TL)** | ns | Ns | ns | ns |
| **Heart/TL (mg/mm)** | ns | Ns | ns | ns |
| **Liver/TL (mg/mm)** | p<0.001 | p<0.001 | p<0.001 | ns |
| **Kidneys/TL (mg/mm)** | p<0.001 | p<0.001 | p<0.05 | p<0.01 |

**Table 1: The effect of HFD feeding on the organ weight in the C57BL6/J mouse A:** Organ weights collected from dissection of animals at 30 and 40 w time points. **B:** Associated statistical comparisons of group mean values. N/A=not applicable, ns = not significant.

## 3.6 Discussion

The difference in weight seen between the groups was somewhat less than that reported at 32 weeks in a study of 45 % HFD feeding to C57BL6/J mice (Noyan-Ashraf et al., 2012) but exceeded that seen after 30 w of feeding C57BL6/J mice a 45 % fat diet (Funato et al., 2009). The increase in absolute fat mass as assessed by QMR by w 29 (158 %) was in good correlation with that published by Funato et al (~170 %)(Funato et al., 2009). The increase in total lean mass at w 29 can be speculated to have arisen due to a hypertrophic muscle stimulus elicited by increased absolute body weight.

Impaired glucose handling ability was expected to arise early in the study (Fearnside et al., 2008). However, since the insulin resistance response to HFD is known to vary between individual animals (Burcelin et al., 2002) fasting glucose and insulin was measured after 5 weeks to verify duration of impaired glucose homeostasis at cardiac evaluation time points. It can be concluded that the HFD perturbs glucose homeostasis within 5 weeks. The natural disease progression in human type 2 DM includes progressive β–cell failure and reduced insulin levels. This was not seen in this model, as

insulin levels remained elevated throughout the 40 w. This was expected (Baribault, 2010). The likely explanation is that compared to humans C57BL6/J mice have a greater capacity for β–cell hyperplasia in response to insulin resistance (Omar et al., 2012). The mild elevation in fasting glucose and maintained elevated insulin levels were in line with a 58 % fat feeding study in C57BL6/J females (Winzell and Ahren, 2004).

The full obesity and glucose handling abnormality reversal, as shown by weight loss, adiposity reduction, and plasma chemistry was expected (Parekh et al., 1998) and will enable a relation to be stated between reversed systemic and cardiac phenotypical findings. The hepatomegalic finding is most likely due to hepatic steatosis as indicated by presented histology. Hepatic steatosis and its reversibility is a well characterised consequence to HFD in mice (Anstee and Goldin, 2006) as well as humans (Durazzo et al., 2012).

A process involving kidney enlargement, inflammation, and fibrosis have previously been reported to present itself as early as after 1 week of 60% HFD feeding in C57BL6/J mice (Decleves et al., 2011). The reversibility after 10 w was only partial which suggests that changes incurred during the HFD feeding may be of a more chronic character compared to those seen in liver, such as renal fibrosis or expansion of functional parenchyma. This was seen in response to 58 % fat HFD feeding in male C57BL6/J mice (Shevalye et al., 2012).

Cardiac functional phenotyping of the study animals was carried out using two modalities, invasive *in vivo* haemodynamics and TTE, to increase the reliability of interpretation. Basic heart rate was assessed using in vivo haemodynamics and showed no differences at w 30, however, at w 40 it seemed that the reversal animals had an on average lower basic heart rate than their control counterparts. There were no

differences comparing heart rate of the HFD animals to neither that of the controls nor reversal group. Invasive haemodynamics offered the opportunity to measure central blood pressure from the ascending part of the aorta just distal to the aortic valve. There were no established differences towards hypertension looking at systolic, diastolic, or mean arterial pressure at either 30 or 40 weeks. LV pressure recordings revealed an isolated significant increase in LVEDP at 30 w. This observation was not seen at 40 w. No differences were reported in analysis of maximum pressure acceleration or deceleration rates at 30 or 40 w comparing control and HFD fed animals. There was a difference at 40 w comparing acceleration rates in controls to that in reversal animals suggesting impaired contractile function in the latter group. TTE at 30 and 40 w did not pick up any convincing abnormalities in systolic nor diastolic function at 30 or 40 w. An approximate 10 % increase in anterior wall thickness at the end of diastole in HFD compared to control animals at 40 w can be interpreted as a sign of impaired relaxation or hypertrophy from HFD feeding but as an isolated significant parameter its impact in my analysis of the whole organ function is small.

In summary of cardiac function analysis: the most direct method used to measure cardiac function, pressure catheterisation, allowed recognition of an elevated end diastolic pressure at 30 w in the absence of hypertension which suggests a mild diastolic dysfunction of cardiac origin. This has previously been reported as an early effect of obesity and insulin resistance (Boudina and Abel, 2007; Dinh et al., 2010; Khavandi et al., 2009). There were no consistent trends seen implying any reversal of impaired diastolic function using *in vivo* haemodynamics. There was a decreased heart rate as well as isolated systolic acceleration rate in the reversal animals at w 40, compared to control animals which could imply an impaired automaticity rate in action potential

generation on a sinus node level, and impaired $Ca^{2+}$ influx rate in the cardiomyocyte, respectively.

These results allow me to conclude that this model of 60 % HFD feeding of C57BL6/J mice permits the study of the impact of induction and reversal of systemic alterations in the form of adipositas, peripheral insulin resistance and hyperglycaemia on cardiac function. I also conclude that the effects on cardiac function are mild.

In an attempt to dissect the origin of changes in cardiac function and to unmask potential whole organ level compensatory effects on cardiomyocyte function, the cardiac muscle will be further interrogated in terms of *in vitro* whole organ tissue characterisation, single cell dynamics and $Ca^{2+}$ handling, as well as myofilament function, in the subsequent chapters of this thesis.

# 4 Characterisation of changes from HFD feeding on insulin signalling, metabolic substrate flux, redox state and fibrosis in myocardial whole tissue

## 4.1 Introduction

The experiments carried out in this chapter aim to elucidate the effects of HFD on myocardial insulin signalling, metabolic substrate preference, redox state, and myocardial fibrosis. It is well known that increased myocardial fibrosis contributes to impaired compliance, and oxidative stress in type 1 DM has been suggested to affect cardiomyocyte $Ca^{2+}$ handling, delaying $Ca^{2+}$ decay and prolonging cardiomyocyte relaxation time (Shao et al., 2011). Both factors thus contribute to impaired compliance affecting the cardiac muscle's ability to physiologically dilate to accommodate increased pre-load, i.e. diastolic dysfunction.

## 4.2 Assessment of myocardial insulin signalling and metabolic substrate utilisation

### 4.2.1 Insulin signalling

Akt is a serine/threonine protein kinase central in mediating insulin's effects on metabolic regulation in the cardiomyocyte. It is activated through phosphorylation by phosphoinositide-dependent kinase 1 (PDK 1) and is thereafter a strong inducer of GLUT4 translocation to the sarcolemma, and also phosphorylates glycogen synthase kinase 3 β (GSK3β) at S9 in an inhibitory fashion to induce glycogen synthesis (Bertrand et al., 2008). Akt phosphorylation has been shown to be reduced (and may thus contribute to insulin resistance) in a HFD induced type 2 DM rat model (Ouwens et al., 2005). Thus the measurement of its phosphorylation at S473 in whole myocardial

extracts was used to investigate signs of decreased insulin signalling activity. However no changes were observed, as illustrated in fFigure 27, either at 30 or 40 weeks.

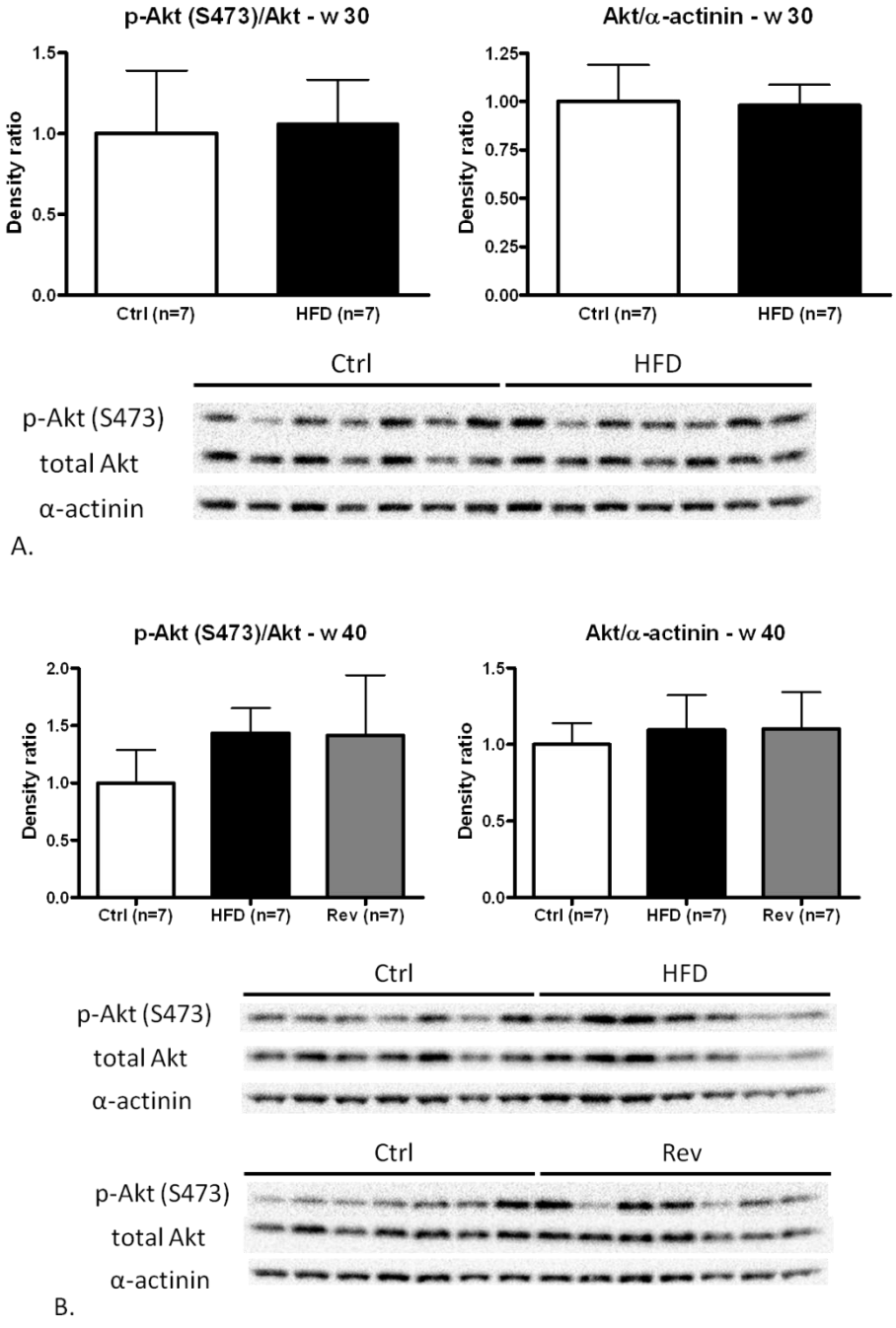



**Figure 27: Myocardial insulin signalling as assessed by Akt phosphorylation A:** No significant changes were observed in Akt phosphorylation or total protein levels at 30 w. **B:** No significant changes were observed in Akt phosphorylation or total protein levels at 40 w. Total protein was normalised to α-actinin. All error bars describe SD.

### 4.2.2 **Assessment of altered metabolic flux**

A combination of quantitative PCR and immunoblotting was used to characterise changes in expression levels and post translational modifications of key proteins involved in glucose and fatty acid import and metabolism.

#### *4.2.2.1 Glucose metabolism*

In line with decreased glucose import in the HFD treated animals the insulin dependent glucose transporter, GLUT4, was found to be down regulated at the mRNA level after 30 (Ctrl (n=8): 1.0 ± 0.20 SD, HFD (n=8): 0.67 ± 0.13 SD) as well as 40 w as shown in Figure 28. The reversal group showed complete recovery of expression levels within 10 w (Ctrl (n=): 1.0 ± 0.13 SD, HFD (n=7): 0.76 ± 0.10 SD, Rev (n=8): 1.0 ± 0.14 SD).

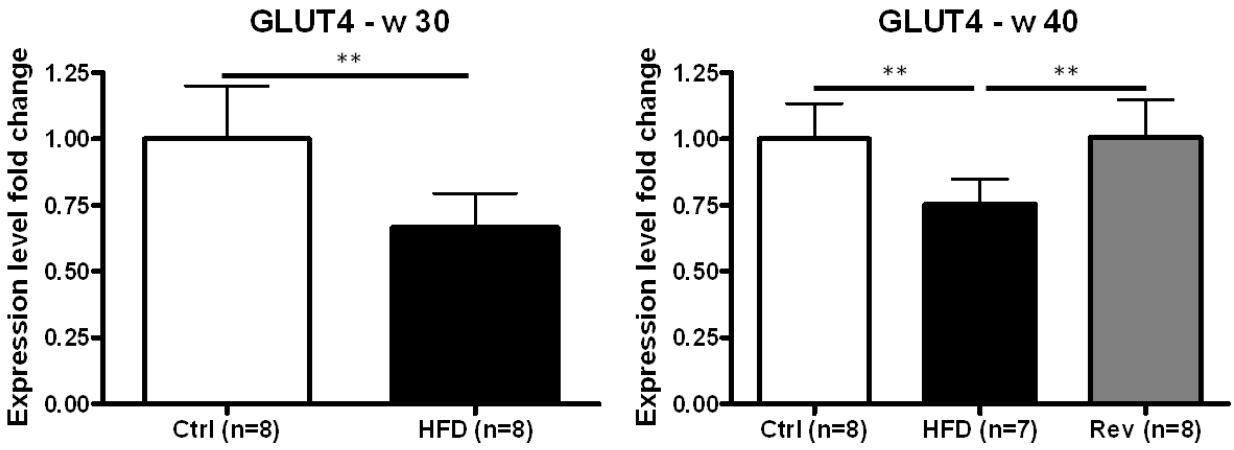



**Figure 28: Effect on GLUT4 expression from HFD feeding** Relative expression levels of the GLUT4 encoding gene at 30 and 40 w. All error bars describe SD. **=p<0.01

Total levels of GSK3β were assessed along with its phosphorylation status at S9 the Akt inhibitory target site (Bertrand et al., 2008), results shown in Figure 29. The level of S9 phosphorylation was not altered in relation to total GSK3β protein level. However, the

latter was upregulated by approximately 40 % at both 30 (Ctrl (n=7): 1.0 ± 0.24 SD, HFD (n=7): 1.44 ± 0.28 SD) and 40 w. After 10 weeks of normal chow the increase was incompletely reversed (Ctrl (n=7): 1.0 ± 1.09 SD, HFD (n=7): 1.42 ± 0.18 SD, Rev (n=7): 1.14 ± 0.27 SD).

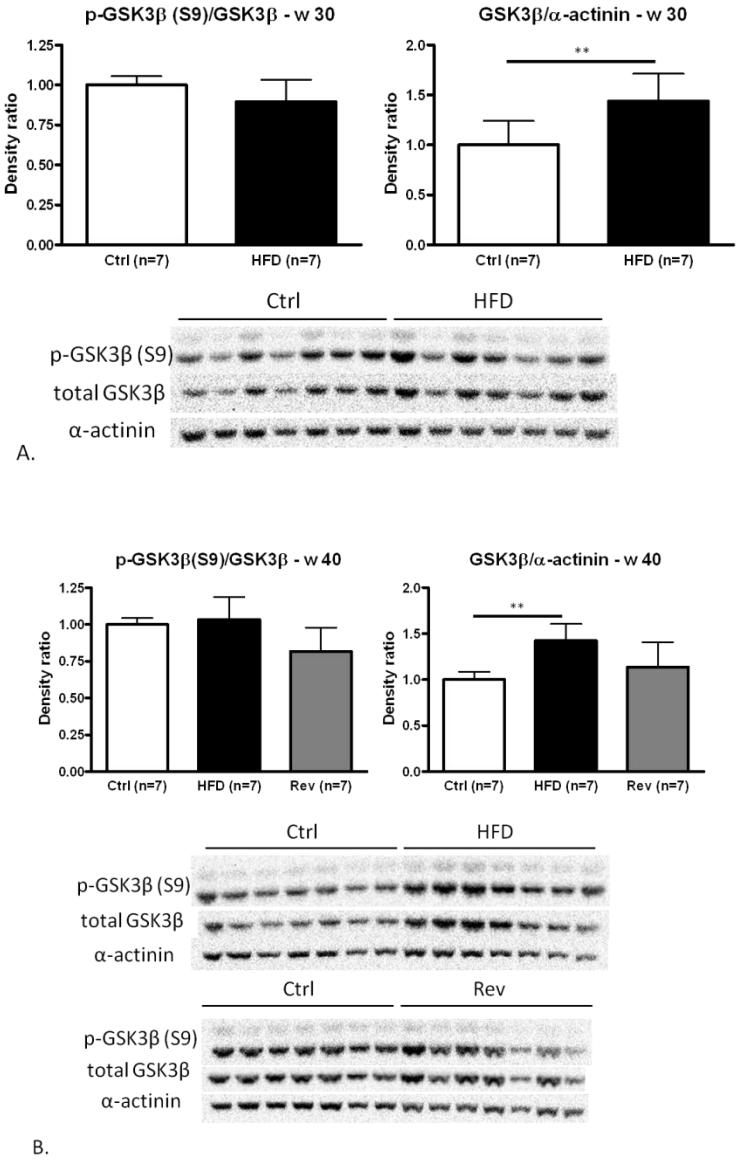
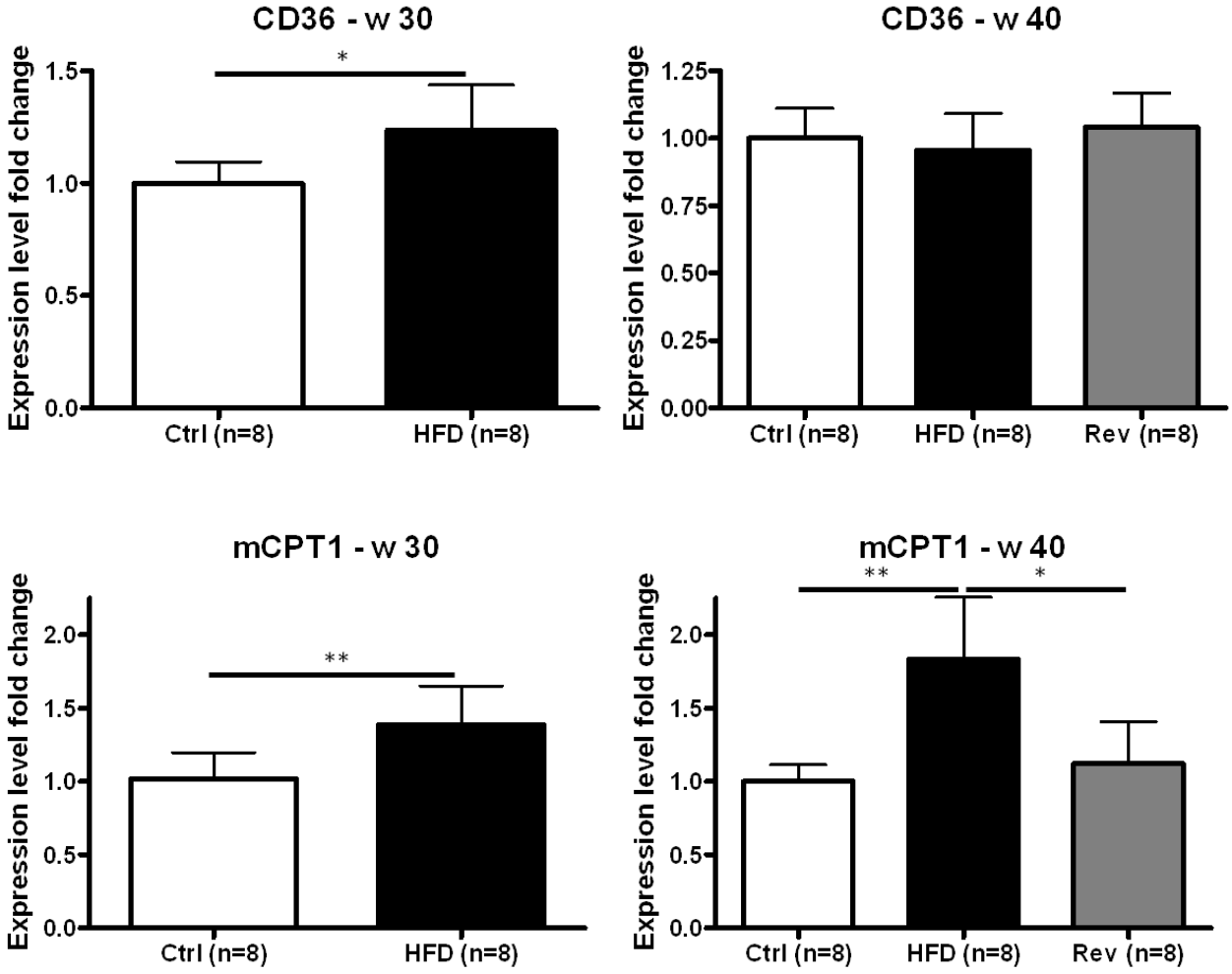
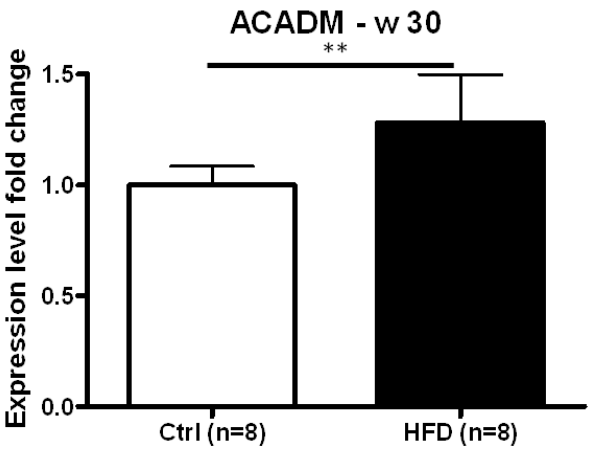


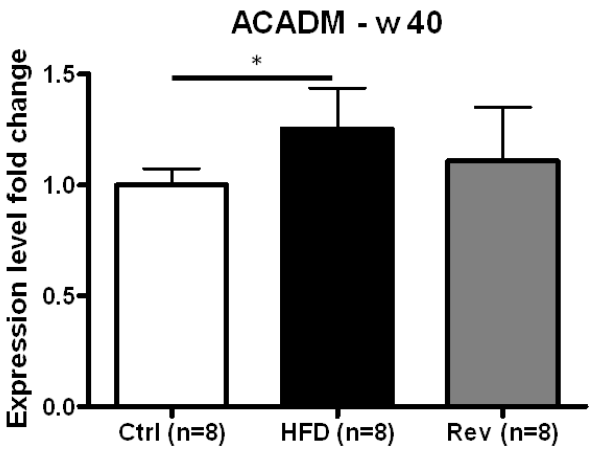

**Figure 29: Effect of HFD feeding on GSK3β phosphorylation and total expression levels A:** Phosphorylation of GSK3β on S9 and total GSK3β protein levels evaluated by immunoblotting at w 30. **B:** Phosphorylation of GSK3β on S9 and total GSK3β protein levels evaluated by immunoblotting at w 40. Total protein levels were normalised using α-actinin as a loading ctrl. All error bars describe SD. **=p<0.01

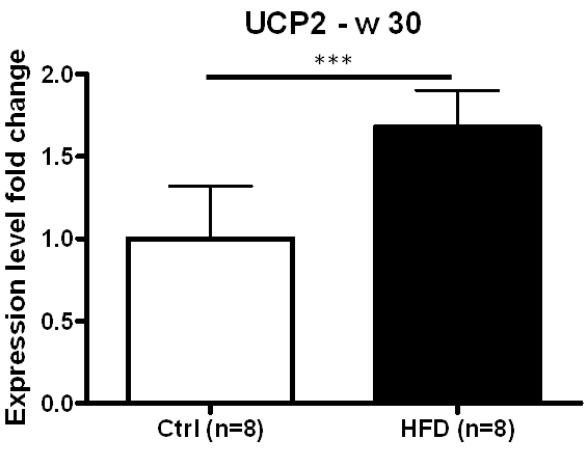
#### *4.2.2.2 Fatty acid metabolism*

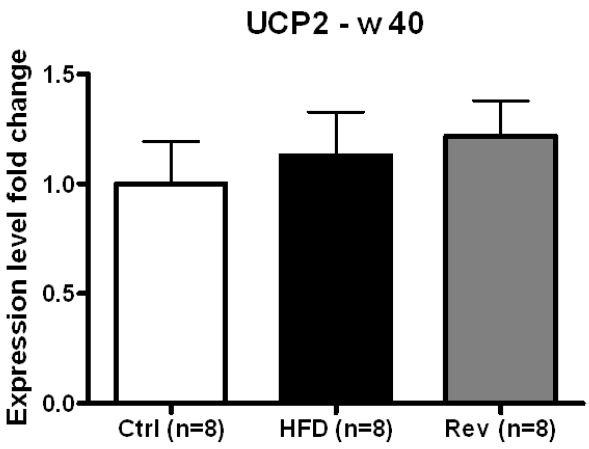
A series of genes encoding proteins involved in fatty acid metabolism were assessed at the mRNA level at both 30 and 40 w to examine whether or not there were signs of increased FFA reliance. Results are shown in Figure 30. These included the sarcolemmal (CD36) and outer mitochondrial membrane fatty acid transport (mCPT1) proteins, mitochondrial medium chain fatty acyl-CoA dehydrogenase (ACADM) in the fatty acid β-oxidation, ETC uncoupling protein (UCP2) and relevant nuclear transcription factors PPAR-α and co-factor PGC1-α.

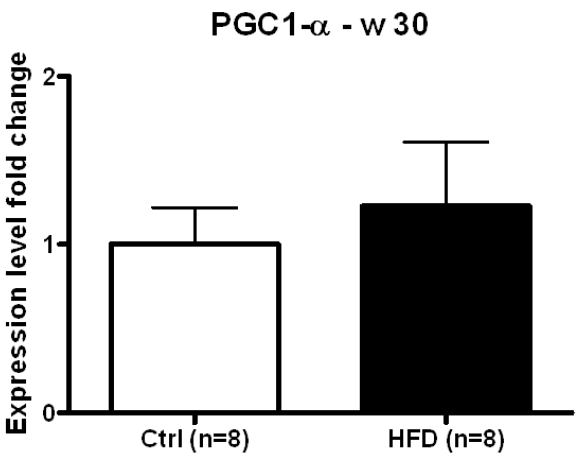


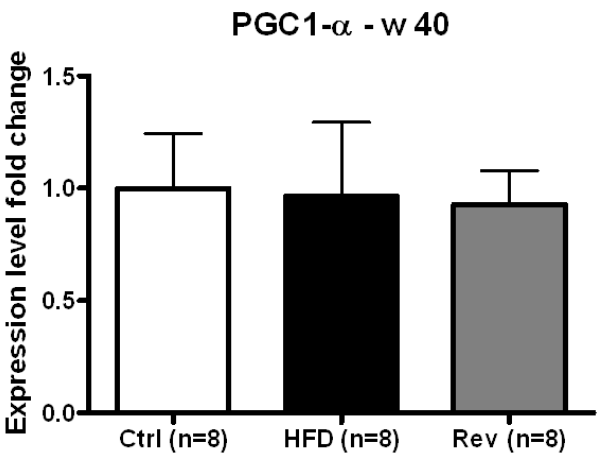

ACADM - w 30
**
Expression level fold change
1.5
1.0
0.5
0.0
Ctrl (n=8)
HFD (n=8)


ACADM - w 40
*
Expression level fold change
1.5
1.0
0.5
0.0
Ctrl (n=8)
HFD (n=8)
Rev (n=8)


UCP2 - w 30
***
Expression level fold change
2.0
1.5
1.0
0.5
0.0
Ctrl (n=8)
HFD (n=8)


UCP2 - w 40
Expression level fold change
1.5
1.0
0.5
0.0
Ctrl (n=8)
HFD (n=8)
Rev (n=8)


PGC1-α - w 30
Expression level fold change
2
1
0
Ctrl (n=8)
HFD (n=8)


PGC1-α - w 40
Expression level fold change
1.5
1.0
0.5
0.0
Ctrl (n=8)
HFD (n=8)
Rev (n=8)

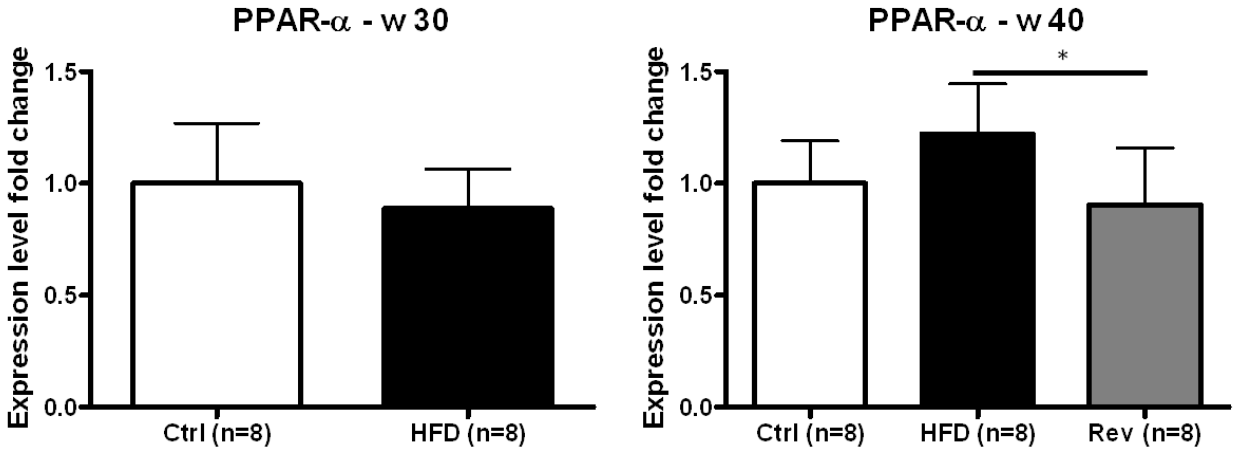



**Figure 30: Myocardial fatty acid handling, UCP2 protein, and relevant transcription factor expression** Proteins involved in myocardial FFA transport and metabolism were investigated at mRNA level at w 30 and 40. *=p<0.05 **=p<0.01. All error bars describe SD.

Sarcolemmal fatty acid transporter CD36 was found to be upregulated after 30 w (Ctrl (n=8): 1.0 ± 0.1 SD, HFD (n=8): 1.24 ± 0.20 SD), a difference that was abolished at w 40. mCPT1 was found consistently upregulated at 30 (Ctrl (n=8): 1.0 ± 0.20 SD, HFD (n=8): 1.39 ± 0.26 SD) and 40 w, and completely reversed after 10 w on control diet (Ctrl (n=8): 1.0 ± 0.11 SD, HFD (n=8): 1.83 ± 0.42 SD, Rev (n=8): 1.12 ± 0.29 SD). ACADM gene expression was found upregulated in the HFD group at 30 (Ctrl (n=8): 1.0 ± 0.08 SD, HFD (n=8): 1.28 ± 0.22 SD) and 40 w. It showed partial reversal after 10 w on ctrl diet (Ctrl (n=8): 1.0 ± 0.07 SD, HFD (n=8): 1.25 ± 0.18 SD, Rev (n=8): 1.11 ± 0.24 SD). Uncoupling protein 2 (UCP2) was upregulated at w 30 (Ctrl (n=8): 1.0 ± 0.30 SD, HFD (n=8): 1.66 ± 0.22 SD) but not at w 40. PGC-1α and PPAR-α showed no differences after neither 30 nor 40 w HFD. A trend towards upregulation of PPAR-α was seen after 40 w in combination with a significant downregulation in the reversal group in comparison to HFD (Ctrl (n=8): 1.0 ± 0.19 SD, HFD (n=8): 1.22 ± 0.23 SD, Rev (n=8): 0.91 ± 0.25 SD).

## 4.3 Assessment of myocardial lipid content

Total tissue TG was extracted from whole heart tissue through wet tissue homogenisation and the levels quantified and normalised to initial amount of raw tissue to assess intramyocardial storage as an effect of increased FFA import in relation to consumption capacity. An import exceeding that of the latter was expected to result in intracellular lipid accumulation.

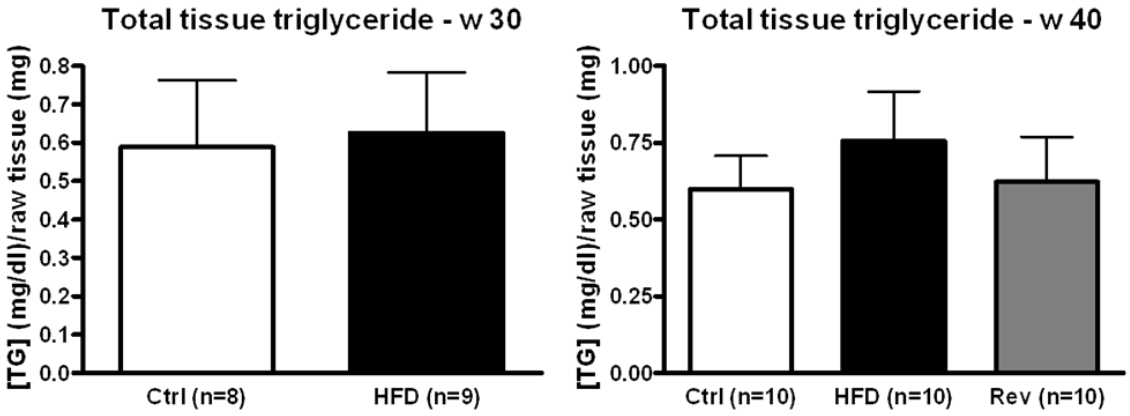



**Figure 31: Effect of HFD on myocardial triglyceride accumulation** Triglycerides were extracted from whole myocardium and concentration was determined in relation to raw tissue weight at w 30 and w 40. All error bars describe SD.

As seen in Figure 31 there were no statistically significant differences in tissue levels of TG, neither at 30 nor 40 weeks although at w 40 a trend was suggested towards increased intramyocardial lipid depositions reversible with diet.

## 4.4 Assessment of myocardial redox status

To examine whether impaired glucose utilisation had altered the redox status in the heart, lucigenin and luminol-derived fluorescence was used to investigate the effects on whole myocardial $O_2^-$ and peroxynitrite production rate.

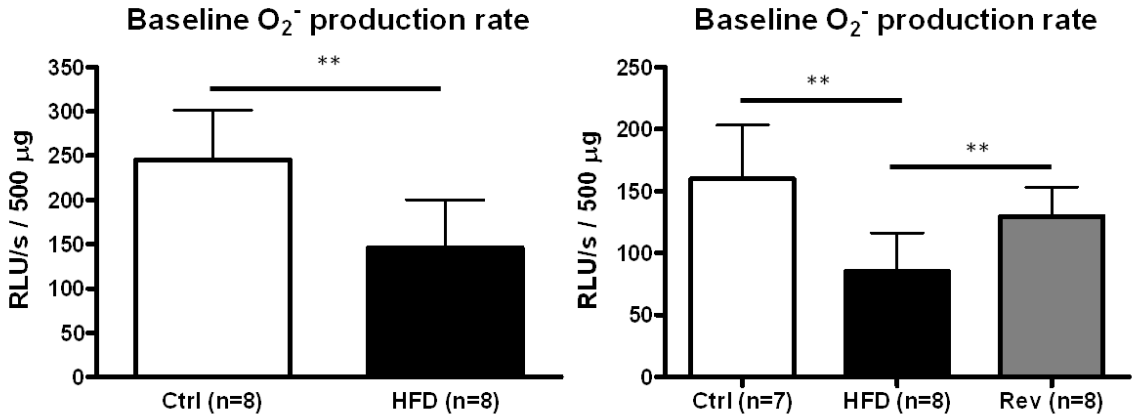



**Figure 32: Effect of HFD feeding on myocardial baseline $O_2^-$ production rate** Baseline production rate of $O_2^-$ in native myocardial homogenates at 30 and 40 w. All error bars describe SD. **=p<0.01.

Baseline $O_2^-$ production rate was determined using lucigenin fluorescence. Results are shown in figure 32. It was significantly reduced in the HFD group at both 30 (Ctrl (n=8): 245.3 RLU/s / 500 µg ± 55.9 SD, HFD (n=8): 145.7 RLU/s / 500 µg ± 54.5 SD) and 40 w. A switch to normal chow partly reversed this change (Ctrl (n=7): 160 RLU/s / 500 µg ± 43.3 SD, HFD (n=8): 85.27 RLU/s / 500 µg ± 31.2 SD, Rev (n=8): 129.6 RLU/s / 500 µg ± 23.55 SD).

NADPH stimulated $O_2^-$ production rate was assessed in order to examine NOX enzyme activity, specifically. As seen in Figure 33 it was significantly increased in the HFD group at 40 w, a change reversed by dietary switch (Ctrl (n=7): 7047 RLU/s / 500 µg ± 1374 SD, HFD (n=7): 10478 RLU/s / 500 µg ± 2452 SD, Rev (n=8): 6732 RLU/s / 500 µg ± 1010 SD). Experiments were also performed in the presence of the NOX inhibitor VAS2870. This compound displayed a greater inhibitory capacity of the $O_2^-$ production rate in the HFD group compared to ctrl at 40 w. This change was also prevented through diet reversal (Ctrl (n=7): 2403 RLU/s / 500 µg ± 640 SD, HFD (n=7): 3687 RLU/s / 500 µg ± 780 SD, Rev (n=8): 2404 RLU/s / 500 µg ± 451 SD).

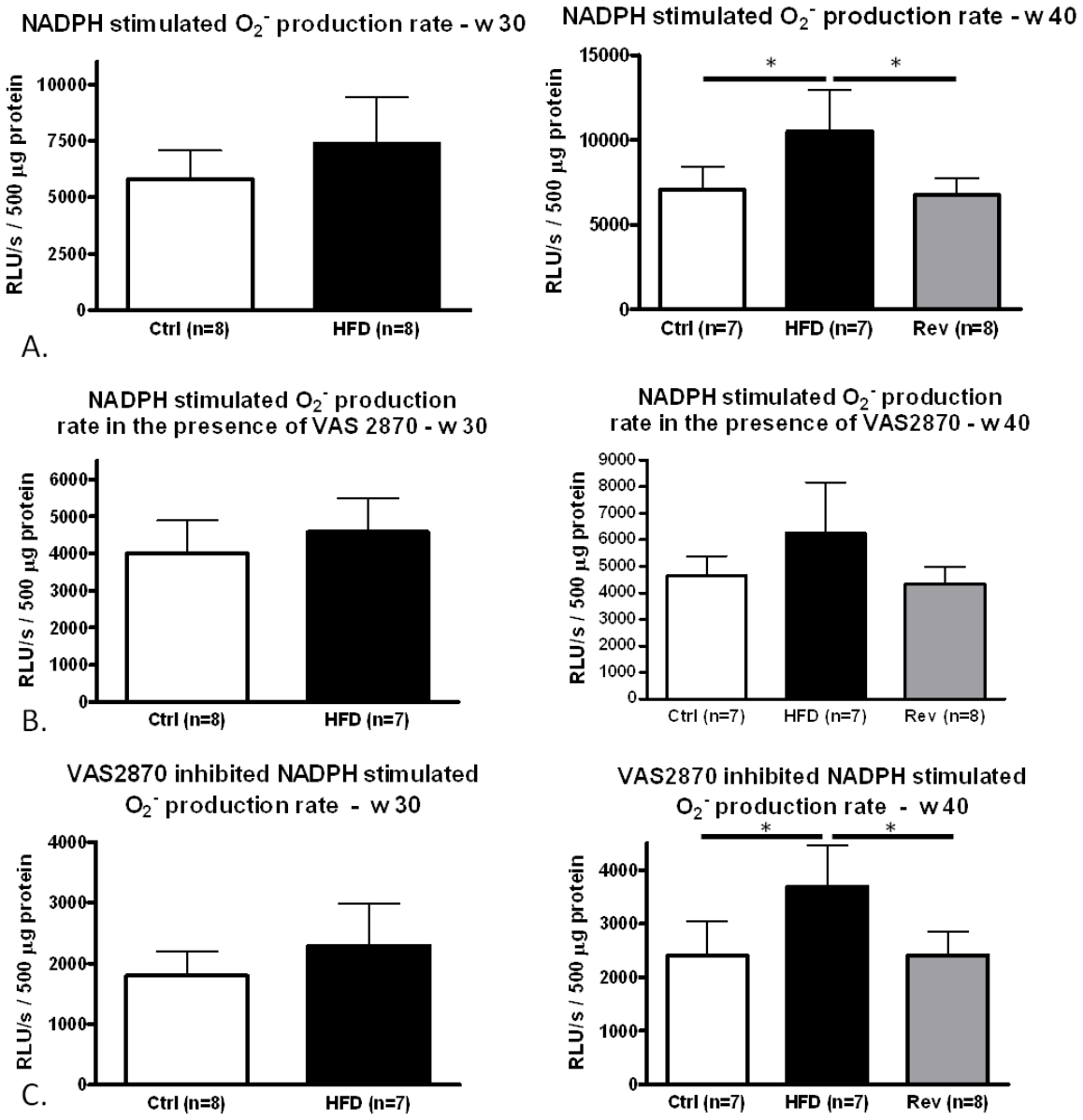



**Figure 33: Effect of HFD feeding on myocardial NOX activity A:** NADPH stimulated $O_2^-$ production rate at 30 and 40 w. **B:** NADPH stimulated $O_2^-$ production rate in the presence of VAS2870. **C:** Absolute inhibition of NADPH-stimulated $O_2^-$ production rate at 30 and 40 w. All error bars describe SD. *=p<0.05

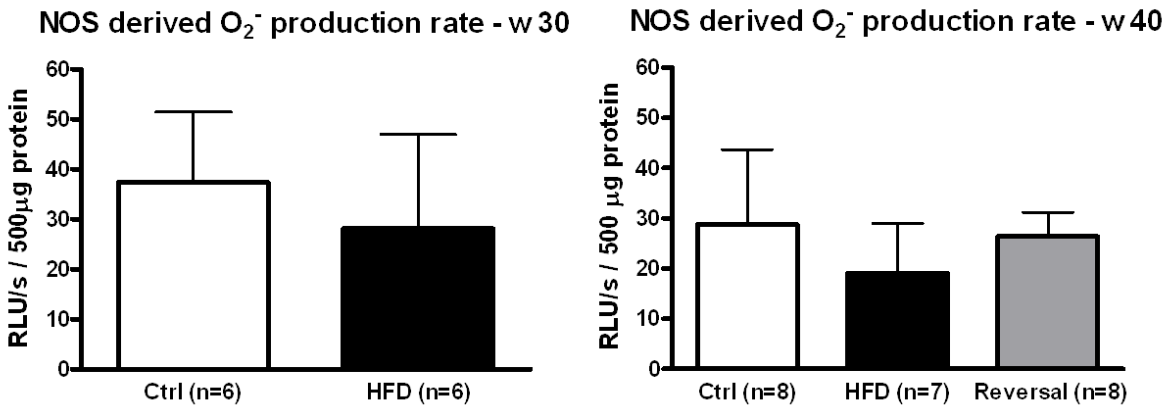



**Figure 34: Effect of HFD feeding on myocardial NOS activity** Absolute inhibited $O_2^-$ production rates by NOS-inhibitor L-NAME at 30 and 40 w. All error bars describe SD.

As shown in Figure 34, $O_2^-$ production rates were also measured in the presence of the NOS inhibitor L-NAME to specifically examine the activity of the NOS enzymes. There were no statistically significant changes in NOS derived $O_2^-$ production as assessed by absolute L-NAME inhibition at baseline at neither 30 nor 40 w.

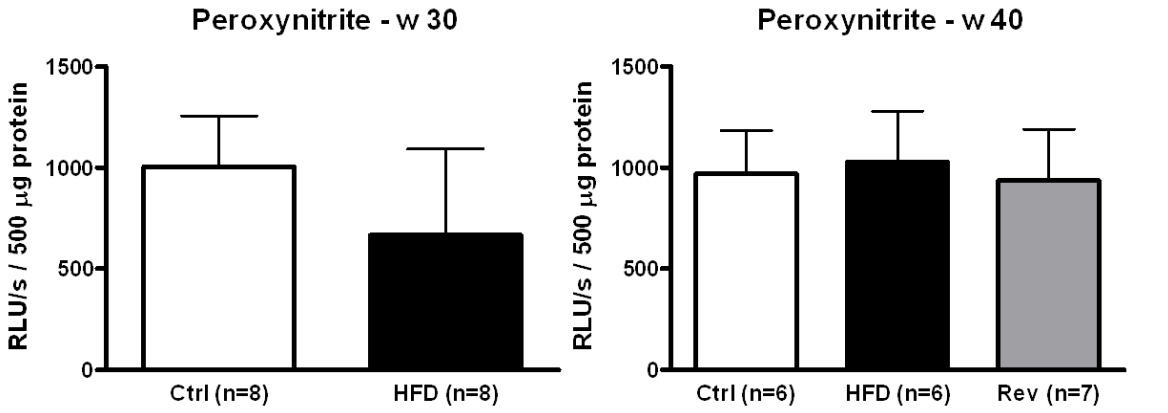



**Figure 35: Effect of HFD feeding on myocardial peroxynitrite generation** Peroxynitrite production rate at 30 and 40 w. All error bars describe SD.

There were no statistically significant changes in peroxynitrite production rate as assessed by absolute urate inhibition at baseline neither at 30 nor 40 w as shown in fFigure 35.

## 4.5 Assessment of cardiac fibrosis

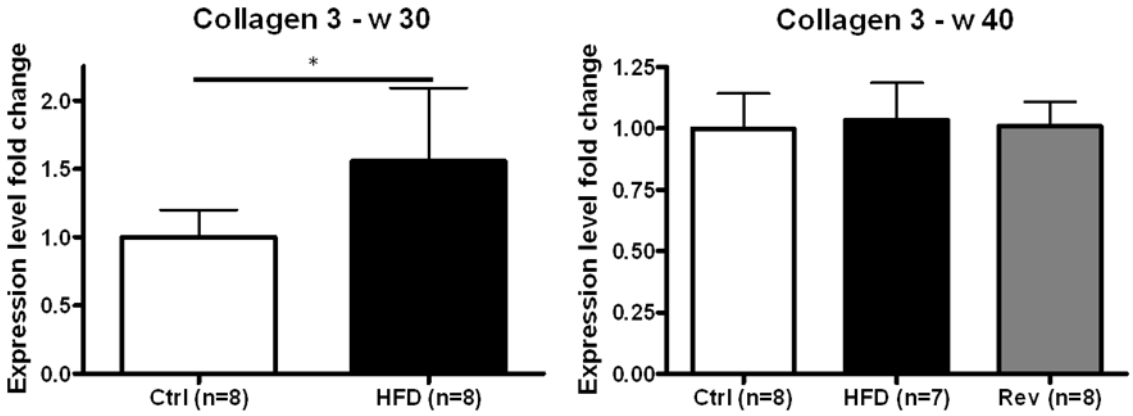



**Figure 36: The effect of HFD on myocardial collagen 3 expression** Collagen isoform 3 expression levels at 30 and 40 w. All error bars SD. *=p<0.05.

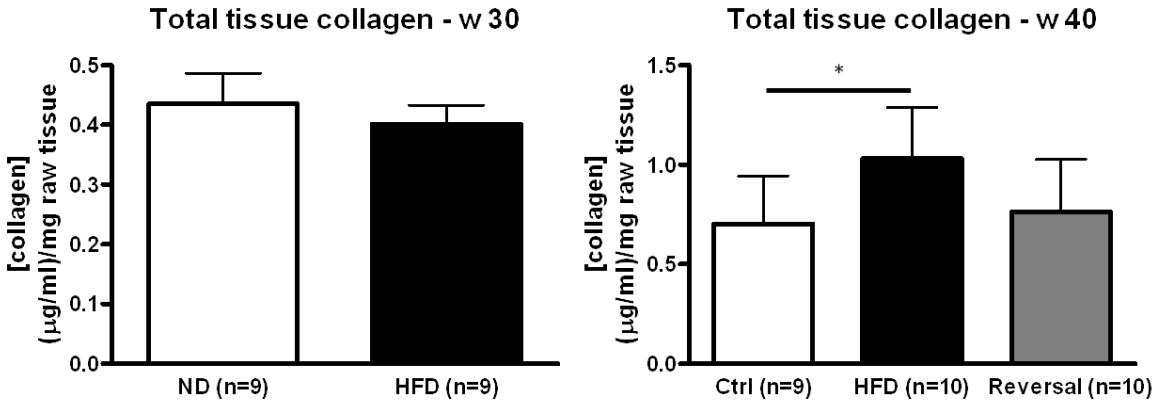



**Figure 37: The effect of HFD on myocardial total collagen content** Total collagen content was assessed after tissue extraction at 30 and 40 w in relation to total tissue weight. All error bars SD. *=p<0.05

As there were signs of decreased compliance from *in vivo* haemodynamics (Fig. 3.7) the status of myocardial collagen production and contents were assessed. Collagen isoform 3 expression was examined at mRNA level. Results are shown in Figure 36. After 30 w the transcription level in the HFD group was upregulated in relation to control (Ctrl (n=8): 1.0 ± 0.20 SD, HFD (n=8): 1.56 ± 0.54 SD), a difference abolished at 40 w.

As seen in Figure 37, there were no differences in total collagen levels after 30 w. At 40 w the total collagen contents of myocardial samples from HFD fed animals were

increased. There was no increase in collagen in the group reversed to a normal diet after 30 w (Ctrl (n=9): 0.70 mg/ml / mg tissue ± 0.24 SD, HFD (n=10): 1.03 mg/ml / mg tissue ± 0.26 SD, Rev (n=10): 0.76 mg/ml / mg tissue ± 0.26 SD).

## 4.6 Discussion

The aim of this chapter was to examine the changes in the intercommunicating processes of insulin signalling, metabolic substrate utilisation, and oxidative stress using whole myocardial tissue extracts.

As seen in chapter 3 the systemic effects on glucose homeostasis were quite mild in the fasting state with an increase in fasting blood glucose of approximately 2.5 mM at 30 and 40 w. When provoked by a glucose injection the relative inability of the animal to efficiently remove glucose from the circulation was made obvious. Since the secretory capacity for insulin was maintained and elevated in the HFD fed animals this is considered to be the result of peripheral insulin resistance. In the myocardium, however, there was little direct evidence of impaired insulin signalling as judged by p-Akt and p-GSK3β levels, suggesting that the myocardial insulin signalling pathway could be more robustly maintained compared to skeletal muscle and liver. This result is however contradicted in a study of HFD in C57BL6/J mice where reduced p-Akt levels were seen in the heart after only 1.5 and 3 weeks. The impact of HFD appeared more severe in this study as the animals suffered subsequent development of impaired insulin secretion and systolic dysfunction after 20 weeks (Park et al., 2005).

Levels of key glucose and fatty acid handling proteins were investigated as indications of substrate flux changes. The insulin sensitive GLUT4 glucose transporter was found to be

down regulated at the mRNA level in the HFD group. GSK3β was found upregulated at the protein level with no changes in S9 phosphorylation normalised to total GSK3β expression. The combination of these findings suggests a decreased dependence on glucose as a metabolic substrate. GLUT4 activity however, as seen in the introduction, is not only dependent on expression levels but also on subcellular localisation which could have been investigated through subcellular fractionation followed by immunoblotting, or immunohistochemistry. This was not attempted. GSK3β works in an inhibitory fashion on glycogen synthase, thus an increase in its level suggests inhibition of glycogen synthesis from glucose. In the present model the interrelation of insulin signalling and metabolic substrate preference can only be speculated upon. GSK3β might be upregulated due to decreased availability of glucose, or a dysregulated response to HFD which inhibits the glucose processing ability in the cardiomyocytes thus conveying insulin resistance at a further downstream level in the insulin signalling pathway. Total GSK3β upregulation has been shown previously, in skeletal muscle, of type 2 DM patients (Nikoulina et al., 2000) and suggestion of GSK3β's ability as a conveyor of insulin resistance was shown by the restoration of systemic glucose levels when administering a GSK3β inhibitor to diabetic animals (Rayasam et al., 2009).

Fatty acid handling proteins were assessed on mRNA level only. The results indicate an increased reliance on fatty acid metabolism upon HFD feeding, as expected from the introduction to this thesis. From the sarcolemmal and outer mitochondrial membrane fatty acid import proteins CD36 and mCPT1, to the mitochondrial β-acid oxidation enzyme ACADM, and electron transport chain associated uncoupling protein, UCP2, increased expression levels of key genes on mRNA were detected. Interestingly, two enzymes, the sarcolemmal CD36 and UCP2 were both transient in their upregulation,

displaying elevated mRNA levels at w 30 which were normalised at w 40. This may reflect how the establishment of a new metabolic equilibrium does not come forth through a simple switch of events but rather a series of reactions and counter-reactions.

Increased CD36 activity or translocation to the sarcolemma is thought to be an important factor in the development of cardiomyocyte lipid accumulation (Angin et al., 2012). Cardiac lipid accumulation was assessed after tissue TG extraction. There was no significant increase in this parameter but a trend towards myocardial lipid accumulation was clear.

With regards to basal $O_2^-$ production rate in whole tissue myocardium, the effect of HFD was surprisingly a decrease at both w 30 and w 40. The reason for oxidative stress in diabetes in usually ascribed to the increased dependence on mitochondrial fatty acid oxidation (Dirkx et al., 2011), increased $FADH_2$ and NADH generation and electron transfer to $O_2$ (Ceriello and Motz, 2004). The altered protein expression profile supports increased dependence on mitochondrial fatty acid oxidation and also, in type 2 DM, an activation of the renin-aldosterone-angiotensin system (RAAS), inducing cytosolic production of $O_2^-$ through NOXs has been reported (Mandavia et al., 2012). The decreased $O_2^-$ production at baseline may be a result of the increased presence of insulin in the circulation in a situation where the myocardial signalling pathway remains intact. Judging by the p-Akt levels there was no obviously impaired myocardial signalling, despite systemic insulin resistance, but rather a tendency towards increased p-Akt/Akt at w 40, comparing control and HFD treated animals. It may however also be argued that since despite the increased concentration of insulin in plasma the p-Akt/Akt was not increased is actually a sign of decreased insulin sensitivity. This trend was not statistically significant using a ANOVA test for multiple group comparisons. It is

noteworthy, however, that increased oxidative stress in diabetes is also suggested to be a cause of insulin resistance (Aroor et al., 2012) through IRS1 phosphorylation inducing proteosomal down regulation, via redox sensitive kinases (Mandavia et al., 2012), and equally how insulin sensitization through metformin decreased oxidative stress (Roberts and Sindhu, 2009). Thus insulin signalling and oxidative stress most likely represent a pathogenetic dialogue in which a vicious circle is enabled. The source of $O_2^-$ which are NOX-enzymes, was measured through NADPH stimulation of $O_2^-$ generation rate, and NOX inhibition by VAS2870. This approach suggested an upregulation of NOX activity, probably through increased RAAS activity as described above even though systemic levels of the RAAS constituents were not measured. No commercial ATII-assays suited for mouse amounts of plasma could be identified at the time of investigation.

L-NAME was used to assess the contribution of NOS enzymes in basal $O_2^-$ production rate. There were no significant differences in production rate after addition of the inhibitor. Also, peroxynitrite was assessed and no significant changes detected. Together these results suggest that no uncoupling of NOS enzymes from nitric oxide to $O_2^-$ production had occurred in the myocardium.

Interestingly, increased $O_2^-$ generation through NOX enzymes and increased fibrosis are commonly reported effects of increased RAAS signalling (Mandavia et al., 2012). Increased fibrosis was indicated by raised total collagen at w 40 as well as heightened relative collagen 3 expression at mRNA level at w 30, but not at 40 w. This increase in total collagen and collagen 3 expressions can be speculated to contribute to the increase in LVEDP seen upon HFD feeding after 30 w.

In conclusion of this chapter it can be stated that no convincing impairment of insulin signalling was detected through phosphorylation level assessments of the key protein

Akt, and also GSK3β. Combined protein and mRNA level assessment of key glucose and FFA handling proteins suggests however that a metabolic switch has occurred independently of reduced insulin signalling. In addition, basal $O_2^-$ production rate was decreased in HFD affected myocardium. This was not due to reduced NOS activity as absolute L-NAME inhibition effect, nor peroxynitrite production rate differed between groups. NOX enzyme contribution to $O_2^-$ generation was found to be elevated. Thus it is plausible that mitochondrial ECT sources of $O_2^-$ were decreased. This is in conflict with the established paradigm concerning effects on redox status from increased fatty acid metabolism and diabetes (Dirkx et al., 2011; Mandavia et al., 2012; Roberts and Sindhu, 2009) and would need further investigation with ETC $O_2^-$ source inhibitors before making more robust claims. It can be speculated however that the increase in systemic insulin levels in conjunction with a preserved or compensated insulin signalling pathway represents an early expression of the established diabetic phenotype, or a phenotype not seen in humans, due to the C57BL6/J mouse line's ability to maintain insulin secretion, which may act to decrease $O_2^-$ production. The upregulation of UCP2 at 30 w supports the finding of decreased mitochondrial $O_2^-$ production rate as it can lower ROS production (Aroor et al., 2012) by relieving the proton gradient in the ETC (Giacco and Brownlee, 2010), but its normalised expression level at w 40 where the $O_2^-$ generation rate is persistently elevated, speaks against it as a decisive factor.

With access to data presented in this chapter a further discussion is warranted regarding the contradicting outcome in the similar study of Park et al. Unlike the results of Park et al who demonstrated impaired systolic function at w 20, there are further important changes to note in the outcome of feeding the same mouse strain a similar fat percentage HFD, 55% by Park et al, vs 60 % in the here presented study. The Park study

was conducted after 20 w of feeding in 28 weeks old mice, as opposed to after 30 w feeding in 34 week old mice. The Park study resulted in decreased levels of intramyocardial fatty-acyl CoA, in my study the total levels of TG was unchanged, but with a trend towards increased levels with time. Park postulates how the increased level of fatty acid metabolism has increased production of mitochondrial free radicals through upregulation of UCPs 2 and 3. Even though the levels of UCP was upregulated after 30 w in my study, the production rate of $O_2^-$ was markedly reduced. Thus, it may be that the decreased production rate of $O_2^-$ has served to maintain cardiac function, unlike the Park study where dysfunction was associated with decreased lipid accumulation intramyocardially and suggested increased free radical generation (Park et al., 2005).

As described in the introduction to this thesis, disturbed intracellular $Ca^{2+}$ homeostasis and increased interstitial fibrosis are both factors affecting diastolic myocardial function in diabetes, both processes suggested as augmented by oxidative stress. Impaired SR $Ca^{2+}$ sequestration through the SERCA, as well as myofilament effects, represent mechanisms that may act within the cardiomyocyte whereas interstitial fibrosis is extracellular. To attempt to distinguish the relative importance of these changes an isolated cardiomyocyte functional assessment was undertaken to study $Ca^{2+}$ handling and unloaded contraction and relaxation dynamics. The results of these inquiries are presented in chapter 5.

# 5 Effects from a HFD on unloaded cardiomyocyte dynamics and intracellular $Ca^{2+}$ transients

## 5.1 Introduction

As described in the introduction to this thesis, the cardiomyocyte itself has been suggested to be a fibrosis-independent target in diabetes related cardiac dysfunction. Studies have attributed this to SERCA modifications due to oxidative stress in both type 1 and type 2 models of diabetes (Li et al., 2006; Shao et al., 2011), changes in SERCA protein levels (Lacombe et al., 2007), and alteration in RyR mRNA levels (Reuter et al., 2008).

## 5.2 Unloaded cardiomyocyte dynamics and $Ca^{2+}$ handling

Cardiac myocytes were isolated from 30 and 40 w hearts and their contractility and $Ca^{2+}$ handling (using the $Ca^{2+}$ sensitive ratiometric dye fura-2) examined at 1 and 3 Hz to assess cardiomyocyte function independently of extracellular confounding factors.

### 5.2.1 **Unloaded cardiomyocyte dynamics**

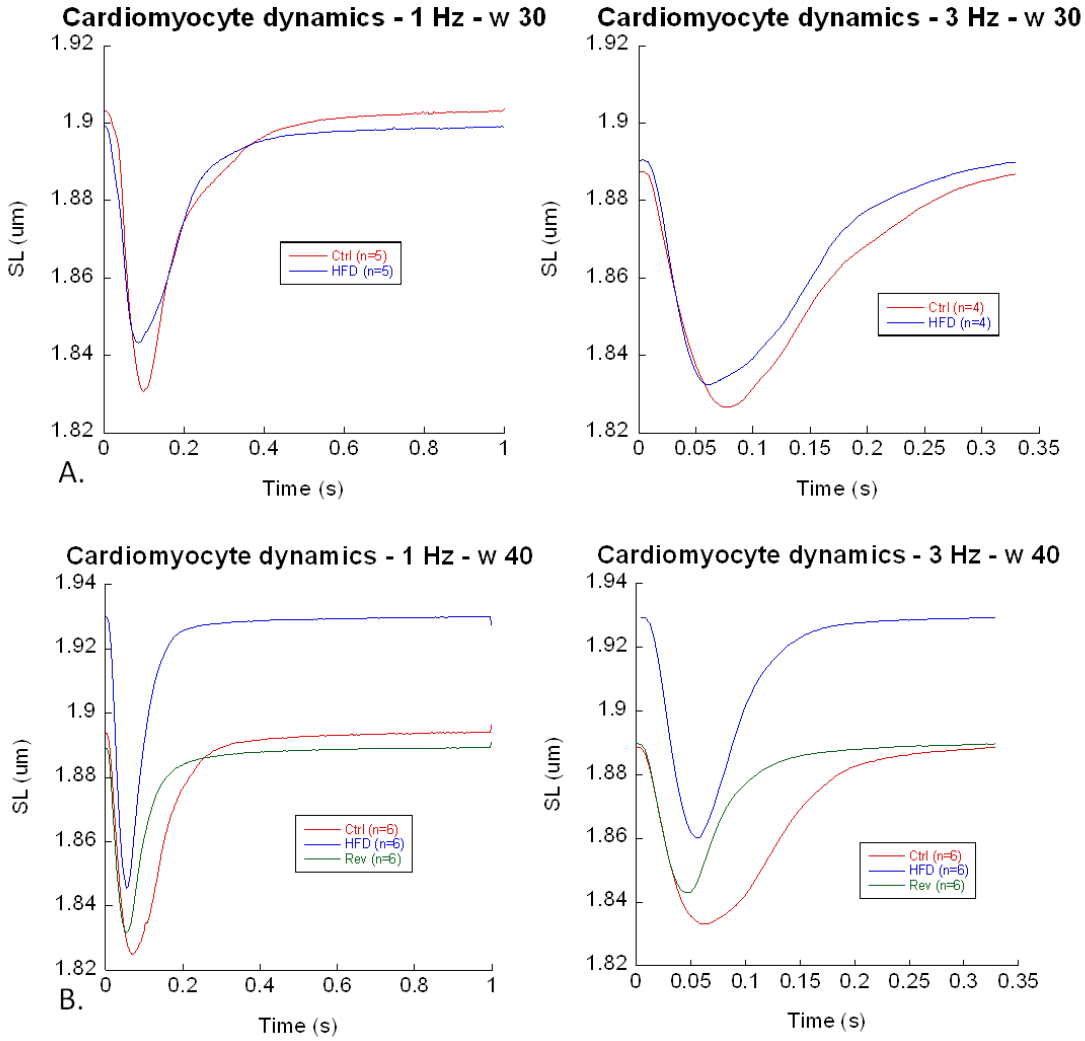



**Figure 38: Single cell contractility traces A:** Averaged contraction-relaxation traces when stimulated at 1 and 3 Hz at w 30. **B:** Averaged contraction relaxation traces when stimulated at 1 and 3 Hz at w 40. 10 cell recordings were obtained from each animal and the data averaged for each animal representing n=1. (SL: sarcomere length)

Single cell dynamics were quantified from averages of individual cardiomyocyte recordings with regards to baseline SL during stimulation, FS, time to 50 % maximum contraction from baseline, and time to 50 % maximum relaxation from peak contraction. These parameters were chosen to quantitatively assess the above average traces shown in Figure 38.

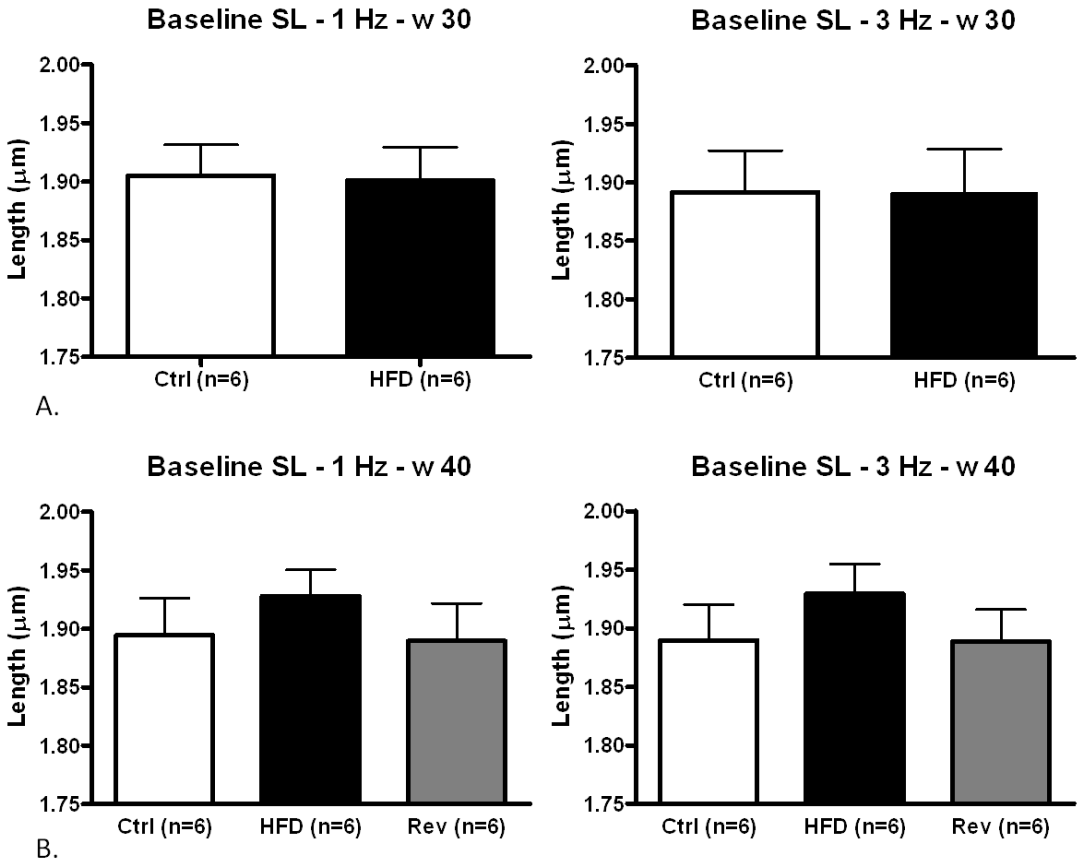



**Figure 39: Single cell baseline sarcomere length A:** SL at full relaxation during 1 and 3 Hz stimulation at w 30. **B:** SL at full relaxation during 1 and 3 Hz stimulation. All error bars describe SD. (SL: sarcomere length)

As illustrated in Figure 39 there were no differences in baseline SL at either 1 or 3 Hz stimulation neither after 30 or 40 weeks. At 40 weeks there was a non-significant increase in baseline SL in the HFD group at both 1 and 3 Hz stimulation.

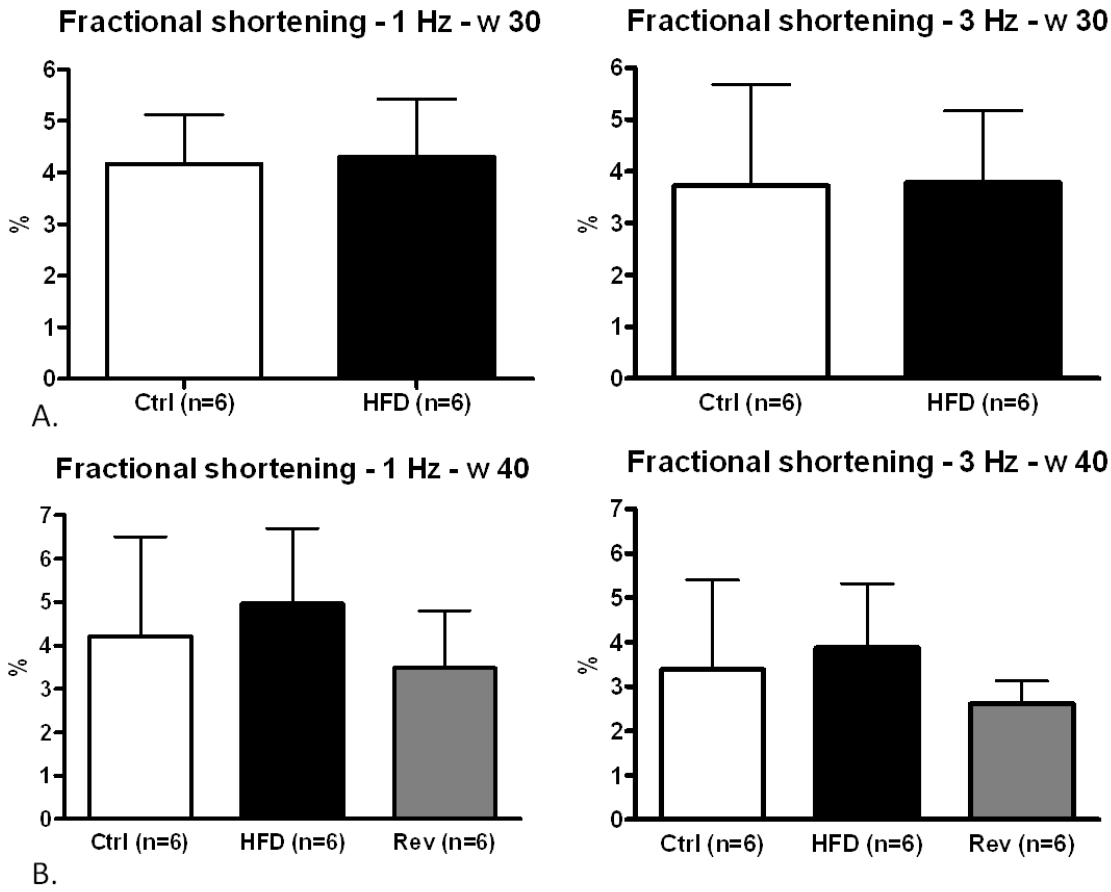



**Figure 40: Single cell fractional shortening A:** SL shortening percentage during contraction at 1 and 3 Hz stimulation after 30 w. **B:** SL shortening percentage during contraction at 1 and 3 Hz stimulation after 40 w. All error bars describe SD.

No statistically significant changes in single cell FS were observed at either 1 or 3 Hz stimulation frequency after 30 or 40 w as can be seen in Figure 40.

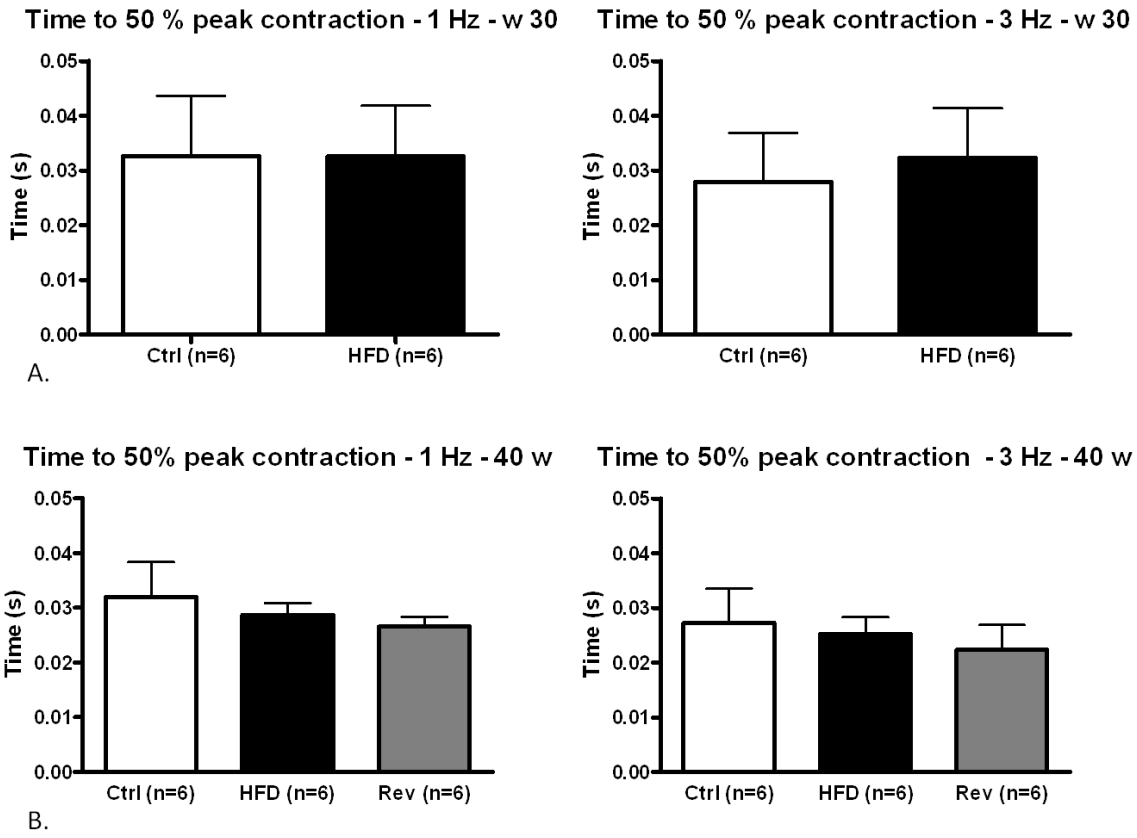



**Figure 41: Single cell contraction rate A:** Time until half maximal contraction amplitude was reached at 1 and 3 Hz stimulation after 30 w. **B:** Time until half maximal contraction amplitude was reached at 1 and 3 Hz stimulation after 40 w. All error bars describe SD.

The time to half peak contraction was used as a measure of contraction velocity. No significant changes in this parameter were detected at either 1 or 3 Hz or after 30 or 40 w as shown in Figure 41.

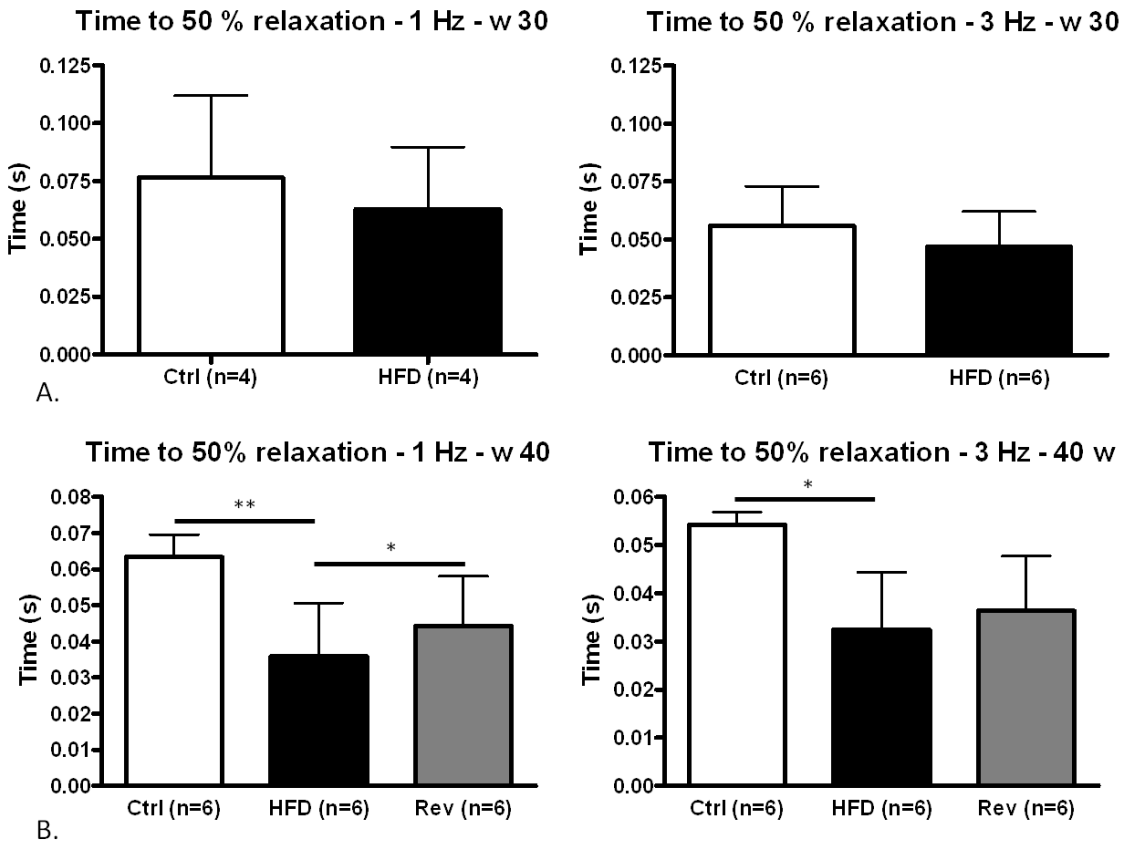



**Figure 42: Single cell relaxation rate A:** Time until half relaxation was reached at 1 and 3 Hz stimulation after 30 w. **B:** Time until half relaxation was reached at 1 and 3 Hz stimulation after 40 w. All error bars describe SD. **=p<0.01, *=p<0.05.

As illustrated in Figure 42, at 30 w there were no differences in relaxation rate in the cardiac myocytes comparing ctrl to HFD. At 40 w an increase in relaxation rate was detected in cardiomyocytes from HFD treated animals at both frequencies. The relaxation rate of cardiomyocytes from the reversal group at 40 w was significantly decreased compared with HFD (and not significantly different from control) at 1 Hz (Ctrl (n=6): 0.063 s ± 0.006 SD, HFD (n=6): 0.036 s ± 0.015 SD, Rev (n=6): 0.044 s ± 0.014 SD) but not at 3 Hz stimulation frequency (Ctrl (n=6): 0.054 s ± 0.003 SD, HFD (n=6): 0.032 s ± 0.012 SD, Rev (n=6): 0.036 s ± 0.011 SD).

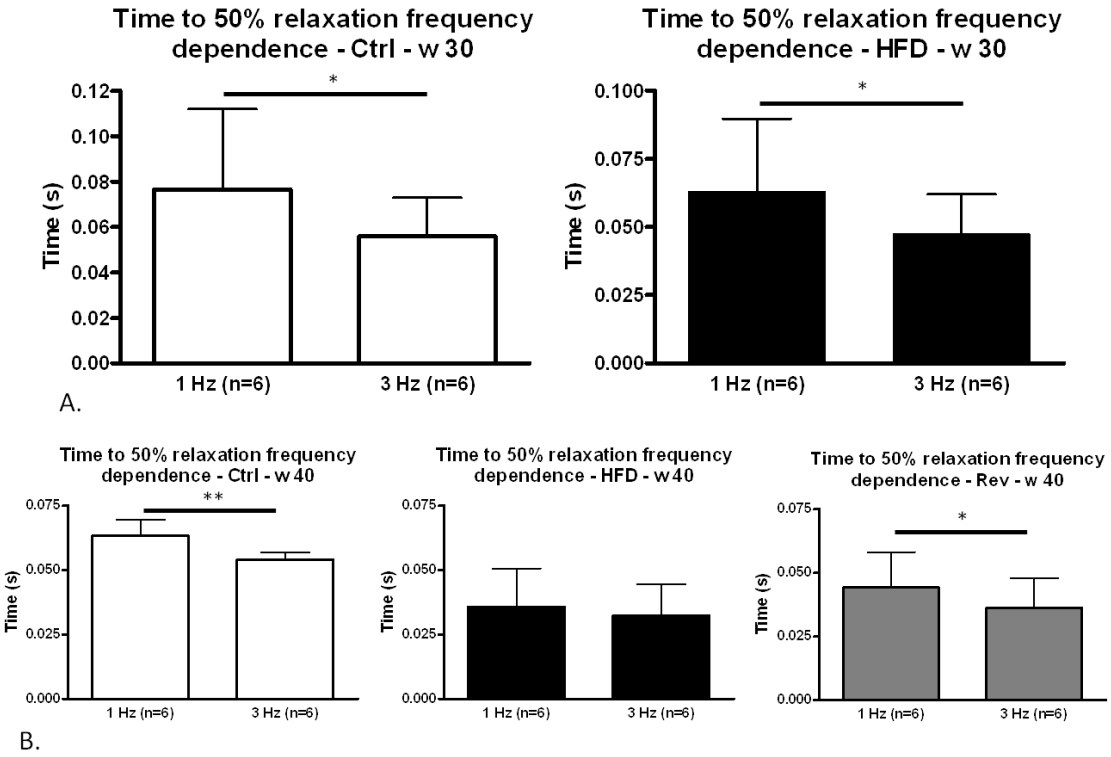



**Figure 43: The effect of stimulation frequency on single cell relaxation rate A:** Comparison of time to 50 % relaxation within groups at 1 Hz and 3 Hz at w 30. **B:** Comparison of time to 50 % relaxation within groups at 1 Hz and 3 Hz at w 40. All error bars describe SD. **=p<0.01, *=p<0.05.

Due to the increased relaxation rate it was suspected that the further increase in relaxation rate upon increased stimulation frequency might have been limited. The relaxation time is expected to shorten as an accommodative response to increased stimulation frequency (Guyton, 2001). As is shown in Figure 43, at 30 w both the ctrl (1 Hz (n=6): 0.076 s ± 0.035 SD, 3 Hz (n=6): 0.056 s ± 0.017 SD) and HFD group (1 Hz (n=6): 0.063 s ± 0.027 SD, 3 Hz (n=6): 0.047 s ± 0.15 SD) displayed a significant increase in relaxation rate upon increased stimulation frequency using pair wise comparison. However, at w 40 where the HFD treated group was found to have increased relaxation rate, its frequency dependence was abolished with regards to relaxation rate (1Hz (n=6): 0.036 s ± 0.015 SD, 3 Hz (n=6): 0.032 s ± 0.011 SD) whereas the ctrl (1 Hz (n=6): 0.063 s ± 0.006 SD, 3 Hz (n=6): 0.054 s ± 0.003 SD) and reversal group (1 Hz (n=6):

0.044 s ± 0.013 SD, 3 Hz (n=6): 0.036 s ± 0.011 SD) showed significant frequency dependence in relaxation rate.

### 5.2.2 $Ca^{2+}$ handling

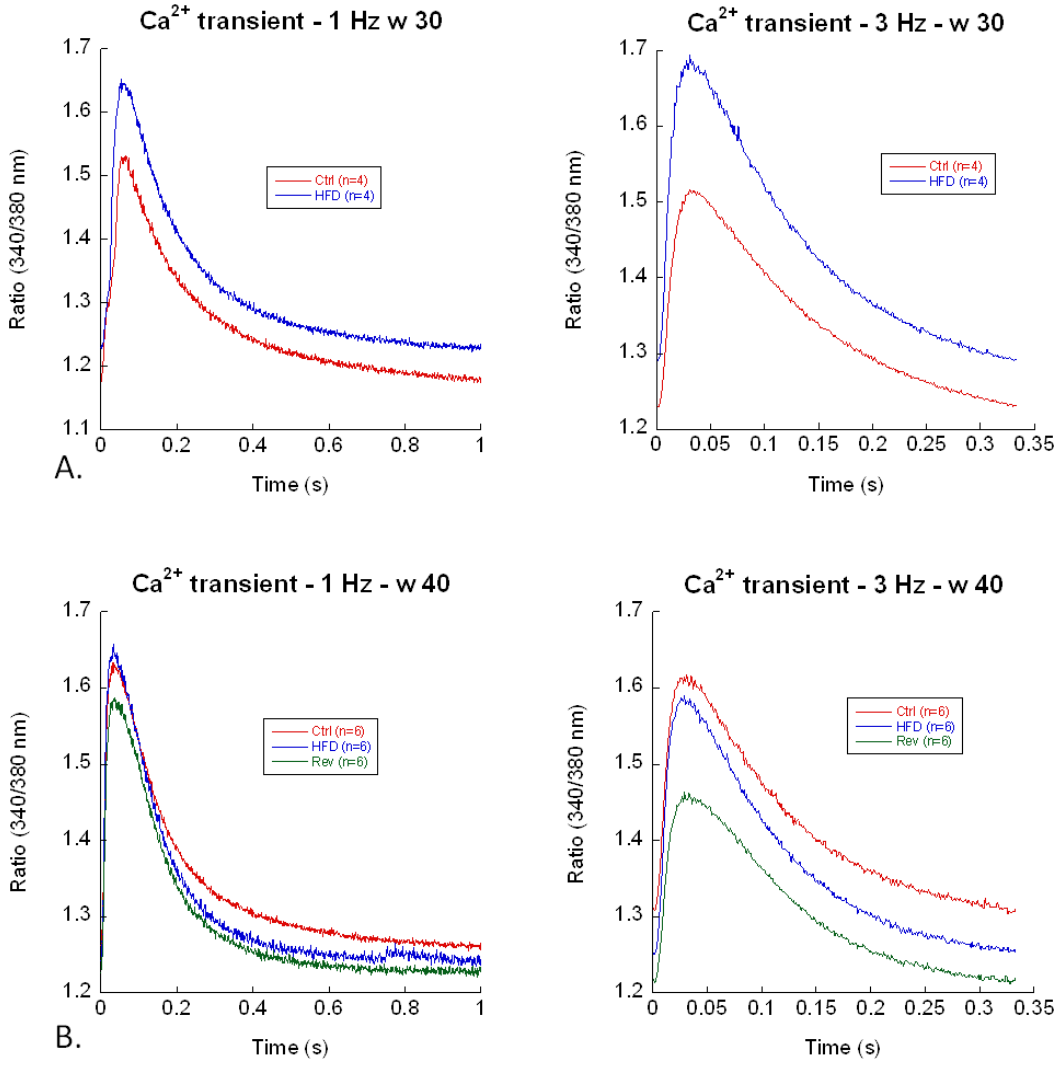



**Figure 44: Single cell $Ca^{2+}$ transient traces A:** Averaged $Ca^{2+}$ transient traces when stimulated at 1 and 3 Hz at w 30. **B:** Averaged $Ca^{2+}$ transient traces when stimulated at 1 and 3 Hz at w 40. 10 cell recordings were obtained from each animal and the data averaged for each animal representing n=1. (Ratio: Fura-2 emission ratio)

Single cell $Ca^{2+}$ transients were quantified from the 340/380 nm ratio data obtained from recordings of individual cardiomyocytes loaded with fura-2. See Figure 44 for the

averages. The parameters baseline $Ca^{2+}$ level, peak $Ca^{2+}$ amplitude, time from baseline to 50 % peak $Ca^{2+}$ amplitude, and time from max amplitude to 50 % $Ca^{2+}$ decay were assessed.

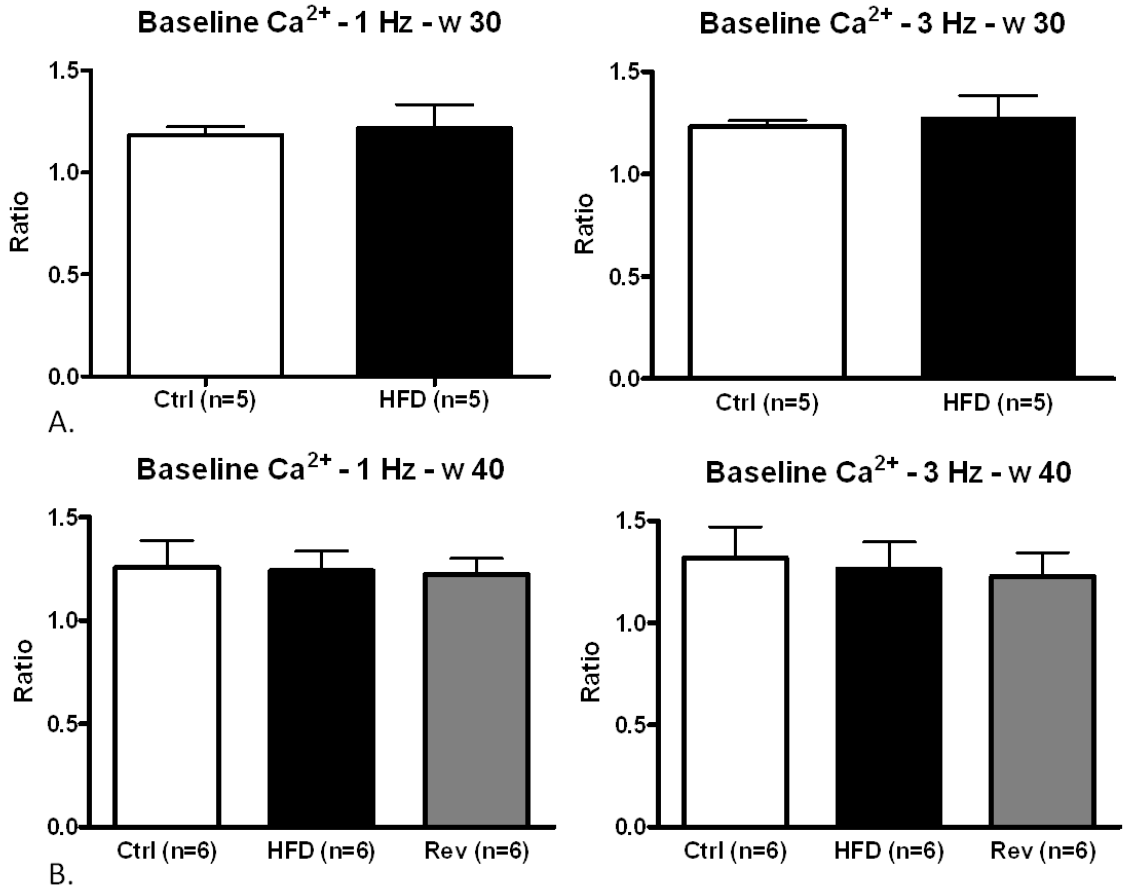



**Figure 45: Single cell baseline $Ca^{2+}$ levels A:** Average baseline $Ca^{2+}$ levels at 1 and 3 Hz stimulation at w 30. **B:** Average baseline $Ca^{2+}$ levels at 1 and 3 Hz stimulation at w 40. All error bars describe SD. (Ratio: Fura-2 340/380 nm emission ratio)

Baseline $Ca^{2+}$ levels were unchanged in cardiomyocytes isolated from HFD mice compared with control as can be seen in Figure 45. No difference was detected independently of stimulation frequency and feeding duration.

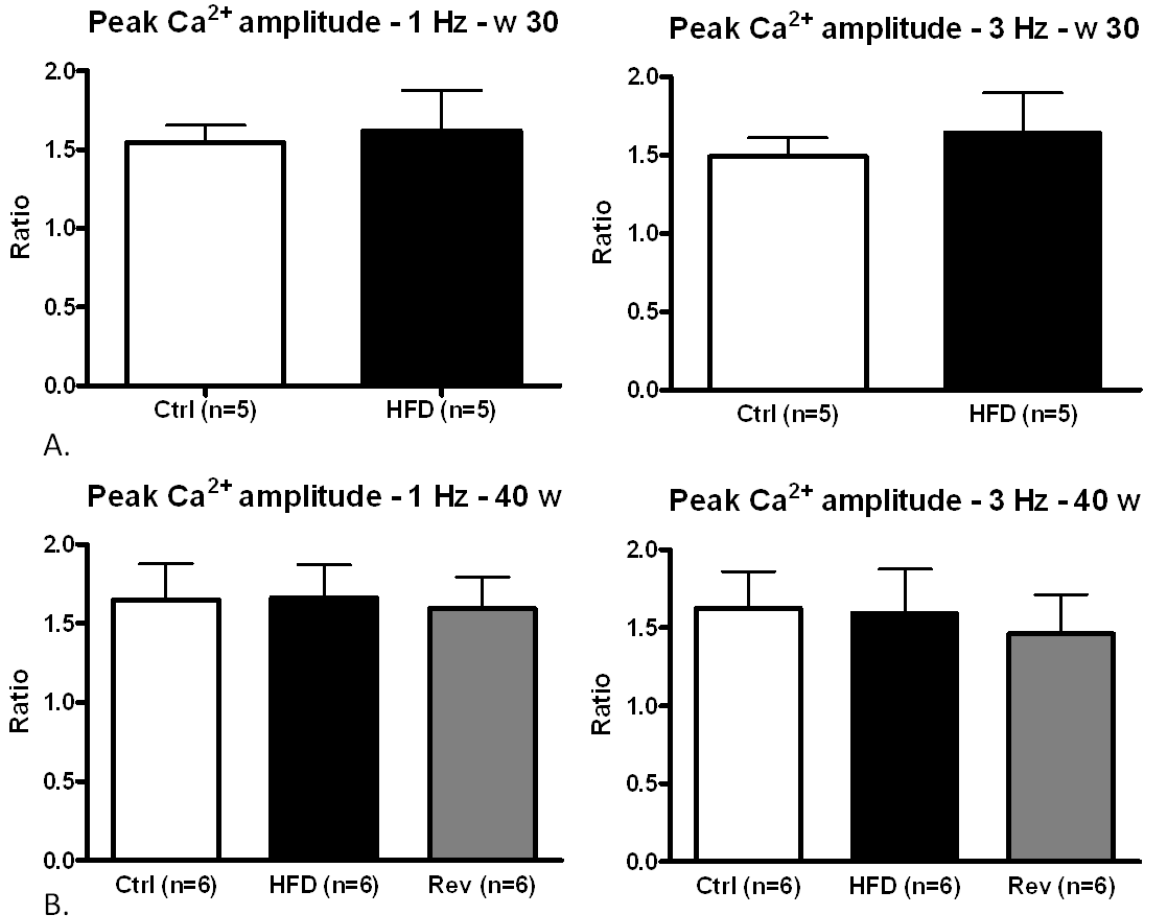



**Figure 46: Single cell maximum $Ca^{2+}$ amplitudes A:** Maximum $Ca^{2+}$ amplitude levels at 1 and 3 Hz stimulation at w 30. **B:** Maximum $Ca^{2+}$ amplitude levels at 1 and 3 Hz stimulation at 40 w. All error bars describe SD. (Ratio: Fura-2 340/380 nm emission ratio)

Maximum $Ca^{2+}$ amplitudes were unaffected by HFD as can be seen in Figure 46. No significant differences in peak amplitude were detected between control and HFD cardiomyocytes at either stimulation frequency or time point.

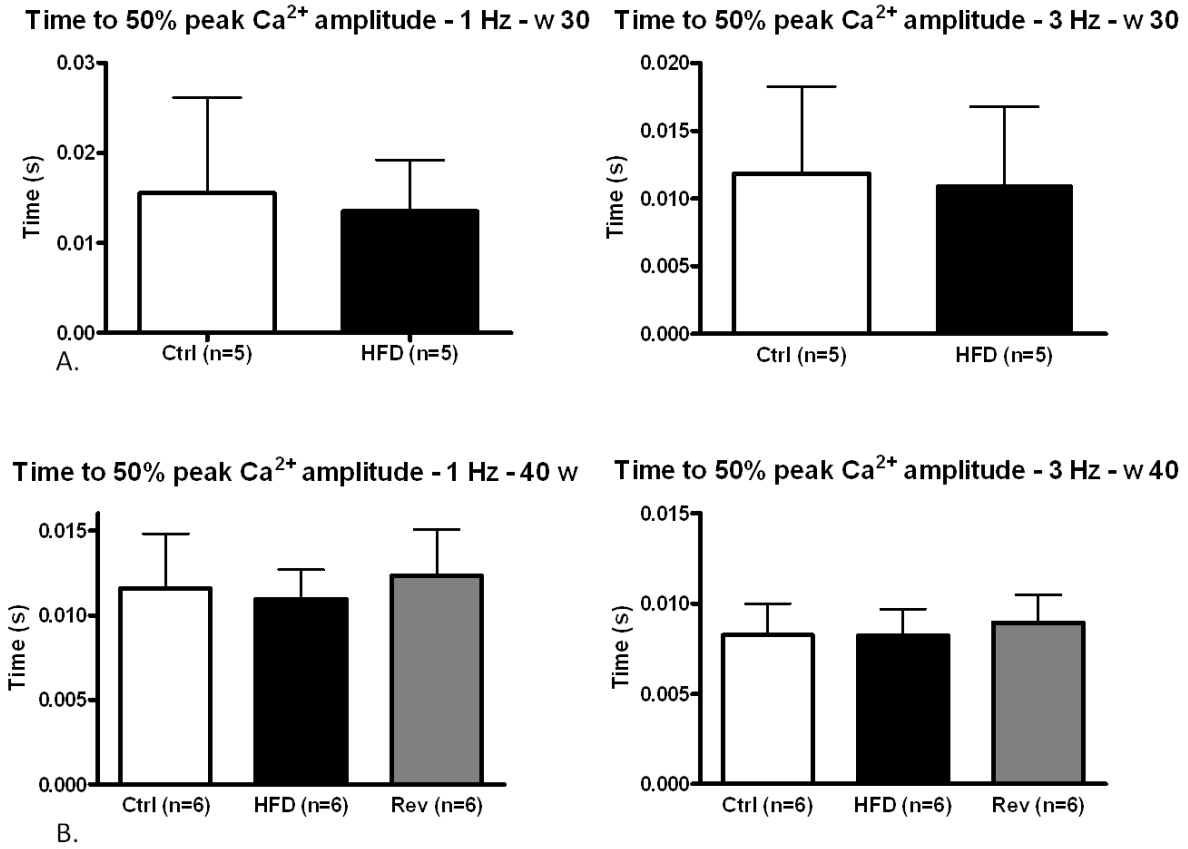



**Figure 47: Single cell $Ca^{2+}$ release rate A:** Time to half maximum $Ca^{2+}$ amplitude at 1 and 3 Hz stimulation after 30 w. **B:** Time to half maximum $Ca^{2+}$ amplitude at 1 and 3 Hz stimulation after 40 w. All error bars describe SD.

As shown in Figure 47 there were no changes detected with regards to rate of $Ca^{2+}$ rise from HFD, independently of stimulation frequency and feeding duration.

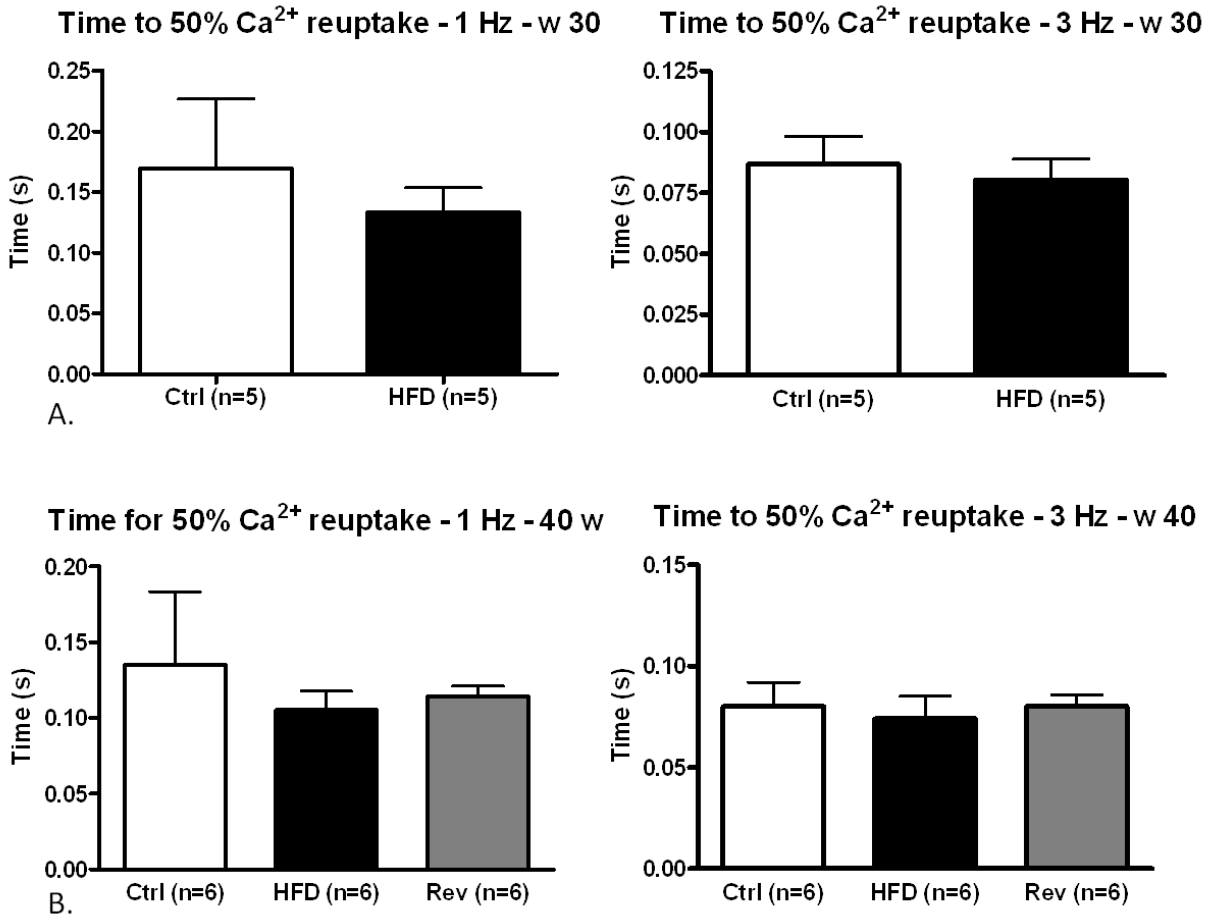



**Figure 48: Single cell $Ca^{2+}$ decay rate A:** Time to half $Ca^{2+}$ level decay at 1 and 3 Hz stimulation at w 30. **B:** Time to half $Ca^{2+}$ level decay at 1 and 3 Hz stimulation at w 40. All error bars describe SD.

There were no differences in rate of $Ca^{2+}$ decay at either stimulation frequency or time point as shown in Figure 48.

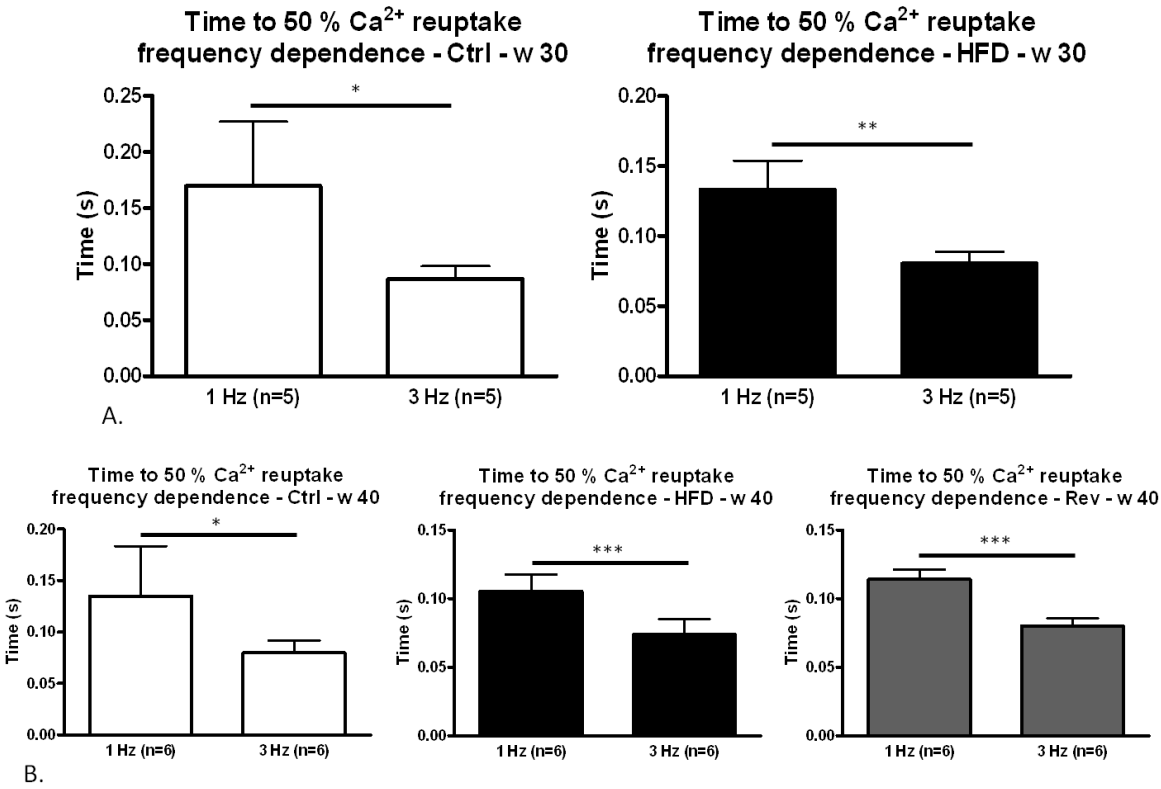



**Figure 49: The effect of stimulation frequency on single cell $Ca^{2+}$ decay rate A:** Comparison of time to 50 % $Ca^{2+}$ reuptake within groups at 1 Hz and 3 Hz at w 30. **B:** Comparison of time to 50 % $Ca^{2+}$ reuptake within groups at 1 Hz and 3 Hz at w 40. All error bars describe SD. ***=p<0.001, **=p<0.01, *=p<0.05.

To examine if the absent increase in relaxation rate upon increased stimulation frequency was due to an inability to increase $Ca^{2+}$ reuptake rate at increased stimulation frequencies, the decay rate was compared at 1 and 3 Hz within all groups. As illustrated in Figure 49 the frequency dependent increase in $Ca^{2+}$ reuptake rate was maintained in ctrl (1 Hz (n=5): 0.17 s ± 0.06 SD, 3 Hz (n=5): 0.09 ± 0.01 SD) and HFD (1 Hz (n=5): 0.13 ± 0.02 SD, 3 Hz (n=5): 0.08 ± 0.009 SD) at 30 w. At 40 w the frequency dependence was also maintained in ctrl (1 Hz (n=6): 0.14 ± 0.05 SD, 3 Hz (n=6): 0.08 s ± 0.01 SD), HFD (1Hz (n=6): 0.11 s ± 0.013 SD, 3 Hz (n=6): 0.08 s ± 0.012 SD), and reversal (1 Hz (n=6): 0.11 s ± 0.007 SD, 3 Hz (n=6): 0.08 s ± 0.006 SD) groups.

## 5.3 $Ca^{2+}$ sarcomere length relationship

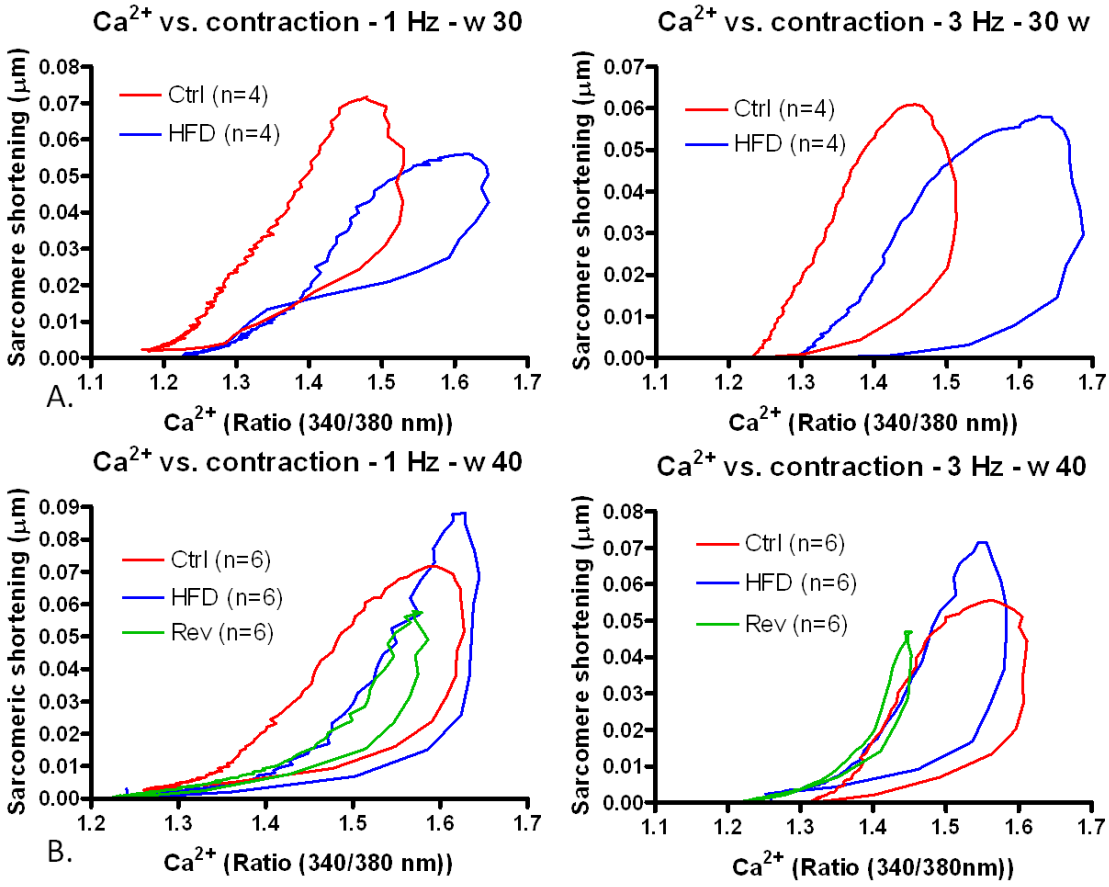



**Figure 50: Single cell $Ca^{2+}$ SL relationship A:** $Ca^{2+}$ contractility relationship at 30 w 1 and 3 Hz stimulation. **B:** $Ca^{2+}$ contractility relationship at 40 w 1 and 3 Hz stimulation.

In an attempt to decipher unloaded myofilament $Ca^{2+}$ sensitivity the fura-2 ratio and time corresponding sarcomere length was analysed with regards to sarcomere shortening. The resulting graphs are shown in Figure 50. Since $Ca^{2+}$ and contractility measurements were conducted in separate cells due to an impairment of contractility from fura-2 loading, only the individual animal $Ca^{2+}$ and SL trace averages could be plotted synchronised with reference to time, most likely contributing to an increased signal to noise ratio. Myofilament $Ca^{2+}$ sensitivity was assessed through fura-2 fluorescence ratio at 50 % relaxation (Spurgeon et al., 1992).

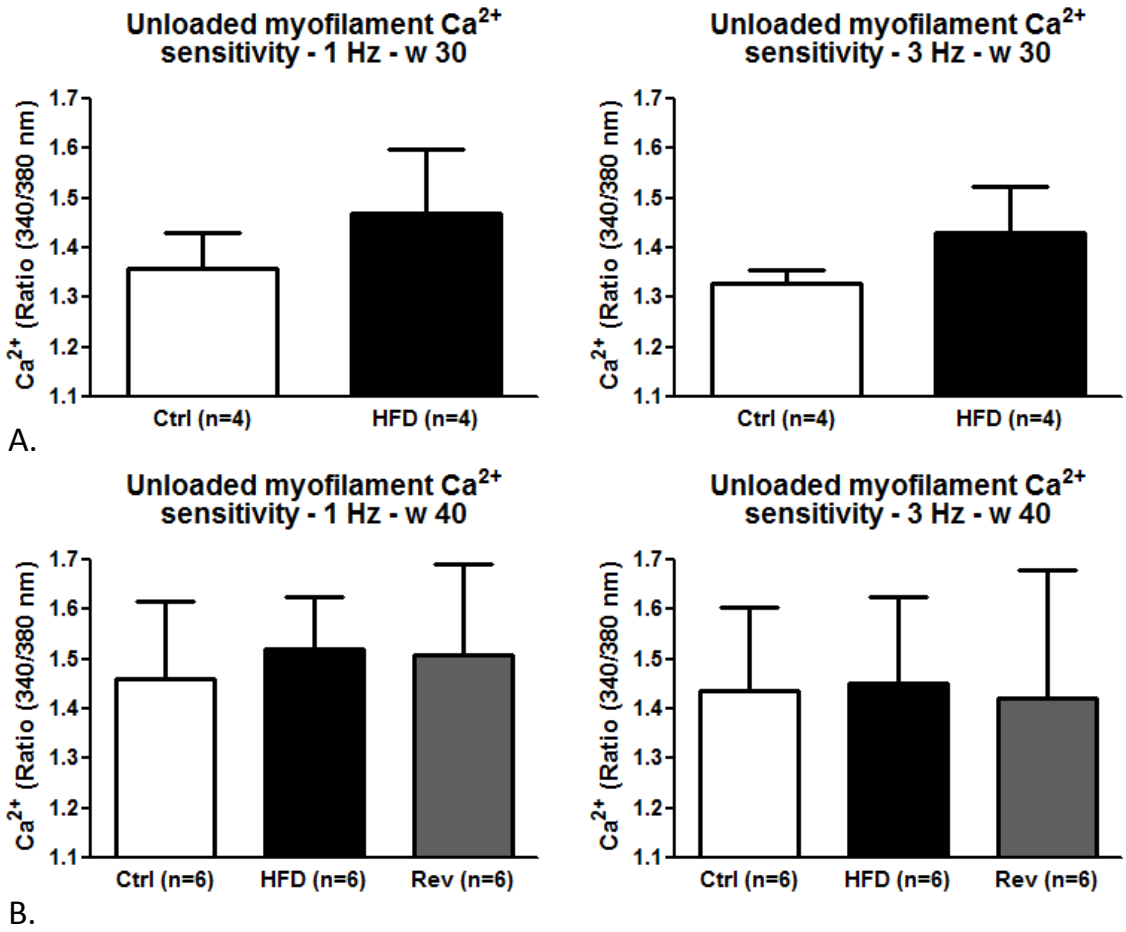



**Figure 51: Single cell based assessment of unloaded myofilament $Ca^{2+}$ sensitivity A:** Unloaded myofilament $Ca^{2+}$ sensitivity at 30 w 1 and 3 Hz stimulation. **B:** Unloaded myofilament $Ca^{2+}$ sensitivity at 40 w 1 and 3 Hz stimulation.

There were no differences to be displayed in terms of myofilament $Ca^{2+}$ sensitivity in the intact unloaded cardiomyocyte using the common trajectory of $Ca^{2+}$ and cell dynamics upon relaxation, as shown in Figure 51.

## 5.4 Discussion

Single cell studies were undertaken to allow study of contractility in the absence of confounding extracellular contribution i.e. fibrosis. A putative primary cardiomyocyte

defect in myocardial relaxation was expected to express itself through increased time to 50 % relaxation from maximum contraction amplitude to signify decreased $Ca^{2+}$ reuptake rate or increased myofilament sensitivity. Unexpectedly, but in line with a previous report from studies in a similar model (Howarth et al., 2005), an increased relaxation rate was observed after 40 w HFD feeding. This finding raises two questions:

1. What is the origin of the increased relaxation rate?
2. How does an increased relaxation rate on cardiomyocyte level correlate with diastolic impairment on a whole myocardial level?

There are two obvious processes to investigate in order to answer the first question: Intracellular $Ca^{2+}$ handling and myofilament function, the latter especially with respect to $Ca^{2+}$ sensitivity and cross-bridge cycling rate. By loading the cardiomyocytes with the $Ca^{2+}$ sensitive dye fura-2 the cytosolic $Ca^{2+}$ levels were monitored throughout contraction and relaxation without finding any differences between groups. To further test the ability of $Ca^{2+}$ handling apparatus a pair wise comparison of the ability to increase the $Ca^{2+}$ reuptake rate upon increased contraction frequency was made within each group. This was fully maintained in all groups. Even though all groups showed a qualitative increase in $Ca^{2+}$ reuptake rate upon chronotropic challenge the expected resultant increase in cardiomyocyte relaxation rate could not be statistically verified in the HFD group, but all others. This suggests that there is an alteration at the level of the myofilament. Decreased myofilament $Ca^{2+}$ sensitivity would be associated with an initiation of relaxation at a higher $[Ca^{2+}]$ and quicker $Ca^{2+}$ - cTnC dissociation. The fact that no changes could be seen in $Ca^{2+}$ baseline levels however, would suggest the absence of a significant alteration in myofilament $Ca^{2+}$ sensitivity and buffering capacity (Schober et al., 2012), even though the SR $Ca^{2+}$ load was not assessed.

In the absence of changes in $Ca^{2+}$ handling and $Ca^{2+}$ activation of the myofilament, the cross-bridge cycling rate is another factor that can affect the unloaded relaxation rate. Secondary phosphorylation of myosin RLC and cMyBP-C may be speculated to affect this process, as well as a relative increase in MHC β in relation to α. The latter has been reported in studies of diabetic effects on the myocardium (Buchanan et al., 2005; Rundell et al., 2004). However, the resultant change is expected to be one of decreased cross bridge cycling rate due to decreased ATP hydrolysis rate, thus the opposite of what is reported here.

The combined increased relaxation rate in the isolated cardiomyocytes and impaired diastolic function on whole organ level are initially counterintuitive. Since the increased LVEDP seen on a whole organ level *in vivo* is an indication of impaired compliance and there were no significantly increased relaxing dynamics (–dP/dt) at this stage it can be assumed that an increase in non compliant fibrosis outweigh the pro-diastolic changes seen on single cell level. There are, however, caveats worth to mention when it comes to extrapolating results seen in unloaded isolated cardiomyocytes to whole myocardium organ function. As seen in the introduction chapter, myocardium function is strongly dependent upon mechanical load and stretch. In the isolated cardiomyocyte system the cells do not face a mechanical load and thus work at a much shorter SL than in the whole heart. To obtain the opportunity of studying $Ca^{2+}$ handling and cardiomyocyte contraction dynamics under mechanical load, other study systems such as intact trabeculae or whole organ function assessment *ad modum* Langendorff in a $Ca^{2+}$ dye loaded heart (Schober et al., 2012), may provide more physiologically relevant information. Also, the stimulation frequencies of 1 and 3 Hz are far from the murine physiological span of ca. 400-800 beats per minute. As seen in this chapter, relations

may change upon increases in stimulation frequency, as well as degree of mechanical load, and it can be speculated that upon a further increase in stimulation frequency to physiological levels the relaxation rate in the control animals may level with that in the HFD fed.

In summary, the combined cardiomyocyte dynamics and $Ca^{2+}$ handling study suggest an effect on myofilament activation or cross bridge dynamics and less so an alteration in $Ca^{2+}$ dynamics. This argument is based on the absence of changes in the break down analysis of the cytosolic $Ca^{2+}$ transient in the presence of clear changes to cardiomyocyte dynamics and on how the chronotropic adjustment in increased $Ca^{2+}$ reuptake rate appears dissociated from a resulting increase in cardiomyocyte relaxation rate in the HFD group at 40 w as opposed to the ctrl and reversal groups. Using averaged $Ca^{2+}$ and SL traces from the same animals but recorded from a different set of cells, matched in time, no difference in myofilament $Ca^{2+}$ sensitivity could be seen. As the relaxation rate was clearly increased at w 40 in the absence of affected $Ca^{2+}$ handling this had been expected. The caveat of using $Ca^{2+}$ and SL traces recorded from separate animals may have had a large impact however, and same cell-analysis of the two parameters is probably needed to draw valid conclusions from this mode of analysis.

In the next chapter results from experiments interrogating mechanically loaded myofilament $Ca^{2+}$ sensitivity and cross bridge cycling rate are presented in an attempt to test the above reasoning in practice.

# 6 Effects from a HFD on myofilament function in C57BL6/J myocardium

## 6.1 Introduction

For the purpose of investigating myofilament $Ca^{2+}$ sensitivity and actomyosin cross bridge cycling rate cardiac trabeculae were subjected to chemical demembranation "skinning" as described in chapter 2. Due to this membrane disruption differences in cellular $Ca^{2+}$ handling between control and experimental groups were eliminated as confounding factors. Through stepwise length extensions I also investigated the compliance of the tissue during diastole, a combined measure of titin and collagen derived passive stiffness (Chung et al., 2011; Granzier and Irving, 1995). These experiments allowed investigation of whether the increased relaxation rate seen in isolated cardiomyocytes was caused by a decrease in myofilament $Ca^{2+}$ sensitivity , or by an increased cross bridge cycling rate.

## 6.2 Myofilament $Ca^{2+}$ sensitivity

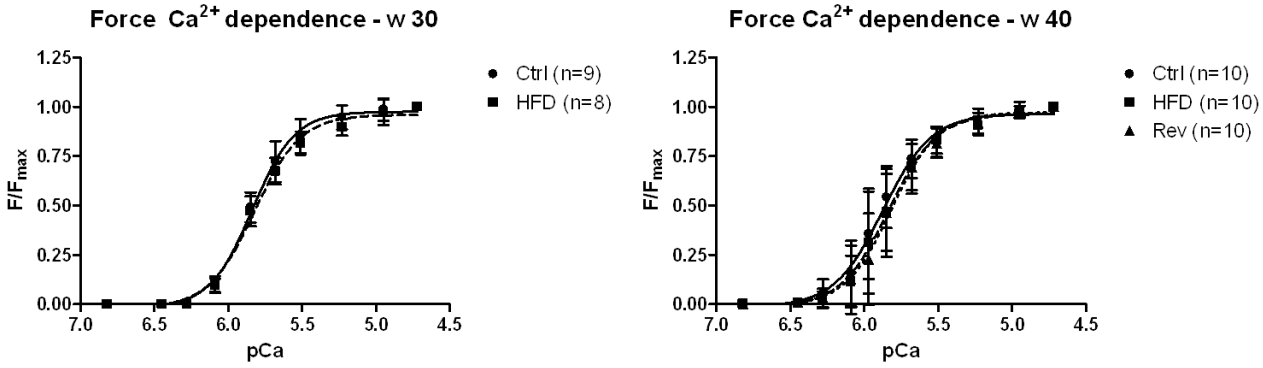



**Figure 52: $Ca^{2+}$ force relationship at 2.2 µm** Force development $Ca^{2+}$ sensitivity at w 30 and 40 w. All error bars describe SD.

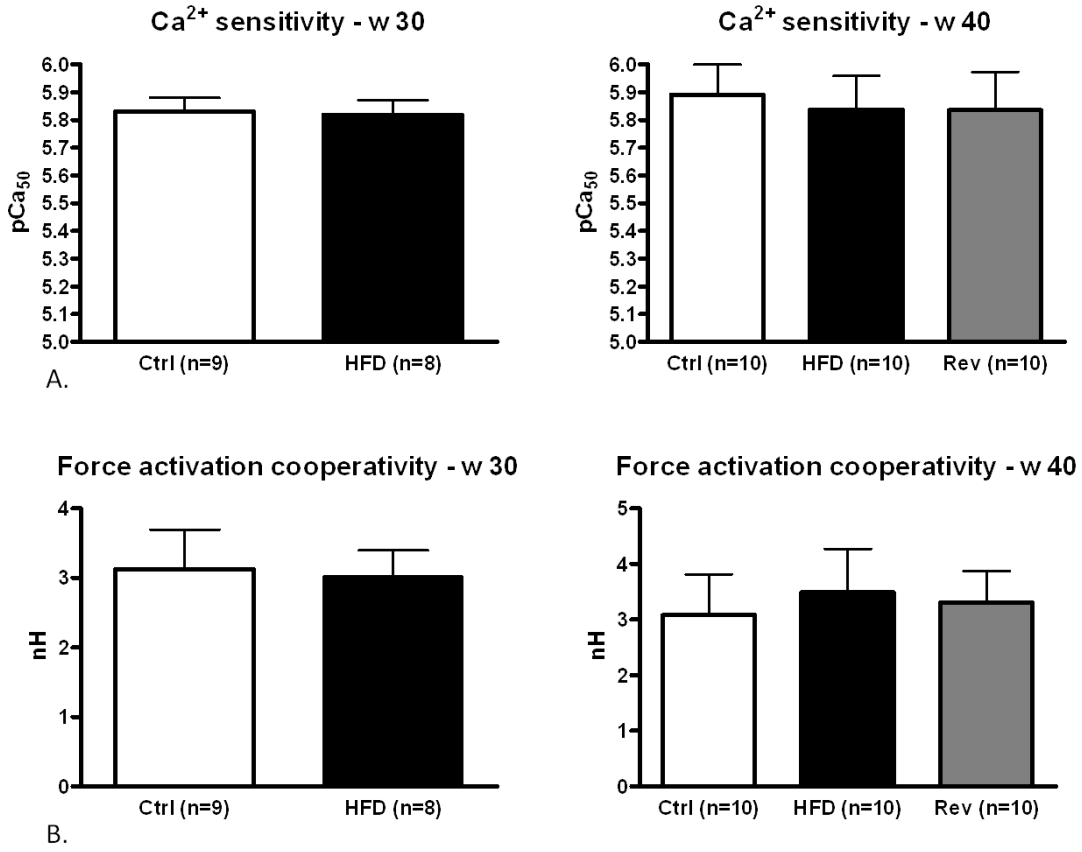



**Figure 53: Effect of HFD feeding on thin filament $Ca^{2+}$ activation A:** $Ca^{2+}$ sensitivity described by $pCa_{50}$ at w 30 and 40. **B:** Thin filament activation cooperativity at w 30 and 40. All error bars describe SD.

$Ca^{2+}$ sensitivity was assessed on the basis of isometric force output at known $[Ca^{2+}]_{free}$ in relation to maximum $Ca^{2+}$ activation, depicted in Figure 52. As can be seen in Figure 53 neither at 30 nor 40 w were there any statistically significant changes to $Ca^{2+}$ sensitivity or thin filament cooperativity.

## 6.3 Actomyosin cross bridge dynamics

As previously mentioned there are reports on increased myocardial β-MHC expression from decreased insulin signalling. Characterisation of actomyosin cross bridge function in the form of maximum tension generation and cross bridge cycling rate was undertaken to investigate possible functional effects.

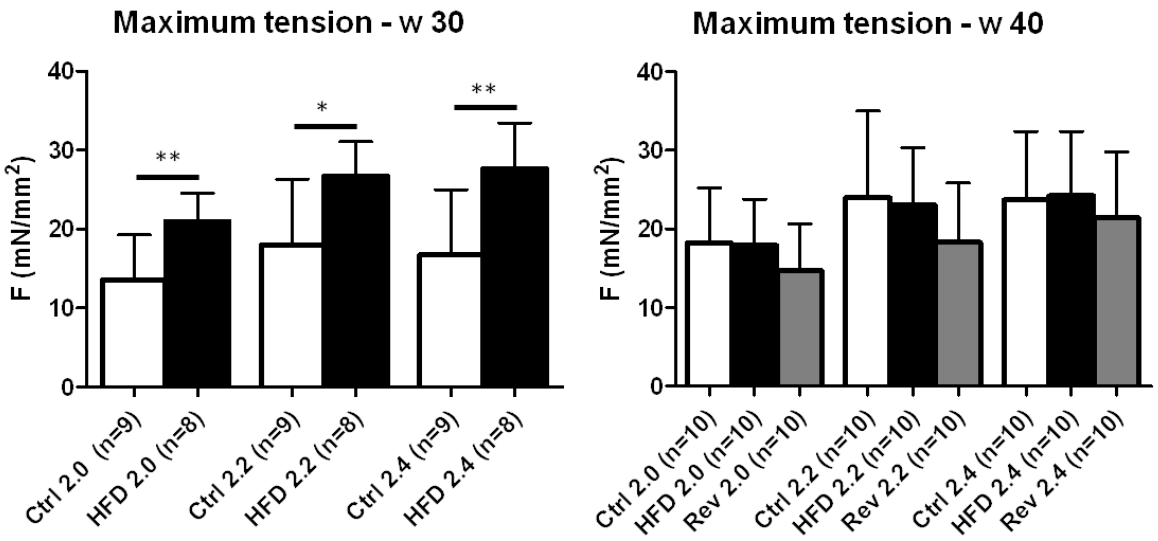



**Figure 54: Effect of HFD feeding on maximum force generation in left ventricle trabeculae** Maximum force generating capacity normalised to cross sectional area at 2.0, 2.2 and 2.4 µm SL at w 30 and 40. *=p<0.05, **=p<0.01. All error bars describe SD.

Maximum tension generation of demembranated trabeculae from LV was compared between the different experimental groups as a step to characterise actomyosin cross bridge interaction. The results are illustrated in Figure 54. At 30 w a significant increase in maximum tension generating capacity was statistically confirmed at 2.0 (Ctrl (n=9): 13.6 mN/mm$^2$ ± 5.7 SD, HFD (n=8): 21.0 mN/mm$^2$ ± 3.6 SD), 2.2 (Ctrl (n=9): 17.9 mN/mm$^2$ ± 8.4 SD, HFD (n=8): 26.7 mN/mm$^2$ ± 4.3 SD), and 2.4 µm SL (Ctrl (n=9): 16.7 mN/mm$^2$ ± 8.3 SD, HFD (n=8): 27.6 mN/mm$^2$ ± 5.8 SD). This change was not discernible at 40 w.

As a further assessment of cross bridge function, rate of tension recovery after total detachment of all cross bridges were assessed. A rapid (0.5 ms) 20 % shortening of the preparation resulting in loss of active tension, was maintained for 20 ms before an equally rapid return to $L_0$. This allowed the determination of force recovery rate after total actomyosin cross bridge interruption which is a measure of cross bridge cycling rate. There were no differences at either time points or SLs as shown in fFigure 55.

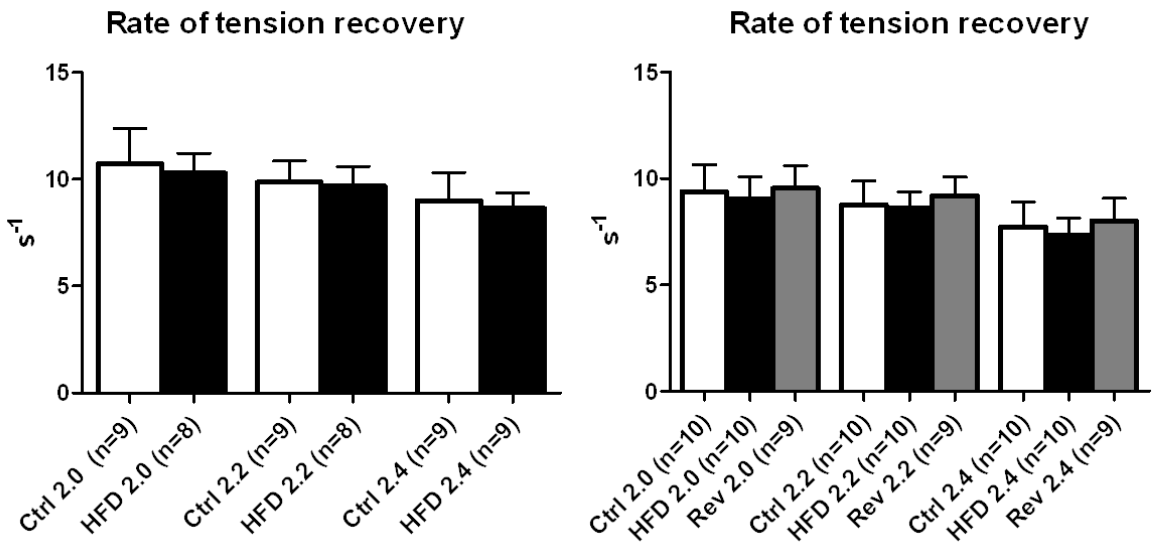



**Figure 55: Effect of HFD feeding on actomyosin cross bridge cycling rate.** Rate of tension redevelopment ($K_{tr}$) after slack at 2.0, 2.2, and 2.4 µm SL at w 30 and 40. All error bars describe SD.

### 6.3.1 **Relative myosin heavy chain isoform expression levels**

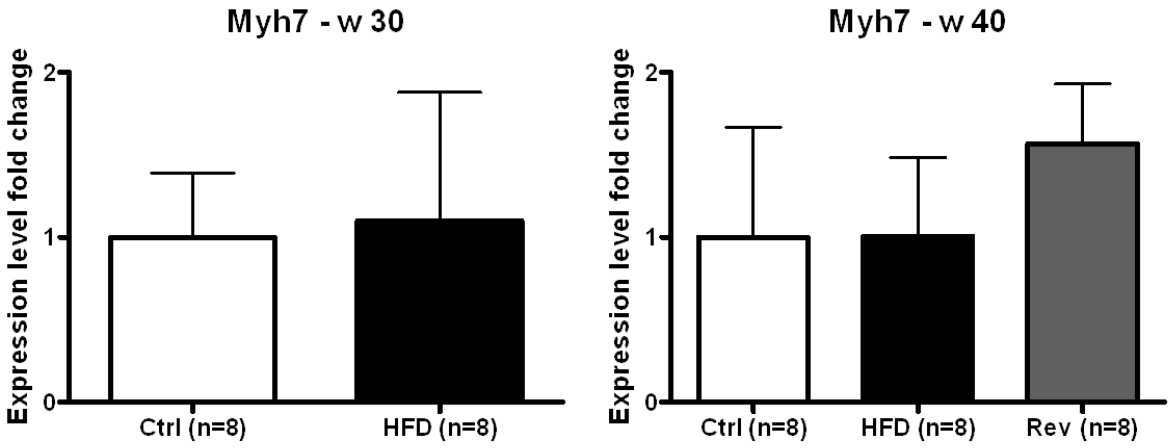



**Figure 56: Effect of HFD feeding on MYH7 expression levels** There were no differences in Myh7 mRNA levels neither at 30 nor 40 w. All error bars describe SD

As there was an increase in maximum tension generation at 30 w in the HFD group which is a known feature of increased β-MHC levels (VanBuren et al., 1995) the relative expression of the corresponding *MYH7* gene was examined on mRNA level. There were no differences in β-MHC expression on mRNA level between groups, neither at 30 nor 40 weeks as shown in Figure 56.

## 6.4 Passive myofilament dynamics

As diastolic impairment was seen in the form of increased LVEDP at w 30 passive tension levels were assessed in demembranated LV trabeculae in relation to slack length at 2.0, 2.2, 2.4 and 2.6 μm at pCa 9.0 and 20 mM BDM for actomyosin inhibition. The latter SL was used as a maximum tension normalisation point. At 30 w there was a significant increase in absolute passive stiffness in the HFD group compared to controls at both 2.2 (Ctrl (n=7): 1.53 $mN/mm^2$ ± 0.31 SEM, HFD (n=5): 3.33 $mN/mm^2$ ± 0.52 SEM) and 2.4 μm sarcomere length (Ctrl (n=7): 5.23 $mN/mm^2$ ± 0.87 SEM, HFD (n=5): 17.2 $mN/mm^2$ ± 3.6 SEM). At 40 w this difference was no longer present. The data is illustrated in Figure 57 below. There were no differences in the tension development rate as a function of SL at either time point of investigation.

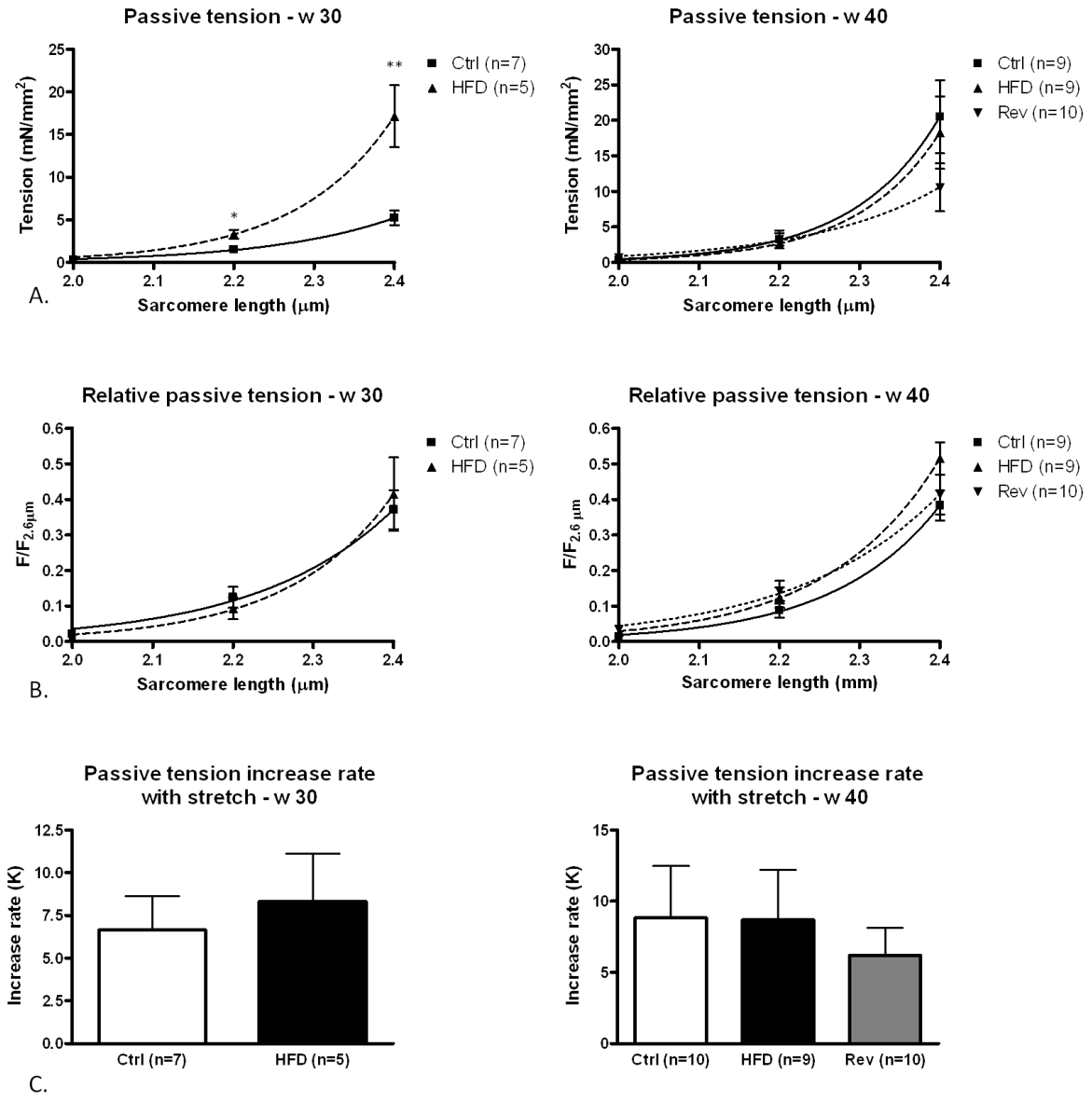



**Figure 57: Effect of HFD on passive tension in demembranated LV cardiac trabeculae upon stretch A:** Absolute tension progression upon passive lengthening at w 30 and 40. **B:** Relative tension progression upon passive lengthening at w 30 and 40. **C:** Passive tension increase rate upon passive lengthening at w 30 and 40. K=exponential growth constant for tension as function of SL. All error bars describe SEM.

### 6.4.1 **Titin isoform expression levels**

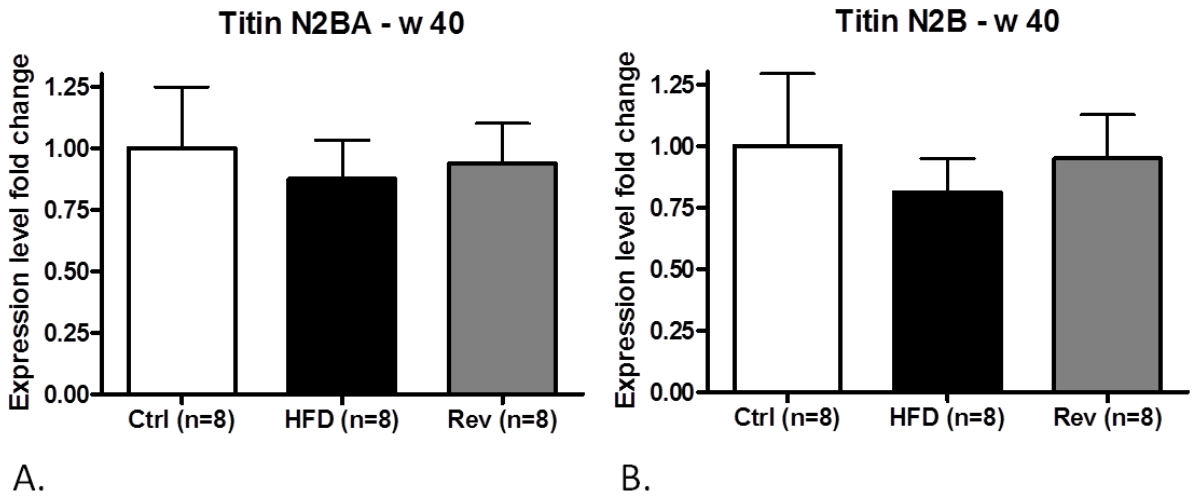



**Figure 58: Effect of HFD on relative expression levels of titin isoforms at w 40 looking at mRNA levels. A:** Relative expression of titin N2BA at w 40. **B:** Relative expression of titin N2B at w 40.

To investigate if differences in titin isoform expression could play a role in the altered diastolic compliance, titin N2BA and titin N2B expression levels were investigated at w 40. There were no differences in the expression level from HFD feeding, see Figure 58.

## 6.5 Determination of contractile protein phosphorylation levels

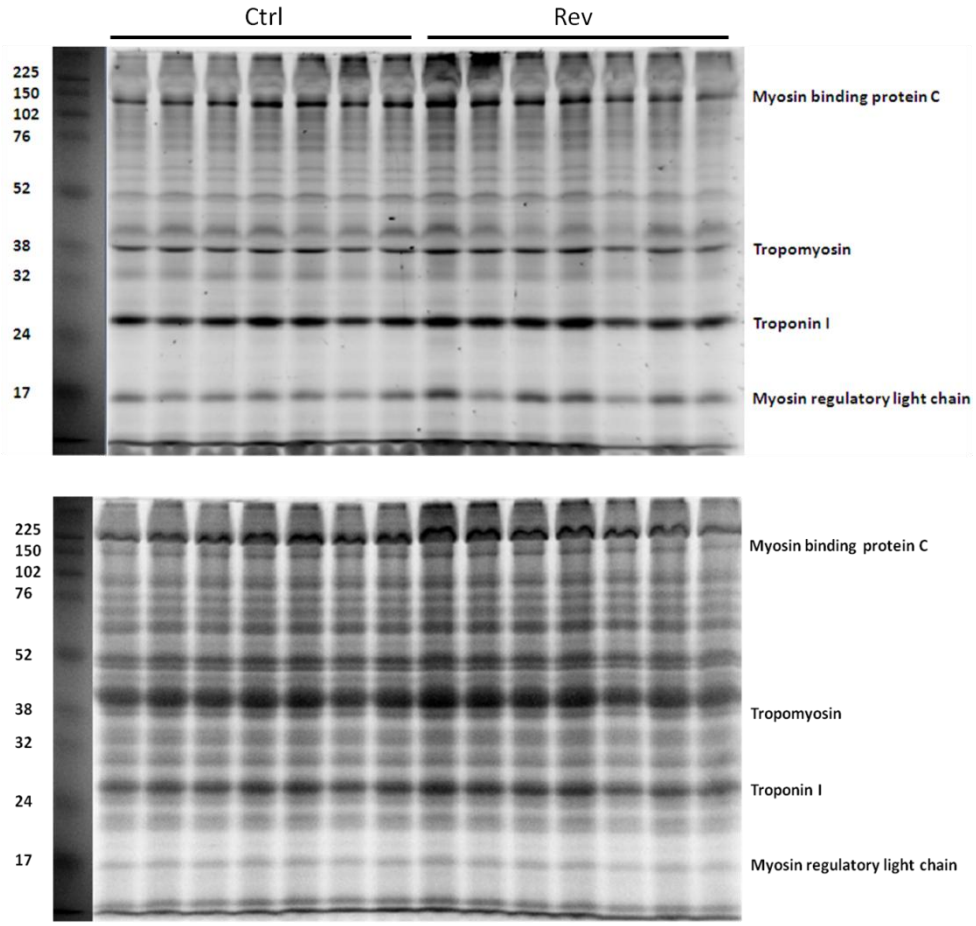



**Figure 59: ProQ Diamond total phosphorylation staining in relation to total protein as assessed by SyproRuby A:** Representative ProQ Diamond stain of whole tissue extracts from control and reversal animals at w 40. **B:** Corresponding total protein stain by SyproRuby®.

Total phosphorylation levels in whole tissue extracts were assessed by staining with ProQ Diamond. For a typical stained gel see Figure 59. Known abundant phosphoproteins were identified through the aid of molecular weight marker and quantified using densitometry in relation to total protein levels as assessed through SyproRuby stain.

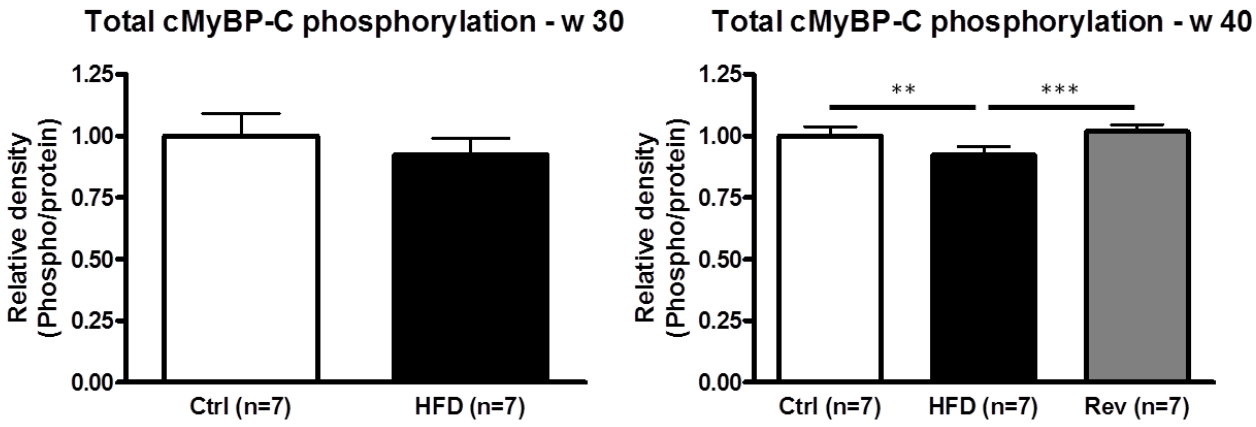



**Figure 60: Effect of HFD feeding on total phosphorylation cMyBP-C levels in relation to total protein as assessed by ProQ diamond and SyproRuby staining** Total phosphorylation levels compared with total protein levels of cMyBP-C at w 30 and 40 as assessed by densitometry. All error bars describe SD. **=p<0.01, ***=p<0.001.

Densitometric analysis of the known phosphoproteins cMyBP-C, TM/cTnT, cTnI, and myosin RLC disclosed a reduction in total phosphorylation levels of cMyBP-C in relation to total protein levels in the HFD group at w 40 (ctrl (n=7): 1.0 ± 0.04 SD, HFD (n=7): 0.92 ± 0.03 SD, Rev (n=7): 1.02 ± 0.03 SD), see Figure 60. Phosphorylation levels of other investigated phosphoproteins were not found significantly altered.

cTnI was probed for phosphorylation at S23/24 through immunoblotting. The results are presented in Figure 61. There was no significant increase in phosphorylation levels at w 30 nor w 40 in the HFD group. At w 40 upon 10 w diet reversal the level of phosphorylation was significantly decreased from that of the HFD group (Ctrl (n=7): 1.0 ± 0.08 SD, HFD (n=6): 1.10 ± 0.11 SD, Rev (n=6): 0.92 ± 0.09 SD).

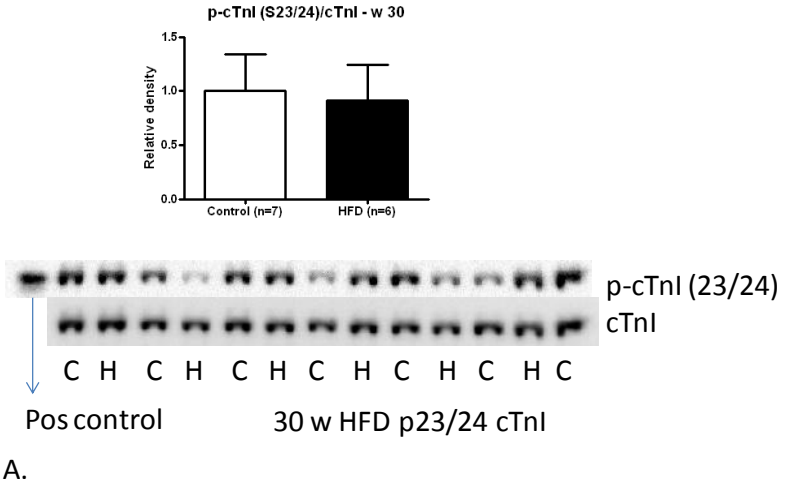
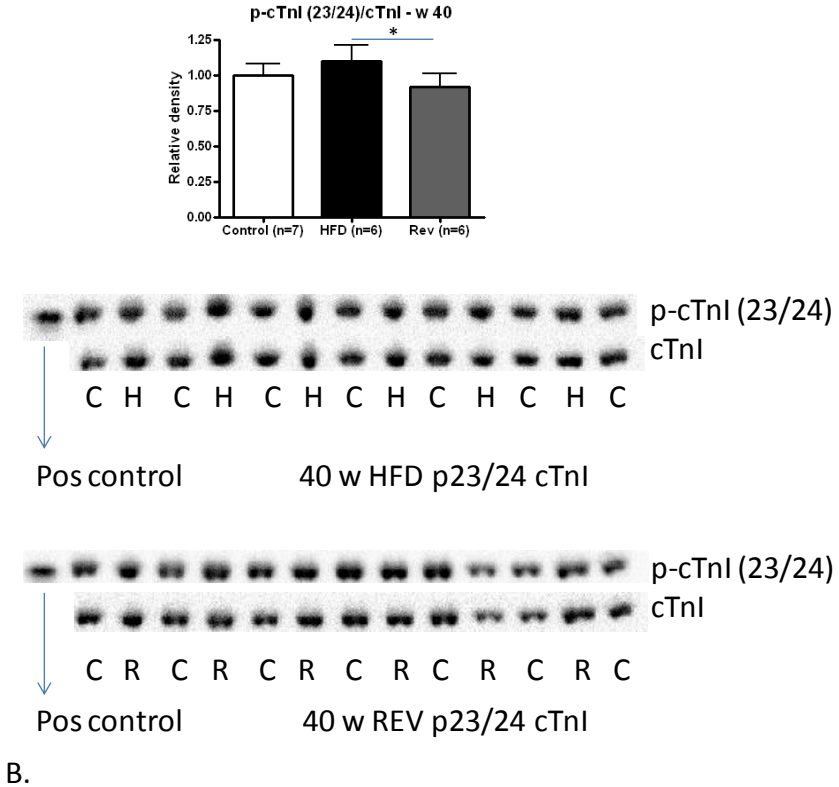



**Figure 61: Effect of HFD feeding on cTnI phosphorylation at S23/24 assessed by immunoblotting A**: There were no significant differences in level of cTnI phosphorylation at S23/24 at 30 w. All error bars describe SD.




**B:** At 40 w the level of S23/24 phosphorylation was not increased in the HFD contra control. The reversal group showed a decreased level of phosphorylation in relation to the HFD group. *=p<0.05. All error bars describe SD.

## 6.6 Discussion

The experiments carried out in this chapter were undertaken to investigate the hypothesis that the increased relaxation rate seen in the more complex single cell

system was caused by either a decrease in myofilament $Ca^{2+}$ sensitivity, or an increased cross bridge cycling rate. The demembranated muscle tissue method carries the advantage of being performed under mechanical load and at set SLs within the physiological working span. Due to time constraints pCa-tension relationships were only assessed at 2.2 μm. The method also carries disadvantages. One is the necessary operational temperature of 10 °C to avoid the development of rigor tension in the core of the preparation. The high degree of α-MHC compared to other larger mammals (Malmqvist et al., 2004) makes the murine myocardium prone to development of rigor tension which will skew the pCa-tension relationship, maximum thin filament cooperativity (nH), and also affect cross bridge assessments. Biphasic tension accelerations during $Ca^{2+}$ activations were interpreted as partial rigor development; such activations were not used for analysis.

The further degree of tissue manipulation through chemical skinning and possible disruption of the cellular equilibrium compared to the *in vivo* situation may cause some alterations to phosphorylation and other secondary protein modification in comparison to that seen in intact cells. It should also be emphasized how the single cell experiments and demembranised trabeculae experiments are carried out at different SLs and different temperatures. Changes in $Ca^{2+}$ sensitivity may be disclosed when the cells are allowed to work in an unloaded state and at 37 °C, as in single cell experiments, instead of 10 °C.

Under the experimental conditions used for the demembranised trabeculae, the chain of molecular events from $Ca^{2+}$ - cTnC association to force output appears to be unaffected by HFD feeding as there were no changes observed in $Ca^{2+}$ sensitivity at either time point. Tropomyosin has previously been suggested as a target of non-specific oxidative

stress as judged by dihydroethidine staining and non-reducing tropomyosin western blots after heart failure induction in rabbits and myocardial infarction in mice causing increased dimer formation (Avner et al., 2012; Heusch et al., 2010). However, no difference was seen in cooperativity of force activation along the thin filament. Thus, there were no indications of gross alterations to tropomyosin function. The increase in NADPH-stimulated ROS production may however be localised to a particular subcellular compartment or to a degree incompatible with reproducing the changes seen in these different models of disease.

Absolute maximum force was increased in the HFD group at w 30, a difference not seen by w 40. An increase in force generation could potentially be ascribed to a MHC isoform switch; a relative increase in β-MHC would generate increased force and lower energy expenditure and thus decreased tension cost (Hoyer et al., 2007), even though the inter-isoform functional differences in terms of isometric force have been suggested to be absent in smaller rodents (Malmqvist et al., 2004). Due to the slower ATPase hydrolysis rate of β-MHC in the cross bridge cycle this switch is accompanied by a decrease in cross-bridge cycling rate. Cross bridge cycling rate was assessed through slack and re-stretch followed by the establishment of the rate of tension regeneration constant ($k_{tr}$). This was found unaltered throughout speaking against alterations MHC isoform switch or that cross bridge cycling rate was a cause for the increased relaxation rate seen in the isolated cardiomyocytes. Quantitative PCR was performed to assess mRNA levels of the β-MHC encoding gene *MYH7*. Expression levels suggested no differences in β-MHC between groups at both time points.

To investigate the possibility that the elevated LVEDP seen in *in vivo* haemodynamic assessments at w 30 was due to passive elements such as titin and fibrosis, skinned

preparations were evaluated in terms of passive compliance in the range from slack to 2.6 μm. Titin has been suggested to play a larger role in passive tension modulation at lower SLs whereas collagen appears to have a larger impact in the higher range (Granzier and Irving, 1995). At 30 w there was a difference in absolute passive tension levels at both 2.2 and 2.4 μm SL tentatively supporting a higher degree of stiffness from either changes in titin phosphorylation, titin isoform switch, or more extensive fibrosis to be a cause of the changes seen on whole organ level. The trend towards increased LVEDP compared to control also included the reversal group at w 40 which in skinned tissue assessments rather showed a strong trend towards decreased passive tension and increased compliance upon stretch. At 40 w this LVEDP rise could, however, no longer be statistically verified. Looking at the relative compliance of the tissues by normalising the force at the different SLs to that at 2.6 μm in individual trabeculae there were no differences to be seen. This was quantified by establishing the exponential growth constant. Focusing on absolute values there appears to have been a dramatic rise in passive stiffness over the last 10 weeks of the study in the control group whereas the reversal group showed a trend towards decreased passive tension in comparison with the control.

The absolute tension measurements are strongly dependent on accurate cross section and SL measurements. Throughout this study, the preparations' cross sectional diameters were measured at three points along the preparation. During dissection, care was taken to produce as symmetrical and uniform a preparation as possible. For consistency the cross sectional area was always approximated to a circular cross area. The actual diameter was measured with a 16.5 μm maximum resolution graticule in the eyepieces which can be considered as low in comparison with fibres of ca. 100 μm

diameter. Thus, the potential for errors in measurements were considerable. Such errors would also be amplified by the square during calculation of cross sectional area. Normalised data simply looking at the progression rate of tension increase suggest that there is no difference in titin nor fibrosis derived passive tension between the groups and at either time points. Although this analysis approach protects against errors in cross sectional area assumptions it is still dependent on correct SL readings. This was however a consistently obtainable measure. Blinding during data acquisition and analysis should protect against any group biases and statistical analysis still support an increase in absolute passive stiffness at 30 w which is obliterated by 40 w. According to total collagen analysis at the 30 and 40 w time points the opposite results would have been expected and one might suggest that the difference seen in this analysis may reflect an increase in collagen still awaiting assembly into force transducing collagen fibres.

Interestingly LVEDP elevation could only be statistically verified through *in vivo* haemodynamics at w 30 even though a trend was seen at w 40. This thus adds weight to the finding of increased absolute passive tension from HFD upon stretch in demembranated samples.

Titin N2BA and N2B isoforms expression levels were investigated at w 40 without seeing any differences which adds little to believe that titin isoform shifts were of importance in the disease phenotype.

Altered phosphorylation levels of cMyBP-C and myosin RLC have been proposed to affect cross bridge dynamics and force generation (Colson et al., 2010; Colson et al., 2012; Scruggs and Solaro, 2011). Densitometric analysis of cMyBP-C in ProQ Diamond stained gels revealed a decreased level of total phosphorylation of cMyBP-C. Although at w 40 the phosphorylation decrease was significant, it was not at w 30 when the

significantly increased force was measured. Thus functional impact of this small but significant chance in cMyBP-C phosphorylation is hard to interpret conclusively. There was a trend towards an increase in cTnI S23/24 phosphorylation levels in relation to total cTnI protein at w 40 and upon reversal onto a normal diet the increase was obliterated. This is a modification well characterised to decrease myofilament $Ca^{2+}$ sensitivity (Layland et al., 2005).

With clear changes to cardiomyocyte dynamics in form of increased relaxation rate and the absence of alterations in $Ca^{2+}$ handling seen in this study and other's (Howarth et al., 2005) changes were expected to be found looking at isolated myofilament function. The functional results presented here, however, do not clearly explain the single cell dynamics finding from the aspect of the myofilament even though trends towards significant increases in cTnI S23/24 phosphorylation level at w 40 were noted. A statistically significant decrease in cTnI S23/24 phosphorylation upon weight loss support this modification to be one of significance in relation to the functional changes described on single cell level.

# 7 Effects on NADPH oxidase 2 (NOX2) over expression on myofilament dynamics

## 7.1 Introduction

As there were functional indications of increased NOX activity in the HFD induced myocardium, the effects of cardiac restricted over expressed NOX2 on myofilament were examined using a murine model available in house. The mouse is heterozygote transgenic with a single inserted copy of the NOX2 gene inserted under control of the MYLC2 promoter. Snap frozen whole hearts from control and transgenic age matched animals were made available by collaborators but no fresh tissues were available for $Ca^{2+}$ transient recordings and unloaded cell dynamics. There were no available data on *in vivo* or *ex vivo* whole organ performance in these mice.

ATII has been suggested to play an important role in the slow force response through modulation of the intracellular $Ca^{2+}$ transient via the $Na^{+}/Ca^{2+}$ exchanger. Through initial ATII and ET-1 release mitochondrial sources of ROS are activated and stipulated to stimulate redox sensitive kinases activating the $Na^{+}/H^{+}$ exchanger increasing intracellular $[Na^{+}]$ activating the $Na^{+}/H^{+}$ -exchanger and increasing intracellular $Na^{+}$ driving a $Ca^{2+}$ influx through the NCX (Cingolani et al., 2012). ATII is however also a potent activator of NOX2 derived $O_2^{-}$ production and as seen from mechanical stretch of isolated intact cardiomyocytes NOX2-derived $O_2^{-}$ bursts may directly sensitize the RyR to $Ca^{2+}$ (Prosser et al., 2011). Judging by preliminary results presented herein, a parallel functional effect on the myofilament from NOX2 activation may also take place.

## 7.2 Verification of the model

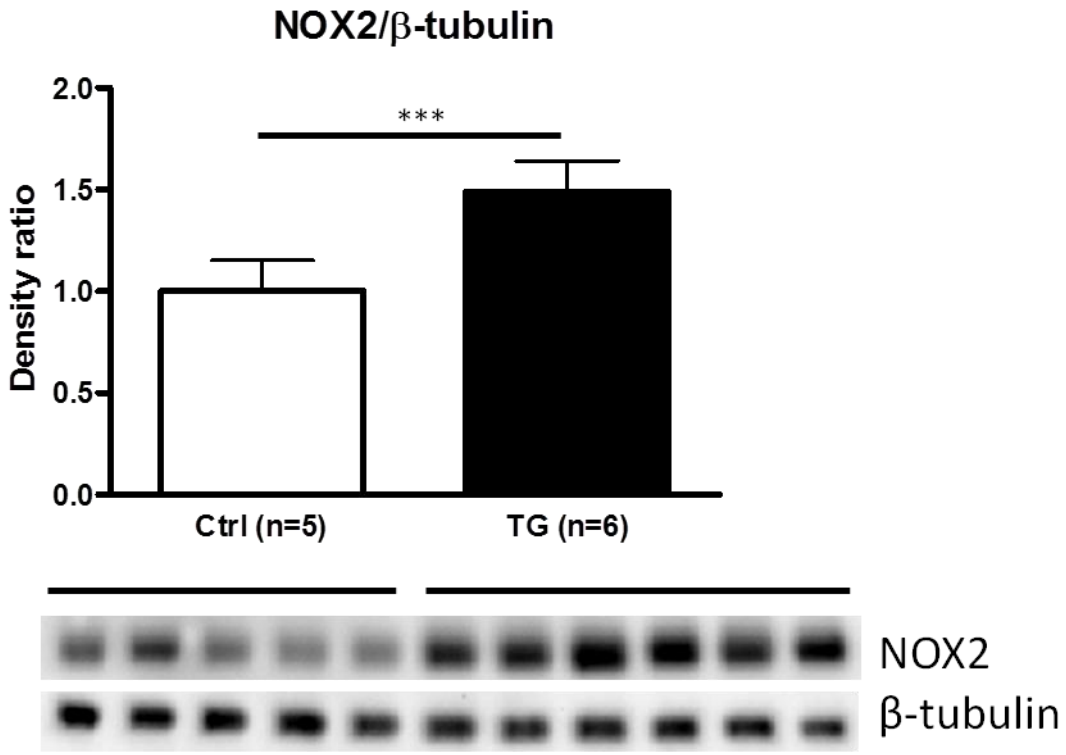



**Figure 62: Confirmation of NOX2 protein overexpression in ventricular myocardium**. Immunoblotting was used to assess total NOX2 protein levels in myocardium from transgenic mice in relation to controls. Expression levels were normalised to β-tubulin. ***=p<0.001. All error bars describe SD. (TG=transgenic)

Protein expression and functional verification of the model was carried out before further experiments. Immunoblotting was used to compare the levels of cardiac NOX2 in control and transgenic mice. Results are shown in Figure 62. A statistically significant ~49 % increase was seen in the transgenic hearts in relation to controls (Ctrl (n=5): 1.0 ± 0.15 SD, NOX2 TG (n=6): 1.49 ± 0.15 SD). The two lines were compared functionally through assessment of $O_2^-$ production rate. The results of this investigation is shown in Figure 63. Transgenic hearts showed increased rates of both baseline (Ctrl (n=6): 180 RLU/s / 500 µg protein ± 25 SD, NOX2 TG (n=6): 280 RLU/s / 500 µg protein ± 60 SD) and apocynin inhibited $O_2^-$ production rate (Ctrl (n=6): -1 RLU/s / 500 µg protein ± 3 SD, NOX2 TG (n=6): 53 RLU/s / 500 µg protein ± 21 SD) compared to control. It should also be mentioned that after inhibition of NOX using apocynin the production rate was still

elevated (Ctrl (n=6): 180 RLU/s / 500 µg protein ± 10 SD, NOX2 TG (n=6): 228 RLU/s / 500 µg protein ± 19 SD) suggesting that the concentration of apocynin was insufficient for complete inhibition of NOX2, or that other sources of $O_2^-$ generation was upregulated along with NOX.

The immunoblotting for NOX2 and $O_2^-$ measurements in this chapter were carried out by Dr Radu Tanacli.

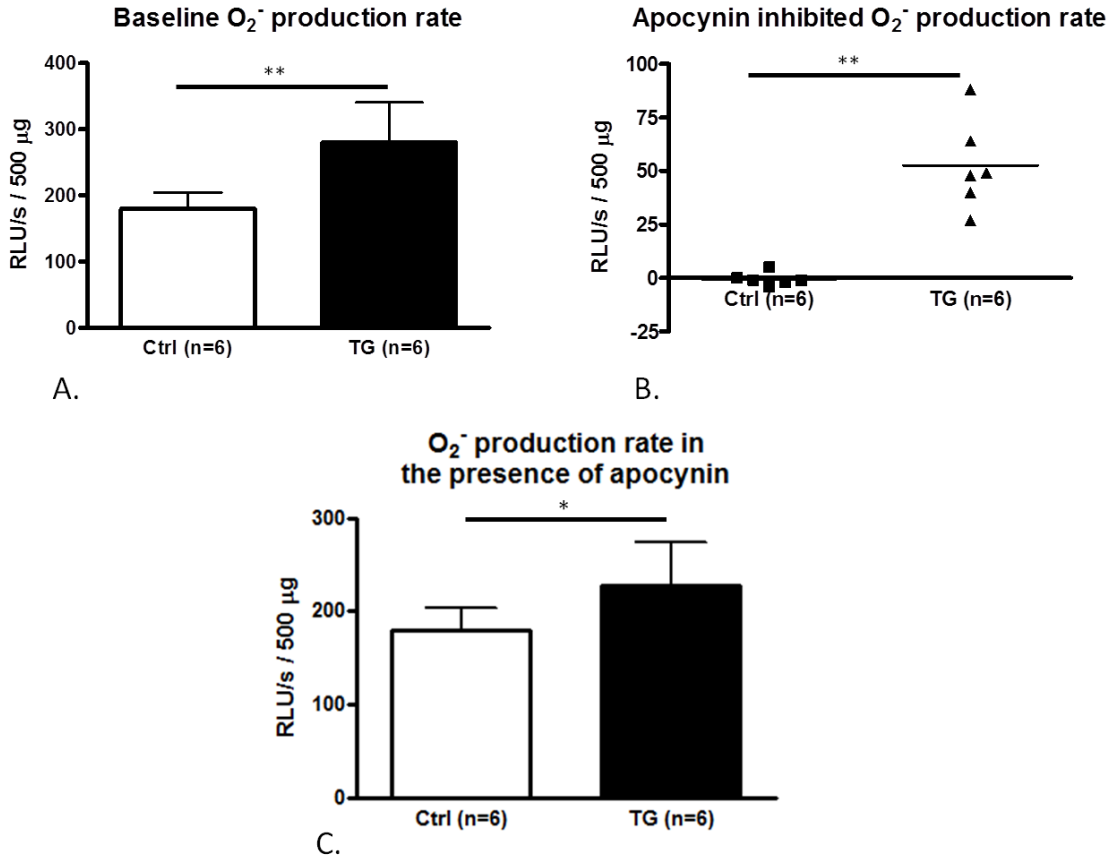



**Figure 63: Functional confirmation of NOX derived overproduction of $O_2^-$ from NOX2 over expression A:** Confirmed increased $O_2^-$ generation rate at baseline**. B:** NOX as a source of increased baseline $O_2^-$ production was verified through apocynin inhibition. **C:** After apocynin the rate of $O_2^-$ production was still elevated in the NOX2 TG animals. *=p<0.05, **=p<0.01. All error bars describe SD. (TG=transgenic)

## 7.3 Morphometric data

NOX2 has been proposed to contribute to the development of cardiac hypertrophy upon ATII signalling (Zhang et al., 2013). The presence of cardiac hypertrophy was assessed after sacrificing the animal and weighing the heart, in relation to animal size, represented by TL, see Figure 64.

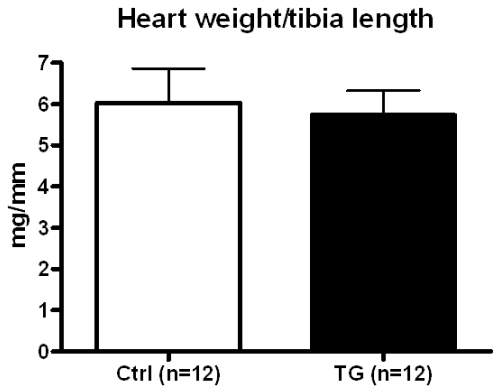



**Figure 64: Assessment of cardiac hypertrophy effect from NOX2 overexpression** Cardiac hypertrophy was assessed as heart weight in relation to tibia length. All error bars describe SD. (TG=transgenic)

There were no signs of overt cardiac hypertrophy as assessed by individual heart weight in relation to TL comparing control and transgenic animals.

## 7.4 Myofilament functional assessment

To test the hypothesis that NOX2 may have an effect on myofilament activation dynamics, investigations into thin and thick filament function was carried out.

### 7.4.1 **Thin filament function**

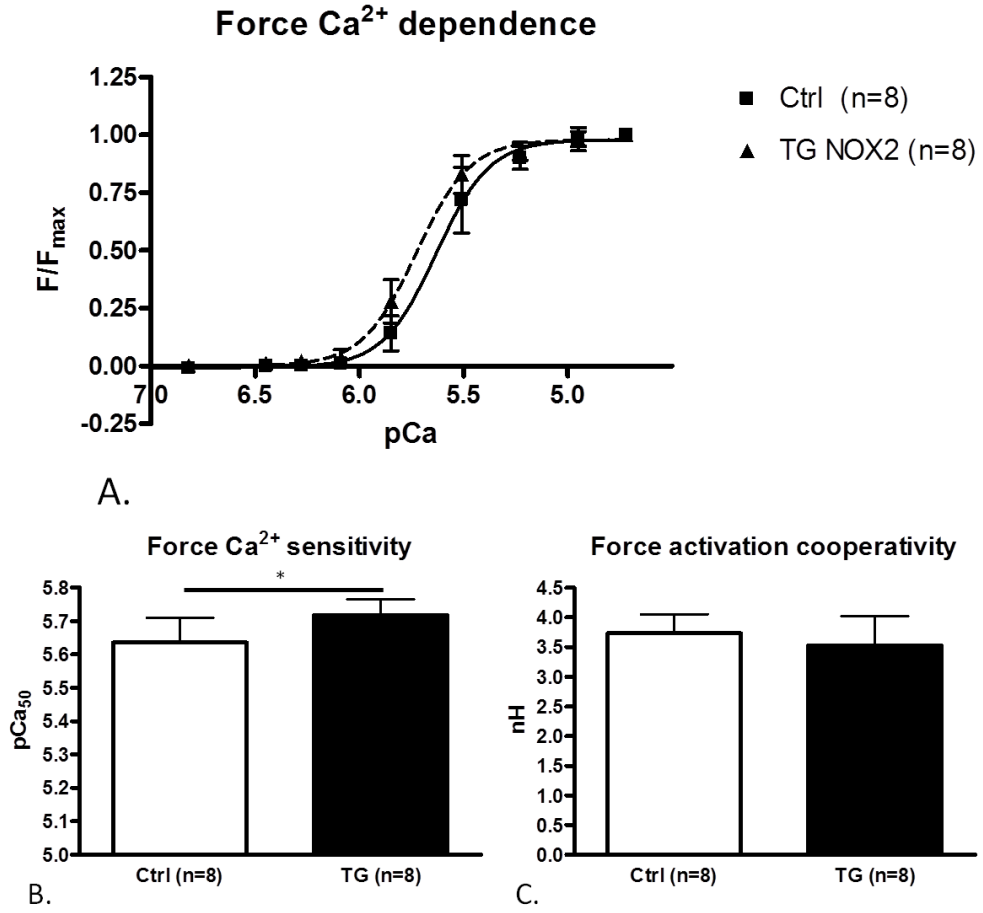



**Figure 65: Assessment of effect from NOX2 overexpression myofilament $Ca^{2+}$ sensitivity** **A:** Active force development at increasing[$Ca^{2+}$] in skinned left ventricle trabeculae. Force normalised to $F_{max}$ . **B:** $Ca^{2+}$ sensitivity described as $pCa_{50}$. **C:** Thin filament cooperativity expressed by the Hill coefficient (nH). *=p<0.05. All error bars describe SD. (TG=transgenic)

Thin filament function was assessed through $Ca^{2+}$ activation of force at clamped SL length of 2.2 µm and fitting the dose response curve to a Hill equation (Equation 1). As seen in Figure 65. There was a significant sensitization to $Ca^{2+}$ in terms of force generation as described by $pCa_{50}$: (Ctrl (n=8): 5.63 ± 0.08 SD, Transgenic (n=8): 5.72 ± 0.05 SD) but no change of cooperativity along the thin filament activation.

### 7.4.2 **Actomyosin cross bridge dynamics**

Actomyosin cross bridge function was assessed through maximum tension and cross bridge cycling rate.

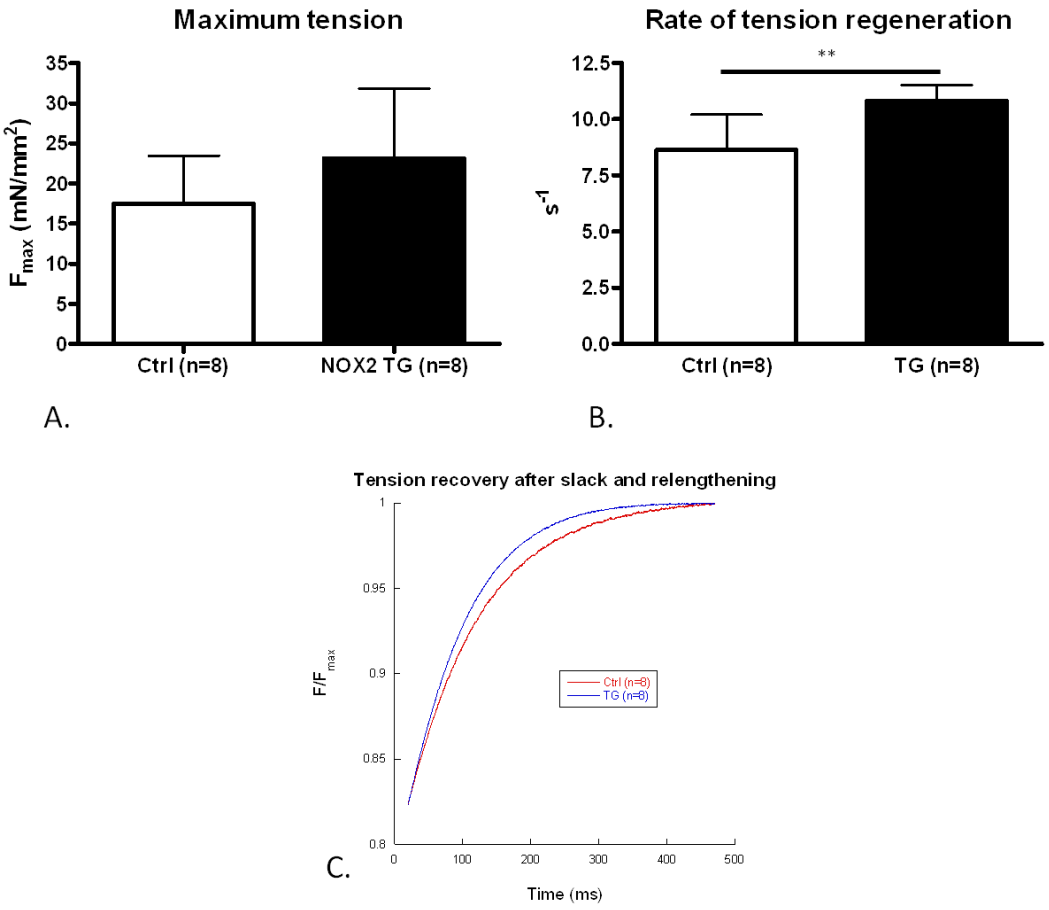



**Figure 66: Assessment of the effect from NOX2 overexpression on actomyosin cross bridge interaction A:** Maximum tension normalised to cross-sectional area at 2.2 µm. **B:** Rate of tension regeneration at 2.2 µm. **C:** Normalised averaged tension recovery traces from Ctrl and TG tissue at 2.2 µm. **=p<0.01. All error bars describe SD.

There was no statistically significant difference in maximum tension generation capacity as a result of NOX2 over expression and $O_2^-$ generation rate as shown in Figure 66 A. The actomyosin cross bridge cycling rate as assessed by tension regeneration rate after rapid (0.5 ms) shortening to 80 % of initial length ($L_0$) for 20 ms duration and rapid re-stretch to $L_0$ (Equation 2) was found upregulated in NOX2 over expressing animals (Ctrl (n=8): 8.3 $s^{-1}$± 1.4 SD, HFD (n=8): 10.8 $s^{-1}$± 0.70 SD), see Figure 66 B and C.

### 7.4.3 **Passive myofilament dynamics**

NOX2 has been suggested to increase profibrotic signalling in the myocardium (Zhang et al., 2013). A change to passive stiffness was therefore investigated through stretch at pCa 9 and actomyosin interaction-inhibited conditions. As shown in Figure 67 there were no differences in absolute passive stiffness at 2.2 or 2.4 µm, or in the tension increase rate upon stretch (Equation 3) as a measure of compliance when comparing demembranated trabeculae from control and NOX2 over expressing LVs.

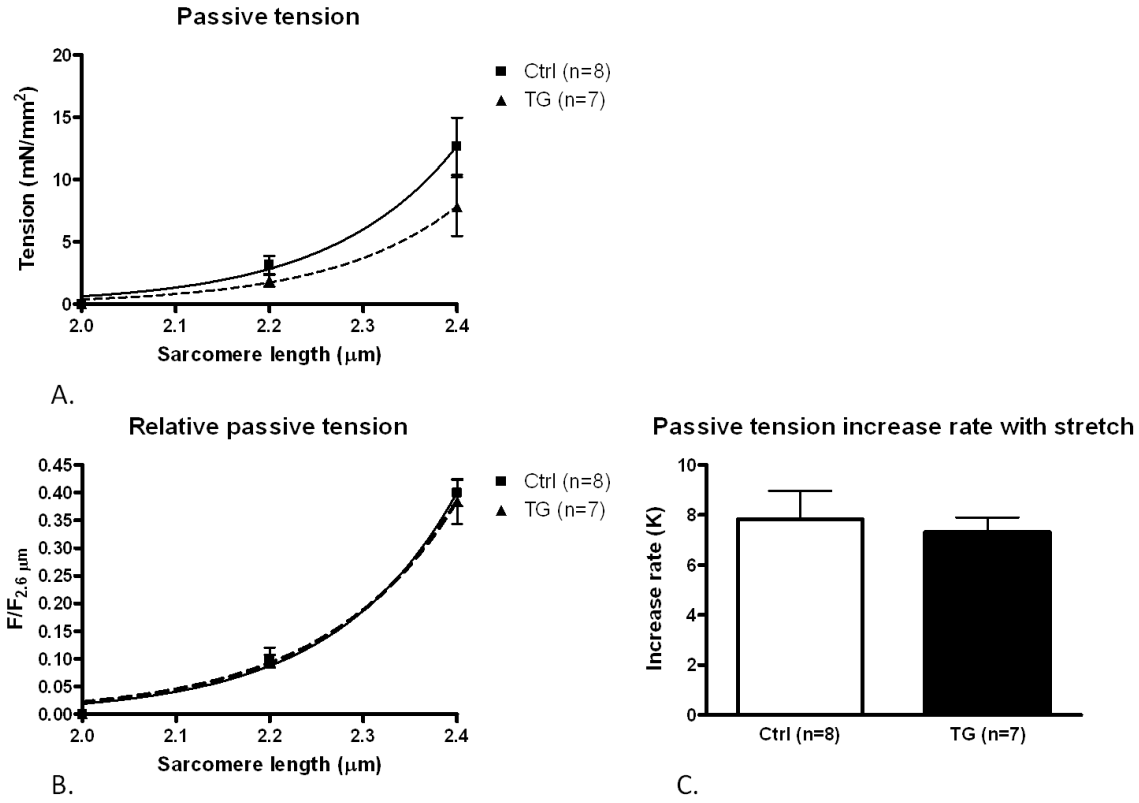



**Figure 67: Assessment of the effects rom NOX2 overexpression on passive stiffness in LV demembranated trabeculae A:** Absolute passive tension in relation to baseline set at 2.0 µm. Error bars describe SEM **B:** Passive tension in relation to that of 2.6 µm. Error bars describe SEM **C:** Quantification of passive compliance as tension increase rate with stretch. Error bars describe SD.

### 7.4.4 **Myofilament protein total phosphorylation assessment**

To examine the possibility that changes to total myofilament protein phosphorylation status was associated with the increase in myofilament $Ca^{2+}$ sensitivity a screen for changes in phosphorylation was performed through ProQ Diamond gel stain. Purified myofilament proteins were solubilised and separated by SDS-PAGE before staining.

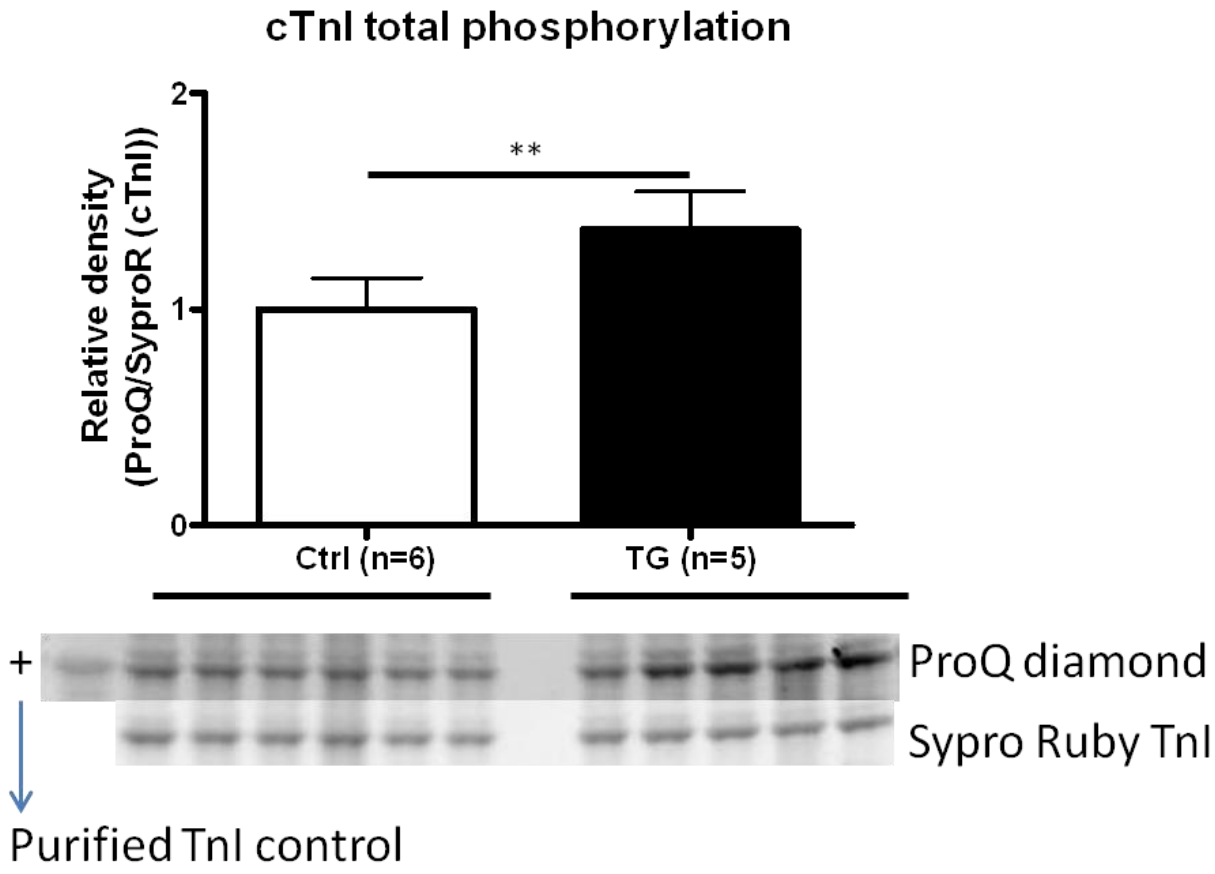



**Figure 68: Assessment of effect of NOX2 overexpression on cTnI total phosphorylation levels.** ProQ Diamond stain was used to measure total cTnI phosphorylation in relation to total cTnI protein levels, through SyproRuby. Comigration with purified cTnI control was used to confirm the correct protein species. **=p<0.01. All error bars describe SD. (TG=transgenic)

Significantly increased levels of cTnI phosphorylation were found in myofilaments isolated from NOX2 TG ventricles, as shown in Figure 68 (Ctrl (n=6): 1.0 ± 0.06 SD, NOX2 TG (n=5): 1.29 ± 0.11 SD).

Immunoblotting was carried out using a phosphospecific antibody to investigate the levels of cTnI phosphorylation at S23/24, the doublet which is the principal site of phosphate incorporation and known target of PKA and also other kinases. The results are shown in Figure 69. There was no increase in cTnI S23/24 phosphorylation compared to total cTnI levels.

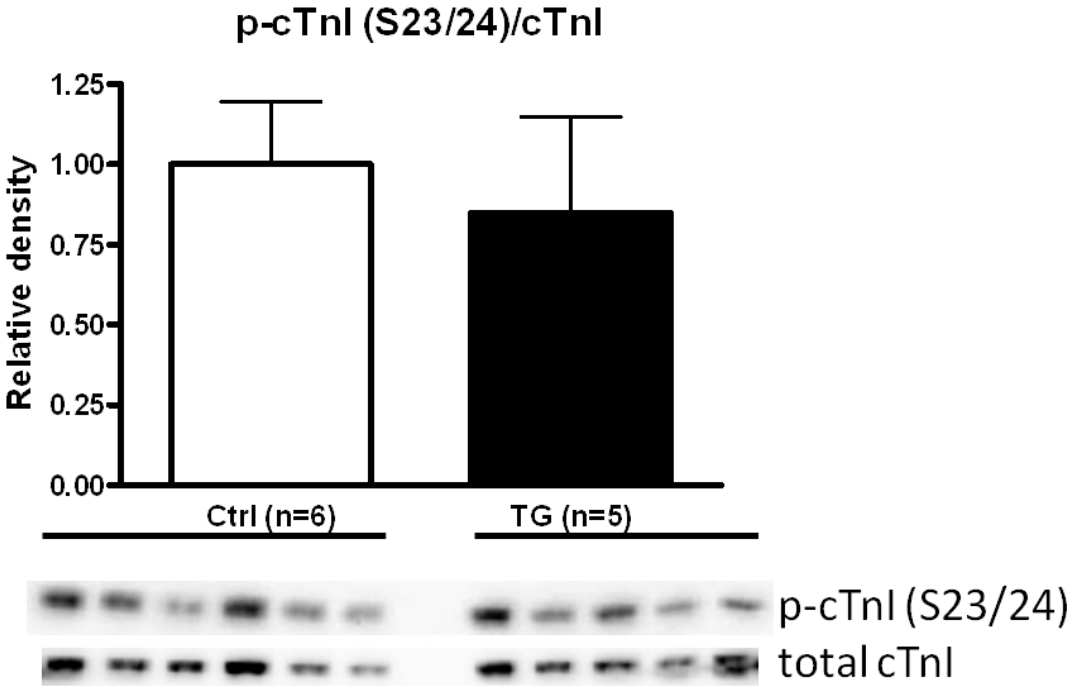



**Figure 69: Effect from NOX2 overexpression on cTnI (S23/24) phosphorylation levels** S23/24 phosphorylation levels were assessed through immunoblotting. All error bars describe SD.

### 7.5 AMPK activity and myofilament sensitisation

AMPK has been shown to increase myofilament $Ca^{2+}$ sensitivity through S150 phosphorylation (Nixon et al., 2012b; Oliveira et al., 2012). As shown in figure 70 by substituting S150 for aspartate (D) on recombinant cTnI (Robinson et al., 2002), and subsequently replacing native cTnI in demembranated cardiac mouse trabeculae the $Ca^{2+}$ sensitivity was shown to increase from phosphorylation (WT (n=6): 5.61 ± 0.03 SD,

S150D (n=6): 5.72 ± 0.12 SD). The increase was attenuated by concomitantly phosphorylating S23/24, previously well known to decrease the sensitivity to $Ca^{2+}$ (S23D/S24D/S150D (n=3): 5.58 ± 0.04 SD). The sensitisation was accompanied by a decrease in cooperativity along the thin filament : (WT (n=6): 3.77 ± 0.64 SD, S150D (n=6): 2.65 ± 0.50 SD, S23D/S24D/S150D (n=3): 3.86 ± 0.53 SD)).

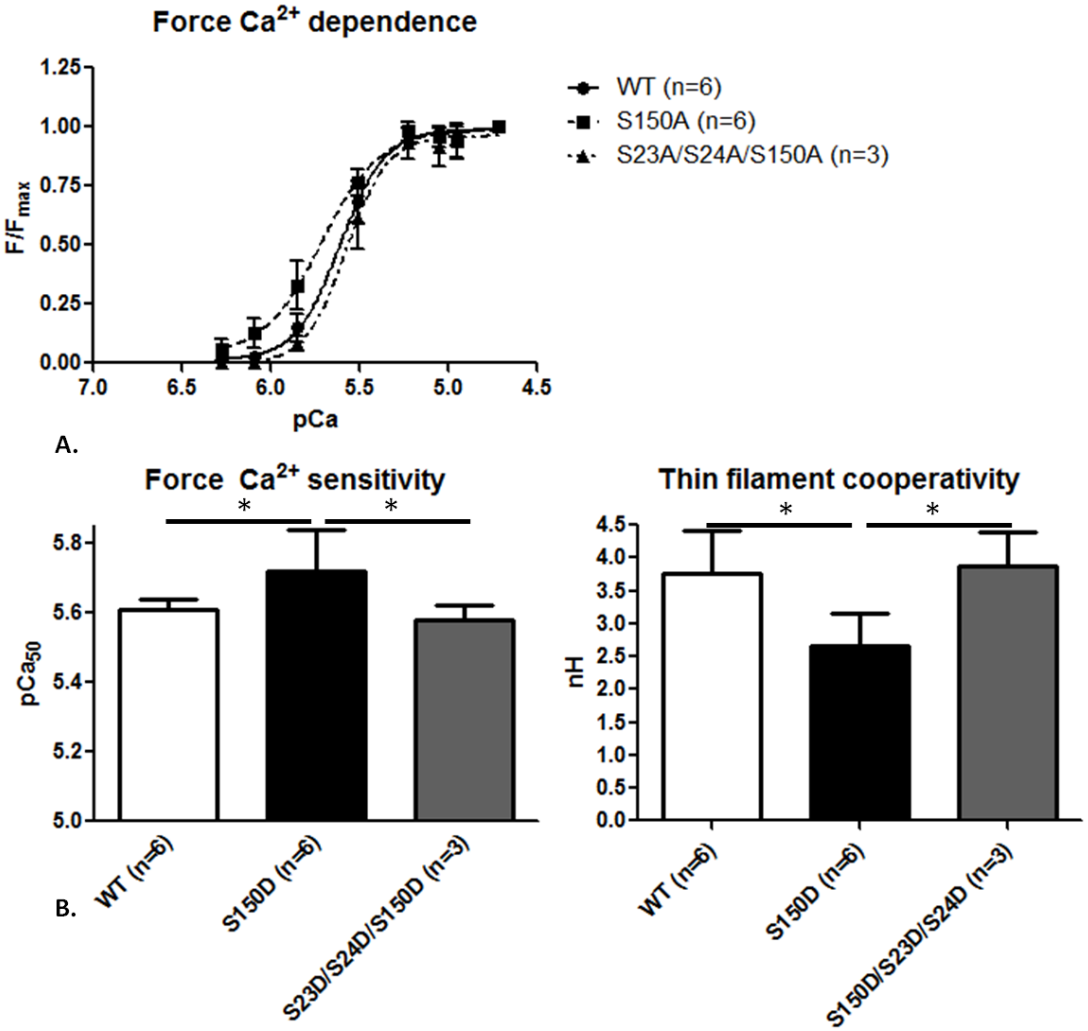



**Figure 70: Effects of S150 phosphorylation on force $Ca^{2+}$ dependence in demembranated cardiac trabeculae A:** S150D induces sensitisation to $Ca^{2+}$ compared to WT, along with a decreased thin filament activation, whereas concomitantly phosphorylating S23/24 reverses the effect **B:** Bar charts representing data derived from A.

### 7.5.1 **Oxidative stress and AMPK activity in C2C12 myoblasts**

As AMPK has been postulated to increase in activity in human skeletal muscle (Morales-Alamo et al., 2012) it may be increased through NOX activation. To test the hypothesis that NOX activity or $O_2^-$ levels may regulate AMPK, C2C12 myoblasts were cultured in the presence of ATII (ctrl), ATII with known NOX inhibitors apocynin and VAS2870 separately, as well as ATII with $O_2^-$ scavenger tirone. AMPK activation was measured by immunoblotting using a phosphospecific antibody raised against p-AMPK (T172), known site of AMPK activation by upstream kinases. The resulting blot and associated densitometric analysis is shown in Figure 71.

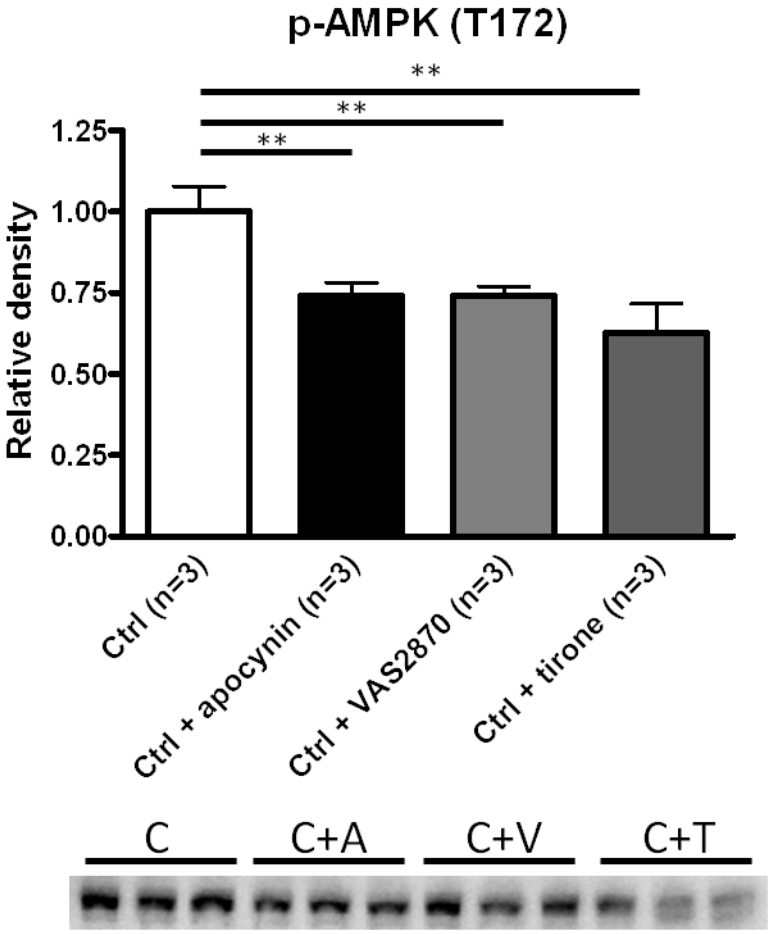



**Figure 71: Effect of NOX inhibition and $O_2^-$ scavenging on AMPK T172 phosphorylation** Levels of AMPK phosphorylation at T172 as assessed by immunoblotting after incubation of C2C12 myoblasts with ATII (Ctrl), ATII+apocynin (C+A), ATII+VAS2870 (C+V), and ATII+tirone (C+T). **=p<0.01. All error bars describe SD.

Significant decreases in AMPK T172 phosphorylation were detected in the presence of apocynin, VAS2870, and tirone, suggesting that NOX inhibition and $O_2^-$ scavenging both cause inhibition of AMPK (Ctrl (n=3): 1.0 ± 0.08 SD, Ctrl + apocynin (n=3): 0.74 ± 0.04 SD, Ctrl + VAS2870 (n=3): 0.74 ± 0.03 SD, Ctrl + tirone: 0.63 ± 0.09 SD).

## 7.6 Discussion

The results presented in this chapter suggest two potentially novel mechanisms of $O_2^-$ signalling in the myocardium. The first is that NOX2 modulation of the myofilament serves the physiological purpose of increasing contractility upon stretch. The second is that chronic over activation of NOX, as reported in hypertension (Montezano and Touyz, 2012), heart failure and hypertrophy (Kuroda et al., 2010; Zhang et al., 2013), and also diabetes (Sedeek et al., 2012) may impair diastolic function through myofilament $Ca^{2+}$ sensitisation which could also potentially raise intracellular $Ca^{2+}$ levels due to altered myofilament $Ca^{2+}$ buffering and initiate hypertrophic calcineurin and NFAT-signalling pathways as seen in HCM (Watkins et al., 2011).

### 7.6.1 **NOX2 as a physiological modulator of cardiac performance**

NOX2 of the cardiomyocyte sarcolemma is known to be activated through tissue stretch (Sedeek et al., 2012; Zhang et al., 2013). Tissue stretch is known to induce a two-step inotropic response in the myocardium, the first response occurs immediately through the Frank-Starling response and the second response after several minutes, the delayed slow force response. Recently a physiological role of NOX2 activation upon stretch has

been proposed through sensitisation of the RyR to $Ca^{2+}$ inducing a larger SR $Ca^{2+}$ release in response to stretch (Prosser et al., 2011). This sensitization may be caused by a direct $O_2^-$ modulation of the RyR or via a second messenger in the form of a redox sensitive kinase such as CaMKII (Zhang et al., 2013).

In the herein interrogated model pro-contractile effects were seen both in terms of $Ca^{2+}$ activation and cross bridge dynamics. These changes are associated with increased phosphorylation of cTnI, a well known modulator of myofilament $Ca^{2+}$ sensitivity. The modified residue is not known at this stage, although S23/24 was interrogated through immunoblotting with no differences detected. This was an expected finding since S23/24 phosphorylation is associated with a desensitisation to $Ca^{2+}$ (Layland et al., 2005) even though PKA activation has previously been reported as required for NOX2 dependent inotropic response to stretch (Zhang et al., 2009). $Ca^{2+}$ sensitization through cTnI phosphorylation has been seen through the PKC action on T144 (Wang et al., 2006) which was not available for immunoblotting, and phosphorylation modification of S150 (Nixon et al., 2012b; Oliveira et al., 2012). Neither this site was able to be examined through immunoblotting (phosphospecific antibody under assessment) but remains a plausible target. Seeing how RLC phosphorylation is known to increase $Ca^{2+}$-sensitivity, it would be of interest to look at this modification in closer detail. In the C2C12 myoblast cell line inhibition of NOX2 as well as passive $O_2^-$ scavenging reduced the degree of activating AMPK activation. These results remain to be established in cardiac myocytes.

The functional changes seen at the myofilament level would in theory cause a more immediate activation of contraction upon $Ca^{2+}$ release from the SR, whereas only the increased cross bridge cycling rate complies with improved diastolic function. This combination of results may thus be labelled as physiologically conflicting. It should also

be mentioned that the cross bridge cycling rate was only assessed at maximum $Ca^{2+}$ activated tension at an approximate $[Ca^{2+}]_{free}$ of pCa 4.7. The situation at lower concentrations was not investigated.

In theory activation of NOX2 upon stretch may form a novel means of increasing myocardial force generation in response to increased pre-load. Since a direct modulatory effect of $O_2^-$ on the myofilament is unlikely due to the short half life of this molecule, secondary messengers in the form of redox sensitive kinases may be involved which would prolong the time from stretch to effect. The mechanism is thus suggested to contribute to the slow force response even though the increased $Ca^{2+}$ sensitivity is a feature which is difficult to combine with increased diastolic function. The increase in $Ca^{2+}$ sensitivity may be due to AMPK phosphorylation of cTnI at the S150 or to modification by other kinases at additional residues. A possible intermediary messenger is the $Ca^{2+}$ and calmodulin dependent protein kinase (CaMKII) which is activated by ROS and involved in EC coupling (Prosser et al., 2011) as well as transcriptional regulation of hypertrophy (Swaminathan et al., 2012) previously proposed in NOX2 dependent regulation of excitation contraction coupling (Zhang et al., 2013).

Phosphorylation of RLC at S14/15 is also known to increase $Ca^{2+}$ sensitivity along with a decreased interfilament spacing affecting force generation dynamics (Colson et al., 2010) and thus would be of interest to examine.

### 7.6.2 **Chronic over activation of NOX2 may impair diastolic function and induce myocardial hypertrophic signalling pathways**

As stated above, NOX2 has been reported as hyperactivated in different chronic and common diseases of the cardiovascular system such as hypertension (Montezano and

Touyz, 2012), heart failure, and hypertrophy (Kuroda et al., 2010; Zhang et al., 2013), as well as diabetes (Sedeek et al., 2012).

Hypertension, hypertrophy and heart failure are clinically related and the two latter often progress from the first via diastolic dysfunction, present in ca. 50 % of hypertensive patients. Abruption of the RAAS through ACE inhibitors and ATII receptor blockers are first line treatments for hypertensive patients (Ginelli and Bella, 2012) which suggests a detrimental effect of NOX2 activity for heart function. Cardiac restricted over expression of ATII in murine myocardium induced hypertrophy along with increased systolic acceleration in normotensive mice (Huggins et al., 2003) suggesting a direct effect of myocardial ATII, independently of increased afterload due to constrictive effects on the vasculature and increased peripheral resistance. No inquiry into myofilament function was performed in the cited study. However, $Ca^{2+}$ sensitisation of the myofilament was seen in a dog model of hypertension induced heart failure with diastolic dysfunction and preserved EF (Hamdani et al., 2013a) as well as in C57BL6/J mice with hypertension derived diastolic dysfunction (Lovelock et al., 2012).

There was no sign of overt cardiac hypertrophy in the NOX2 over expressing hearts investigated in this study. Unfortunately no *in vivo* or *ex vivo* whole organ function data was available to test the hypothesis that the changes seen on the myofilament level may affect the function of the heart as a whole organ. A lot of work remains to clarify the relevance of the effects of NOX2 activation on cardiac function via $Ca^{2+}$ sensitisation and increased cross bridge cycling rate, to identify the residue of modification and to dissect the signalling pathway leading from NOX2 activation to cTnI phosphorylation. Initial attempts of investigating the effects of S150 phosphorylation suggest this residue as a target in increasing $Ca^{2+}$ sensitivity.

# 8 Discussion

## 8.1 HFD feeding alters myocardial performance on whole organ as well as single cardiomyocyte level

This study aimed to examine the effects of HFD-induced obesity and impaired glucose handling on myocardial function. The first aim was to determine whether the effect was tangible on a whole organ level and the second aim was to determine the relative contribution to the phenotype of the intracellular changes ($Ca^{2+}$ handling and myofilament mechanics) and extracellular events, such as fibrosis. A third aim was to investigate the reversibility of observed changes with weight loss.

### 8.1.1 The whole organ effect from HFD is mild and suggestive of cardiac diastolic impairment

The impaired glucose handling ability induced by HFD feeding was shown to be present already after 5 weeks and further characterised through IPGTTs from week 8 onwards. Thus the animals were insulin resistant for at least 25 weeks at the time of the first cardiac functional assessment. In order to address whether or not there was an effect on cardiac performance two separate modalities of investigation were used to characterise *in vivo* whole organ function. In line with the definition of diabetic cardiomyopathy - diastolic dysfunction in the absence of coronary atherosclerosis and hypertension (Boudina and Abel, 2007; Khavandi et al., 2009) - the HFD animals in the study exhibited elevated LVEDP after 30 w as measured through pressure catheterisation of the LV. This was the only whole organ parameter which came out as significant in this ambitious *in vivo* function characterisation endeavour. Thus I would like to state that the 60 % fat

diet fed C57BL6/J mouse represents a mild, but likely physiologically truthful, model of early stage insulin resistance effects on cardiac function. The absence of statistically significant differences on a whole organ level at w 40 made conclusions about the effect from diet reversal difficult even though trends in *in vivo* haemodynamics both in LVEDP as well as contractile dynamics, suggest that there was little effect from a 10 w diet reversal. In fact a decreased systolic pressure acceleration rate comparing ctrl and reversal animals was seen at w 40 indicating a lack of beneficial effects.

### 8.1.2 Increased cardiomyocyte relaxation rate likely due to myofilament desensitisation to $Ca^{2+}$

The effects on the single cell level were rather the opposite of what had been expected from previous other models of diabetic cardiomyopathy where a decreased relaxing rate was seen, in a type 1 DM model (Choi et al., 2002) and *Ob/ob* model of type 2 DM (Li et al., 2006). Many reports suggest an impaired $Ca^{2+}$ handling to be crucial in impaired cardiomyocyte relaxation in different models: STZ 1 (Choi et al., 2002; Lacombe et al., 2007), *Ob/ob* (Li et al., 2006), and human right atrial strips (Reuter et al., 2008). Our results reproduced those reported by Howarth et al who fed the C57BL6/J mouse a HFD before studying cellular dynamics and saw an increased relaxation rate without altered $Ca^{2+}$ profile (Howarth et al., 2005). No myofilament function inquiry was carried out in the Howarth study.

My combined study of unloaded cardiomyocyte contractility and $Ca^{2+}$ handling, along with isometric tension measurements in skinned LV trabeculae has supported the proposal made by Howarth et al that the effect on a cellular level of increased relaxation rate is due to myofilament desensitisation to $Ca^{2+}$ (Howarth et al., 2005). Following the

paradigm that unloaded cellular dynamics is regulated by two processes, $Ca^{2+}$ handling and myofilament dynamics (Spurgeon et al., 1992), the absence of differences in cellular $Ca^{2+}$ handling should warrant the conclusion that the relevant change has occurred on the myofilament. Also, after 40 w of HFD, as the increased relaxation rate was seen, challenging the myocytes with increased stimulation frequency, from 1 Hz to 3 Hz, the relaxation rate of the HFD treated animals did not manage to further decrease unlike the controls and reversal animals. However, the increase in $Ca^{2+}$ reuptake was maintained verifying that the $Ca^{2+}$ handling process was not affected but rather the effect of the increased $Ca^{2+}$ decay rate was not conveyed to increased relaxation via the myofilament.

The demembranated trabeculae studies allowed the measurement of the force-$Ca^{2+}$ relationship at constant SL. No change towards decreased $Ca^{2+}$ sensitivity was seen at w 40. A complementary measure of $Ca^{2+}$ sensitivity was obtained from the unloaded cardiomyocyte data by plotting $Ca^{2+}$ ratio versus cell contractility and examining the relaxation phase of these loops. During relaxation the $Ca^{2+}$ transient decay and cell re-lengthening reaches parallel trajectories which correspond to a state of $Ca^{2+}$ - cTnC equilibrium, thus a measure of myofilament $Ca^{2+}$ sensitivity (Spurgeon et al., 1992). In my study, $Ca^{2+}$ and SL shortening were not measured from the same cells which I argue added noise to the data sets presented here: time synchronised $Ca^{2+}$ vs. SL average recordings from the same animals, however not, the same cells.

Phosphorylation of cTnI by PKA on S23/24 is a well characterised physiological mechanism for decreasing myofilament $Ca^{2+}$ sensitivity (Layland et al., 2005). Decreased $Ca^{2+}$ sensitivity results in increased relaxation as $Ca^{2+}$ dissociates from cTnC at higher $[Ca^{2+}]_{free}$. Through immunoblotting I detected a trend towards increased levels of phosphorylation at S23/24 in HFD animals and a significant reduction upon diet

reversal at w 40, the point of increased relaxation rate, whereas at w 30 no trends were seen. This result links the clear increase in relaxation rate to the myofilament.

#### *8.1.2.1 Increased NOX activity may affect cardiomyocyte contractility via PKA*

cTnI S23/24 phosphorylation occurs via PKA. PKA is a known redox sensitive kinase via hydrogen peroxide ($H_2O_2$) which activates translocation of PKA to the myofilaments independently of β-adrenergic stimulation and cAMP levels (Brennan et al., 2006). $H_2O_2$ is generated via $O_2^-$ generated from NOXs (Zhang et al., 2013). Increased activity has been suggested to mediate in the inotropic response to NOX dependent ET-1 stimulation (Zhang et al., 2009) as well as to the increased mitochondrial $O_2^-$ production in heart failure resulting in subendocardial contractile dysfunction (Andre et al., 2013). It thus seems that the source of PKA activating $O_2^-$ is less well defined than PKA's ability to be activated in fact by oxidative stress. The NADPH dependent increase in $O_2^-$ production could only be statistically confirmed at w 40 (Fig. 4.7), in correlation with trend towards increased cTnI (S23/24) phosphorylation and single cell relaxation rate.

### 8.1.3 **Elevated LVEDP rise may be due to extracellular fibrosis**

The increase seen in LVEDP at w 30 is not readily explained by a myofilament $Ca^{2+}$ desensitisation. Passive tension was measured in skinned cardiac LV trabeculae to test whether the LVEDP increase detected through *in vivo* haemodynamics at w 30 was likely to be due to changes in titin or fibrosis. In absolute terms an increase in passive stiffness was shown at both 2.2 and 2.4 μm at w 30, but not at w 40 which is surprising as one would expect a disease progression with time. Myocardial fibrosis cannot be excluded as a cause for the increased LVEDP seen at w 30 and the trend towards it at w 40, based on

results from a combination of assays. A colorimetric assay was employed to measure total collagen levels in the LV myocardium. At w 30 there was no difference in total collagen levels whereas at w 40 this was increased in the HFD group. Quantitative PCR showed an increased collagen 3 mRNA level at w 30, a difference that was abolished by w 40. These results are hard to reconcile with the LVEDP increase at w 30. Total collagen, measured by total hydroxyproline content did not take into account whether or not the collagen had been organised into insoluble collagen fibres capable of relaying passive tension. To determine this, a soluble collagen assay would need to be performed and its result deducted from the total collagen count to obtain the amount of insoluble collagen fibres.

There was no difference in titin N2B and N2BA isoform expression levels at w 30 or 40. Titin phosphorylation status was not assessed.

### 8.1.4 **Conclusions regarding origins of HFD induced cardiac dysfunction**

#### *8.1.4.1 Cardiomyocyte confined changes*

There was a clear increase in relaxation rate of the unloaded cells at 1 as well as 3 Hz. This change was partly reversed in cardiomyocytes isolated from the diet reversal group after w 40 at 1 Hz stimulation only. There was no alteration to $Ca^{2+}$ handling neither was the $Ca^{2+}$ transient affected, nor was there any impairment in frequency dependent $Ca^{2+}$ reuptake ability. The isometric skinned fibre technique for measuring myofilament $Ca^{2+}$ sensitivity could not show a decreased myofilament $Ca^{2+}$sensitivity. A modification well known to decrease myofilament $Ca^{2+}$ sensitivity, cTnI S23/24 phosphorylation (Layland et al., 2005), was found significantly decreased upon reversal compared to HFD fed mice

at w 40 and trended towards an increase in HFD fed mice compared to controls; it is therefore a plausible cause for the increased relaxation rate.

#### *8.1.4.2 Whole organ changes*

The whole organ diastolic impairment is most likely due to changes in passive tension mediators such as increased collagen fibres resulting in fibrosis. This is supported by the increase in passive tension upon stretch in skinned trabeculae at w 30. There was no difference in cross bridge cycling rate, no increased $Ca^{2+}$ sensitivity, or altered $Ca^{2+}$ transient in the unloaded cells, that could have accounted for the increased LVEDP. The relative contribution of these two passive tension elements requires further work in order to be deciphered.

### 8.1.5 **Desired methodological improvements**

As the equilibrium between active and passive tension and $Ca^{2+}$ signalling is dependent on SL, as well as temperature, the evaluation of these processes in unloaded cardiomyocytes as well as skinned cardiac trabeculae, set at fixed SLs, at a temperature of 10°C is far from ideal in replicating the *in vivo* situation. It would have been desirable to carry out concomitant $Ca^{2+}$ and force measurements in intact trabeculae at 37 °C under sinusoidal length changes, or fura-2 loaded whole hearts under mechanical load and at physiologically relevant SLs. Indeed, imposing length alterations during investigation may increase the sensitivity of detecting increased relaxation rate due to myofilament $Ca^{2+}$ desensitisation from β-adrenergic stimulation (Layland and Kentish, 2002).

It may also be argued that the endocardial trabeculae are not representative of the whole myocardium and passive tension would be more reliably assessed through a demembranated whole heart in a Langendorff set-up. To decipher the relative contribution from titin and fibrosis alterations an initial pressure volume curve in an non-ionic detergent perfused heart would be followed by a 600 mM KCl perfusion shown to extract all myofilament contribution to passive stiffness and allow a relative assessment of the extracellular matrix, i.e. fibrosis contribution to observed changes (Chaturvedi et al., 2010).

## 8.2 Cardiac restricted NOX2 over-expression causes myofilament $Ca^{2+}$ sensitisation

### 8.2.1 Background

#### *8.2.1.1 ROS play a central role in mediating force response to stretch*

The generation of ROS from multiple intracellular sources in response to mechanical stretch has been reported in different studies; it has been hypothesised that the slow force response to stretch is dependent on both NOX2 and mitochondrial ROS in causing an increase in cytosolic [$Ca^{2+}$]. In feline cardiac slices Caldiz et al concluded that an ATII-dependent increase in NOX as well as mitochondrial $O_2^-$ production was needed to transmit the inotropic effect of stretch. This conclusion was reached using inhibitors of NOX (apocynin) as well as the mitochondrial potassium ATP channel (glybenclamide). The effect was conveyed by redox sensitive kinases activating the sodium hydrogen exchanger (NHE-1) increasing $Na^+$ influx activating the NCX causing an increased systolic [$Ca^{2+}$] (Caldiz et al., 2007). De Giusti et al reached a similar conclusion in isolated feline cardiomyocytes, studying the inotropic response to ATII under unloaded

conditions, noticing how the response to ET-1 was abolished using the mitochondrial ETC inhibitor rotenone as well as NHE blocker HOE642 laying out the same series of events as Caldiz (De Giusti et al., 2008). Zhang and co-workers investigated other sources of ROS in the inotropic induction after mechanical stretch in unloaded murine cardiomyocytes from neuronal NOS -/- mice. Their study showed that the absence of nNOS expression had no effect on the ET-1 induced inotropic response whereas NOX inhibitor apocynin totally prevented the effect (Zhang et al., 2009). This suggests that the NOX family appears to have a central role to play in the inotropic response to stretch.

That the $Ca^{2+}$ transient has an important role to play in the slow force response appears well established. However, the possibility of an amplifying effect on the myofilament should not be disregarded. It has been proposed that redox-sensitive PKA may be involved in the inotropic response to stretch (Zhang et al., 2009). PKA is a well known modifier of $Ca^{2+}$ handling as well as myofilament dynamics directly as well as indirectly, through CaMKII activation, PLN phosphorylation inducing an increase in $Ca^{2+}$ re-uptake rate, increased $Ca^{2+}$ transient amplitude through effects on the RyR (Bers, 2008) and cTnI phosphorylation at S23/24, causing a desensitisation to $Ca^{2+}$ and increased cross bridge cycling rate (Layland et al., 2005) thus facilitating relaxation (Layland and Kentish, 2002) and LV accommodation of increased preload. As described in the introduction to this thesis other kinases that target the myofilament have also been shown to be activated by stretch. Monasky et al inhibited the redox-sensitive PKC and saw a reduction in the stretch-induced increased contraction as well as relaxation rate in conjunction with attenuated myosin RLC phosphorylation; the same experiment with PKA inhibition only decreased time to peak contraction but was associated with a reversal of stretch-induced phosphorylation of cTnI and attenuated phosphorylation of

myosin RLC (Monasky et al., 2012). Investigating the force stretch response in human atrial trabeculae Kockskämper was able to associate an ATII-dependent but NHE-independent increase in force upon stretch with increased myosin RLC phosphorylation and increased myofilament $Ca^{2+}$ sensitivity without effects on the $Ca^{2+}$ transient (Kockskamper et al., 2008a). The same author compared atrial and ventricular effects showing that in human ventricle, unlike in atrium the force response to stretch is indeed mediated by NHE in addition to MLCK phosphorylation of myosin RLC. The authors conclude that the MLCK activation occurs via $Ca^{2+}$/calmodulin (Kockskamper et al., 2008b). Interestingly, ET-1 stimulation was concluded to exert an inotropic response via myosin RLC phosphorylation and $Ca^{2+}$ sensitisation in rabbit ventricular myocardium (Chu and Endoh, 2005).

NOX2 is situated in the sarcolemmal T-tubules in close vicinity to central proteins in the CICR process, that is the LTCC, CaMKII, and the RyR, all proteins reported as redox sensitive (Zhang et al., 2013; Zhang et al., 2009). Prosser et al elegantly showed in intact cardiomyocytes that microtubule-mediated NOX2 activation upon stepwise stretch causes a release of $O_2^-$ which induces an immediate and increased frequency of $Ca^{2+}$ sparks (non-AP mediated $Ca^{2+}$ release from the SR) via the RyR, suggesting that the RyR is sensitised to $Ca^{2+}$ by NOX2 generated $O_2^-$ directly as the effect was reproducible through $H_2O_2$ superfusion and inhibitable with NOX inhibitor diphenyleneiodonium (DPI) (Prosser et al., 2011). This signalling event would be expected to have an immediate effect on $Ca^{2+}$ handling. It has also been suggested that the activation of NOX2 induces a sensitisation of the RyR by activation of CaMKII which in turn phosphorylates RyR (Bers, 2008; Zhang et al., 2013) representing an amplification of the signal.

In conclusion the effects of myofilament phosphorylation in the slow force response appear to be considered of less importance than the role of intracellular $Ca^{2+}$ handling. $Ca^{2+}$ sensitisation of the myofilament from myosin RLC phosphorylation initially appears counteracting in relation to the desensitising changes seen from PKA activation, also occurring in situations of stretch, which has the opposite, lusitropic effect. It may be postulated that in combination with increased cross bridge cycling rate, $Ca^{2+}$ sensitisation may serve to potentiate the contractile response at a given [$Ca^{2+}$], and that in combination with increased $Ca^{2+}$ transient decay rate, the lusitropic effect of increased cross bridge cycling rate may overpower the anti-lusitropic effect of myofilament $Ca^{2+}$ sensitisation thus in combination providing a net effect supporting cardiac output.

#### *8.2.1.2 NOX2 is suggested to play a role in hypertension, and cardiac hypertrophy and arrhythmia, features of heart failure*

The role of NOX2 and NOX4 appears central in cardiac disease progression from hypertension towards heart failure. Even though they both produce $O_2^-$, they appear to have different effects. NOX2 is activated in the situation of increased ATII stimulation and mechanical stretch, glucose and insulin stimulation, and also by other known pro-hypertrophic stimulus such as tumour necrosis factor-α (TNF- α). NOX2 KO mice have shown to develop less hypertrophy in response to ATII infusion, but not in response to pressure overload (Lassegue et al., 2012; Sirker et al., 2011; Zhang et al., 2013). Cardiac-restricted ATII over-production in these mice has been shown to induce cardiac hypertrophy independent of systemic hypertension (Huggins et al., 2003), supporting the notion that in terms of NOX2-induced cardiac hypertrophy, ATII stimulation has a

bigger role to play than mechanical load. However, in terms of cardiac dysfunction and fibrosis induced by pressure overload, the NOX2 KO mice appeared protected (Sirker et al., 2011). NOX4 however, has been suggested to convey a protective effect in its ability to induce capillary growth and preserve myocardial perfusion in hypertrophy. Its endoplasmatic, intranuclear, and mitochondrial position within the cardiomyocyte as opposed to NOX2's sarcolemmal localisation suggests a role for NOX4 in pro-angiogenic transcriptional regulation (Sirker et al., 2011; Zhang et al., 2013).

NOX2 has also been suggested to play a role in the induction of atrial fibrillation. Inhibition of the NOX2-activating Rac-1 through statin treatment reduced atrial fibrillation occurrence, as did ACE inhibitors and ATII receptor blockers (Zhang et al., 2013). Also, NOX2-derived ROS have been shown to be elevated in the right atrium during early stages of atrial fibrillation (Kim et al., 2005; Reilly et al., 2011).

#### *8.2.1.3 $Ca^{2+}$ sensitisation of the myofilament is a postulated mediator of inotropy, diastolic dysfunction, hypertrophy, and arrhythmia*

$Ca^{2+}$ sensitisation of the myofilament mediates a higher contractile response at lower [$Ca^{2+}$], thus contributing to increased contractility. As stated above, $Ca^{2+}$ sensitisation of the myofilament has been suggested to play a role in the inotropic response initiated by ET-1 stimulation on ventricular myocardium (Chu and Endoh, 2005). In this study and others (Kockskamper et al., 2008a; Kockskamper et al., 2008b), phosphorylation of myosin RLC has been shown to be associated with ATII signalling, which is central in the slow force response to stretch (Cingolani et al., 2012; De Giusti et al., 2008). PKC-ε which is involved in ATII/ET-1 signalling in the cardiac myocyte has also been shown to induce $Ca^{2+}$ sensitisation of the myofilament as part of its induction of inotropy in ventricular

rat cardiomyocytes although no modifications of myofilament proteins were positively identified in that study (Kang and Chung, 2012). Also PKC βII has been suggested to mediate cTnI T144 phosphorylation and induce $Ca^{2+}$ sensitisation and increased inotropy, although only in the absence of S23/24 phosphorylation (Wang et al., 2006). This effect appears hard to translate to an *in vivo* setting where impaired contractility has been observed in transgenic mice over expressing PKCβ (Steinberg, 2012).

In a pathophysiological setting increased inotropy may however also be associated with impaired relaxation often seen in models of increased $Ca^{2+}$ sensitivity on the myofilament level. One example is the sarcomeric HCM causing mutations where increased myofilament $Ca^{2+}$ sensitivity appears to be a common feature (Robinson et al., 2007). In HCM thin filament mutations directly alter sensitivity through cTnC $Ca^{2+}$ affinity and thick filament mutations alter $Ca^{2+}$ sensitivity through increased actomyosin interaction. The increased $Ca^{2+}$ sensitivity is postulated to increase myofilament $Ca^{2+}$ causing intracellular [$Ca^{2+}$] at the end of diastole to rise and induce $Ca^{2+}$ activated hypertrophic signalling pathways such as calcineurin-NFAT-CaMKII – pathway (Watkins et al., 2011). Elevated intracellular $Ca^{2+}$ buffering through $Ca^{2+}$ sensitisation of the myofilament alters the intracellular $Ca^{2+}$ transient profile, as described by Schober et al. who investigated the fura-2 derived $Ca^{2+}$ signal from whole mouse hearts expressing different $Ca^{2+}$ sensitising mutations of cTnT. The increased buffering capacity raised end diastolic [$Ca^{2+}$] and increased SR $Ca^{2+}$ load causing increased propensity for pause dependent arrhythmias, an effect mimicked by the $Ca^{2+}$ sensitizing agent EMD57033 (Schober et al., 2012).

### 8.2.2 **NOX2 over-expression increases myofilament $Ca^{2+}$ sensitivity and cross bridge cycling rate – physiological and pathogenetic implications**

In the mouse model of NOX2 over-expression, there was a two-fold increase in NOX2-derived $O_2^-$ production in the absence of NADPH stimulation. Measurements of the force-pCa relationship in demembranated trabeculae revealed increased $Ca^{2+}$ sensitivity along with increased cross bridge cycling rate at high [$Ca^{2+}$]. This was associated with increased total phosphorylation level on cTnI, a well known modulator of $Ca^{2+}$ sensitivity. Although there has been speculation on its existence (Zhang et al., 2013) the direct link between NOX2 specific upregulation and $Ca^{2+}$ sensitisation of the myofilament has not been described previously and may shed further light on the series of events causing the slow force response. The fact that NOX2 activity and $Ca^{2+}$ sensitisation of the myofilament have the common effect of hypertrophy makes this finding interesting from a therapeutic point of view.

A lot of work remains to dissect the pathway that links NOX2 activation to cTnI phosphorylation. A major clue as to where to start will be the identification of the modified cTnI amino acid. Based upon the known functional effects of phosphorylation, likely candidates are T144, a target of PKC (Layland et al., 2005; Wang et al., 2006) and S150, which is modified by AMPK (Nixon et al., 2012b; Oliveira et al., 2012). PKC is known to be upregulated by ATII and ET-1 signaling (Layland et al., 2005), closely related to NOX2 activity whereas the relationship between oxidative stress and AMPK activation in cardiomyocytes appear less well characterised. In order to investigate a possible connection between NOX2 and AMPK activation, I co-incubated C2C12 myoblasts with ATII and apocynin and VAS2870 separately. Both inhibitors were able to reduce phosphorylation levels of AMPK at T172, a well characterised activating

modification of AMPK via liver kinase B 1 (LKB-1) and CaMKKβ (Carling et al., 2012). None of these two kinases are known to be activated by ROS, unlike the CaMKII which is spatially associated with the NOX2 in the sarcolemmal T-tubules. In human skeletal muscle the influence of ROS on CaMKII and AMPK activation was assessed by western blotting for CaMKII phosphoT286 and AMPK phosphoT172 levels respectively. It was found that sprint exercise increased the production of ROS as well as T286 and T172 phosphorylation, an association which was inhibited through ingestion of antioxidants before exercise despite preserved reduced AMP/ATP ratio suggesting that AMPK may be activated through increased ROS production via redox sensitive CaMKII (Morales-Alamo et al., 2012). Thus I would suggest that AMPK via or independently of CaMKII has the potential to mediate a phosphorylation of cTnI in response to NOX2-related increased $O_2^-$ production which, in the acute setting could serve to increase inotropic response through activation of actomyosin interaction at relatively low [$Ca^{2+}$] and increase force acceleration through improved cross bridge kinetics, and in the chronic setting impair diastolic function and increase the risk of arrhythmia.

#### *8.2.2.1 Future work*

This hypothesis may be tested in an intact trabeculae system where preparation length can be altered and force output recorded upon electrical pacing, in conjunction with measurement of intracellular $Ca^{2+}$ and $O_2^-$ production. This system would also enable the measurement of $Ca^{2+}$ sensitivity through force-$Ca^{2+}$ loops, similar to the contractility-$Ca^{2+}$ plots obtained from analysis of unloaded murine cardiomyocytes. It would also be possible to investigate whether cTnI phosphorylation is induced in response to stretch. Using pharmacological agents activating and inhibiting suggested

key signaling molecules (as for AMPK AICAR and Compound C respectively, and for NOX2 ATII and VAS2870/apocynin) their relative importance would be attempted to be deciphered. Finally a transgenic approach blocking phosphorylation of S150 through alanine (S→A) replacement can be attempted to determine the importance of this modification in relaying an inotropic response to stretch and hypertrophy in response to ATII signalling.

# 9 References

Abel, E.D., Litwin, S.E., and Sweeney, G. (2008). Cardiac remodeling in obesity. Physiological reviews *88*, 389-419.

Abel, E.D., O'Shea, K.M., and Ramasamy, R. (2012). Insulin resistance: metabolic mechanisms and consequences in the heart. Arteriosclerosis, thrombosis, and vascular biology *32*, 2068-2076.

Al-Khayat, H.A., Kensler, R.W., Squire, J.M., Marston, S.B., and Morris, E.P. (2013). Atomic model of the human cardiac muscle myosin filament. Proceedings of the National Academy of Sciences of the United States of America *110*, 318-323.

Andre, L., Fauconnier, J., Reboul, C., Feillet-Coudray, C., Meschin, P., Farah, C., Fouret, G., Richard, S., Lacampagne, A., and Cazorla, O. (2012). Subendocardial Increase in Reactive Oxygen Species Production Affects Regional Contractile Function in Ischemic Heart Failure. Antioxidants & redox signaling *18*, 1009-1020.

Andre, L., Fauconnier, J., Reboul, C., Feillet-Coudray, C., Meschin, P., Farah, C., Fouret, G., Richard, S., Lacampagne, A., and Cazorla, O. (2013). Subendocardial increase in reactive oxygen species production affects regional contractile function in ischemic heart failure. Antioxidants & redox signaling *18*, 1009-1020.

Angin, Y., Steinbusch, L.K., Simons, P.J., Greulich, S., Hoebers, N.T., Douma, K., van Zandvoort, M.A., Coumans, W.A., Wijnen, W., Diamant, M.*, et al.* (2012). CD36 inhibition

prevents lipid accumulation and contractile dysfunction in rat cardiomyocytes. The Biochemical journal *448*, 43-53.

Anstee, Q.M., and Goldin, R.D. (2006). Mouse models in non-alcoholic fatty liver disease and steatohepatitis research. International journal of experimental pathology *87*, 1-16.

Antoniades, C., Demosthenous, M., Reilly, S., Margaritis, M., Zhang, M.H., Antonopoulos, A., Marinou, K., Nahar, K., Jayaram, R., Tousoulis, D.*, et al.* (2012). Myocardial redox state predicts in-hospital clinical outcome after cardiac surgery effects of short-term pre-operative statin treatment. Journal of the American College of Cardiology *59*, 60-70.

Antonova, P., Jacobs, D.I., Bojar, M., Cerny, R., Ciharova, K., Frick, M.A., Fintel, B., DeHovitz, J., and Bennett, C.L. (2010). Czech health two decades on from the Velvet Revolution. Lancet *375*, 179-181.

Aroor, A.R., Mandavia, C., Ren, J., Sowers, J.R., and Pulakat, L. (2012). Mitochondria and Oxidative Stress in the Cardiorenal Metabolic Syndrome. Cardiorenal medicine *2*, 87-109.

Ashley, C.C., and Ridgway, E.B. (1968). Simultaneous recording of membrane potential, calcium transient and tension in single muscle fibers. Nature *219*, 1168-1169.

Atkinson, M.A., and Leiter, E.H. (1999). The NOD mouse model of type 1 diabetes: as good as it gets? Nature medicine *5*, 601-604.

Avner, B.S., Hinken, A.C., Yuan, C., and Solaro, R.J. (2010). H2O2 alters rat cardiac sarcomere function and protein phosphorylation through redox signaling. American journal of physiology Heart and circulatory physiology *299*, H723-730.

Avner, B.S., Shioura, K.M., Scruggs, S.B., Grachoff, M., Geenen, D.L., Helseth, D.L., Jr., Farjah, M., Goldspink, P.H., and Solaro, R.J. (2012). Myocardial infarction in mice alters sarcomeric function via post-translational protein modification. Molecular and cellular biochemistry *363*, 203-215.

Bardswell, S.C., Cuello, F., Rowland, A.J., Sadayappan, S., Robbins, J., Gautel, M., Walker, J.W., Kentish, J.C., and Avkiran, M. (2010). Distinct sarcomeric substrates are responsible for protein kinase D-mediated regulation of cardiac myofilament Ca2+ sensitivity and cross-bridge cycling. The Journal of biological chemistry *285*, 5674-5682.

Barefield, D., and Sadayappan, S. (2010). Phosphorylation and function of cardiac myosin binding protein-C in health and disease. Journal of molecular and cellular cardiology *48*, 866-875.

Baribault, H. (2010). Mouse models of type II diabetes mellitus in drug discovery. Methods Mol Biol *602*, 135-155.

Belke, D.D., Betuing, S., Tuttle, M.J., Graveleau, C., Young, M.E., Pham, M., Zhang, D., Cooksey, R.C., McClain, D.A., Litwin, S.E.*, et al.* (2002). Insulin signaling coordinately regulates cardiac size, metabolism, and contractile protein isoform expression. The Journal of clinical investigation *109*, 629-639.

Bers, D.M. (2000). Calcium fluxes involved in control of cardiac myocyte contraction. Circulation research *87*, 275-281.

Bers, D.M. (2002). Cardiac excitation-contraction coupling. Nature *415*, 198-205.

Bers, D.M. (2008). Calcium cycling and signaling in cardiac myocytes. Annual review of physiology *70*, 23-49.

Bers, D.M. (2011). Ca(2)(+)-calmodulin-dependent protein kinase II regulation of cardiac excitation-transcription coupling. Heart rhythm : the official journal of the Heart Rhythm Society *8*, 1101-1104.

Bers, D.M., and Grandi, E. (2009). Calcium/calmodulin-dependent kinase II regulation of cardiac ion channels. Journal of cardiovascular pharmacology *54*, 180-187.

Bertrand, L., Horman, S., Beauloye, C., and Vanoverschelde, J.L. (2008). Insulin signalling in the heart. Cardiovascular research *79*, 238-248.

Blair, E., Redwood, C., Ashrafian, H., Oliveira, M., Broxholme, J., Kerr, B., Salmon, A., Ostman-Smith, I., and Watkins, H. (2001). Mutations in the gamma(2) subunit of AMP-activated protein kinase cause familial hypertrophic cardiomyopathy: evidence for the central role of energy compromise in disease pathogenesis. Human molecular genetics *10*, 1215-1220.

Boudina, S., and Abel, E.D. (2007). Diabetic cardiomyopathy revisited. Circulation *115*, 3213-3223.

Boudina, S., Bugger, H., Sena, S., O'Neill, B.T., Zaha, V.G., Ilkun, O., Wright, J.J., Mazumder, P.K., Palfreyman, E., Tidwell, T.J.*, et al.* (2009). Contribution of impaired myocardial insulin signaling to mitochondrial dysfunction and oxidative stress in the heart. Circulation *119*, 1272-1283.

Bracken, N., Howarth, F.C., and Singh, J. (2006). Effects of streptozotocin-induced diabetes on contraction and calcium transport in rat ventricular cardiomyocytes. Annals of the New York Academy of Sciences *1084*, 208-222.

Brennan, J.P., Bardswell, S.C., Burgoyne, J.R., Fuller, W., Schroder, E., Wait, R., Begum, S., Kentish, J.C., and Eaton, P. (2006). Oxidant-induced activation of type I protein kinase A is mediated by RI subunit interprotein disulfide bond formation. The Journal of biological chemistry *281*, 21827-21836.

Buchanan, J., Mazumder, P.K., Hu, P., Chakrabarti, G., Roberts, M.W., Yun, U.J., Cooksey, R.C., Litwin, S.E., and Abel, E.D. (2005). Reduced cardiac efficiency and altered substrate metabolism precedes the onset of hyperglycemia and contractile dysfunction in two mouse models of insulin resistance and obesity. Endocrinology *146*, 5341-5349.

Burcelin, R., Crivelli, V., Dacosta, A., Roy-Tirelli, A., and Thorens, B. (2002). Heterogeneous metabolic adaptation of C57BL/6J mice to high-fat diet. American journal of physiology Endocrinology and metabolism *282*, E834-842.

Burgoyne, J.R., Mongue-Din, H., Eaton, P., and Shah, A.M. (2012). Redox signaling in cardiac physiology and pathology. Circulation research *111*, 1091-1106.

Caldiz, C.I., Garciarena, C.D., Dulce, R.A., Novaretto, L.P., Yeves, A.M., Ennis, I.L., Cingolani, H.E., Chiappe de Cingolani, G., and Perez, N.G. (2007). Mitochondrial reactive oxygen species activate the slow force response to stretch in feline myocardium. The Journal of physiology *584*, 895-905.

Carley, A.N., and Severson, D.L. (2005). Fatty acid metabolism is enhanced in type 2 diabetic hearts. Biochimica et biophysica acta *1734*, 112-126.

Carling, D., Thornton, C., Woods, A., and Sanders, M.J. (2012). AMP-activated protein kinase: new regulation, new roles? The Biochemical journal *445*, 11-27.

Cazorla, O., Wu, Y., Irving, T.C., and Granzier, H. (2001). Titin-based modulation of calcium sensitivity of active tension in mouse skinned cardiac myocytes. Circulation research *88*, 1028-1035.

Ceriello, A., and Motz, E. (2004). Is oxidative stress the pathogenic mechanism underlying insulin resistance, diabetes, and cardiovascular disease? The common soil hypothesis revisited. Arteriosclerosis, thrombosis, and vascular biology *24*, 816-823.

Chaturvedi, R.R., Herron, T., Simmons, R., Shore, D., Kumar, P., Sethia, B., Chua, F., Vassiliadis, E., and Kentish, J.C. (2010). Passive stiffness of myocardium from congenital heart disease and implications for diastole. Circulation *121*, 979-988.

Cheng, Y., Li, W., McElfresh, T.A., Chen, X., Berthiaume, J.M., Castel, L., Yu, X., Van Wagoner, D.R., and Chandler, M.P. (2011). Changes in myofilament proteins, but not Ca(2)(+) regulation, are associated with a high-fat diet-induced improvement in contractile function in heart failure. American journal of physiology Heart and circulatory physiology *301*, H1438-1446.

Choi, K.M., Zhong, Y., Hoit, B.D., Grupp, I.L., Hahn, H., Dilly, K.W., Guatimosim, S., Lederer, W.J., and Matlib, M.A. (2002). Defective intracellular Ca(2+) signaling contributes to cardiomyopathy in Type 1 diabetic rats. American journal of physiology Heart and circulatory physiology *283*, H1398-1408.

Chu, L., and Endoh, M. (2005). Wortmannin inhibits the myofilament Ca2+ sensitization induced by endothelin-1. European journal of pharmacology *507*, 135-143.

Chung, C.S., Bogomolovas, J., Gasch, A., Hidalgo, C.G., Labeit, S., and Granzier, H.L. (2011). Titin-actin interaction: PEVK-actin-based viscosity in a large animal. Journal of biomedicine & biotechnology *2011*, 310791.

Cingolani, H.E., Alvarez, B.V., Ennis, I.L., and Camilion de Hurtado, M.C. (1998). Stretch-induced alkalinization of feline papillary muscle: an autocrine-paracrine system. Circulation research *83*, 775-780.

Cingolani, H.E., Perez, N.G., Cingolani, O.H., and Ennis, I.L. (2012). The Anrep effect: 100 years later. American journal of physiology Heart and circulatory physiology *304,* 175-182.

Cole, B.K., Keller, S.R., Wu, R., Carter, J.D., Nadler, J.L., and Nunemaker, C.S. (2010). Valsartan protects pancreatic islets and adipose tissue from the inflammatory and metabolic consequences of a high-fat diet in mice. Hypertension *55*, 715-721.

Colson, B.A., Locher, M.R., Bekyarova, T., Patel, J.R., Fitzsimons, D.P., Irving, T.C., and Moss, R.L. (2010). Differential roles of regulatory light chain and myosin binding protein-C phosphorylations in the modulation of cardiac force development. The Journal of physiology *588*, 981-993.

Colson, B.A., Patel, J.R., Chen, P.P., Bekyarova, T., Abdalla, M.I., Tong, C.W., Fitzsimons, D.P., Irving, T.C., and Moss, R.L. (2012). Myosin binding protein-C phosphorylation is the principal mediator of protein kinase A effects on thick filament structure in myocardium. Journal of molecular and cellular cardiology *53*, 609-616.

Coven, D.L., Hu, X., Cong, L., Bergeron, R., Shulman, G.I., Hardie, D.G., and Young, L.H. (2003). Physiological role of AMP-activated protein kinase in the heart: graded activation during exercise. American journal of physiology Endocrinology and metabolism *285*, E629-636.

Cuello, F., Bardswell, S.C., Haworth, R.S., Yin, X., Lutz, S., Wieland, T., Mayr, M., Kentish, J.C., and Avkiran, M. (2007). Protein kinase D selectively targets cardiac troponin I and

regulates myofilament Ca2+ sensitivity in ventricular myocytes. Circulation research *100*, 864-873.

De Giusti, V.C., Correa, M.V., Villa-Abrille, M.C., Beltrano, C., Yeves, A.M., de Cingolani, G.E., Cingolani, H.E., and Aiello, E.A. (2008). The positive inotropic effect of endothelin-1 is mediated by mitochondrial reactive oxygen species. Life sciences *83*, 264-271.

de Tombe, P.P., Mateja, R.D., Tachampa, K., Ait Mou, Y., Farman, G.P., and Irving, T.C. (2010). Myofilament length dependent activation. Journal of molecular and cellular cardiology *48*, 851-858.

Decleves, A.E., Mathew, A.V., Cunard, R., and Sharma, K. (2011). AMPK mediates the initiation of kidney disease induced by a high-fat diet. Journal of the American Society of Nephrology : JASN *22*, 1846-1855.

DeSantiago, J., Maier, L.S., and Bers, D.M. (2002). Frequency-dependent acceleration of relaxation in the heart depends on CaMKII, but not phospholamban. Journal of molecular and cellular cardiology *34*, 975-984.

Dinh, W., Lankisch, M., Nickl, W., Scheyer, D., Scheffold, T., Kramer, F., Krahn, T., Klein, R.M., Barroso, M.C., and Futh, R. (2010). Insulin resistance and glycemic abnormalities are associated with deterioration of left ventricular diastolic function: a cross-sectional study. Cardiovascular diabetology *9*, 63.

Dirkx, E., Schwenk, R.W., Glatz, J.F., Luiken, J.J., and van Eys, G.J. (2011). High fat diet induced diabetic cardiomyopathy. Prostaglandins, leukotrienes, and essential fatty acids *85*, 219-225.

Dobesh, D.P., Konhilas, J.P., and de Tombe, P.P. (2002). Cooperative activation in cardiac muscle: impact of sarcomere length. American journal of physiology Heart and circulatory physiology *282*, H1055-1062.

Dong, W.J., An, J., Xing, J., and Cheung, H.C. (2006). Structural transition of the inhibitory region of troponin I within the regulated cardiac thin filament. Archives of biochemistry and biophysics *456*, 135-142.

Du, H., Shao, J., Gu, P., Lu, B., Ye, X., and Liu, Z. (2012). Improvement of glucose tolerance by rhein with restored early-phase insulin secretion in db/db mice. Journal of endocrinological investigation *35*, 607-612.

Durazzo, M., Belci, P., Collo, A., Grisoglio, E., and Bo, S. (2012). Focus on therapeutic strategies of nonalcoholic Fatty liver disease. International journal of hepatology *2012*, 464706.

Dyck, J.R., and Lopaschuk, G.D. (2006). AMPK alterations in cardiac physiology and pathology: enemy or ally? The Journal of physiology *574*, 95-112.

Edes, I.F., Czuriga, D., Csanyi, G., Chlopicki, S., Recchia, F.A., Borbely, A., Galajda, Z., Edes, I., van der Velden, J., Stienen, G.J.*, et al.* (2007). Rate of tension redevelopment is not

modulated by sarcomere length in permeabilized human, murine, and porcine cardiomyocytes. American journal of physiology Regulatory, integrative and comparative physiology *293*, R20-29.

Eisner, D., Bode, E., Venetucci, L., and Trafford, A. (2012). Calcium flux balance in the heart. Journal of molecular and cellular cardiology *58,* 110-117.

England, J., and Loughna, S. (2013). Heavy and light roles: myosin in the morphogenesis of the heart. Cellular and molecular life sciences : CMLS *70*, 1221-1239.

Fabiato, A., and Fabiato, F. (1975). Dependence of the contractile activation of skinned cardiac cells on the sarcomere length. Nature *256*, 54-56.

Falcao-Pires, I., Hamdani, N., Borbely, A., Gavina, C., Schalkwijk, C.G., van der Velden, J., van Heerebeek, L., Stienen, G.J., Niessen, H.W., Leite-Moreira, A.F.*, et al.* (2011). Diabetes mellitus worsens diastolic left ventricular dysfunction in aortic stenosis through altered myocardial structure and cardiomyocyte stiffness. Circulation *124*, 1151-1159.

Fearnside, J.F., Dumas, M.E., Rothwell, A.R., Wilder, S.P., Cloarec, O., Toye, A., Blancher, C., Holmes, E., Tatoud, R., Barton, R.H.*, et al.* (2008). Phylometabonomic patterns of adaptation to high fat diet feeding in inbred mice. PloS one *3*, e1668.

Frank, O. (1895). Zur Dynamik des Herzmuskels. Z Biol, 370-447.

Fuchs, F., and Smith, S.H. (2001). Calcium, cross-bridges, and the Frank-Starling relationship. News in physiological sciences : an international journal of physiology produced jointly by the International Union of Physiological Sciences and the American Physiological Society *16*, 5-10.

Funato, H., Tsai, A.L., Willie, J.T., Kisanuki, Y., Williams, S.C., Sakurai, T., and Yanagisawa, M. (2009). Enhanced orexin receptor-2 signaling prevents diet-induced obesity and improves leptin sensitivity. Cell metabolism *9*, 64-76.

Ge, Y., Rybakova, I.N., Xu, Q., and Moss, R.L. (2009). Top-down high-resolution mass spectrometry of cardiac myosin binding protein C revealed that truncation alters protein phosphorylation state. Proceedings of the National Academy of Sciences of the United States of America *106*, 12658-12663.

Giacco, F., and Brownlee, M. (2010). Oxidative stress and diabetic complications. Circulation research *107*, 1058-1070.

Giger, J., Qin, A.X., Bodell, P.W., Baldwin, K.M., and Haddad, F. (2007). Activity of the beta-myosin heavy chain antisense promoter responds to diabetes and hypothyroidism. American journal of physiology Heart and circulatory physiology *292*, H3065-3071.

Ginelli, P., and Bella, J.N. (2012). Treatment of diastolic dysfunction in hypertension. Nutrition, metabolism, and cardiovascular diseases : NMCD *22*, 613-618.

Goldberg, I.J., Trent, C.M., and Schulze, P.C. (2012). Lipid metabolism and toxicity in the heart. Cell metabolism *15*, 805-812.

Gordon, A.M., Homsher, E., and Regnier, M. (2000). Regulation of contraction in striated muscle. Physiological reviews *80*, 853-924.

Gordon, A.M., Regnier, M., and Homsher, E. (2001). Skeletal and cardiac muscle contractile activation: tropomyosin "rocks and rolls". News in physiological sciences : an international journal of physiology produced jointly by the International Union of Physiological Sciences and the American Physiological Society *16*, 49-55.

Goyal, B., and Mehta, A. (2012). Diabetic cardiomyopathy: Pathophysiological mechanisms and cardiac dysfuntion. Human & experimental toxicology *32,* 571-590.

Granzier, H.L., and Irving, T.C. (1995). Passive tension in cardiac muscle: contribution of collagen, titin, microtubules, and intermediate filaments. Biophysical journal *68*, 1027-1044.

Gregorio, C.C., and Antin, P.B. (2000). To the heart of myofibril assembly. Trends in cell biology *10*, 355-362.

Grieve, D.J., Byrne, J.A., Siva, A., Layland, J., Johar, S., Cave, A.C., and Shah, A.M. (2006). Involvement of the nicotinamide adenosine dinucleotide phosphate oxidase isoform Nox2 in cardiac contractile dysfunction occurring in response to pressure overload. Journal of the American College of Cardiology *47*, 817-826.

Guyton, A.C. (2001). Textbook of Medicla Physiology, Vol 1, 10th edn (Philadelphia, Pennsylvania, USA: W.B Saunders Company).

Hamdani, N., Bishu, K.G., von Frieling-Salewsky, M., Redfield, M.M., and Linke, W.A. (2013a). Deranged myofilament phosphorylation and function in experimental heart failure with preserved ejection fraction. Cardiovascular research *97*, 464-471.

Hamdani, N., Krysiak, J., Kreusser, M.M., Neef, S., Dos Remedios, C.G., Maier, L.S., Kruger, M., Backs, J., and Linke, W.A. (2013b). Crucial Role for Ca2+/Calmodulin-Dependent Protein Kinase-II in Regulating Diastolic Stress of Normal and Failing Hearts via Titin Phosphorylation. Circulation research *112,* 664-674.

Hanft, L.M., Korte, F.S., and McDonald, K.S. (2008). Cardiac function and modulation of sarcomeric function by length. Cardiovascular research *77*, 627-636.

Hardie, D.G., Ross, F.A., and Hawley, S.A. (2012). AMPK: a nutrient and energy sensor that maintains energy homeostasis. Nature reviews Molecular cell biology *13*, 251-262.

Haworth, R.S., Cuello, F., Herron, T.J., Franzen, G., Kentish, J.C., Gautel, M., and Avkiran, M. (2004). Protein kinase D is a novel mediator of cardiac troponin I phosphorylation and regulates myofilament function. Circulation research *95*, 1091-1099.

Hernandez, O.M., Jones, M., Guzman, G., and Szczesna-Cordary, D. (2007). Myosin essential light chain in health and disease. American journal of physiology Heart and circulatory physiology *292*, H1643-1654.

Heusch, P., Canton, M., Aker, S., van de Sand, A., Konietzka, I., Rassaf, T., Menazza, S., Brodde, O.E., Di Lisa, F., Heusch, G.*, et al.* (2010). The contribution of reactive oxygen species and p38 mitogen-activated protein kinase to myofilament oxidation and progression of heart failure in rabbits. British journal of pharmacology *160*, 1408-1416.

Hidalgo, C., Hudson, B., Bogomolovas, J., Zhu, Y., Anderson, B., Greaser, M., Labeit, S., and Granzier, H. (2009). PKC phosphorylation of titin's PEVK element: a novel and conserved pathway for modulating myocardial stiffness. Circulation research *105*, 631-638, 617 p following 638.

Hofmann, P.A., and Fuchs, F. (1988). Bound calcium and force development in skinned cardiac muscle bundles: effect of sarcomere length. Journal of molecular and cellular cardiology *20*, 667-677.

Hofmann, P.A., Menon, V., and Gannaway, K.F. (1995). Effects of diabetes on isometric tension as a function of [Ca2+] and pH in rat skinned cardiac myocytes. The American journal of physiology *269*, H1656-1663.

Hong, E.G., Jung, D.Y., Ko, H.J., Zhang, Z., Ma, Z., Jun, J.Y., Kim, J.H., Sumner, A.D., Vary, T.C., Gardner, T.W.*, et al.* (2007). Nonobese, insulin-deficient Ins2Akita mice develop type 2 diabetes phenotypes including insulin resistance and cardiac remodeling. American journal of physiology Endocrinology and metabolism *293*, E1687-1696.

Howarth, F.C., Qureshi, M.A., Gbewonyo, A.J., Tariq, S., and Adeghate, E. (2005). The progressive effects of a fat enriched diet on ventricular myocyte contraction and intracellular Ca2+ in the C57BL/6J mouse. Molecular and cellular biochemistry *273*, 87-95.

Hoyer, K., Krenz, M., Robbins, J., and Ingwall, J.S. (2007). Shifts in the myosin heavy chain isozymes in the mouse heart result in increased energy efficiency. Journal of molecular and cellular cardiology *42*, 214-221.

Huggins, C.E., Domenighetti, A.A., Pedrazzini, T., Pepe, S., and Delbridge, L.M. (2003). Elevated intracardiac angiotensin II leads to cardiac hypertrophy and mechanical dysfunction in normotensive mice. Journal of the renin-angiotensin-aldosterone system : JRAAS *4*, 186-190.

Huxley, A.F., and Niedergerke, R. (1954). Structural changes in muscle during contraction; interference microscopy of living muscle fibres. Nature *173*, 971-973.

Huxley, H., and Hanson, J. (1954). Changes in the cross-striations of muscle during contraction and stretch and their structural interpretation. Nature *173*, 973-976.

Ishikawa, T., Kajiwara, H., and Kurihara, S. (1999). Alterations in contractile properties and Ca2+ handling in streptozotocin-induced diabetic rat myocardium. The American journal of physiology *277*, H2185-2194.

Jeremy, R.W., Ambrosio, G., Pike, M.M., Jacobus, W.E., and Becker, L.C. (1993). The functional recovery of post-ischemic myocardium requires glycolysis during early reperfusion. Journal of molecular and cellular cardiology *25*, 261-276.

Jeremy, R.W., Koretsune, Y., Marban, E., and Becker, L.C. (1992). Relation between glycolysis and calcium homeostasis in postischemic myocardium. Circulation research *70*, 1180-1190.

Jweied, E.E., McKinney, R.D., Walker, L.A., Brodsky, I., Geha, A.S., Massad, M.G., Buttrick, P.M., and de Tombe, P.P. (2005). Depressed cardiac myofilament function in human diabetes mellitus. American journal of physiology Heart and circulatory physiology *289*, H2478-2483.

Kang, M., and Chung, K.Y. (2012). PKC-epsilon mediates multiple endothelin-1 actions on systolic Ca2+ and contractility in ventricular myocytes. Biochemical and biophysical research communications *423*, 600-605.

Katz, A.M. (2002). Ernest Henry Starling, his predecessors, and the "Law of the Heart". Circulation *106*, 2986-2992.

Kentish, J.C., McCloskey, D.T., Layland, J., Palmer, S., Leiden, J.M., Martin, A.F., and Solaro, R.J. (2001). Phosphorylation of troponin I by protein kinase A accelerates relaxation and crossbridge cycle kinetics in mouse ventricular muscle. Circulation research *88*, 1059-1065.

Khavandi, K., Khavandi, A., Asghar, O., Greenstein, A., Withers, S., Heagerty, A.M., and Malik, R.A. (2009). Diabetic cardiomyopathy--a distinct disease? Best practice & research Clinical endocrinology & metabolism *23*, 347-360.

Kim, Y.M., Guzik, T.J., Zhang, Y.H., Zhang, M.H., Kattach, H., Ratnatunga, C., Pillai, R., Channon, K.M., and Casadei, B. (2005). A myocardial Nox2 containing NAD(P)H oxidase contributes to oxidative stress in human atrial fibrillation. Circulation research *97*, 629-636.

Kim, Y.M., Kattach, H., Ratnatunga, C., Pillai, R., Channon, K.M., and Casadei, B. (2008). Association of atrial nicotinamide adenine dinucleotide phosphate oxidase activity with the development of atrial fibrillation after cardiac surgery. Journal of the American College of Cardiology *51*, 68-74.

King, A.J. (2012). The use of animal models in diabetes research. British journal of pharmacology *166*, 877-894.

Kobayashi, T., Jin, L., and de Tombe, P.P. (2008). Cardiac thin filament regulation. Pflugers Archiv : European journal of physiology *457*, 37-46.

Kockskamper, J., Khafaga, M., Grimm, M., Elgner, A., Walther, S., Kockskamper, A., von Lewinski, D., Post, H., Grossmann, M., Dorge, H.*, et al.* (2008a). Angiotensin II and myosin light-chain phosphorylation contribute to the stretch-induced slow force response in human atrial myocardium. Cardiovascular research *79*, 642-651.

Kockskamper, J., von Lewinski, D., Khafaga, M., Elgner, A., Grimm, M., Eschenhagen, T., Gottlieb, P.A., Sachs, F., and Pieske, B. (2008b). The slow force response to stretch in atrial and ventricular myocardium from human heart: functional relevance and subcellular mechanisms. Progress in biophysics and molecular biology *97*, 250-267.

Kruger, M., Babicz, K., von Frieling-Salewsky, M., and Linke, W.A. (2010). Insulin signaling regulates cardiac titin properties in heart development and diabetic cardiomyopathy. Journal of molecular and cellular cardiology *48*, 910-916.

Kruger, M., Kotter, S., Grutzner, A., Lang, P., Andresen, C., Redfield, M.M., Butt, E., dos Remedios, C.G., and Linke, W.A. (2009). Protein kinase G modulates human myocardial passive stiffness by phosphorylation of the titin springs. Circulation research *104*, 87-94.

Kruger, M., and Linke, W.A. (2011). The giant protein titin: a regulatory node that integrates myocyte signaling pathways. The Journal of biological chemistry *286*, 9905-9912.

Kuroda, J., Ago, T., Matsushima, S., Zhai, P., Schneider, M.D., and Sadoshima, J. (2010). NADPH oxidase 4 (Nox4) is a major source of oxidative stress in the failing heart. Proceedings of the National Academy of Sciences of the United States of America *107*, 15565-15570.

Lacombe, V.A., Viatchenko-Karpinski, S., Terentyev, D., Sridhar, A., Emani, S., Bonagura, J.D., Feldman, D.S., Gyorke, S., and Carnes, C.A. (2007). Mechanisms of impaired calcium

handling underlying subclinical diastolic dysfunction in diabetes. American journal of physiology Regulatory, integrative and comparative physiology *293*, R1787-1797.

Lassegue, B., San Martin, A., and Griendling, K.K. (2012). Biochemistry, physiology, and pathophysiology of NADPH oxidases in the cardiovascular system. Circulation research *110*, 1364-1390.

Layland, J., and Kentish, J.C. (2002). Myofilament-based relaxant effect of isoprenaline revealed during work-loop contractions in rat cardiac trabeculae. The Journal of physiology *544*, 171-182.

Layland, J., Solaro, R.J., and Shah, A.M. (2005). Regulation of cardiac contractile function by troponin I phosphorylation. Cardiovascular research *66*, 12-21.

Lehman, W., Hatch, V., Korman, V., Rosol, M., Thomas, L., Maytum, R., Geeves, M.A., Van Eyk, J.E., Tobacman, L.S., and Craig, R. (2000). Tropomyosin and actin isoforms modulate the localization of tropomyosin strands on actin filaments. Journal of molecular biology *302*, 593-606.

LeWinter, M.M., and Granzier, H. (2010). Cardiac titin: a multifunctional giant. Circulation *121*, 2137-2145.

Li, S.Y., Yang, X., Ceylan-Isik, A.F., Du, M., Sreejayan, N., and Ren, J. (2006). Cardiac contractile dysfunction in Lep/Lep obesity is accompanied by NADPH oxidase activation,

oxidative modification of sarco(endo)plasmic reticulum Ca2+-ATPase and myosin heavy chain isozyme switch. Diabetologia *49*, 1434-1446.

Lopaschuk, G.D., Folmes, C.D., and Stanley, W.C. (2007). Cardiac energy metabolism in obesity. Circulation research *101*, 335-347.

Lopaschuk, G.D., Ussher, J.R., Folmes, C.D., Jaswal, J.S., and Stanley, W.C. (2010). Myocardial fatty acid metabolism in health and disease. Physiological reviews *90*, 207-258.

Lovelock, J.D., Monasky, M.M., Jeong, E.M., Lardin, H.A., Liu, H., Patel, B.G., Taglieri, D.M., Gu, L., Kumar, P., Pokhrel, N.*, et al.* (2012). Ranolazine improves cardiac diastolic dysfunction through modulation of myofilament calcium sensitivity. Circulation research *110*, 841-850.

Luther, P.K., Bennett, P.M., Knupp, C., Craig, R., Padron, R., Harris, S.P., Patel, J., and Moss, R.L. (2008). Understanding the organisation and role of myosin binding protein C in normal striated muscle by comparison with MyBP-C knockout cardiac muscle. Journal of molecular biology *384*, 60-72.

Luther, P.K., Winkler, H., Taylor, K., Zoghbi, M.E., Craig, R., Padron, R., Squire, J.M., and Liu, J. (2011). Direct visualization of myosin-binding protein C bridging myosin and actin filaments in intact muscle. Proceedings of the National Academy of Sciences of the United States of America *108*, 11423-11428.

Malmqvist, U.P., Aronshtam, A., and Lowey, S. (2004). Cardiac myosin isoforms from different species have unique enzymatic and mechanical properties. Biochemistry *43*, 15058-15065.

Mandavia, C.H., Aroor, A.R., Demarco, V.G., and Sowers, J.R. (2012). Molecular and metabolic mechanisms of cardiac dysfunction in diabetes. Life sciences *92,* 601-608.

Martyn, D.A., and Gordon, A.M. (2001). Influence of length on force and activation-dependent changes in troponin c structure in skinned cardiac and fast skeletal muscle. Biophysical journal *80*, 2798-2808.

McDonald, K.S. (2011). The interdependence of Ca2+ activation, sarcomere length, and power output in the heart. Pflugers Archiv : European journal of physiology *462*, 61-67.

Milligan, R.A., Whittaker, M., and Safer, D. (1990). Molecular structure of F-actin and location of surface binding sites. Nature *348*, 217-221.

Mizushige, K., Yao, L., Noma, T., Kiyomoto, H., Yu, Y., Hosomi, N., Ohmori, K., and Matsuo, H. (2000). Alteration in left ventricular diastolic filling and accumulation of myocardial collagen at insulin-resistant prediabetic stage of a type II diabetic rat model. Circulation *101*, 899-907.

Monasky, M.M., Taglieri, D.M., Jacobson, A.K., Haizlip, K.M., Solaro, R.J., and Janssen, P.M. (2012). Post-translational modifications of myofilament proteins involved in length-

dependent prolongation of relaxation in rabbit right ventricular myocardium. Archives of biochemistry and biophysics *535,* 22-29.

Montessuit, C., and Lerch, R. (2012). Regulation and dysregulation of glucose transport in cardiomyocytes. Biochimica et biophysica acta *1833,* 848-856.

Montezano, A.C., and Touyz, R.M. (2012). Molecular mechanisms of hypertension--reactive oxygen species and antioxidants: a basic science update for the clinician. The Canadian journal of cardiology *28*, 288-295.

Morales-Alamo, D., Ponce-Gonzalez, J.G., Guadalupe-Grau, A., Rodriguez-Garcia, L., Santana, A., Cusso, M.R., Guerrero, M., Guerra, B., Dorado, C., and Calbet, J.A. (2012). Increased oxidative stress and anaerobic energy release, but blunted Thr172-AMPKalpha phosphorylation, in response to sprint exercise in severe acute hypoxia in humans. J Appl Physiol *113*, 917-928.

Murakami, K., Stewart, M., Nozawa, K., Tomii, K., Kudou, N., Igarashi, N., Shirakihara, Y., Wakatsuki, S., Yasunaga, T., and Wakabayashi, T. (2008). Structural basis for tropomyosin overlap in thin (actin) filaments and the generation of a molecular swivel by troponin-T. Proceedings of the National Academy of Sciences of the United States of America *105*, 7200-7205.

Muthu, P., Kazmierczak, K., Jones, M., and Szczesna-Cordary, D. (2012). The effect of myosin RLC phosphorylation in normal and cardiomyopathic mouse hearts. Journal of cellular and molecular medicine *16*, 911-919.

Muthu, P., Wang, L., Yuan, C.C., Kazmierczak, K., Huang, W., Hernandez, O.M., Kawai, M., Irving, T.C., and Szczesna-Cordary, D. (2011). Structural and functional aspects of the myosin essential light chain in cardiac muscle contraction. FASEB journal : official publication of the Federation of American Societies for Experimental Biology *25*, 4394-4405.

Niggli, E., Ullrich, N.D., Gutierrez, D., Kyrychenko, S., Polakova, E., and Shirokova, N. (2012). Posttranslational modifications of cardiac ryanodine receptors: Ca(2+) signaling and EC-coupling. Biochimica et biophysica acta *1833,* 866-875.

Nikoulina, S.E., Ciaraldi, T.P., Mudaliar, S., Mohideen, P., Carter, L., and Henry, R.R. (2000). Potential role of glycogen synthase kinase-3 in skeletal muscle insulin resistance of type 2 diabetes. Diabetes *49*, 263-271.

Nixon, B.R., Liu, B., Scellini, B., Tesi, C., Piroddi, N., Ogut, O., John Solaro, R., Ziolo, M.T., Janssen, P.M., Davis, J.P.*, et al.* (2012a). Tropomyosin Ser-283 pseudo-phosphorylation slows myofibril relaxation. Archives of biochemistry and biophysics *535,* 30-38.

Nixon, B.R., Thawornkaiwong, A., Jin, J., Brundage, E.A., Little, S.C., Davis, J.P., Solaro, R.J., and Biesiadecki, B.J. (2012b). AMP-activated protein kinase phosphorylates cardiac troponin I at Ser-150 to increase myofilament calcium sensitivity and blunt PKA-dependent function. The Journal of biological chemistry *287*, 19136-19147.

Noyan-Ashraf, M.H., Shikatani, E.A., Schuiki, I., Mukovozov, I., Wu, J., Li, R.K., Volchuk, A., Robinson, L.A., Billia, F., Drucker, D.J.*, et al.* (2012). A Glucagon-Like Peptide-1 Analogue Reverses the Molecular Pathology and Cardiac Dysfunction of a Mouse Model of Obesity. Circulation *127, 74-85*.

Oliveira, S.M., Zhang, Y.H., Solis, R.S., Isackson, H., Bellahcene, M., Yavari, A., Pinter, K., Davies, J.K., Ge, Y., Ashrafian, H.*, et al.* (2012). AMP-activated protein kinase phosphorylates cardiac troponin I and alters contractility of murine ventricular myocytes. Circulation research *110*, 1192-1201.

Omar, B., Pacini, G., and Ahren, B. (2012). Differential development of glucose intolerance and pancreatic islet adaptation in multiple diet induced obesity models. Nutrients *4*, 1367-1381.

Orchard, C., and Brette, F. (2008). t-Tubules and sarcoplasmic reticulum function in cardiac ventricular myocytes. Cardiovascular research *77*, 237-244.

Ouwens, D.M., Boer, C., Fodor, M., de Galan, P., Heine, R.J., Maassen, J.A., and Diamant, M. (2005). Cardiac dysfunction induced by high-fat diet is associated with altered myocardial insulin signalling in rats. Diabetologia *48*, 1229-1237.

Parekh, P.I., Petro, A.E., Tiller, J.M., Feinglos, M.N., and Surwit, R.S. (1998). Reversal of diet-induced obesity and diabetes in C57BL/6J mice. Metabolism: clinical and experimental *47*, 1089-1096.

Park, S.Y., Cho, Y.R., Kim, H.J., Higashimori, T., Danton, C., Lee, M.K., Dey, A., Rothermel, B., Kim, Y.B., Kalinowski, A.*, et al.* (2005). Unraveling the temporal pattern of diet-induced insulin resistance in individual organs and cardiac dysfunction in C57BL/6 mice. Diabetes *54*, 3530-3540.

Patterson, S.W., and Starling, E.H. (1914). On the mechanical factors which determine the output of the ventricles. The Journal of physiology *48*, 357-379.

Perez, N.G., Nolly, M.B., Roldan, M.C., Villa-Abrille, M.C., Cingolani, E., Portiansky, E.L., Alvarez, B.V., Ennis, I.L., and Cingolani, H.E. (2011). Silencing of NHE-1 blunts the slow force response to myocardial stretch. J Appl Physiol *111*, 874-880.

Pfeiffer, S., Leopold, E., Schmidt, K., Brunner, F., and Mayer, B. (1996). Inhibition of nitric oxide synthesis by NG-nitro-L-arginine methyl ester (L-NAME): requirement for bioactivation to the free acid, NG-nitro-L-arginine. British journal of pharmacology *118*, 1433-1440.

Prosser, B.L., Ward, C.W., and Lederer, W.J. (2011). X-ROS signaling: rapid mechano-chemo transduction in heart. Science *333*, 1440-1445.

Pyle, W.G., and Solaro, R.J. (2004). At the crossroads of myocardial signaling: the role of Z-discs in intracellular signaling and cardiac function. Circulation research *94*, 296-305.

Rayasam, G.V., Tulasi, V.K., Sodhi, R., Davis, J.A., and Ray, A. (2009). Glycogen synthase kinase 3: more than a namesake. British journal of pharmacology *156*, 885-898.

Reilly, S.N., Jayaram, R., Nahar, K., Antoniades, C., Verheule, S., Channon, K.M., Alp, N.J., Schotten, U., and Casadei, B. (2011). Atrial sources of reactive oxygen species vary with the duration and substrate of atrial fibrillation: implications for the antiarrhythmic effect of statins. Circulation *124*, 1107-1117.

Reuter, H., Gronke, S., Adam, C., Ribati, M., Brabender, J., Zobel, C., Frank, K.F., Wippermann, J., Schwinger, R.H., Brixius, K.*, et al.* (2008). Sarcoplasmic Ca2+ release is prolonged in nonfailing myocardium of diabetic patients. Molecular and cellular biochemistry *308*, 141-149.

Roberts, C.K., and Sindhu, K.K. (2009). Oxidative stress and metabolic syndrome. Life sciences *84*, 705-712.

Robinson, P., Griffiths, P.J., Watkins, H., and Redwood, C.S. (2007). Dilated and hypertrophic cardiomyopathy mutations in troponin and alpha-tropomyosin have opposing effects on the calcium affinity of cardiac thin filaments. Circulation research *101*, 1266-1273.

Robinson, P., Mirza, M., Knott, A., Abdulrazzak, H., Willott, R., Marston, S., Watkins, H., and Redwood, C. (2002). Alterations in thin filament regulation induced by a human cardiac troponin T mutant that causes dilated cardiomyopathy are distinct from those induced by troponin T mutants that cause hypertrophic cardiomyopathy. The Journal of biological chemistry *277*, 40710-40716.

Rundell, V.L., Geenen, D.L., Buttrick, P.M., and de Tombe, P.P. (2004). Depressed cardiac tension cost in experimental diabetes is due to altered myosin heavy chain isoform expression. American journal of physiology Heart and circulatory physiology *287*, H408-413.

Russell, R.R., 3rd, Bergeron, R., Shulman, G.I., and Young, L.H. (1999). Translocation of myocardial GLUT-4 and increased glucose uptake through activation of AMPK by AICAR. The American journal of physiology *277*, H643-649.

Sanchez, G., Escobar, M., Pedrozo, Z., Macho, P., Domenech, R., Hartel, S., Hidalgo, C., and Donoso, P. (2008). Exercise and tachycardia increase NADPH oxidase and ryanodine receptor-2 activity: possible role in cardioprotection. Cardiovascular research *77*, 380-386.

Sandow, A. (1952). Excitation-contraction coupling in muscular response. The Yale journal of biology and medicine *25*, 176-201.

Santos, C.X., Anilkumar, N., Zhang, M., Brewer, A.C., and Shah, A.M. (2011). Redox signaling in cardiac myocytes. Free radical biology & medicine *50*, 777-793.

Schober, T., Huke, S., Venkataraman, R., Gryshchenko, O., Kryshtal, D., Hwang, H.S., Baudenbacher, F.J., and Knollmann, B.C. (2012). Myofilament Ca sensitization increases cytosolic Ca binding affinity, alters intracellular Ca homeostasis, and causes pause-dependent Ca-triggered arrhythmia. Circulation research *111*, 170-179.

Scruggs, S.B., and Solaro, R.J. (2011). The significance of regulatory light chain phosphorylation in cardiac physiology. Archives of biochemistry and biophysics *510*, 129-134.

Sedeek, M., Montezano, A.C., Hebert, R.L., Gray, S.P., Di Marco, E., Jha, J.C., Cooper, M.E., Jandeleit-Dahm, K., Schiffrin, E.L., Wilkinson-Berka, J.L.*, et al.* (2012). Oxidative stress, Nox isoforms and complications of diabetes--potential targets for novel therapies. Journal of cardiovascular translational research *5*, 509-518.

Shao, C.H., Capek, H.L., Patel, K.P., Wang, M., Tang, K., DeSouza, C., Nagai, R., Mayhan, W., Periasamy, M., and Bidasee, K.R. (2011). Carbonylation contributes to SERCA2a activity loss and diastolic dysfunction in a rat model of type 1 diabetes. Diabetes *60*, 947-959.

Sheikh, F., Ouyang, K., Campbell, S.G., Lyon, R.C., Chuang, J., Fitzsimons, D., Tangney, J., Hidalgo, C.G., Chung, C.S., Cheng, H.*, et al.* (2012). Mouse and computational models link Mlc2v dephosphorylation to altered myosin kinetics in early cardiac disease. The Journal of clinical investigation *122*, 1209-1221.

Shen, X., and Bornfeldt, K.E. (2007). Mouse models for studies of cardiovascular complications of type 1 diabetes. Annals of the New York Academy of Sciences *1103*, 202-217.

Shevalye, H., Lupachyk, S., Watcho, P., Stavniichuk, R., Khazim, K., Abboud, H.E., and Obrosova, I.G. (2012). Prediabetic nephropathy as an early consequence of the high-calorie/high-fat diet: relation to oxidative stress. Endocrinology *153*, 1152-1161.

Shiels, H.A., and White, E. (2008). The Frank-Starling mechanism in vertebrate cardiac myocytes. The Journal of experimental biology *211*, 2005-2013.

Sirker, A., Zhang, M., and Shah, A.M. (2011). NADPH oxidases in cardiovascular disease: insights from in vivo models and clinical studies. Basic research in cardiology *106*, 735-747.

Solaro, R.J., and Kobayashi, T. (2011). Protein phosphorylation and signal transduction in cardiac thin filaments. The Journal of biological chemistry *286*, 9935-9940.

Solaro, R.J., Pang, D.C., and Briggs, F.N. (1971). The purification of cardiac myofibrils with Triton X-100. Biochimica et biophysica acta *245*, 259-262.

Spurgeon, H.A., duBell, W.H., Stern, M.D., Sollott, S.J., Ziman, B.D., Silverman, H.S., Capogrossi, M.C., Talo, A., and Lakatta, E.G. (1992). Cytosolic calcium and myofilaments in single rat cardiac myocytes achieve a dynamic equilibrium during twitch relaxation. The Journal of physiology *447*, 83-102.

Squire, J.M. (1997). Architecture and function in the muscle sarcomere. Current opinion in structural biology *7*, 247-257.

Squire, J.M., Al-Khayat, H.A., Knupp, C., and Luther, P.K. (2005). Molecular architecture in muscle contractile assemblies. Advances in protein chemistry *71*, 17-87.

Srinivasan, K., and Ramarao, P. (2007). Animal models in type 2 diabetes research: an overview. The Indian journal of medical research *125*, 451-472.

Steinberg, S.F. (2012). Cardiac actions of protein kinase C isoforms. Physiology (Bethesda) *27*, 130-139.

Steinberg, S.F. (2013). Oxidative stress and sarcomeric proteins. Circulation research *112*, 393-405.

Sumandea, M.P., Pyle, W.G., Kobayashi, T., de Tombe, P.P., and Solaro, R.J. (2003). Identification of a functionally critical protein kinase C phosphorylation residue of cardiac troponin T. The Journal of biological chemistry *278*, 35135-35144.

Sun, Y.B., Lou, F., and Irving, M. (2009). Calcium- and myosin-dependent changes in troponin structure during activation of heart muscle. The Journal of physiology *587*, 155-163.

Surwit, R.S., Feinglos, M.N., Rodin, J., Sutherland, A., Petro, A.E., Opara, E.C., Kuhn, C.M., and Rebuffe-Scrive, M. (1995). Differential effects of fat and sucrose on the development of obesity and diabetes in C57BL/6J and A/J mice. Metabolism: clinical and experimental *44*, 645-651.

Suzuki, T., Palmer, B.M., James, J., Wang, Y., Chen, Z., VanBuren, P., Maughan, D.W., Robbins, J., and LeWinter, M.M. (2009). Effects of cardiac myosin isoform variation on myofilament function and crossbridge kinetics in transgenic rabbits. Circulation Heart failure *2*, 334-341.

Swaminathan, P.D., Purohit, A., Hund, T.J., and Anderson, M.E. (2012). Calmodulin-dependent protein kinase II: linking heart failure and arrhythmias. Circulation research *110*, 1661-1677.

Sweeney, H.L., Bowman, B.F., and Stull, J.T. (1993). Myosin light chain phosphorylation in vertebrate striated muscle: regulation and function. The American journal of physiology *264*, C1085-1095.

Takeda, S. (2005). Crystal structure of troponin and the molecular mechanism of muscle regulation. Journal of electron microscopy *54 Suppl 1*, i35-41.

ten Freyhaus, H., Huntgeburth, M., Wingler, K., Schnitker, J., Baumer, A.T., Vantler, M., Bekhite, M.M., Wartenberg, M., Sauer, H., and Rosenkranz, S. (2006). Novel Nox inhibitor VAS2870 attenuates PDGF-dependent smooth muscle cell chemotaxis, but not proliferation. Cardiovascular research *71*, 331-341.

Van Belle, T.L., Taylor, P., and von Herrath, M.G. (2009). Mouse Models for Type 1 Diabetes. Drug discovery today Disease models *6*, 41-45.

VanBuren, P., Harris, D.E., Alpert, N.R., and Warshaw, D.M. (1995). Cardiac V1 and V3 myosins differ in their hydrolytic and mechanical activities in vitro. Circulation research *77*, 439-444.

Vanburen, P., and Palmer, B.M. (2010). Cooperative activation of the cardiac myofilament: the pivotal role of tropomyosin. Circulation *121*, 351-353.

Venetucci, L.A., Trafford, A.W., O'Neill, S.C., and Eisner, D.A. (2008). The sarcoplasmic reticulum and arrhythmogenic calcium release. Cardiovascular research *77*, 285-292.

Vitiello, D., Boissiere, J., Doucende, G., Gayrard, S., Polge, A., Faure, P., Goux, A., Tanguy, S., Obert, P., Reboul, C.*, et al.* (2011). beta-Adrenergic receptors desensitization is not involved in exercise-induced cardiac fatigue: NADPH oxidase-induced oxidative stress as a new trigger. J Appl Physiol *111*, 1242-1248.

Wagner, S., Rokita, A.G., Anderson, M.E., and Maier, L.S. (2012). Redox Regulation of Sodium and Calcium Handling. Antioxidants & redox signaling *18,* 1063-1077.

Wang, H., Grant, J.E., Doede, C.M., Sadayappan, S., Robbins, J., and Walker, J.W. (2006). PKC-betaII sensitizes cardiac myofilaments to Ca2+ by phosphorylating troponin I on threonine-144. Journal of molecular and cellular cardiology *41*, 823-833.

Wang, X., and Su, H. (2010). Unraveling enigma in the z-disks. Circulation research *107*, 321-323.

Wang, Y.P., and Fuchs, F. (1994). Length, force, and Ca(2+)-troponin C affinity in cardiac and slow skeletal muscle. The American journal of physiology *266*, C1077-1082.

Wang, Z.V., Mu, J., Schraw, T.D., Gautron, L., Elmquist, J.K., Zhang, B.B., Brownlee, M., and Scherer, P.E. (2008). PANIC-ATTAC: a mouse model for inducible and reversible beta-cell ablation. Diabetes *57*, 2137-2148.

Watkins, H., Ashrafian, H., and Redwood, C. (2011). Inherited cardiomyopathies. The New England journal of medicine *364*, 1643-1656.

Wende, A.R., Symons, J.D., and Abel, E.D. (2012). Mechanisms of lipotoxicity in the cardiovascular system. Current hypertension reports *14*, 517-531.

Winzell, M.S., and Ahren, B. (2004). The high-fat diet-fed mouse: a model for studying mechanisms and treatment of impaired glucose tolerance and type 2 diabetes. Diabetes *53 Suppl 3*, S215-219.

Wu, Y., Cazorla, O., Labeit, D., Labeit, S., and Granzier, H. (2000). Changes in titin and collagen underlie diastolic stiffness diversity of cardiac muscle. Journal of molecular and cellular cardiology *32*, 2151-2162.

Yamasaki, R., Wu, Y., McNabb, M., Greaser, M., Labeit, S., and Granzier, H. (2002). Protein kinase A phosphorylates titin's cardiac-specific N2B domain and reduces passive tension in rat cardiac myocytes. Circulation research *90*, 1181-1188.

Zhang, M., Perino, A., Ghigo, A., Hirsch, E., and Shah, A.M. (2013). NADPH oxidases in heart failure: poachers or gamekeepers? Antioxidants & redox signaling *18*, 1024-1041.

Zhang, Y.H., Dingle, L., Hall, R., and Casadei, B. (2009). The role of nitric oxide and reactive oxygen species in the positive inotropic response to mechanical stretch in the mammalian myocardium. Biochimica et biophysica acta *1787*, 811-817.

# Appendix 1 – Solutions

All reagents from Sigma Aldrich unless otherwise stated

## Molecular biology buffers

**Urea lysis buffer (mM):** Urea 7; SDS 1 % w/v; glycerol 10% v/v; Tris-HCl 10 (pH 6.8); EDTA 1; Protease inhibitors EDTA-free 1/50ml (Roche diagnostics, UK. Cat. No: 11873580001); PhosStop 1/10 ml (Roche diagnostics, UK. Cat. No: 04906837001); Na-orthovanadate 1; dithiothreitol (DTT) 5.

**2x SDS-PAGE Stacking gel buffer (mM)**

Tris-HCl (25), SDS 1 % w/v, pH 6.8 with NaOH

**2x SDS-PAGE Resolving gel buffer (mM)**

Tris-base (750), SDS 1 % (w/v), pH 8.8 with NaOH

**SDS-PAGE running buffer (mM)**

Tris-HCl (25), Glycine (19.2), SDS 0.1 %

**Transfer buffer (mM)**

Tris-base (48), glycine (390), methanol 20% (v/v), SDS 0.1 % (w/v)

**Protein sample loading buffer 6 x concentrated**

Stacking gel buffer 40 % (v/v), glycerol 40 % (v/v), SDS 2 % (w/v), 2-mercaptoethanol 10 % (v/v), MQ water 10 % v/v.

## Single cell buffers

**Tyrode's solution (mM):** NaCl 130; KCl 5.6; HEPES 5; $NaH_2PO_4$ 0.4; $MgCl_2$ 3.5; Taurine 20; Glucose 10.

**BSA-enriched Tyrode's solution:** BSA 1 % w/v in Tyrode's solution.

**Digestive enzyme enriched Tyrode's solution:** 80 % volume Tyrode's solution; 20 % volume BSA enriched Tyrode's solution; Collagenase type 275 U/mg, (Worthington Biochemical corporation, NJ, USA. Cat. No: 41E12715) 1 mg/ml; Protease (Sigma Aldrich Cat. No: P6911) 0.1 mg/ml.

**Collagenase solution (mM):** 83.5 % volume Tyrode's solution; 16.5% volume BSA-enriched Tyrode's solution; Collagenase type 275 U/mg, (Worthington Biochemical corporation, NJ, USA. Cat. No: 41E12715) 1 mg/ml; $CaCl_2$ 0.075.

**Enzyme stopping solution (mM):** BSA-enriched Tyrode's solution; $CaCl_2$ 0.1.

**Storage solution (mM):** NaCl 120; KCl 5.6; $MgSO_4$ 5; $CaCl_2$ 0.2; Na-pyruvate 5; HEPES 10; Taurine 20; Glucose 20.

**Perfusion solution (mM):** NaCl 140; KCl 5.6; $MgCl_2$ 1.2; HEPES 5; $CaCl_2$ 1.4; Glucose 10.

All above solutions were brought to pH 7.4 at room temperature using NaOH.

## Demembranated trabeculae buffers

**Relaxing solution (mM):** EGTA 10; $MgCl_2$ 5.6; KCl 100; Imidazole 20; ATP 5; Creatine phosphate 10; Creatine kinase (15 U/ml); Protease inhibitors EDTA-free 1/50ml (Roche diagnostics, UK. Cat. No: 11873580001)

**Activating solution (mM):** $CaCl_2$ 10.4; EGTA 10; $MgCl_2$ 5.6; KCl 68.8; Imidazole 20; ATP 5; Creatine phosphate 10; Creatine kinase (15 U/ml); Protease inhibitors EDTA-free 1/50ml (Roche diagnostics, UK. Cat. No: 11873580001)

**Dissecting solution (mM):** EGTA 10; $MgCl_2$ 5.6; KCl 100; Imidazole 20; ATP 5; Creatine phosphate 10; Creatine kinase (15 U/ml); 2,3-Butanedione monoxime (BDM) 20; Protease inhibitors EDTA-free 1/50ml (Roche diagnostics, UK. Cat. No: 11873580001)

All above solutions were brought to pH 7.0 at 10 °C using KOH.

## Myofilament isolation buffers (mM)

**Lysis buffer:**
Sucrose 300; imidazole 10; protease inhibitor tabl 1/50 ml (Roche diagnostics, UK. Cat. No: 11873580001); PhosStop 1/10 ml (Roche diagnostics, UK. Cat. No: 04906837001).

**Standard isolation buffer:**
KCl 60; Imidazole 30; $MgCl_2$ 2; protease inhibitor tabl 1/50 ml (Roche diagnostics, UK. Cat. No: 11873580001); PhosStop 1/10 ml (Roche diagnostics, UK. Cat. No: 04906837001).

**EGTA buffer:** Standard isolation buffer + EGTA 2; protease inhibitor tabl 1/50 ml (Roche diagnostics, UK. Cat. No: 11873580001); PhosStop 1/10 ml (Roche diagnostics, UK. Cat. No: 04906837001).

**Triton X-100:**
Standard isolation buffer + Triton X-100 1% v/v; protease inhibitor tabl 1/50 ml (Roche diagnostics, UK. Cat. No: 11873580001); PhosStop 1/10 ml (Roche diagnostics, UK. Cat. No: 04906837001).

All pH at 7.0 at room temperature

## Reactive oxygen species measurement buffers

**Krebs-HEPES buffer (mM):**

NaCl 99; KCl 4.7; $MgSO_4$ 1.2; $KH_2PO_4$ 1; $CaCl_2$ 1.9; $NaHCO_3$ 25; glucose 11.1; Na-HEPES 20; Protease inhibitor tabl 1/50 ml (Roche diagnostics, UK. Cat. No: 11873580001).

pH 7.4 at room temperature.

## Histology buffers

**Oil Red O stock:**

Oil Red O (0.5 g), 100 ml isopropranol

**Oil Red O working solution:**

30 ml Oil Red O stock solution, 20 ml MQ $H_20$. Pass through a 0.45 μm diameter filter under pressure.

**Alum haematoxylin:**

$KAl(SO_4)_2$ (50 g), haematoxylin (1 g), $NaIO_3$ (0.2g), glacial acetic acid (20 ml), MQ $H_20$ (1000 ml).

**Glycerine mounting jelly*:***

Gelatin (10 g), MQ $H_20$ 60 ml, glycerol 70 ml, phenol (0.25 g).

# The effects of high fat diet feeding on cardiac function in the C57BL6/J mouse strain

**Henrik CA Isackson**

**Exeter College**

**A thesis submitted for the degree of D.Phil, Hilary term, 2013**

## ABSTRACT

It has been established that placing the C57BL6/J mouse on a high fat diet induces obesity and impaired glucose homeostasis, and produces a model that is pathophysiologically relevant to the human condition of the metabolic syndrome. The cardiovascular changes in this model have been relatively poorly explored. I have focussed my work on understanding the effects of this diet on cardiac function using *in vivo* cardiac functional assessment in combination with *in vitro* analysis of intact single cardiomyocyte dynamics and $Ca^{2+}$ handling, as well as demembranated left ventricle trabeculae for the study of myofilament function. High fat diet caused increased left ventricular end diastolic pressure after 30 weeks as assessed by *in vivo* pressure catheterisation. This change was associated with, increased passive tension in demembranated trabeculae at 30 w, increased collagen 3 expression on mRNA level and increased total tissue collagen from high fat diet after 40 weeks. Reversion to normal diet for 10 weeks had no discernible effect on whole organ function compared with animals continually fed with the high fat diet, despite body fat content and glucose homeostasis becoming normalised. Isolated cardiomyocytes exhibited increased relaxation rate after 40 weeks which was partly reversed by a return to normal diet. The increased cardiomyocyte relaxation rate occurred without changes to the intracellular $Ca^{2+}$ transient, thus suggesting it may be caused by altered myofilament $Ca^{2+}$ sensitivity. There was no established decreased myofilament $Ca^{2+}$ sensitivity seen in demembranated trabeculae at week 40, even though trends were seen towards increased phosphorylation of serines 23/24 of cardiac troponin I, a modification known to induce $Ca^{2+}$ desensitisation.

It is concluded that high fat diet feeding in the C57BL6/J mouse is a mild but valid model for studying the effects on cardiac function of obesity and impaired glucose handling. It results in impaired diastolic function at the whole organ level after 30 weeks feeding. This effect is likely principally caused by extracellular deposition of collagen (which reduces compliance) rather than by changes at the cardiomyocyte level. This whole organ diastolic alteration appears to become established, not responding to dietary fat reduction. The increased relaxation rate of cardiomyocytes more likely originates from changes at the myofilament level as opposed to $Ca^{2+}$ handling although this could not be statistically verified in this study.

As high fat diet feeding was found to increase myocardial NADPH oxidase activity, myofilament function was also assessed in a mouse model of NADPH oxidase 2 over-expression. NADPH oxidase 2 over-expression was found to cause myofilament sensitisation to $Ca^{2+}$ and increased actomyosin cross bridge cycling rate at maximum $Ca^{2+}$ activation. This was associated with an increased total phosphorylation of cardiac troponin I independent of phosphorylation of serines 23/24. This finding may represent a new signalling pathway linking NADPH oxidase 2 activity to contractile activation via the myofilament but appears opposite to myofilament changes induced by high fat diet feeding.

**DECLARATION**

The data presented in this thesis are as a result of investigations carried out by the author. Exceptions are credited in the text and are as follows: Dr Alexander Stockenhuber performed Oil Red O stain of liver cryosections, Dr Mohammed Bellahcene carried out *in vivo* haemodynamics, Dr Arash Yavari carried out transthoracic echocardiography, Dr Gabor Czibik carried out quantitative reverse transcriptase-polymerase chain reactions, and Dr Radu Tanacli carried out the immunoblotting for NADPH oxidase 2 and superoxide generation rate experiments presented in Chapter 7.

Henrik Isackson

April 2013

**ACKNOWLEDGEMENTS**

I am grateful towards my DPhil supervisors Dr Charles Redwood and Prof Hugh Watkins who have both been supportive during the application process as well as in the execution of the study presented in this thesis. An explicit thank you is due to Charles for his day to day supervision and constant availability for advice.

I am indebted to Prof Barbara Casadei for allowing me to use her single cardiomyocyte rig, and to her group members for advice regarding the single cardiomyocyte isolation technique. The same applies to the group of Dr Charis Antoniades with respect to reactive oxygen species assays.

The following members of the Watkins group, past and present, have all been helpful in discussing experimental strategies and the meaning and importance of findings, as well as contributing to a good atmosphere over the course of the work towards a DPhil: Dr Houman Ashrafian, Dr Mohamed Bellahcene, Dr James Brown, Dr Gabor Czibik, Dr Matthew Daniels, Dr Katja Gehmlich, Dr Matthew Kelly, Mr Adam Piers, Dr Katalin Pinter, Dr Paul Robinson, Miss Violetta Steeples, Dr Alex Stockenhuber, Dr Radu Tanacli, Mr Philip Townsend, Mr Cameron Turtle, and Dr Arash Yavari.

Much gratitude is also directed to my former supervisors for introducing me to muscle physiology and staying in contact. Prof Anders Arner at the Karolinska Institute in Stockholm, as well as Prof Chris Ashley and Dr Peter Griffiths in the Department of Physiology, Anatomy, and Genetics in Oxford. All have always shown an accommodating and enthusiastic approach towards educating and helping a novice.

I am especially grateful to my close friends Adam, Al, Gabor, and Radu for their social as well as scientific support during these years in Oxford.

The last paragraph I write before submission I want to dedicate to my family in Sweden for their love and patience with my long stints abroad: my dear mother and father, Dorthy and Anders, as well as my two beautiful sisters, Anna and Charlotte.

The work presented herein had not been possible without the financial support of the British Heart Foundation.

# TABLE OF CONTENTS

ABSTRACT i

DECLARATION ii

ACKNOWLEDGEMENTS iii

TABLE OF CONTENTS iv

LIST OF FIGURES, TABLES, AND EQUATIONS xi

LIST OF ABBREVIATIONS xiv

1 Introduction ..... 1

1.1 Cardiomyocyte contractility ..... 1

1.1.1 The initiation of cardiomyocyte contraction ..... 1

1.1.1.1 Excitation contraction coupling ..... 1

1.1.1.1.1 Calcium induced calcium release (CICR) ..... 2

1.1.1.1.2 Cytosolic $Ca^{2+}$ extrusion ..... 4

There are two major pathways for $Ca^{2+}$ extrusion from the cardiomyocyte cytoplasm: trans-sarcolemmal extrusion and SR reuptake. ..... 4

1.1.1.2 Myofilament dynamics ..... 5

1.1.1.2.1 The sarcomeric protein assembly ..... 5

**The thick filament** ..... 6

Cardiac myosin light chains (MLCs) ..... 7

Cardiac myosin binding protein C (cMyBP-C) ..... 8

**The thin filament** ..... 8

Actin ..... 9

Tropomyosin ..... 9

Troponin ..... 10

**The Z-disk proteins and titin filaments** ..... 12

1.1.1.2.2 Thick and thin filament interaction – the sliding filament theory and cross-bridge cycling ..... 13

1.1.1.3 $Ca^{2+}$ handling and myofilament - interplay ..... 15

1.2 Regulation of cardiomyocyte contractility ..... 16

1.2.1 Physiological regulation of myofilament interaction ..... 17
1.2.1.1 Mechanistic regulation of sarcomeric contractility ..... 17
1.2.1.2 Intracellular signalling regulation of sarcomeric contractility ..... 19
1.2.1.2.1 Thin filament phosphorylation ..... 19
cTnI and cTnT are both known to be modified through phosphorylation by different kinases ..... 19
1.2.1.2.1.1 Functional effects of cTnI phosphorylation ..... 19
1.2.1.2.1.2 Functional effects of cTnT phosphorylation ..... 21
1.2.1.2.1.3 Functional effects of tropomyosin phosphorylation ..... 21
1.2.1.2.2 Thick filament phosphorylation ..... 21
1.2.1.2.2.1 Functional effects of RLC phosphorylation ..... 22
1.2.1.2.2.2 Functional effects of cMyBP-C phosphorylation ..... 22
1.2.1.2.3 Titin phosphorylation ..... 22
1.2.1.3 How does stretch affect sarcomeric phosphorylation levels? ..... 23
1.2.2 Cardiac redox signalling and contractile regulation ..... 24
1.2.2.1 ROS generation ..... 24
1.2.3 Physiological regulation of intracellular $Ca^{2+}$ handling ..... 24
1.2.3.1 $Ca^{2+}$ transient regulation through phosphorylation ..... 25
1.2.3.2 Physiological contractile regulation through redox signalling ..... 26
1.2.3.2.1 The slow force response to stretch – the Anrep effect ..... 27
1.3 Cardiac metabolism ..... 28
1.3.1 Myocardial fatty acid oxidation ..... 29
1.3.2 Myocardial glucose metabolism ..... 30
1.3.3 Myocardial substrate selectivity, cross-talk, and its alteration in disease states ..... 32
1.3.3.1 Myocardial metabolism in ischemia ..... 33
1.3.3.2 Myocardial metabolism in obesity and diabetes ..... 34
1.4 Diabetes mellitus and cardiac contractility ..... 35
1.4.1 Diabetic cardiomyopathy ..... 36
1.4.2 Proposed pathogenetic mechanisms in diabetes ..... 36
1.4.2.1 Lipotoxicity ..... 36
1.4.2.2 Myocardial fibrosis in diabetes ..... 37
1.4.2.3 Effects on $Ca^{2+}$ handling ..... 37

1.4.2.4 Effects on myofilament function ..... 39
1.4.2.5 Concomitant recordings of $Ca^{2+}$ handling and myofilament function in diabetes ..... 40
1.4.3 The cardiac phenotype in type 2 diabetes mellitus is usually confounded – diabetes, RAAS, and oxidative stress ..... 42
1.5 Mouse models of diabetes ..... 44
1.5.1 Type 1 DM-models ..... 44
1.5.1.1 Pharmacologically induced ..... 44
1.5.1.2 Genetic ..... 45
1.5.1.3 Spontaneous models ..... 46
1.5.2 Type 2 DM-models ..... 47
1.5.2.1 Diet induced ..... 47
1.5.2.2 Spontaneous ..... 47
1.5.3 A model of hypoinsulinaemia and peripheral insulin resistance ..... 48
1.6 Aim of this thesis, choice of model, and study design ..... 49
1.6.1 Aim of this thesis ..... 49
1.6.2 Choice of model ..... 49
1.6.3 Study design ..... 50
2 Material and methods ..... 51
2.1 Mouse line ..... 51
2.2 Mouse husbandry ..... 51
2.3 Diets ..... 51
2.4 Reagents and solutions ..... 52
2.5 Whole organism and plasma chemistry assessments ..... 52
2.5.1 Growth development curve ..... 52
2.5.2 Quantitative magnetic resonance (QMR) ..... 52
2.5.3 Glucose handling abilities ..... 53
2.5.3.1 Fasting blood glucose ..... 53
2.5.3.2 Intraperitoneal glucose tolerance test ..... 53
2.5.4 Plasma analysis ..... 54
2.5.4.1 Plasma separation ..... 54
2.5.4.2 Determination of plasma insulin concentration ..... 54
2.6 *In vivo* cardiac phenotyping ..... 55

2.6.1 *In vivo* haemodynamics ..... 55
2.6.1 Transthoracic echocardiography (TTE) ..... 56
2.7 Tissue harvesting ..... 57
2.8 Histology ..... 58
2.8.1 Organ preservation ..... 58
2.8.1.1 Cryosection preparation ..... 58
2.8.2 Sectioning and staining ..... 58
2.8.2.1 Cryosectioning ..... 58
2.8.2.2 Oil red O stain for lipid ..... 58
2.9 Molecular biology ..... 59
2.9.1 Frozen homogenisation ..... 59
2.9.2 Standard protein extraction procedure ..... 59
2.9.3 Myofilament isolation ..... 59
2.9.4 Protein concentration determination ..... 60
2.9.5 Sodium dodecyl sulphate polyacrylamide gel electrophoresis (SDS-PAGE) ..... 60
2.9.6 Protein total phosphorylation level determination by ProQ diamond staining ..... 61
2.9.7 Total protein levels determined by SyproRuby staining ..... 61
2.9.8 Immunoblotting ..... 62
2.9.8.1 Antibodies utilised ..... 63
2.9.8.2 Membrane stripping ..... 63
2.10 Quantitative reverse transcriptase-polymerase chain reaction (qRT-PCR) ..... 63
2.10.1 Oligos used ..... 64
2.11 Total tissue collagen levels ..... 65
2.12 Total tissue triglyceride levels ..... 66
2.13 Chemiluminescent determination of tissue reactive oxygen species (ROS) generation rate ..... 67
2.13.1.1 Superoxide ($O_2^-$) ..... 67
2.13.1.2 Peroxynitrite ($ONOO^-$) ..... 68
2.14 Study of single cardiomyocyte dynamics and $Ca^{2+}$ transients ..... 69
2.14.1 Cell isolation and preparation ..... 69
2.14.2 Single cell contractility recordings ..... 70

2.14.3 Single cell intracellular $Ca^{2+}$ transient recording ..... 72
2.15 Demembranated trabeculae ..... 73
2.15.1 Preparation of demembranated trabeculae ..... 73
2.15.2 Force recording from demembranated trabeculae ..... 74
2.15.2.1 Initial confirmation of function ..... 75
2.15.2.2 $Ca^{2+}$ induced isometric tension ..... 76
2.15.2.3 Rapid shortening and re-stretch ..... 77
2.15.2.4 Passive tension upon stretch ..... 78
2.15.2.5 Analysis of demembranated trabeculae data ..... 79
2.16 C2C12 cell culture and incubation experiments ..... 79
2.17 Statistical analysis ..... 80
3 Verification of the HFD fed C57BL6/J mouse as a model for studying the influences of obesity and systemic insulin resistance on cardiac function ..... 81
3.1 Introduction ..... 81
3.2 Weight development ..... 82
3.2.1 Total body weight ..... 82
3.2.2 Body composition analysis by quantitative magnetic resonance (QMR) ..... 83
3.3 Glucose homeostasis ..... 85
3.4 Cardiac *in vivo* phenotyping ..... 87
3.4.1 *In vivo* haemodynamics ..... 87
3.4.2 Transthoracic echocardiography (TTE) ..... 90
3.5 Post mortem dissection findings ..... 94
3.6 Discussion ..... 97
4 Characterisation of changes from HFD feeding on insulin signalling, metabolic substrate flux, redox state and fibrosis in myocardial whole tissue ..... 101
4.1 Introduction ..... 101
4.2 Assessment of myocardial insulin signalling and metabolic substrate utilisation ..... 101
4.2.1 Insulin signalling ..... 101
4.2.2 Assessment of altered metabolic flux ..... 103
4.2.2.1 Glucose metabolism ..... 103
4.2.2.2 Fatty acid metabolism ..... 105
4.3 Assessment of myocardial lipid content ..... 108

4.4 Assessment of myocardial redox status ..... 108
4.5 Assessment of cardiac fibrosis ..... 112
4.6 Discussion ..... 113
5 Effects from a HFD on unloaded cardiomyocyte dynamics and intracellular $Ca^{2+}$ transients ..... 119
5.1 Introduction ..... 119
5.2 Unloaded cardiomyocyte dynamics and $Ca^{2+}$ handling ..... 119
5.2.1 Unloaded cardiomyocyte dynamics ..... 120
5.2.2 $Ca^{2+}$ handling ..... 126
5.3 $Ca^{2+}$ sarcomere length relationship ..... 132
5.4 Discussion ..... 133
6 Effects from a HFD on myofilament function in C57BL6/J myocardium ..... 137
6.1 Introduction ..... 137
6.2 Myofilament $Ca^{2+}$ sensitivity ..... 137
6.3 Actomyosin cross bridge dynamics ..... 138
6.3.1 Relative myosin heavy chain isoform expression levels ..... 140
6.4 Passive myofilament dynamics ..... 141
6.4.1 Titin isoform expression levels ..... 143
6.5 Determination of contractile protein phosphorylation levels ..... 144
6.6 Discussion ..... 146
7 Effects on NADPH oxidase 2 (NOX2) over expression on myofilament dynamics ..... 152
7.1 Introduction ..... 152
7.2 Verification of the model ..... 153
7.3 Morphometric data ..... 155
7.4 Myofilament functional assessment ..... 155
7.4.1 Thin filament function ..... 156
7.4.2 Actomyosin cross bridge dynamics ..... 157
7.4.3 Passive myofilament dynamics ..... 158
7.4.4 Myofilament protein total phosphorylation assessment ..... 159
7.5 AMPK activity and myofilament sensitisation ..... 160
7.5.1 Oxidative stress and AMPK activity in C2C12 myoblasts ..... 162
7.6 Discussion ..... 163
7.6.1 NOX2 as a physiological modulator of cardiac performance ..... 163

7.6.2 Chronic over activation of NOX2 may impair diastolic function and induce myocardial hypertrophic signalling pathways ..... 165
8 Discussion ..... 167
8.1 HFD feeding alters myocardial performance on whole organ as well as single cardiomyocyte level ..... 167
8.1.1 The whole organ effect from HFD is mild and suggestive of cardiac diastolic impairment ..... 167
8.1.2 Increased cardiomyocyte relaxation rate likely due to myofilament desensitisation to $Ca^{2+}$ ..... 168
8.1.2.1 Increased NOX activity may affect cardiomyocyte contractility via PKA ..... 170
8.1.3 Elevated LVEDP rise may be due to extracellular fibrosis ..... 170
8.1.4 Conclusions regarding origins of HFD induced cardiac dysfunction ..... 171
8.1.4.1 Cardiomyocyte confined changes ..... 171
8.1.4.2 Whole organ changes ..... 172
8.1.5 Desired methodological improvements ..... 172
8.2 Cardiac restricted NOX2 over-expression causes myofilament $Ca^{2+}$ sensitisation. ..... 173
8.2.1 Background ..... 173
8.2.1.1 ROS play a central role in mediating force response to stretch ..... 173
8.2.1.2 NOX2 is suggested to play a role in hypertension, and cardiac hypertrophy and arrhythmia, features of heart failure ..... 176
8.2.1.3 $Ca^{2+}$ sensitisation of the myofilament is a postulated mediator of inotropy, diastolic dysfunction, hypertrophy, and arrhythmia ..... 177
8.2.2 NOX2 over-expression increases myofilament $Ca^{2+}$ sensitivity and cross bridge cycling rate – physiological and pathogenetic implications ..... 179
8.2.2.1 Future work ..... 180
9 References ..... 182
Appendix 1 ..... 217

## LIST OF FIGURES, TABLES, AND EQUATIONS

**Figure 1:** Cardiomyocyte $Ca^{2+}$ handling ..... 2
**Figure 2:** Cardiac sarcomeric protein assembly ..... 6
**Figure 3:** Actomyosin cross-bridge cycling ..... 15
**Figure 4:** Cardiac metabolism ..... 29
**Figure 5:** Cardiac transmitral valve Doppler flow profile. ..... 57
**Figure 6:** $O_2^-$ production rate assessment through lucigenin assisted luminometry. ..... 68
**Figure 7:** Isolated murine cardiomyocytes ..... 70
**Figure 8:** Single cardiomyocyte contractility trace. ..... 71
**Figure 9:** Single cardiomyocyte $Ca^{2+}$ transient trace ..... 73
**Figure 10:** Tension trace during slack and re-stretch of a cardiac LV trabecula. ..... 77
**Figure 11:** Tension trace during passive stretch of relaxed cardiac LV trabeculae. ..... 79
**Figure 12:** Study time line ..... 82
**Figure 13:** The effect of HFD on weight development in the male C57BL6/J mouse ..... 83
**Figure 14:** Distribution of lean and fat mass upon HFD feeding in the male C57BL6/J mouse. ..... 84
**Figure 15:** Effect of HFD on fasting blood glucose and insulin in the C57BL6/J mouse . 86
**Figure 16:** Effect of HFD feeding on peripheral insulin resistance in the C57BL6/J mouse ..... 86
**Figure 17:** Heart rate as assessed by intraventricular pressure catheterisation ..... 87
**Figure 18:** Pressure recording from the proximal aorta. ..... 88
**Figure 19:** Pressure recording from the left ventricle ..... 88
**Figure 20:** Maximum left ventricle pressure acceleration and deceleration rates ..... 89
**Figure 21:** Left ventricle ejection fraction and shortening by transthoracic echocardiography ..... 90
**Figure 22:** Left ventricle end diastolic and systolic volumes by transthoracic echocardiography ..... 91
**Figure 23:** Left ventricle end diastolic wall diameters by transthoracic echocardiography ..... 92
**Figure 24:** Diastolic function as by transmitral Doppler flow pattern. ..... 93
**Figure 25:** Effects of HFD on heart size in the C57BL6/J mouse ..... 94
**Figure 26:** Hepatic lipid accumulation assessment as by Oil-Red O staining ..... 95
**Figure 27:** Myocardial insulin signalling as assessed by Akt phosphorylation. ..... 102
**Figure 28:** Effect on GLUT4 expression from HFD feeding ..... 103
**Figure 29:** Effect of HFD feeding on GSK3β phosphorylation and total expression levels ..... 104
**Figure 30:** Myocardial fatty acid handling. ..... 107
**Figure 31:** Effect of HFD on myocardial triglyceride accumulation ..... 108
**Figure 32:** Effect of HFD feeding on myocardial baseline $O_2^-$ production rate. ..... 109
**Figure 33:** Effect of HFD feeding on myocardial NOX activity ..... 110
**Figure 34:** Effect of HFD feeding on myocardial NOS activity. ..... 111
**Figure 35:** Effect of HFD feeding on myocardial peroxynitrite generation ..... 111

**Figure 36:** The effect of HFD on myocardial collagen 3 expression. 112
**Figure 37:** The effect of HFD on myocardial total collagen content 112
**Figure 38:** Single cell contractility traces 120
**Figure 39:** Single cell baseline sarcomere length 121
**Figure 40:** Single cell fractional shortening 122
**Figure 41:** Single cell contraction rate 123
**Figure 42:** Single cell relaxation rate 124
F**igure 43:** The effect of stimulation frequency on single cell relaxation rate 125
**Figure 44:** Single cell $Ca^{2+}$ transient traces 126
**Figure 45:** Single cell baseline $Ca^{2+}$ levels 127
**Figure 46:** Single cell maximum $Ca^{2+}$ amplitudes 128
**Figure 47:** Single cell $Ca^{2+}$ release rate 129
**Figure 48:** Single cell $Ca^{2+}$ decay rate 130
**Figure 49:** The effect of stimulation frequency on single cell $Ca^{2+}$ decay rate. 131
**Figure 50:** Single cell $Ca^{2+}$ SL relationship 132
**Figure 51:** Single cell based assessment of unloaded myofilament $Ca^{2+}$ sensitivity. 133
**Figure 52:** $Ca^{2+}$ force relationship at 2.2 μm. 137
**Figure 53:** Effect of HFD feeding on thin filament $Ca^{2+}$ activation. 138
**Figure 54:** Effect of HFD feeding on maximum force generation in left ventricle trabeculae 139
**Figure 55:** Effect of HFD feeding on actomyosin cross bridge cycling rate 140
**Figure 56:** Effect of HFD feeding on MYH7 expression levels 140
**Figure 57:** Effect of HFD on passive tension in demembranated LV cardiac trabeculae upon stretch 142
**Figure 58:** Effect of HFD on relative expression levels of titin isoforms at w 40 lookign at mRNA levels 143
**Figure 59:** ProQ Diamond total phosphorylation staining in relation to total protein as assessed by SyproRuby. 144
**Figure 60:** Effect of HFD feeding on total phosphorylation cMyBP-C levels in relation to total protein as assessed by ProQ diamond and SyproRuby staining. 145
**Figure 61:** Effect of HFD feeding on cTnI phosphorylation at S23/24 assessed by immunoblotting. 146
**Figure 62:** Confirmation of NOX2 protein overexpression in ventricular myocardium 153
**Figure 63:** Functional confirmation of NOX derived overproduction of $O_2^-$ from NOX2 over expression 154
**Figure 64:** Assessment of cardiac hypertrophy effect from NOX2 overexpression 155
**Figure 65:** Assessment of effect from NOX2 overexpression myofilament $Ca^{2+}$ sensitivity 156
**Figure 66:** Assessment of the effect from NOX2 overexpression on actomyosin cross bridge interaction. 157
**Figure 67:** Assessment of the effects rom NOX2 overexpression on passive stiffness in LV demembranated trabeculae. 158

**Figure 68:** Assessment of effect of NOX2 overexpression on cTnI total phosphorylation levels....159
**Figure 69:** Effect from NOX2 overexpression on cTnI (S23/24) phosphorylation levels. ....160
**Figure 70:** Effects of S150 phosphorylation on force $Ca^{2+}$ dependence in demembranated cardiac trabeculae ....161
**Figure 71:** Effect of NOX inhibition and $O_2^-$ scavenging on AMPK T172 phosphorylation ....162

**Table 1:** The effect of HFD feeding on the organ weight in the C57BL6/J mouse....97

**Equation 1:** Four parameter Hill equation....76
**Equation 2:** Single exponential curve fit ....77
**Equation 3:** Exponential growth equation....78

## List of abbreviations

| | |
|---|---|
| ACER | animal care and ethical review |
| ADP | adenosine diphosphate |
| AMP | adenosine monophosphate |
| AMPK | AMP activated kinase |
| AP | action potential |
| ATII | angiotensin II |
| ATP | adenosine triphosphate |
| AV | atrioventricular |
| BCA | bicinchoninic acid |
| BDM | 2,3-Butanedione monoxime |
| CaMKII | $Ca^{2+}$ calmodulin kinase II |
| CCD-camera | charge-couple device camera |
| CICR | $Ca^{2+}$ induced $Ca^{2+}$ release |
| cMHC | cardiac myosin heavy chain |
| cMyBP-C | cardiac myosin binding protein C |
| CO | cardiac output |
| cTnC, I, T | cardiac troponin C, I, T |
| ctrl | control |
| DA | distal arthrogryposis |
| DAP | diastolic arterial pressure |
| DM | diabetes mellitus |
| DMSO | dimethyl sulfoxide |
| DMEM | Dulbecco's modified Eagle's media |
| EAD | early after depolarisation |
| EC-coupling | excitation-contraction coupling |
| ECG | electrocardiography, electrocardiogram |
| EF | ejection fraction |
| EGTA | ethylene glycol tetraacetic acid |
| ELC | essential light chain |
| ELISA | enzyme linked immunosorbent assay |
| ET-1 | endothelin-1 |
| $FADH_2$ | flavine adenine dinucleotide, reduced form |
| FAT/CD36 | fatty acid transporter/cluster of differentiation 36 |
| FATBP | fatty acid transport binding protein |
| FFA | free fatty acid |
| FS | fractional shortening |
| G-6-P | glucose-6-phosphate |
| GA | general anaesthesia |
| GAD | glutamic acid decarboxylase |
| GLUT | glucose transporter |
| GSK3β | glycogen synthase kinase 3β |
| HCM | hypertrophic cardiomyopathy |
| HEPES | 4-(2-hydroxyethyl)-1-piperazineethanesulfonic acid |
| HFD | high fat diet |
| HFSD | high fat and sugar diet |
| HRPO | horse-radish peroxidase |
| HSD | high sugar diet |
| IPGTT | intraperitoneal glucose tolerance test |

| | |
|---|---|
| IR | insulin receptor |
| IRS | insulin receptor substrate |
| IVC | individually ventilated cages |
| IVRT | isovolumic relaxation time |
| LAD | left anterior descending |
| LTCC | L-type $Ca^{2+}$ channel |
| LV | left ventricle |
| LVEDD | left ventricle end diastolic dimension |
| LVEDP | left ventricle end diastolic pressure |
| LVEF | left ventricle ejection fraction |
| LVESD | left ventricle end systolic dimension |
| LVESP | left ventricle end systolic pressure |
| MAP | mean arterial pressure |
| MCT | monocarboxylate transporter |
| mCPT1 | muscle carnitine palmitoyl transferase-1 |
| MLCK | myosin light chain kinase |
| NADH | nicotinamide adenine dinucleotide, reduced form |
| NADPH | nicotinamide adenine dinucleotide phosphate, reduced form |
| NCX | sodium calcium exchanger |
| NOS | nitric oxide synthase |
| NOX | NADPH oxidase |
| OCT | optimal cutting temperature |
| PBS | phosphate buffered saline |
| PDH | pyruvate dehydrogenase |
| PDK | pyruvate dehydrogenase kinase |
| PFK | phosphofructokinase |
| PGC1α | peroxisome proliferator-activated receptor gamma coactivator 1-α |
| PI3K | phosphatidylinositol 3 kinase |
| PKA, B, C, D, G | protein kinase A, B, C, D, G |
| PLN | phospholamban |
| PPARα | peroxisome proliferator-activated receptor α |
| QMR | quantitative magnetic resonance |
| RAAS | renin-angiotensin-aldosterone-system |
| rev | reversal |
| RLC | regulatory light chain |
| RyR | ryanodine receptor |
| SAP | systolic arterial pressure |
| SDS | sodium dodecyl sulfate |
| SDS-PAGE | SDS-polyacrylamide gel electrophoresis |
| SERCA | sarcoendoplasmatic reticulum |
| SL | sarcomere length |
| SR | sarcoplasmatic reticulum |
| TG | triglyceride/transgenic |
| TGF | transforming growth factor |
| TL | tibia length |
| TTE | transthoracic echocardiography |
| T-tubule | transverse tubule |